Ab initio description of lattice dynamics in oxide semiconductors

Ab initio Beschreibung der Gitterdynamik in oxidischen Halbleitern

JUSTUS-LIEBIG-
UNIVERSITÄT
GIESSEN

DISSERTATION

submitted for the degree of

Doctor rerum naturalium
(*Dr. rer. nat.*)

by
M. Sc. Marcel Giar

Supervisor: Prof. Dr. Christian Heiliger
AG Theoretische Festkörperphysik

Institut für Theoretische Physik
Justus-Liebig-Universität Gießen

Gießen, October 2017

Contents

1 Introduction

In modern electronic structure theory of solid state materials, large focus is put on the description of optical properties. This often implies optical absorption spectra of semiconducting/insulating materials and related quantities such as Raman scattering intensities. A reliable description of optical properties of materials is invaluable for a wide field of practical applications such as optoelectronics and solar cell fabrication.

In recent years, density functional theory (DFT) has become the "workhorse" for *ab initio* calculations in the field of solid state theory.[1–4] While traditional formulations were limited to a static quantum mechanical description of a solid, more recently time-dependent DFT (TDDFT) has emerged as an accurate formulation of time-dependent quantum mechanics.[5,6]

The description of the interaction of light with a solid boils down to the calculation of the dielectric susceptibility $\chi(\omega)$, or likewise the dielectric function $\epsilon(\omega)$. The accuracy of the theoretical description is demonstrated by the "correctness" of the calculated dielectric functions in comparision to experiment. A large pool of methods exists for describing dielectric properties of a material, ranging from computationally rather cheap to very sophisticated methods, all of which differ by their predictive power. The simplest conceivable method for calculating ϵ within the DFT framework is the independent particle approximation (IPA). In order to overcome the well-documented band gap problem, many body perturbation theory is included by the so-called *GW* approximation.[7,8] The inclusion of electron-hole pairs for the optical absorption spectra is achieved by means of the Bethe-Salpeter equation (BSE).[9]

From a physical point of view, Raman scattering combines the optical absorption properties governed by the electronic subsystem and the vibrational properties of a solid as described by quasiparticles called "phonons". It therefore is a very versatile tool for the analysis of material properties. As a result, this technique lends itself nicely for, e.g., (i) identifying materials by their Raman spectroscopic "fingerprint", (ii) analysing defect structures[10,11] or crystal surfaces, (iii) clinical diagnostics of cells, tissues, or foreign matter present in the human body.[i]

A schematic representation for an experimental Raman scattering setup is shown in fig. 1.1: A monochromatic light beam (in many cases a laser in the visible part of the electromagnetic spectrum) is sent on a material sample. While a large amount of the incident light beam will be scattered elastically, a tiny fraction will penetrate the crystal and is scattered inelastically by elementary excitations of the material such as phonons. The scattered light with its energy changed by the scattering process is amplified by an appropriate setup of optical devices. The data is analysed by a computer yielding the Raman spectrum which gives a detailed account of the energy of the scattering phonons (the phonon frequency is measured by the so-called "Raman shift").[12]

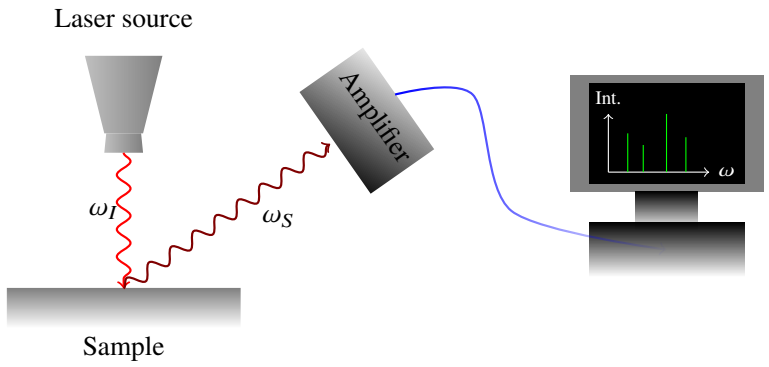

FIGURE 1.1: Schematic representation of the measurement setup used for collecting Raman spectra. A laser beam of frequency ω_I impinges on the surface of a material sample. A tiny portion penetrates the sample and is scattered by elementary excitations of the material such as phonons. The light is backscattered inelastically with frequency ω_S ($\omega_S \neq \omega_I$) and is amplified by an appropriate set of optical devices. The signal is analysed by a computer to give the Raman spectrum (intensity vs frequency of the phonons).

[i] See for example `https://www.raman4clinics.eu`

The measured intensity in a Raman experiment is proportional to λ_L^{-4} (λ_L: laser wavelength); therefore, intensities are generally increased when the laser energy is increased. Measured intensities can vary drastically when changing the laser excitation energy, depending on whether the optical excitation is resonant or non-resonant with an electronic transition. Briefly, non-resonant Raman scattering involves electrons being promoted to "virtual states", while in case of resonant Raman scattering real electronic transitions between (eigen)states of the solid occur. These transitions may eventually lead to the formation of electron-hole pairs (excitons).

Obviously, for an accurate theoretical description of Raman scattering, the correct calculation of the optical absorption gap and the inclusion of excitons appear to be very important. However, standard DFT methods like the local density approximation (LDA) or the generalised gradient approximation (GGA) oftentimes poorly describe the electronic band gap and do not account for excitonic effects. Approaches like hybrid functionals[13–16] or LDA+U in many cases can remedy the shortcomings of the standard methods in terms of the accuracy of the calculated band gap. Due to the evaluation of an additional non-local term (exchange kernel), hybrid calculations usually involve a very large computational effort ($\lesssim 10\times$ larger than standard DFT calculations). Nevertheless, in order to obtain a good description of the Raman scattering properties of a material, the vibrational *as well as* the electronic properties need to be accurately described. Luckily, calculations based on the LDA($+U$)/GGA($+U$) often result in a good description of the vibrational properties of semiconducting materials (as will become obvious in this work).

Apart from the dielectric function, the other key ingredient for the calculation of Raman scattering intensities are (zone-centre) phonons. Many physical phenomena of solids such as thermal conductivity and the related field of thermoelectrics, thermodynamic properties (especially the heat capacity), and of course Raman and infra-red spectroscopy are connected to phonons. Being able to reliably calculate lattice vibrational properties therefore is desireable, indeed. The quantity of interest in phonon calculations are the interatomic force constants (FCs) which, loosely speaking, are generalised spring constants connecting atoms. Within the framework of *ab initio* approaches, FCs are either calculated from density functional perturbation theory (DFPT),[17–19] or from numerical derivatives (frozen phonon approach). However, DFPT generally is not implemented for more "advanced" methods such as hybrid functionals,[13–16] making the finite difference approach a welcome alternative. Recent developments concerning this method have made it competitive with DFPT calculations.[20]

A central quantity related to Raman scattering is the so-called Raman susceptibility α^m which essentially is the derivative of the dielectric susceptibity χ along a phonon displacement pattern $\mathbf{u}_m$:

$$\alpha^m \propto \lim_{h\to 0} \frac{\chi(\{\mathbf{x}^{(0)}\} + h\mathbf{u}_m) - \chi(\{\mathbf{x}^{(0)}\})}{h}, \tag{1.1}$$

where $\{\mathbf{x}^{(0)}\}$ are atomic equilibrium positions. In order to obtain a full Raman spectrum, this derivative must be evaluated for all phonon modes of the crystal that allow for Raman scattering (indeed, not all modes are "Raman active"). Therefore, the computational complexity and the respective effort are largely enhanced in comparison to "common" electronic structure calculations. Raman susceptibilities can be calculated from DFPT, however, within this formalism only the static limit of the dielectric function (ϵ^∞) can be obtained. Therefore, the dependence of the Raman intensities on the laser frequency cannot be assessed. Another possibility is to calculate the derivative from eq. (1.1) with a suitable finite difference stencil. This can be done in conjunction with any method used for the calculation $\epsilon(\omega)$ (IPA, *GW*, BSE, ...). Indeed, a theoretically accurate description of the Raman scattering properties of a solid is (contrary to some people's unsophisticated conviction) beyond state of the art.

An example comparing the usage of both the IPA and the BSE approach for the calculation of the Raman susceptibility is shown in fig. 1.2.[12] In the special case of Si, in comparison to experiment, the computationally very demanding BSE approach yields much better results than the conceptually rather simple IPA. Indeed, this points towards the necessity of including excitonic effects in the calculation of Raman spectra. However, in case of more complicated materials (indeed, these are the particularly interesting cases in many applications) possessing lower symmetry and different kinds of atoms, employing methods as demanding as BSE results in a very large computational effort. For example, Gillet [12] has estimated the (maximal) storage demand for

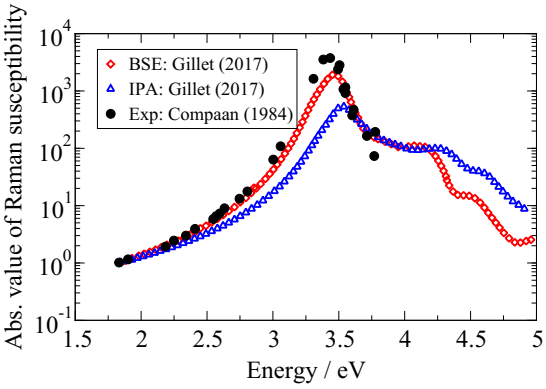

FIGURE 1.2: Comparison of the theoretical (BSE and IPA) and experimental Raman susceptibility of silicon.[12,21] The scale of the ordinate in arbitrary units.

the calculation of a converged dielectric function of Si (2 atoms per unit cell) using BSE to ~34 TB, and computational time on (sequential) computers is assumed to range from days to years.[12] Requirements for the computation of Raman scattering intensities should even be larger. Even for modern computer architectures that are combined to powerful supercomputers this provides an exceptional challenge. For comparison, the groundstate structure of CuO[22] has 16 atoms in the magnetic unit cell and "only" monoclinic symmetry. In effect, required computational resources are accordingly higher for calculations of optical properties from BSE.

In the present work, lattice dynamical calculations as well as calculations of the Raman scattering intensities will be carried out for the material system of copper oxides, consisting of cubic Cu_2O, tetragonal Cu_4O_3, and monoclinic CuO. This system of binary oxides has recieved recent attention due to its potential applications in solar cell fabrication.[23] These sustainable materials provide a unique possibility to tune the optical and electronic properties from insulating to metallic conduction.

Cu_2O exhibits an unusual Raman spectrum which appears to be dominated by point defects such as certain types of Cu-vacancies.[10,11] While CuO is rather well-studied in terms of its Raman scattering properties at room temperature, its low-temperature Raman spectrum is considerably different.[24] CuO exhibits a change in structure at 213 K (an antiferromagnetic phase change to be more precise),[22] and the resulting changes in vibrational properties are worthwhile investigating. Cu_4O_3, which is a phase to be considered intermediate to Cu_2O and CuO, indeed is not too extensively studied in terms of its vibrational as well as electronic properties. In particular, Raman spectra so far have only been measured and not calculated.

In view of this, it shall be the main purpose of the work to investigate the vibrational properties of copper oxides in detail. The calculations will involve phonon dispersions and derived quantities of all three phases based on the finite difference approach for the FCs (section 3.3). Special attention will also be paid to the Raman scattering properties of CuO and Cu_4O_3 (section 3.4).

This thesis is structured as follows: In chapter 2 the theoretical foundations needed for the calculation of vibrational properties of solids from *ab initio* methods are summarised. The chapter 3 is devoted to (1) the description of the phonon dispersions of the copper oxides. Special emphasis is put on the treatment of dipole-dipole interactions that arise for long-wavelength vibrations in polar materials. (2) The Raman scattering properties of CuO and Cu_4O_3. In this context the room temperature and the low temperature phases of CuO are compared. Raman spectra are compared to experiment and explanations for the differences found for the room temperature and the low temperature Raman spectrum are outlined. Additionally, the dependence of the Raman properties of Cu_4O_3 under equilibrium conditions and hydrostatic pressure are examined. Calculations are compared to recent experimental results, yielding rather good accordance for the Raman scattering intensities.

2 Theoretical Foundations

This chapter contains the theoretical methods upon which the calculations in this work rely. Above all, this is density functional theory (DFT) which is the state-of-the-art method for calculating the electronic structure of materials within the field of solid state theory (section 2.1). DFT gives access to all "ingredients" needed for the calculation of material properties such as the phonon dispersion and Raman scattering intensities.

The fundamentals of the (classical) theory of lattice dynamics are outlined in section 2.2. Particular emphasis is put on the role of the treatment of lattice vibrations in polar semiconducting/insulating materials which is more complicated than in the case of elemental materials due to the presence of long-ranged dipole-dipole interactions. Apart from that, a rather qualitative account on the theory of Raman scattering is given. Within this scope, some remarks on the lattice dynamical applications of group theory are made, which in my view is one the most beautiful methods in the field of theoretical solid state science.

2.1 The electronic structure

2.1.1 The electronic many-body problem

Calculations within the field of solid state science often deal with an electronic many-body problem. The general physics of a solid state system may be described through Schrödinger's equation, in particular through an appropriate Hamiltonian operator H. In case of periodic bulk systems—as they are considered within this work—this requires the treatment of atomic nuclei and their electrons. The non-relativistic, time-independent Hamiltonian operator is of the form:

$$H = T_{\text{nucl}} + T_{\text{e}} + v_{\text{e-e}} + v_{\text{nucl-e}} + v_{\text{nucl-nucl}}, \tag{2.1}$$

with

- T_{nucl} . . . kinetic energy of nuclei
- T_{e} . . . kinetic energy of electrons
- $v_{\text{e-e}}$ . . . potential for electron-electron interaction
- $v_{\text{nucl-e}}$ . . . potential for nuclei-electron interaction
- $v_{\text{nucl-nucl}}$ . . . potential for nuclei-nuclei interaction.

The resulting eigenvalue equation is

$$H\,|\Phi\rangle = E\,|\Phi\rangle\,. \tag{2.2}$$

The wavefunction for a system governed by this Hamiltonian operator will depend on electron coordinates and the positions of the nuclei, $\Phi \equiv \Phi(\mathbf{r}_1, \ldots, \mathbf{r}_{N_\text{e}}; \mathbf{R}_1, \ldots \mathbf{R}_{N_\text{nucl}})$, $N_{\text{e/nucl}}$ being the number of electrons/nuclei. Thence, the above eigenvalue equation (2.2) can only be solved within very drastic approximations. The most common one is the so-called Born-Oppenheimer approximation.[25] The assumption of this approximation scheme is that, due to the large difference in masses, the reaction of the electronic system to a movement of the nuclei essentially is instantaneous. As a consequence, the potential felt by the electrons due to the nuclei is approximately quasi-static. Therefore, for the further treatment, the only terms retained from the above expression for the Hamiltonian, eq. (2.1), are

$$H_\text{e} = T_\text{e} + v_{\text{e-e}} + v_{\text{nucl-e}}. \tag{2.3}$$

From Born-Oppenheimer approximation it follows that the interaction of the electrons with the nuclei is to be viewed as an external potential, v_{ext}. The interaction of the electrons amongst each other is purely coulombic.

Then, the eigenvalue equation for the purely electronic part of the Hamiltonian reads (atomic Hartree units used: $\hbar = m_\mathrm{e} = 1$)

$$\left(-\tfrac{1}{2}\sum_{k=1}^{N_\mathrm{e}}\frac{\partial^2}{\partial\mathbf{r}_k^2} + \tfrac{1}{2}\sum_{k\neq k'}^{N_\mathrm{e}}\frac{1}{|\mathbf{r}_k-\mathbf{r}_{k'}|} + \sum_{k=1}^{N_\mathrm{e}} v_\mathrm{ext}(\mathbf{r}_k)\right)\Psi(\{\mathbf{r}_{k'}\}) = E_\mathrm{e}(\{\mathbf{x}_s\})\Psi(\{\mathbf{r}_{k'}\}), \tag{2.4}$$

where the electron eigenenergy parametrically depends on the coordinates of the nuclei $\{\mathbf{x}_s\}_{s=1,\ldots,N_\mathrm{nucl}}$. Unfortunately, the wavefunction $|\Psi\rangle$ still depends on all electronic coordinates which – for a typical number of 10^{23} electrons in a solid – renders infeasible a direct solution of the latter equation.

2.1.2 Density functional theory (DFT)

Instead of aiming at directly solving for the many-particle wavefunction $|\Psi\rangle$ resorting to the electron density, $n(\mathbf{r})$, given by

$$n(\mathbf{r}) = N_\mathrm{e}\int d^3\mathbf{r}_2\cdots\int d^3\mathbf{r}_{N_\mathrm{e}}\left|\Psi(\mathbf{r},\mathbf{r}_2,\ldots,\mathbf{r}_{N_\mathrm{e}})\right|^2, \tag{2.5}$$

has proven to be an adjuvant approach. The key ideas behind this approach have been formulated by Hohenberg and Kohn [1] (HK) in 1964 and later were generalised by Levy[3]. The based-upon theory has become known as density functional theory (DFT).

Density as a basic variable The statements of the above-mentioned approach are contained in the following theorem:

Theorem (Hohenberg-Kohn theorem)**.** *For a given non-degenerate groundstate the density $n(\mathbf{r})$ uniquely specifies the external potential $v_\mathrm{ext}(\mathbf{r})$ up to a constant. Particularly,*

*(i) The total energy is a **functional** of the electron density:*

$$E_\mathrm{HK}[n] := \int d^3\mathbf{r}\; v_\mathrm{ext}(\mathbf{r})n(\mathbf{r}) + F_\mathrm{HK}[n], \tag{2.6a}$$

$$F_\mathrm{HK}[n] := \min_{|\Psi\rangle\to n}\langle\Psi|T_\mathrm{e}+v_\mathrm{ee}|\Psi\rangle\,. \tag{2.6b}$$

The minimisation is to be carried out over all wavefunctions $|\Psi\rangle$ that give rise to the electron density $n(\mathbf{r})$. $F_\mathrm{HK}[n]$ is a universal functional in the sense that, for a particular system, it does not depend on the external potential v_ext.

(ii) The energy functional obeys a variational principle,

$$E_\mathrm{HK}[n] \geq E_\mathrm{HK}[n_\mathrm{gs}], \tag{2.7a}$$

$$\delta E_\mathrm{HK}[n]|_{n_\mathrm{gs}} = 0, \tag{2.7b}$$

where n_gs is the groundstate density.

(iii) The energy functional assumes the groundstate energy E_gs when the density equals the groundstate density,

$$E_\mathrm{HK}[n_\mathrm{gs}] = E_\mathrm{gs}. \tag{2.8}$$

The rather formidable endeavour of finding the minimum of $\langle\Psi|H_\mathrm{e}|\Psi\rangle$ with respect to the $3N_\mathrm{e}$-dimensional wavefunction $|\Psi\rangle$ has been converted into finding the minimum of $E_\mathrm{HK}[n]$ with respect to the 3-dimensional quantity $n(\mathbf{r})$.

Kohn-Sham equations The Hohenberg-Kohn theorem rigorously identifies the energy as a unique functional of the electron density. However, it does not offer any concrete procedure for finding the universal functional F_{HK}. From the formally exact HK variational principle Kohn and Sham[2] (KS) extracted a practical scheme involving non-interacting particles $|\varphi_k\rangle$ moving in an effective potential that mimics the influence of the other electrons. The clue is that this system of non-interacting particles produces the *same* electron density as the interacting one.

For non-interacting particles the density is easily calculated:

$$n(\mathbf{r}) = \sum_{k=1}^{N_\mathrm{e}} |\varphi_k(\mathbf{r})|^2, \tag{2.9}$$

while the kinetic energy functional of the interacting system, $T[n]$, is replaced by a *non-interacting kinetic energy functional*

$$T_\mathrm{s}[n] = -\tfrac{1}{2} \sum_{k=1}^{N_\mathrm{e}} \int d^3\mathbf{r}\ \varphi_k^*(\mathbf{r}) \frac{\partial^2}{\partial \mathbf{r}^2} \varphi_k(\mathbf{r}). \tag{2.10}$$

Then, let the energy functional assume the form

$$\begin{aligned} E_{\mathrm{KS}}[n] &= T_\mathrm{s}[n] + \int d^3\mathbf{r}\ v_{\mathrm{ext}}(\mathbf{r}) n(\mathbf{r}) \\ &+ \tfrac{1}{2} \int d^3\mathbf{r} \int d^3\mathbf{r}'\ \frac{n(\mathbf{r}) n(\mathbf{r}')}{|\mathbf{r} - \mathbf{r}'|} + E_{\mathrm{xc}}[n](\mathbf{r}). \end{aligned} \tag{2.11}$$

This expression defines the exchange-correlation energy E_{xc} that accounts for particle interactions. Variation of the total energy function with respect to $\langle\varphi_k|$ and enforcing normalisation of the KS-orbitals $|\varphi_k\rangle$ with Lagrangian parameters ϵ_k:

$$\frac{\delta}{\delta \langle\varphi_{k'}|} \left[E_{\mathrm{KS}}[n](\mathbf{r}) - \sum_{k=1}^{N_\mathrm{e}} \epsilon_k \left(\langle\varphi_k|\varphi_k\rangle - 1 \right) \right] = 0, \tag{2.12}$$

which, with the aid of eq. (2.9), results in a set of self-consistent (SCF) Schrödinger-like equations known as KS-equations:

$$\left(-\frac{1}{2} \frac{\partial^2}{\partial \mathbf{r}^2} - v_{\mathrm{KS}}[n](\mathbf{r}) - \epsilon_k \right) \varphi_k(\mathbf{r}) = 0, \tag{2.13}$$

with the previously mentioned (effective) KS-potential

$$v_{\mathrm{KS}}[n](\mathbf{r}) = v_{\mathrm{ext}}(\mathbf{r}) + \int d^3\mathbf{r}'\ \frac{n(\mathbf{r}')}{|\mathbf{r} - \mathbf{r}'|} + \frac{\delta}{\delta n(\mathbf{r}')} E_{\mathrm{xc}}[n](\mathbf{r}) \Big|_{n=n_{\mathrm{gs}}}. \tag{2.14}$$

A schematic representation of the self-consistent solution procedure is presented in Fig. 2.1. The essential details of this section may be summarized as follows:[4]

- The task of calculating the groundstate of an interacting many-particle system has been transferred to solving for the groundstate of a non-interacting single particle system with an effective potential. This fictitious local potential, $v_{\mathrm{KS}}(\mathbf{r})$, for non-interacting particles as represented by the orbitals $|\varphi_k\rangle$, produces the interacting particle density $n(\mathbf{r})$ of the fully interacting system.
- Neither the KS-orbitals $|\varphi_k\rangle$ nor the Lagrangian multipliers ϵ_k—although commonly interpreted as *(eigen)energies*—bear a direct physical meaning. The connection to physics is given by (i) the connection to the correct particle density $n(\mathbf{r})$, and (ii) that the eigenvalues ϵ_k deliver correct ionisation energies (see Almbladh and Barth [26]).

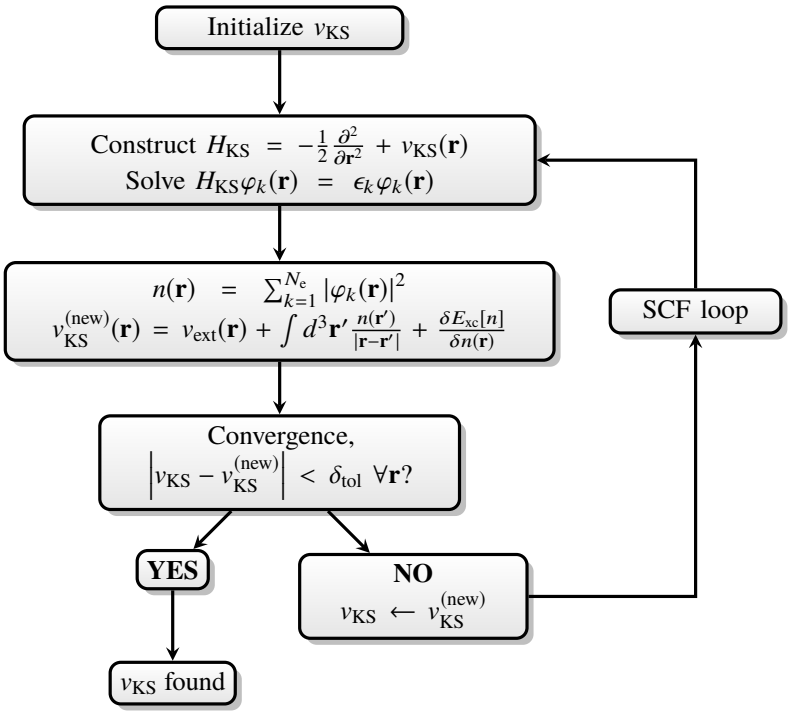

FIGURE 2.1: Schematic representation of the self-consistent procedure for the solution of the Kohn-Sham equations. δ_{tol} is a numerical tolerance value used to quantify the level of convergence of the KS-potential between consecutive iterations within the self-consistent loop.

2.2 Lattice dynamics

2.2.1 Equations of motion of a crystal lattice

In the following I shall consider an infinitely extended crystal generated by unit cells containing a certain number of atoms. The lattice points are obtained as integer linear combinations of some generating lattice vectors $\mathbf{a}_1$, $\mathbf{a}_2$, $\mathbf{a}_3$,

$$\mathbf{R}_l = \sum_{\mu=1}^{3} l_\mu \mathbf{a}_\mu, \quad l_\mu \in \mathbb{Z} \text{ and } l = \{l_\mu\}_{\mu=1,2,3} \tag{2.15}$$

while the equilibrium position of the sth atom in the lth unit cell is given by

$$\mathbf{x}_{l,s}^{(0)} = \mathbf{R}_l + \mathbf{x}_s^{(0)}. \tag{2.16}$$

The total potential energy U of the crystal within Born-Oppenheimer approximation is given by $U = E_\mathrm{e} + v_\mathrm{nucl-nucl}$ and may be considered as a function of the instantaneous atomic positions, $U \equiv U(\{\mathbf{x}_{l,s}\})$, with $\mathbf{x}_{l,s} = \mathbf{x}_{l,s}^{(0)} + \mathbf{u}_{l,s}$. As such it may be expanded about the equilibrium positions of the atoms in powers of atomic displacements $\mathbf{u}_{l,s}$:

$$U(\{\mathbf{x}_{l,s}\}) = U(\{\mathbf{x}_{l,s}^{(0)}\}) + \sum_{l,s,\mu} U_{l,s,\mu}^{(1)} u_{l,s,\mu} + \tfrac{1}{2} \sum_{ll',ss',\mu\mu'} U_{ll',ss',\mu\mu'}^{(2)} u_{l,s,\mu} u_{l',s',\mu'} + \cdots, \tag{2.17}$$

where in the so-called harmonic approximation higher-order terms than the second are neglected. The derivatives $U_{l,s,\mu}^{(1)}$, $U_{ll',ss',\mu\mu'}^{(2)}$, ... are evaluated at the equilibrium positions:

$$U_{l,s,\mu}^{(1)} = \left.\frac{\partial U(\{\mathbf{x}_{l,s}\})}{\partial u_{l,s,\mu}}\right|_{\{\mathbf{x}_{l,s}^{(0)}\}} \tag{2.18a}$$

$$U_{ll',ss',\mu\mu'}^{(2)} = \left.\frac{\partial^2 U(\{\mathbf{x}_{l,s}\})}{\partial u_{l,s,\mu} \partial u_{l',s',\mu'}}\right|_{\{\mathbf{x}_{l,s}^{(0)}\}}. \tag{2.18b}$$

The first-order coefficients simply represent the forces on the atoms which for the equilibrium positions must vanish, $U_{l,s,\mu}^{(1)} = -F_{l,s,\mu} = 0 \ \forall l, s, \mu$ if $\{\mathbf{x}_{l,s}\} = \{\mathbf{x}_{l,s}^{(0)}\} \ \forall l, s$. The second-order coefficients, henceforth denoted as $C_{l's'\mu'}^{l\,s\,\mu}$, are called interatomic force constants (FCs). These coefficients are symmetric in the indices (l, s, μ) and (l', s', μ'),

$$C_{l's'\mu'}^{l\,s\,\mu} = C_{l\,s\,\mu}^{l's'\mu'}, \tag{2.19}$$

which, assuming the crystal potential to be at least twice continuously differentiable, follows from the fact that the mixed second-order derivative is independent of the order in which the derivatives are taken. Further, due to the translational invariance of the crystal, the FCs must depend on the lattice vectors $\mathbf{R}_l$, $\mathbf{R}_{l'}$ only through their difference:

$$C_{l's'\mu'}^{l\,s\,\mu} = C_{0\ \ s'\mu'}^{l-l's\,\mu} = C_{l'-ls'\mu'}^{0\ \ s\,\mu}. \tag{2.20}$$

The equations of motion of the atoms in the crystal,

$$M_s \ddot{u}_{l,s,\mu} = F_{l,s,\mu} = -\frac{\partial U}{\partial u_{l,s,\mu}} = -\sum_{l',s',\mu'} C_{l's'\mu'}^{l\,s\,\mu} u_{l',s',\mu'}, \tag{2.21}$$

by making the substitution

$$u_{l,s,\mu} \equiv u_{l,s,\mu}(t) = w_{s,\mu}/\sqrt{M_s}\, e^{i\mathbf{q}^T\mathbf{R}_l - i\omega t} \tag{2.22}$$

may be transformed into a hermitian eigenvalue problem

$$\sum_{s',\mu'} C_{s'\mu'}^{s\,\mu}(\mathbf{q}) \big/ (M_s M_{s'})^{1/2}\, w_{m,\mathbf{q}}^{s',\mu'} = \omega_{m,\mathbf{q}}^2 w_{m,\mathbf{q}}^{s,\mu} \tag{2.23}$$

of the dynamical matrix $C_{s'\mu'}^{s\,\mu}(\mathbf{q})$ which is the lattice Fourier transform of the FCs

$$C_{s'\mu'}^{s\,\mu}(\mathbf{q}) = \sum_{l'} C_{l's'\mu'}^{0\,s\,\mu} e^{i\mathbf{q}^T\mathbf{R}_{l'}}. \tag{2.24}$$

2.2.2 Properties of the dynamical matrix

Since the dynamical matrix $C^{s\,\mu}_{s'\mu'}(\mathbf{q})$ is hermitian, the squared mode frequencies $\omega^2_{m,\mathbf{q}}$ are purely real and the eigenvectors $\{w_{s,\mu}(\mathbf{q})\}$ obey the orthonormality and closure conditions:

$$\sum_{s,\mu}[w^{s,\mu}_{m,\mathbf{q}}]^* w^{s,\mu}_{m',\mathbf{q}} = \delta_{mm'} \tag{2.25a}$$

$$\sum_{m} w^{s,\mu}_{m,\mathbf{q}}[w^{s',\mu'}_{m,\mathbf{q}}]^* = \delta_{ss'}\delta_{\mu\mu'}. \tag{2.25b}$$

Further, from eq. (2.24) it follows that $C^{s\,\mu}_{s'\mu'}(-\mathbf{q}) = [C^{s\,\mu}_{s'\mu'}(\mathbf{q})]^*$, such that, using the eigenvalue equation (2.23), the dispersion relation has the property that $\omega^2_{m\mathbf{q}} = \omega^2_{m,-\mathbf{q}}$.

From the demand of the forces $F_{l,s,\mu}$ being invariant under a rigid body translation it follows that the condition on the FCs reads

$$\sum_{l',s'} C^{0\,s\,\mu}_{l's'\mu'} = \sum_{s'} C^{s\,\mu}_{s'\mu'}(\mathbf{q}=\mathbf{0}) = 0 \quad \forall s,\mu,\mu'. \tag{2.26}$$

Using the eigenvalue equation, eq. (2.23), and setting $\mathbf{q}=\mathbf{0}$ and $w^{s,\mu}_{m,\mathbf{q}=\mathbf{0}} = \sqrt{M_s}u^{s,\mu}_{m,\mathbf{q}=\mathbf{0}}$:

$$\sum_{s'\mu'} C^{s\,\mu}_{s'\mu'}(\mathbf{q}=\mathbf{0})u^{s',\mu'}_{m,\mathbf{q}=\mathbf{0}} = \omega^2_{m,\mathbf{q}=\mathbf{0}} M_s u^{s,\mu}_{m,\mathbf{q}=\mathbf{0}}. \tag{2.27}$$

If now $\forall\mu'$ the displacement vector $u^{s',\mu'}_{m,\mathbf{q}=\mathbf{0}}$ is independent of the atomic index s', $u^{s',\mu'}_{m,\mathbf{q}=\mathbf{0}} \equiv u^{\mu'}_m$, the left-hand side vanishes due to the property expressed in eq. (2.26). The trivial solution $u^{\mu}_m \equiv 0$ shall be excluded and hence the only conclusion is that $\omega^2_{m\mathbf{q}=\mathbf{0}} = 0$ for each of the three values of μ. Such modes are referred to as acoustic modes, and therefore the condition formulated through eq. (2.26) is called "acoustic sum rule". The remaining $3N_{\mathrm{nucl}} - 3$ modes are called "optical modes", where N_{nucl} denotes the number of atoms per unit cell.

Under symmetry operations of the spacegroup of the crystal, $\{S|\mathbf{v}^{(S)} + \mathbf{R}_p\}$[i], atomic positions transform as $x_{l+p,s',\mu'} = \sum_\mu S_{\mu'\mu}x_{l,s,\mu} + v^{(S)}_{\mu'} + R_{p,\mu'}$. The FCs transform according to[27]

$$C^{l_1\,s_1\,\mu_1}_{l_{1'}s_{1'}\mu_{1'}} = \sum_{\mu\mu'} S_{\mu_1\mu}S_{\mu_{1'}\mu'}C^{l\,s\,\mu}_{l's'\mu'} \quad l_1, l_{1'} = l+p, l'+p. \tag{2.28}$$

The resulting transformation law for the dynamical matrix is

$$C(S\mathbf{q}) = \Gamma(S;\mathbf{q})C(\mathbf{q})\left[\Gamma(S;\mathbf{q})\right]^{-1}, \tag{2.29}$$

where

$$\Gamma^{s\,\mu}_{s'\mu'}(S;\mathbf{q}) = S_{\mu\mu'}\delta_{s,F(s';S)}\exp[i\mathbf{q}^T(\{S|\mathbf{v}^{(S)} + \mathbf{R}_p\}^{-1}\mathbf{x}_s - \mathbf{x}_{s'})], \tag{2.30}$$

and $F(s,S)$ is an atom transformation table that tells which atom s' is reached from atom s upon applying the spacegroup operation with rotational part S.[27] The eigenvalue equation (2.23) at the rotated wavevector $S\mathbf{q}$

$$\sum_{s',\mu'} C^{s\,\mu}_{s'\mu'}(S\mathbf{q}) \big/ (M_s M_{s'})^{1/2}\, w^{s',\mu'}_{m,S\mathbf{q}} = \omega^2_{m,S\mathbf{q}} w^{s,\mu}_{m,S\mathbf{q}}, \tag{2.31}$$

upon operating with $[\Gamma(\mathbf{q};S)]^{-1}$ from the left and with the aid of equation (2.29) becomes[27]

$$\sum_{s',\mu'} C^{s\,\mu}_{s'\mu'}(\mathbf{q}) \big/ (M_s M_{s'})^{1/2}\,[[\Gamma(S;\mathbf{q})]^{-1}\mathbf{w}_{m,S\mathbf{q}}]_{s',\mu'} = \omega^2_{m,S\mathbf{q}}[[\Gamma(S;\mathbf{q})]^{-1}\mathbf{w}_{m,S\mathbf{q}}]_{s,\mu}. \tag{2.32}$$

[i] Note that the spacegroup (let me call it $\mathcal{G}$) is infinite dimensional since the translations $\mathbf{R}_p$ of the infinite lattice are included. A finite dimensional group is obtained by considering the quotient group $\mathcal{G}/\mathcal{T}$, where I denote by $\mathcal{T}$ the group of all lattice translations. Loosely speaking this amounts to dropping $\mathbf{R}_p$ and just considering the action of $\{S|\mathbf{v}^{(S)}\}$ within one unit cell and applying periodic boundary conditions whenever such an operation sends an atom outside the unit cell.

Comparing the latter equation and equation (2.23), it is obvious that the $\{\omega^2_{m,S\mathbf{q}}\}$ are also eigenvalues of the dynamical matrix at the unrotated $\mathbf{q}$-vector, $C^{s\,\mu}_{s'\mu'}(\mathbf{q})$, leading to the conclusion that

$$\omega^2_{m,S\mathbf{q}} = \omega^2_{m,\mathbf{q}}. \tag{2.33}$$

Indeed, the matrices $\Gamma(S;\mathbf{q})$ can be used to determine the independent elements of the dynamical matrix $C(\mathbf{q})$. In case the wavevector $\mathbf{q}$ is left invariant by the rotational part S of a spacegroup operation, $S\mathbf{q} = \mathbf{q} + \mathbf{G}$ ($\mathbf{G}$: reciprocal lattice vector), the above transformation law (2.29) becomes:[27]

$$C(\mathbf{q}) = \Gamma(S;\mathbf{q})C(\mathbf{q})\left[\Gamma(S;\mathbf{q})\right]^{-1}. \tag{2.34}$$

In combination with the property $C(-\mathbf{q}) = [C(\mathbf{q})]^*$,[27] additional constraints on the elements of the dynamical matrix can be formulated. If an operation S_- of the rotational parts of the spacegroup operations is such that $S_-\mathbf{q} = -\mathbf{q} + \mathbf{G}_-$, then[27]

$$C(\mathbf{q}) = [\Gamma(S_-;\mathbf{q})C(\mathbf{q})\left[\Gamma(S_-;\mathbf{q})\right]^{-1}]^*. \tag{2.35}$$

Even if no such element is amongst the rotational parts of the space group operations, the latter relation can be used to determine the independent elements of $C(\mathbf{q})$. Letting $\overline{S}$ be such that $(-\overline{S})\mathbf{q} = \mathbf{q} + \overline{\mathbf{G}}$, then it is true that

$$C(\mathbf{q}) = [\Gamma(\overline{S};\mathbf{q})C(\mathbf{q})[\Gamma(\overline{S};\mathbf{q})]^{-1}]^*. \tag{2.36}$$

Conversely, if $\overline{S}$ is such that $(-\overline{S})\mathbf{q} = \mathbf{q}' + \mathbf{G}'$:

$$C(\mathbf{q}') = [\Gamma(\overline{S};\mathbf{q})C(\mathbf{q})[\Gamma(\overline{S};\mathbf{q})]^{-1}]^*. \tag{2.37}$$

All relations just mentioned can, for example, be used to symmetrise dynamical matrices obtained from numerical calculations like the direct method described in the next section.

2.2.3 Thermodynamic functions from the phonon dispersion

Within the harmonic approximation the thermodynamic functions can be computed from simple summations over functions of the phonon eigenfrequencies. The vibrational entropy S^{ph} and the lattice specific heat at constant volume C_v^{ph} are of most interest in this work. The expressions for these quantities are ($\hbar \to 1$, k_{B}: Boltzmann constant)[28]

$$S^{\mathrm{ph}}(T) = k_{\mathrm{B}}/N_{\mathbf{q}} \sum_{\mathbf{q},m} \left\{ \frac{\omega_{m\mathbf{q}}}{2k_{\mathrm{B}}T} \coth\left(\frac{\omega_{m\mathbf{q}}}{2k_{\mathrm{B}}T}\right) - \ln\left[2\sinh\left(\frac{\omega_{m\mathbf{q}}}{2k_{\mathrm{B}}T}\right)\right]\right\} \tag{2.38}$$

$$C_v^{\mathrm{ph}}(T) = k_{\mathrm{B}}/N_{\mathbf{q}} \sum_{\mathbf{q},m} \frac{\left(\frac{\omega_{m\mathbf{q}}}{2k_{\mathrm{B}}T}\right)^2}{\sinh^2\left(\frac{\omega_{m\mathbf{q}}}{2k_{\mathrm{B}}T}\right)}. \tag{2.39}$$

Within Debye theory the constant-volume heat capacity per unit cell is[28]

$$C^{\mathrm{ph}}_{v,\mathrm{D}}(T) = 9N_{\mathrm{nucl}}k_{\mathrm{B}}\left(\frac{T}{\Theta_{\mathrm{D}}}\right)^3 \int_0^{\frac{\Theta_{\mathrm{D}}}{T}} d\xi\, \frac{\xi^4 e^{\xi}}{(e^{\xi}-1)^2}. \tag{2.40}$$

In this expression Θ_{D} is the Debye characteristic temperature. The Debye temperature as a function of T is calculated by minimising with respect to Θ_{D} the residual of calculated (measured) specific heat and eq. (2.40),

$$\min_{\Theta_{\mathrm{D}}} \left| C_v^{\mathrm{ph}}(T) - C^{\mathrm{ph}}_{v,\mathrm{D}}(T) \right|^2. \tag{2.41}$$

2.2.4 Dynamical matrices from the direct method

Theoretical approaches based on *ab initio* methods for calculating vibrational properties of solid are either based on density functional perturbation theory (DFPT) (see e.g. Giannozzi et al. [17], Baroni et al. [18], Gonze and Lee [19], and Gonze [29]) or the direct method (see e.g. Kresse et al. [30], Parlinski et al. [31], and Walle and Ceder [32]).

In DFPT-based calculations dynamical matrices are computed in reciprocal space on a grid of wavevectors from first-order changes of the wavefunctions due to atomic displacements. Starting from these dynamical matrices FCs in real space are calculated by means of the discrete Fourier transform. In order to have access to dynamical matrices at arbitrary $\mathbf{q}$-vectors in the first BZ, Fourier interpolation is used. Within the direct method the workflow proceeds in the other direction: forces on atoms due to finite atomic displacements are calculated in supercells. The size of the supercell must be chosen according to the desired interaction range to be covered by the FCs. FCs are evaluated from the forces through a finite difference scheme and dynamical matrices follow from a lattice Fourier transform from real to reciprocal space. Both methods—at least in principle—deliver the same information, however, they differ in complexity and applicability. For example, the implementation of the perturbative treatment of atomic displacement can be quite intricate for approaches to the electronic problem such as the projector augmented-wave method[33,34] (PAW). The direct method, on the other hand, is comparatively easy to implement and should be more feasible for systems requiring, e.g., spin-polarised calculations since only self-consistent calculations for the forces have to be performed. The drawback clearly is the necessity to compute numerical derivatives using forces.

In the work at hand the direct method is used for calculating vibrational properties of oxide semiconductors. Based on a unit cell with real space translations $\{\mathbf{a}_\mathrm{p}^{(j)}\}_{j=1,2,3}$ a supercell with generating translations $\mathbf{a}_\mathrm{s}^{(j)} = \sum_{j'=1}^{3} \mathbf{a}_\mathrm{p}^{(j')} M_{j'j}$ is constructed, where $M \in \mathbb{Z}_{3\times3}$, such that the volume of the supercell is $\det M \times \Omega_0$. For the reciprocal lattices corresponding to the real space lattices the relations is $\mathbf{g}_\mathrm{s}^{(j)} = \sum_{j'=1}^{3} \mathbf{g}_\mathrm{p}^{(j')} [M^{-T}]_{j'j}$, where M^{-T} is the inverse of the transpose of M. Within these supercells one atom s' at a time is displaced by $\mathbf{u}_{l',s'}^{(\mu')}$ (μ' indicates the displacement direction) and forces on the other atoms $\{\mathbf{F}_{l,s}(\mathbf{u}_{l',s'}^{(\mu')})\}_{s=1,\ldots,N_\mathrm{nucl}}^{l=1,\ldots,\det M}$ are calculated from DFT in a self-consistent calculation. The FCs are assessed from a 2-point finite difference stencil ($C_{l'\,s'\mu'}^{l\;s\;\mu} = \frac{\partial^2 E_\mathrm{KS}}{\partial u_{l,s,\mu} \partial u_{l',s',\mu'}} = -\frac{\partial F_{l',s',\mu'}}{\partial u_{l,s,\mu}} = \frac{\partial^2 E_\mathrm{KS}}{\partial u_{l',s',\mu'} \partial u_{l,s,\mu}} = -\frac{\partial F_{l,s,\mu}}{\partial u_{l',s',\mu'}}$):

$$C_{l'\,s'\mu'}^{l\;s\;\mu} \approx -\frac{F_{l,s,\mu}(+\mathbf{u}_{l',s'}^{(\mu')}) - F_{l,s,\mu}(-\mathbf{u}_{l',s'}^{(\mu')})}{2u_{l',s'}^{(\mu')}}, \tag{2.42}$$

where displacements in positive and negative directions have to be considered, and l, l' label primitive translations contained in the supercell. A 3×3 sub-matrix reads

$$C_{l'\,s'}^{l\;s} = -\begin{bmatrix} \frac{1}{2u}\Delta F_{l,s,x}(\mathbf{u}_{l',s'}^{(x)}) & \frac{1}{2u}\Delta F_{l,s,x}(\mathbf{u}_{l',s'}^{(y)}) & \frac{1}{2u}\Delta F_{l,s,x}(\mathbf{u}_{l',s'}^{(z)}) \\ \frac{1}{2u}\Delta F_{l,s,y}(\mathbf{u}_{l',s'}^{(x)}) & \frac{1}{2u}\Delta F_{l,s,y}(\mathbf{u}_{l',s'}^{(y)}) & \frac{1}{2u}\Delta F_{l,s,y}(\mathbf{u}_{l',s'}^{(z)}) \\ \frac{1}{2u}\Delta F_{l,s,z}(\mathbf{u}_{l',s'}^{(x)}) & \frac{1}{2u}\Delta F_{l,s,z}(\mathbf{u}_{l',s'}^{(y)}) & \frac{1}{2u}\Delta F_{l,s,z}(\mathbf{u}_{l',s'}^{(z)}) \end{bmatrix}, \tag{2.43}$$

with $\Delta F_{l,s,\mu}(\mathbf{u}_{l',s'}^{(\mu')}) = F_{l,s,\mu}(+\mathbf{u}_{l',s'}^{(\mu')}) - F_{l,s,\mu}(-\mathbf{u}_{l',s'}^{(\mu')})$, and, since the displacement length is the same for each direction, it is simply called u.

The peculiarity about forces obtained from most DFT codes[35–40] is the imposition of periodic boundary conditions. As a result, the forces contain the influence of all displaced atoms in the periodic images of the supercell. Through these forces the periodic contributions enter the FCs, which is the reason why these are often termed cumulative FCs:[31] $C_{l'\,s'\mu'}^{l\;s\;\mu} = \sum_{L'} {}^{\mathrm{phy}}C_{l'+L'\,s'\mu'}^{l\quad s\;\mu}$ (${}^{\mathrm{phy}}C_{l'\,s'\mu'}^{l\;s\;\mu}$: true physical FCs), and the summation extends over all periodic images of the supercell. At this point it is adjuvant to consider the equations of motion eq. (2.21). Partitioning the sum over lattice points and noting that—upon imposing periodic boundary conditions—the displacement is the *same* in all periodic images of the supercell it is immediate that[41]

$$F_{l,s,\mu} = -\sum_{L'} \sum_{l,'s',\mu'} C_{l'+L'\,s'\mu'}^{l\quad s\;\mu} u_{L'+l,s',\mu'} = -\sum_{l',s',\mu'} u_{l',s',\mu'} \left[\sum_{L'} C_{l'+L'\,s'\mu'}^{l\quad s\;\mu} \right].$$

As a matter of fact, it follows that the FCs have contributions from periodic repetitions of the supercell.

At wavevectors $\mathbf{q}_\mathrm{c}$ that are reciprocal lattice vectors of the direct super-lattice the dynamical matrix can be obtained exactly without any further approximation[31,42] (of course approximations through the numerical parameters etc. still are present). For these wavevectors commensurable with the supercell it holds that $\exp(+i\mathbf{q}_\mathrm{c}^T\mathbf{R}_\mathrm{s}^{(L)}) = 1$ since $\mathbf{q}_\mathrm{c}^T\mathbf{R}_\mathrm{s}^{(L)} = 2\pi \times \text{integer}$, with $\mathbf{R}_\mathrm{s}^{(L)}$ a lattice vector of the direct super-lattice. Thence, using the FCs $C^{l\,s\,\mu}_{l's'\mu'}$ in eq. (2.24),[31,41]

$$C^{s\,\mu}_{s'\mu'}(\mathbf{q}_\mathrm{c}) \overset{!}{=} {}^{\mathrm{phy}}C^{s\,\mu}_{s'\mu'}(\mathbf{q}_\mathrm{c}) = \sum_{L'}\sum_{l'} {}^{\mathrm{phy}}C^{l\quad s\,\mu}_{l'+L's'\mu'} \exp[+i\mathbf{q}_\mathrm{c}^T(\mathbf{R}_\mathrm{s}^{(L')} + \mathbf{R}_\mathrm{p}^{(l')} - \mathbf{R}_\mathrm{p}^{(l)})], \tag{2.44}$$

exact dynamical matrices $C^{s\,\mu}_{s'\mu'}(\mathbf{q}_\mathrm{c})$ at the commensurable wavevectors may be obtained because interactions are summed to infinity.

The commensurable $\mathbf{q}_\mathrm{c}$-vectors are determined from the matrix M relating the basis vectors of the primitive lattice and the superlattice in real space. The columns ${}^{(\mathrm{p})}\mathbf{Q}_\mathrm{c}^{(i)}$ of its reciprocal $M^{-T} \in \mathbb{Q}_{3\times3}$ can be taken as generating vectors of a grid of commensurate wavevectors referring to the translations of the reciprocal lattice corresponding to the primitive real space lattice.[ii] In this basis the commensurable wavevectors are constructed according to

$${}^{(\mathrm{p})}\mathbf{q}_\mathrm{c} = \sum_{i=1}^{3} m_i\, {}^{(\mathrm{p})}\mathbf{Q}_\mathrm{c}^{(i)} \text{ with } m_i \in \mathbb{Z} \text{ chosen such that } {}^{(\mathrm{p})}q_\mathrm{c}^{\mu} \in [0,1)\ \forall\mu, \tag{2.45}$$

and with respect to the Cartesian basis

$$\mathbf{q}_\mathrm{c} = {}^{(\mathrm{p})}q_\mathrm{c}^1\mathbf{g}_\mathrm{p}^{(1)} + {}^{(\mathrm{p})}q_\mathrm{c}^2\mathbf{g}_\mathrm{p}^{(2)} + {}^{(\mathrm{p})}q_\mathrm{c}^3\mathbf{g}_\mathrm{p}^{(3)} = \underbrace{[\mathbf{g}_\mathrm{p}^{(1)},\mathbf{g}_\mathrm{p}^{(2)},\mathbf{g}_\mathrm{p}^{(3)}]M^{-T}}_{=[\mathbf{g}_\mathrm{s}^{(1)},\mathbf{g}_\mathrm{s}^{(2)},\mathbf{g}_\mathrm{s}^{(3)}]}\mathbf{m} \text{ with } \mathbf{m} \in \mathbb{Z}_3.$$

Reviewing the relation $\mathbf{q}_\mathrm{c}^T\mathbf{R}_\mathrm{s}^{(L)} = 2\pi \times \text{integer}$, since $\mathbf{R}_\mathrm{s}^{(L)} = \mathbf{a}_\mathrm{s}^{(1)}L_1 + \mathbf{a}_\mathrm{s}^{(2)}L_2 + \mathbf{a}_\mathrm{s}^{(3)}L_3$ with $L_\mu \in \mathbb{Z}\ \forall\mu$:

$$\mathbf{q}_\mathrm{c}^T\mathbf{R}_\mathrm{s}^{(L)} = \mathbf{m}^T[\mathbf{g}_\mathrm{s}^{(1)}\mathbf{g}_\mathrm{s}^{(2)}\mathbf{g}_\mathrm{s}^{(3)}]^T[\mathbf{a}_\mathrm{s}^{(1)}\mathbf{a}_\mathrm{s}^{(2)}\mathbf{a}_\mathrm{s}^{(3)}]\mathbf{L} = 2\pi \times \underbrace{\mathbf{m}^T\mathbb{1}_3\mathbf{L}}_{\in\mathbb{Z}}, \tag{2.46}$$

it is found that wavevectors constructed according to eq. (2.45) indeed have the demanded property.

2.2.5 Dynamical matrices for polar insulating materials

In non-polar materials such as elemental semiconductors Si, Ge etc. the FCs are sufficiently short-ranged in order to assure convergence of the lattice Fourier transform eq. (2.24) after having summed over a decent number of real space vectors $\mathbf{R}_l$. However, in insulating materials with polar chemical bonding (e.g. GaAs or NaCl) atomic displacements are accompanied by electric dipoles.[iii] These electric dipoles are mediated at linear order through Born effective charges, $Z^*_{s,\mu\mu'}$, which are the coefficient of proportionality between the macroscopic polarisation $\mathcal{P}_{\mathrm{mac},\mu}$ and the atomic displacements $u_{s,\mu'}$:[19]

$$Z^*_{s,\mu\mu'} = \Omega_0 \frac{\partial\mathcal{P}_{\mathrm{mac},\mu}}{\partial u^{s,\mu'}_{\mathbf{q}=\mathbf{0}}}, \tag{2.47}$$

where $\Omega_0 = \det(\mathbf{a}_1,\mathbf{a}_2,\mathbf{a}_3)$ is the unit cell volume. The FCs therefore have a contribution from dipole-dipole interactions (coulombic part) and a non-coulombic (short-ranged) part.

[ii] The relation between the generating vectors of the primitive and the super-lattice is $[\mathbf{a}_\mathrm{p}^{(1)},\mathbf{a}_\mathrm{p}^{(2)},\mathbf{a}_\mathrm{p}^{(3)}]M = [\mathbf{a}_\mathrm{s}^{(1)},\mathbf{a}_\mathrm{s}^{(2)},\mathbf{a}_\mathrm{s}^{(3)}]$. Taking the inverse-transpose of both sides and multiplying by 2π leads to $[\mathbf{g}_\mathrm{p}^{(1)},\mathbf{g}_\mathrm{p}^{(2)},\mathbf{g}_\mathrm{p}^{(3)}]M^{-T} = [\mathbf{g}_\mathrm{s}^{(1)},\mathbf{g}_\mathrm{s}^{(2)},\mathbf{g}_\mathrm{s}^{(3)}]$.

[iii] In fact, formally also quadrupole or octupole moments are possible[19] but shall not be treated here.

In recent years two approaches have emerged that address the difficulties related to the long-range nature of the dipole-dipole interactions: The first is due to Gonze and Lee [19] (henceforth referred to as Gonze's method) and the second was introduced by Wang et al. [43] (henceforth referred to as Wang's method). Gonze's scheme is based on Ewald summation techniques and so far has only been implemented within codes treating phonons by DFPT.[39,40,44] Wang's approach is to add a constant term, which is non-analytic for $\mathbf{q} \to \mathbf{0}$, to the FCs in real space in order to account for the vibration-induced dipole-dipole interactions. Lately Wang's method has often been used in conjunction with the direct method,[43,45–53] and has been implemented into many phonon codes.[40,52,54–57]

2.2.5.1 Gonze's method

The method of Gonze and Lee [19] starts with the observation that in polar semiconducting or insulating materials the dynamical matrices at wavevector $\mathbf{q}$ can be split into a short-ranged (non-Coulomb) and a long-ranged (Coulomb) part:

$$C^{s\,\mu}_{s'\mu'}(\mathbf{q}) = {}^{\mathrm{sr}}C^{s\,\mu}_{s'\mu'}(\mathbf{q}) + {}^{\mathrm{dd}}C^{s\,\mu}_{s'\mu'}(\mathbf{q}). \tag{2.48}$$

A similar separation is also valid for the FCs in real space (${}^{\mathrm{sr}}C^{0\,s\,\mu}_{l's'\mu'}$ + ${}^{\mathrm{dd}}C^{0\,s\,\mu}_{l's'\mu'}$) and the dipole-dipole contribution to the FCs is of the form

$$\begin{aligned} {}^{\mathrm{dd}}C^{0\,s\,\mu}_{l's'\mu'} &= 1/\sqrt{\det \epsilon^{\infty}} \times \sum_{\nu\nu'} Z^{*}_{s,\nu\mu} Z^{*}_{s',\nu'\mu'} \\ &\times \left[\frac{[D^{0\,s}_{l's'}]^2 (\epsilon^{\infty})^{-1}_{\nu\nu'} - [(\epsilon^{\infty})^{-1}\mathbf{d}^{0\,s}_{l's'}]_{\nu}[(\epsilon^{\infty})^{-1}\mathbf{d}^{0\,s}_{l's'}]_{\nu'}}{[D^{0\,s}_{l's'}]^5} \right], \end{aligned} \tag{2.49}$$

with $\mathbf{d}^{0\,s}_{l's'} = \mathbf{R}_{l'} + \mathbf{x}_{s'} - \mathbf{x}_{s}$, and the inverse of the dielectric permittivity tensor, $(\epsilon^{\infty})^{-1}$, acts as a metric tensor in real space, $D^{0\,s}_{l's'} = \sqrt{[\mathbf{d}^{0\,s}_{l's'}]^T (\epsilon^{\infty})^{-1} \mathbf{d}^{0\,s}_{l's'}}$. The important result here is that the dipole-dipole part—as represented through eq. (2.49)—decreases only as the inverse of the third power of the interatomic distance, ${}^{\mathrm{dd}}C^{0\,s\,\mu}_{l's'\mu'} \propto \left|\mathbf{d}^{0\,s}_{l's'}\right|^{-3}$, making the series eq. (2.24) *converge slowly* for these FCs. Note that the onsite term with $\mathbf{R}_{l'} = \mathbf{0}$, and $s = s'$ even is divergent. Indeed, if in practical calculations for a polar material the Fourier sum from eq. (2.24) is used to calculate the dynamical matrices from the FCs, this may result in unphysical results for the phonon frequencies near the BZ centre. The reason is that in practise the FCs generally are only known at a rather limited number of points $\mathbf{R}_{l'}$ in real space (e.g., if only a "small" supercell is used in the direct method for the calculation of the FCs). Therefore, not enough terms might be included in eq. (2.24) as to make the series converge. The goal must therefore be to map the problem to a more quickly convergent series, and to account for the long-ranged part of the FCs in a different manner.

The treatment of the poorly convergent series becomes feasible in the following way: The dynamical matrix at wavevector $\mathbf{q}$ is obtained as the sum of a *rapidly convergent lattice Fourier transform* of some short-ranged FCs ${}^{\mathrm{sr}}C^{0\,s\,\mu}_{l's'\mu'}$ (which are assumed to decay as $\left|\mathbf{d}^{0\,s}_{l's'}\right|^{-4}$ or faster), and a dipole-dipole part as computed using Ewald summation techniques:[19]

$$C^{s\,\mu}_{s'\mu'}(\mathbf{q}) = \sum_{l'} {}^{\mathrm{sr}}C^{0\,s\,\mu}_{l's'\mu'} e^{i\mathbf{q}^T\mathbf{R}_{l'}} + {}^{\mathrm{dd}}C^{s\,\mu}_{s'\mu'}(\mathbf{q}), \tag{2.50}$$

which is a partitioning scheme in accordance with eq. (2.48). The dipole-dipole part is derived from the

following set of equations:[19]

$$
\begin{aligned}
{}^{\mathrm{dd}}C^{s\,\mu}_{s'\mu'}(\mathbf{q}) &= \sum_{\nu\nu'} Z^*_{s,\nu\mu} Z^*_{s',\nu'\mu'}\, {}^{\mathrm{dd}}\overline{C}^{s\,\nu}_{s'\nu'}(\mathbf{q}) \\
&\quad -\delta_{ss'} \sum_{s''} \sum_{\nu\nu'} Z^*_{s,\nu\mu} Z^*_{s'',\nu'\mu'}\, {}^{\mathrm{dd}}\overline{C}^{s\,\nu}_{s''\nu'}(\mathbf{q}=\mathbf{0}) \qquad (2.51a) \\
{}^{\mathrm{dd}}\overline{C}^{s\,\mu}_{s'\mu'}(\mathbf{q}) &= \frac{4\pi}{\Omega_0} \sum_{\substack{\text{If } |\mathbf{q}|\neq 0\text{: } \mathbf{G} \\ \text{If } |\mathbf{q}|=0\text{: } \mathbf{G}\neq\mathbf{0}}} (q_\mu + G_\mu)(q_{\mu'} + G_{\mu'}) F_0(\mathbf{q}+\mathbf{G}) e^{i(\mathbf{q}+\mathbf{G})^T(\mathbf{x}_s - \mathbf{x}_{s'})} \\
&\quad - \sum_{\substack{l' \\ D^{0\,s}_{l's'}\neq 0}} \eta^3 H_{\mu\mu'}(\eta[(\epsilon^\infty)^{-1}\mathbf{d}^{0\,s}_{l's'}], \eta D^{0\,s}_{l's'}) e^{i\mathbf{q}^T\mathbf{R}_{l'}} \Big/ \sqrt{\det \epsilon^\infty} \\
&\quad - \frac{4}{3\sqrt{\pi}} \eta^3 \delta_{ss'} (\epsilon^\infty)^{-1}_{\mu\mu'} \Big/ \sqrt{\det \epsilon^\infty}, \qquad (2.51b)
\end{aligned}
$$

where η is the Ewald-parameter and

$$
\begin{aligned}
F_0(\mathbf{q}+\mathbf{G}) &= e^{-\epsilon^\infty(\mathbf{q}+\mathbf{G})/4\eta^2} / \epsilon^\infty(\mathbf{q}+\mathbf{G}) \qquad (2.52) \\
H_{\mu\mu'}(\mathbf{x}, y) &= \frac{x_\mu x_{\mu'}}{y^2} \left[\frac{3\,\mathrm{erfc}\, y}{y^3} + \frac{2e^{-y^2}}{\sqrt{\pi}} \left(\frac{3}{y^2} + 2 \right) \right] \\
&\quad -(\epsilon^\infty)^{-1}_{\mu\mu'} \left(\frac{\mathrm{erfc}\, y}{y^3} + \frac{2}{\sqrt{\pi}} \frac{e^{-y^2}}{y^2} \right), \qquad (2.53)
\end{aligned}
$$

with $\epsilon^\infty(\mathbf{q}+\mathbf{G}) = (\mathbf{q}+\mathbf{G})^T \epsilon^\infty (\mathbf{q}+\mathbf{G})$. The Born effective charges and the dielectric permittivity tensor are calculated from DFPT from a response to atomic displacements/an electric field, leaving the short-ranged FCs as the only unknown quantities.

Therefore, the slow convergence of the Fourier series is bypassed because only the short-ranged part of the FCs are used to calculate it. The dipole-dipole part also does not pose a problem: For a suitable choice of the Ewald paramater η, sums in real (sum over l'-index), reciprocal space (sum over $\mathbf{G}$-vectors) can be carried out until convergence by including enough shells of vectors.

For practical calculations the key issue clearly is to obtain the short-ranged FCs in order to compute the first term of equation (2.50). Since Gonze's method is commonly used for phonon calculations based on dynamical matrices from DFPT,[39,40,44] the starting point is a set of dynamical matrices $C^{s\,\mu}_{s'\mu'}(\mathbf{q}_{j_1 j_2 j_3})$ on a grid of wavevectors $\mathscr{G}_\mathbf{q}$ that homogeneously samples the BZ:

$$
\mathscr{G}_\mathbf{q} = \left\{ \mathbf{q}_{j_1 j_2 j_3} \,\middle|\, \mathbf{q}_{j_1 j_2 j_3} = \sum_{r=1}^{3} j_r \mathbf{g}_r / \mathscr{N}_r \text{ with } 0 \leq j_r < \mathscr{N}_r;\ \mathscr{N}_r \in \mathbb{N}_{>0}\ \forall r \right\}, \qquad (2.54)
$$

where $\mathbf{g}_1, \mathbf{g}_2, \mathbf{g}_3$ shall denote the reciprocal lattice vectors of the crystal at hand. DFPT directly provides the required dynamical matrices by computing the response of the electronic system to atomic displacements characterised by a wavevector $\mathbf{q}_{j_1 j_2 j_3}$.

Based on these ingredients it is now easy to formulate a recipe for an efficient interpolation of dynamical matrices over the entire BZ. Interpolation in this context means that dynamical matrices at arbitrary wavevectors $\mathbf{q}$ (i.e., particularly at points *not* contained in the original grid $\mathscr{G}_\mathbf{q}$) can be computed based on the dynamical matrices on the grid $\mathscr{G}_\mathbf{q}$:

(I) $\forall \mathbf{q}_{j_1 j_2 j_3} \in \mathscr{G}_\mathbf{q}$: Calculate the dipole-dipole part ${}^{\mathrm{dd}}C^{s\,\mu}_{s'\mu'}(\mathbf{q}_{j_1 j_2 j_3})$ with eqs. (2.51).

(II) $\forall \mathbf{q}_{j_1 j_2 j_3} \in \mathscr{G}_\mathbf{q}$: Isolate the short-ranged part of the dynamical matrix:

$$
{}^{\mathrm{sr}}C^{s\,\mu}_{s'\mu'}(\mathbf{q}_{j_1 j_2 j_2}) = C^{s\,\mu}_{s'\mu'}(\mathbf{q}_{j_1 j_2 j_3}) - {}^{\mathrm{dd}}C^{s\,\mu}_{s'\mu'}(\mathbf{q}_{j_1 j_2 j_3}).
$$

(III) Determine the short-ranged FCs in a box in real space with volume $\mathscr{N}_1\mathscr{N}_2\mathscr{N}_3 \times \Omega_0$ (centred around atoms s at $\mathbf{R}_l \equiv \mathbf{0}$) by inverse Fourier transform:

$$\begin{aligned} {}^{\mathrm{sr}}C^{0\,s\,\mu}_{l's'\mu'} &= \sum_{\mathbf{q}_{j_1j_2j_3}\in\mathscr{G}_\mathbf{q}} {}^{\mathrm{sr}}C^{s\,\mu}_{s'\mu'}(\mathbf{q}_{j_1j_2j_3}) e^{-i[\mathbf{q}_{j_1j_2j_3}]^T\mathbf{R}_{l'}} \Big/ \mathscr{N}_1\mathscr{N}_2\mathscr{N}_3, \quad \text{if } \mathbf{d}^{0\,s}_{l's'} \in \text{ box} \\ &= 0, \quad \text{if } \mathbf{d}^{0\,s}_{l's'} \notin \text{ box}. \end{aligned}$$

The number of real space lattice points $\mathbf{R}_{l'}$ contained in the box equals $\mathscr{N}_1\mathscr{N}_2\mathscr{N}_3$.

(IV) Interpolate to arbitrary wavevectors $\mathbf{q}$ using eq. (2.50) after having calculated the dipole-dipole part (eqs. (2.51)) at this $\mathbf{q}$-vector (Fourier interpolation).

Since the approach just reviewed "corrects" the short- comings of the Fourier interpolation based on the full FCs ($C^{0\,s\,\mu}_{l's'\mu'}$ and *not* ${}^{\mathrm{sr}}C^{0\,s\,\mu}_{l's'\mu'}$), it will be referred to as dipole-dipole corrections.

I close this section with some remarks on eqs. (2.51): Care needs to be taken in the limit $\mathbf{q} \to \mathbf{0}$. In order to see this consider again the first term in eq. (2.51b) and include explicitly the $\mathbf{G} = \mathbf{0}$ term:

$$\begin{aligned} &\lim_{\mathbf{q}\to\mathbf{0}} \frac{4\pi}{\Omega_0}\frac{q_\mu q_{\mu'}}{\epsilon^\infty(\mathbf{q})} + \lim_{\mathbf{q}\to\mathbf{0}} \frac{4\pi}{\Omega_0}\frac{q_\mu q_{\mu'}}{\epsilon^\infty(\mathbf{q})} \left(e^{i\mathbf{q}^T(\mathbf{x}_s - \mathbf{x}_{s'})} e^{-\epsilon^\infty(\mathbf{q})/4\eta^2} - 1 \right) \\ + \quad &\lim_{\mathbf{q}\to\mathbf{0}} \sum_{\mathbf{G}\neq\mathbf{0}} (\mathbf{G}\text{–terms with well-defined limit for } \mathbf{q} \to \mathbf{0}). \end{aligned} \tag{2.55}$$

Expanding the exponentials in the second term in powers of $q = \|\mathbf{q}\|$,

$$\begin{aligned} \exp(i\mathbf{q}^T\boldsymbol{\Delta}\mathbf{x}^s_{s'} - \epsilon^\infty(\mathbf{q})/4\eta^2) = 1 + i\hat{\mathbf{q}}^T\boldsymbol{\Delta}\mathbf{x}^s_{s'}q - \tfrac{1}{2}(\hat{\mathbf{q}}^T\boldsymbol{\Delta}\mathbf{x}^s_{s'})^2q^2 \\ - \epsilon^\infty(\hat{\mathbf{q}})q^2/4\eta^2 + \cdots, \end{aligned}$$

it is obvious that the q^{-2} denominator is compensated such that the single terms go to zero as $\propto q$, and $\propto q^2$, respectively. Therefore, only the first and the third term of eq. (2.55) remain in this limit implying that in the $\mathbf{G}$-sum in eq. (2.51b) the $\mathbf{G} = \mathbf{0}$ term is to be skipped. Note that in eq. (2.51b) $C^{s\,\mu}_{s'\mu'}(\mathbf{q} = \mathbf{0})$ is defined without the term $\frac{4\pi}{\Omega_0}q_\mu q_{\mu'}/\epsilon^\infty(\mathbf{q})$. As a consequence, when computing the dynamical matrix at the Brillouin zone (BZ) center $\mathbf{q} = \mathbf{0}$, this term must be added explicitly:

$$\begin{aligned} \lim_{\mathbf{q}\to\mathbf{0}} C^{s\,\mu}_{s'\mu'}(\mathbf{q}) &= {}^{\mathrm{sr}}C^{s\,\mu}_{s'\mu'}(\mathbf{q} = \mathbf{0}) + {}^{\mathrm{dd}}C^{s\,\mu}_{s'\mu'}(\mathbf{q} = \mathbf{0}) + {}^{\mathrm{na}}C^{s\,\mu}_{s'\mu'}(\hat{\mathbf{q}}) \\ &= {}^{\mathrm{ana}}C^{s\,\mu}_{s'\mu'}(\mathbf{q} = \mathbf{0}) + {}^{\mathrm{na}}C^{s\,\mu}_{s'\mu'}(\hat{\mathbf{q}}), \end{aligned} \tag{2.56}$$

with

$${}^{\mathrm{na}}C^{s\,\mu}_{s'\mu'}(\hat{\mathbf{q}}) = \frac{4\pi}{\Omega_0}\frac{\sum_\nu \hat{q}_\nu Z^*_{s,\nu\mu} \sum_{\nu'} \hat{q}_{\nu'} Z^*_{s',\nu'\mu'}}{\epsilon^\infty(\hat{\mathbf{q}})}. \tag{2.57}$$

In fact, the first and the second term of the former equation comprise the analytical part of the dynamical matrix at the BZ centre, therefore motivating the notation ${}^{\mathrm{ana}}C^{s\,\mu}_{s'\mu'}(\mathbf{q} = \mathbf{0})$. For the third term, however, the limiting value depends on the direction $\hat{\mathbf{q}}$ along which the limit is taken implying that the limit is non-unique. It is therefore commonly referred to as *non-analytical* (note the superscript "na") term. As a result, there is a directionality introduced for phonon mode frequencies depending on which direction is used in the non-analytical term. This will not be the case for modes for which $\sum_{\nu'} \hat{q}_{\nu'} \sum_{s'\mu'} Z^*_{s',\nu'\mu'} w^{s',\mu'}_{m,\mathbf{q}=\mathbf{0}}/\sqrt{M_s} = 0$, i.e., for those modes that lie in a subspace orthogonal to the subspace in which the non-analytical term acts. Eigenvectors fulfilling the former condition are common to ${}^{\mathrm{ana}}C^{s\,\mu}_{s'\mu'}(\mathbf{q} = \mathbf{0})/\sqrt{M_sM_{s'}}$ and $({}^{\mathrm{ana}}C^{s\,\mu}_{s'\mu'}(\mathbf{q} = \mathbf{0}) + {}^{\mathrm{na}}C^{s\,\mu}_{s'\mu'}(\hat{\mathbf{q}}))/\sqrt{M_sM_{s'}}$.

Modes for which $\hat{\mathbf{q}} \parallel \sum_{s'} Z^*_{s'} \mathbf{w}^{s'}_{m,\mathbf{q}=\mathbf{0}}/\sqrt{M_s}$ are called *longitudinal* optic (LO), since they have components along the direction $\hat{\mathbf{q}}$, and $\mathbf{w}_{m,\mathbf{q}=\mathbf{0}}$ is an eigenvector of $({}^{\mathrm{ana}}C^{s\,\mu}_{s'\mu'}(\mathbf{q} = \mathbf{0}) + {}^{\mathrm{na}}C^{s\,\mu}_{s'\mu'}(\hat{\mathbf{q}}))/\sqrt{M_sM_{s'}}$. Obviously, frequencies of these modes will depend on the direction according to eq. (2.56). Conversely, if $\hat{\mathbf{q}} \perp \sum_{s'} Z^*_{s'} \mathbf{w}^{s'}_{m,\mathbf{q}=\mathbf{0}}/\sqrt{M_s}$ a phonon mode is termed *transversal* optic (TO), if it does not couple to the direction $\hat{\mathbf{q}}$. Phonons in the long-wavelength limit that couple to the limiting direction may be associated with a

macroscopic polarization, and thus a homogeneous electric field. From Maxwell's equations, the polarization induced by a longitudinal phonon in the $\mathbf{q} \to \mathbf{0}$ limit generates a macroscopic electric field which exerts a force on the atoms, hence affecting the phonon frequency. In particular, this frequency will be *different* from the purely transversal case. This (direction-dependent) difference in frequency of LO and TO modes is known as "LO-TO splitting". In case of degenerate phonon modes (2-fold or 3-fold degenerate), the degeneracy will be lifted, if the direction $\hat{\mathbf{q}}$ is such that one of the degenerate modes has longitudinal character, i.e., if $\sum_{\nu'} \hat{q}_{\nu'} \sum_{s'\mu'} Z^*_{s',\nu'\mu'} w^{s',\mu'}_{m,\mathbf{q}=\mathbf{0}} / \sqrt{M_s} \neq 0$.

2.2.5.2 Wang's method

Wang et al. [43] compute the Fourier transform with the full FCs from the direct method for an arbitray $\mathbf{q}$-vector and add the non-analytic term from eq. (2.57) with the result that:[43,50]

$$\widetilde{C}^{s\,\mu}_{s'\mu'}(\mathbf{q}) = C^{s\,\mu}_{s'\mu'}(\mathbf{q}) + {}^{\mathrm{na}}C^{s\,\mu}_{s'\mu'}(\hat{\mathbf{q}})\chi(\mathbf{q}), \tag{2.58}$$

where $\chi(\mathbf{q}) = \frac{1}{|\det M|} \sum_l e^{i\mathbf{q}^T \mathbf{R}_l}$ is a geometrical factor. For this factor the following cases are to be considered:[43,50]

(i) $\mathbf{q} = \mathbf{0}$: In this case $\chi(\mathbf{q}) = 1$ and the limiting contribution to the dynamical matrix of eq. (2.57) is recovered.

(ii) $\mathbf{q} = \mathbf{q}_c$: In this case $\chi(\mathbf{q}) = 0$ and the non-analytical term does not play a role. The dynamical matrices are exactly described through the FCs obtained from the direct method.

(iii) $\mathbf{q} \neq \mathbf{0} \wedge \mathbf{q} \neq \mathbf{q}_c$: In this case $\chi(\mathbf{q}) \neq 0$ and lattice waves with wavevector not captured by the supercell must be treated. The dynamical matrix from eq. (2.58) then is approximately constructed by Fourier interpolation. For small wavevectors the vibrational pattern might result in macroscopic electric fields complicating the interpolation procedure.

2.2.6 Raman scattering

When light travels through a semiconducting/isolating solid, most of it is either reflected or transmitted; a tiny amount, however, will be scattered. The scattering may, for example, occur through the presence of defects (point defects, dislocations, ...), that generally scatter light elastically (i.e., without a change in energy). Apart from that, light can also be scattered *inelastically* by elementary excitations of the crystal such as lattice vibrations (phonons), which was first observed by Raman [58, 59].

Generalities In case of inelastic scattering of light by phonons, the scattering process is characterised by a scattering frequency ω_m (also termed "Raman shift") which amounts to the energy absorbed by the crystal (Stokes scattering), or emitted by the crystal (anti-Stokes scattering). Energy absorption involves "creation" of a phonon, while emission means a phonon is "annihilated". The incident and scattered frequencies are related by $\omega_S = \omega_I \pm \omega_m$, where "+" is for anti-Stokes scattering, and "−" is for Stokes scattering. In case of a Stokes scattering process, a quantum mechanical treatment reveals that the probability for the creation of a photon (and hence the intensity of this scattering event) is proportional to $(n_m + 1)$,[60] where $n_m \equiv n_m(T) = [\exp(\omega_m / k_\mathrm{B}T) - 1]^{-1}$ is the Bose-Einstein occupation factor. The additional term +1 corresponds to spontaneous emission of a phonon, while the n_m term describes stimulated phonon emission. Similarly, an anti-Stokes scattering event is proportional to the number of available states n_m. The ratio of intensities is given by

$$\mathscr{I}_{\mathrm{anti-Stokes}} / \mathscr{I}_{\mathrm{Stokes}} \propto n_m/(n_m + 1) = e^{-\omega_m / k_\mathrm{B}T}, \tag{2.59}$$

indicating that the scattered intensity of an anti-Stokes process is much smaller than that of the Stokes process if $\omega_m \gg k_\mathrm{B}T$. Another possibility, however, is that the light is backscattered elastically such that $\omega_I = \omega_S$. This scenario is called Rayleigh scattering, and indeed, this is the most probable scattering event.

Furthermore, momentum conservation demands $\mathbf{k}_S = \mathbf{k}_I \pm \mathbf{q}$. Assuming visible light for the incident radiation, it is a good approximation to assume $\omega_I \approx \omega_S \gg \omega_m$ (visible light: ∼1.6 eV to 3.2 eV; (optical) phonons: ∼40 meV to 120 meV), and hence $|\mathbf{k}_I| \approx |\mathbf{k}_S|$ with a magnitude of $\sim 10^5\,\mathrm{cm}^{-1}$, much lower than

those of reciprocal-lattice vectors ($|\mathbf{G}| \sim 10^8\,\mathrm{cm}^{-1}$). Therefore, $|\mathbf{q}| \approx 0$, meaning that only Γ phonons will contribute to the first-order Raman process.[iv]

At linear order, the quantity describing the interaction of a solid with electromagnetic radiation (light) is the linear dielectric susceptibility χ, which is a second-rank Cartesian tensor. It is related to the dielectric tensor $\epsilon_{\mu\mu'}$ by $\epsilon_{\mu\mu'} = \delta_{\mu\mu'} + 4\pi\chi_{\mu\mu'}$. The susceptibility relates the polarisation $\mathbf{P}$ induced by the incident light beam and its electric field vector, $\mathbf{P} = \chi\mathbf{E}_I$, where the incident/scattered electric field vectors can be described by plane waves with wavevectors $\mathbf{k}_{I,S}$ and frequencies $\omega_{I,S}$: $\mathbf{E}_{I,S}(\mathbf{r}, t) = \mathbf{E}_{I,S}\exp(i\mathbf{k}_{I,S}^T\mathbf{r} - i\omega_{I,S}t)$.

The effect of the phonons is to modulate the wavefunctions and energy levels of the solid. As a result, the atomic vibrations contribute an additional term to χ, the so-called "transition susceptibility" $\delta\chi$. Let $\chi \to \chi + \delta\chi$, and[61]

$$\delta\chi = \sum_{\mathbf{q},m} \chi^m(\mathbf{q})Q_{m,\mathbf{q}} + \tfrac{1}{2}\sum_{\mathbf{q}\mathbf{q}',mm'} \chi^{mm'}(\mathbf{q},\mathbf{q}')Q_{m,\mathbf{q}}Q_{m',\mathbf{q}'} + \cdots, \tag{2.60}$$

with $\chi^m(\mathbf{q}) = \frac{\partial\chi}{\partial Q_{m,\mathbf{q}}}\big|_0$, $\chi^{mm'}(\mathbf{q},\mathbf{q}') = \frac{\partial^2\chi}{\partial Q_{m,\mathbf{q}}\partial Q_{m',\mathbf{q}'}}\big|_0, \ldots$ The $\{Q_{m,\mathbf{q}}\}$ are the "normal coordinates" of the lattice vibrations and relate an arbitrary atomic displacement and the eigenvectors of the phonon spectrum:[28,61] $u_{l,s,\mu} = 1/\sqrt{N}\sum_{\mathbf{q},m} Q_{m,\mathbf{q}} w^{s,\mu}_{m,\mathbf{q}}/\sqrt{M_s}\exp(i\mathbf{q}^T\mathbf{R}_l)$. Since only Γ phonons are considered, the lattice index l can be dropped and the normal coordinate merely is a scaling constant of the displacement related with the mth mode at the Brillouin zone centre. The derivative $\frac{\partial\chi}{\partial Q_{m,\Gamma}}\big|_0$ must be viewed as a directional derivative along the displacement vector $u^{s,\mu}_m = w^{s,\mu}_m/\sqrt{M_s}$:[12] $\frac{\partial\chi}{\partial Q_{m,\Gamma}}\big|_0 \equiv \frac{d}{dt}\chi(\{\mathbf{x}^{(0)}_s\} + t\mathbf{u}_{m,\Gamma})\big|_{t=0} = \sum_{s,\gamma}\frac{\partial\chi}{\partial u_{s,\gamma}}\big|_0 u^{s,\gamma}_{m,\Gamma}$, and $\frac{\partial\chi}{\partial u_{s,\gamma}}$ is the gradient of χ with respect to atomic displacements.

The central quantity in the description of Raman scattering is the scattering efficiency (cgs-units; Stokes process):[12,62]

$$S^m_{\mathrm{eff}} = \left|[\mathbf{e}_S]^T\mathscr{R}^m\mathbf{e}_I\right|^2 = \frac{(\omega_I - \omega_m)^4}{c^4}\left|[\mathbf{e}_S]^T\alpha^m\mathbf{e}_I\right|^2\frac{\hbar}{2\omega_m}(n_m + 1), \tag{2.61}$$

which introduces the Raman susceptibilities[12,62]

$$\alpha^m_{\mu\mu'} \equiv \alpha^m_{\mu\mu'}(\omega_{\mathrm{L}}) = (4\pi)^{-1}\sqrt{\Omega_0}\sum_{s,\gamma}\left.\frac{\partial\epsilon_{\mu\mu'}(\omega_{\mathrm{L}})}{\partial u_{s,\gamma}}\right|_0 u^{s,\gamma}_{m,\mathbf{q}=\mathbf{0}}, \tag{2.62}$$

where $\omega_I \to \omega_{\mathrm{L}}$ to indicate that the incoming light usually is a laser (hence the subscript "L"), and $\mathscr{R}^m$ is the Raman tensor.

Indeed, the rather heuristic and qualitative discussion the Raman effect above is unsatisfactory from a mathematical and a physical point of view. In order to embrace the full complexity of the phenomenon of inelastic light scattering from a solid in the presence of excitations such as phonons, a quantum mechanical treatment is indispensable. A detailed outline of the complete microscopic theory will, however, not be given. In what follows, only a summary of the excitations and interactions will be outlined.

Following Yu and Cardona [60], in order to give an account of the microscopic processes involved in phonon Raman scattering, the state of three "systems" involved must be specified:

- Incident/scattered photons with frequencies $\omega_{I,S}$,
- electrons in the semiconductor/insulator,
- and the phonon involved in the scattering.

The involved interactions are (i) electron-*photon* interaction (interaction Hamiltonian $H_{\mathrm{e-R}}$; subscript "R" is for radiation), (ii) and electron-*phonon* interaction (interaction Hamiltonian $H_{\mathrm{e-ph}}$).

Generally, it must be distinguished between resonant and non-resonant Raman scattering. In non-resonant Raman scattering, an electron is excited into a so-called "virtual state", which essentially is a very short-lived, non-observable quantum state. In particular, this state is not "an eigenstate of anything", and therefore cannot really be reconciled with the (static) electronic picture based on eigensolutions of the many-body system predominant in computational solid state physics. The electronic virtual state then couples to the phonon

[iv] In case of multi-phonon Raman scattering, more than just one $\mathbf{q}$-point is involved. Therefore, the proper generalisation is that the *sum* over all involved phonon wavevectors $\mathbf{q}$ vanishes, $\sum_i \mathbf{q}_i = \mathbf{0}$.

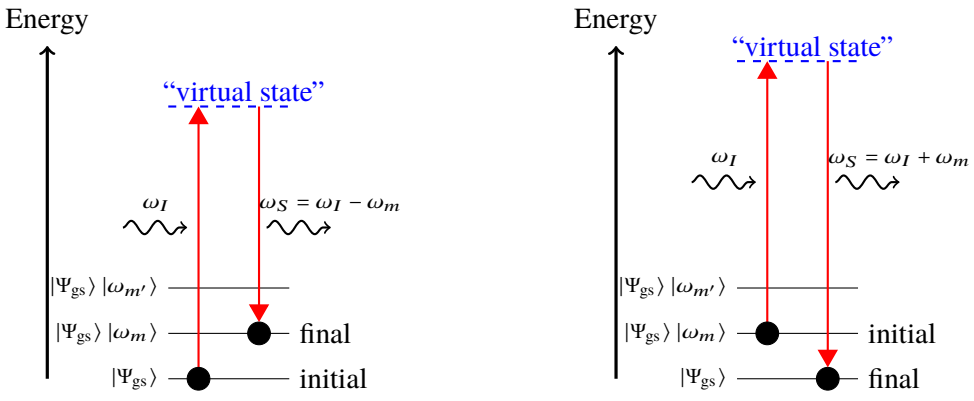

(a) Stokes process. **(b)** Anti-Stokes process.

FIGURE 2.2: Pictorial representation of (a) the Stokes, and (b) the anti-Stokes first-order Raman process. $|\Psi_{gs}\rangle$ is the (electronic) groundstate, $|\Psi_{gs}\rangle\,|\omega_m\rangle$, $|\Psi_{gs}\rangle\,|\omega_{m'}\rangle$ are states of the system that differ by their vibrational parts. Vibrational states are bound states of the potential generated by the groundstate electronic configuration. The transitions involved in both scattering processes occur solely within the vibrational (phononic) subsystem. This assumption is satisfied by Born-Oppenheimer's approximation.

subsystem to re-emit the scattered photon. A pictorial representation of non-resonant Stokes/anti-Stokes scattering is given in fig. 2.2. In resonant Raman scattering, ω_I fits an electronic transition energy, be it an interband transition from valence to conduction band or an excitonic excitation (both are electron-hole pairs correlated by Coulomb interaction). The resulting electron-hole pair then scatters from phonons via the electron-phonon interaction, and recombines to give the final-state photon (the scattered photon with frequency ω_S). It should be remarked that the just-described processes occur instantaneously. That is, there is no "chronology" in the processes between photon absorption an re-emission.

The complete expression of the first-order scattering probability for the case involving electron-hole pairs is given by Yu and Cardona [60] and consists of six terms, where the energies ω_I, ω_m are combined in several denominators, leading to resonant and anti-resonant terms. In the Born-Oppenheimer approximation (which is generally used in first principles calculations), i.e., letting the electrons respond immediately to the atomic motion, it is possible to show that this expression[60] is equivalent to the derivative of the dielectric function with respect to atomic displacements.[12]

Group theoretical considerations It is expedient to consider the symmetry properties of the Raman tensor $\mathscr{R}^m$. In deriving the symmetry properties of the Raman tensor, it is inevitable to investigate its transformation properties under the symmetry operations of the space group $\mathcal{G}$ of the crystal. Since $|\mathbf{q}| \approx 0$, it is possible to analyse the symmetry of $\mathscr{R}^m$ based on the factor group which is isomorphic to the point group of the *crystal* (the set of rotational parts of the space group operations). The factor group is the quotient group $\mathcal{G}/\mathcal{T}$, $\mathcal{T}$ being the group of (primitive) lattice translations. In this context it must be appreciated that the space group itself is infinite dimensional because it includes in the infinite group of lattice translations.

The Raman tensor derives from the dielectric susceptibilities χ that is a second-rank polar tensor, because it relates two polar vectors being, e.g., $\mathbf{P}$ and $\mathbf{E}_I$. That means, $\mathscr{R}^m$ transforms under the elements $\{S^{(j)}\}$ ($j = 1, \ldots, |\mathcal{G}_\mathrm{p}|$) of the point group of the crystal (let it be denoted by $\mathcal{G}_\mathrm{p}$; $|\mathcal{G}_\mathrm{p}|$ is the order of the group) like a rank-two polar tensor: $\mathscr{R}^m{}_{\mu\mu'} \to \sum_{\nu\nu'}[D^{(j)}(S)]_{\mu\nu}[D^{(j)}(S)]_{\mu'\nu'}\mathscr{R}^m{}_{\nu\nu'}$, i.e., each component of the second-rank tensor transforms like the component of a "vector" (a rank-one tensor, whose components transform like $T_\mu \to \sum_{\mu'}[D^{(j)}(S)]_{\mu\mu'}T_{\mu'}$). $[D^{(j)}(S)]_{\mu\mu'}$ is a real-valued unitary 3×3 matrix representation of the jth symmetry element $S^{(j)} \in \mathcal{G}_\mathrm{p}$.

Given the point group of the crystal, group theory is essentially about finding the smallest possible matrix representations of the elements $S^{(j)} \in \mathcal{G}_\mathrm{p}$; these representations are called "irreducible" (irreducible representation→irrep).[63] The $3N_\mathrm{nucl}$-dimensional eigenspace V_Γ of the dynamical matrix at Γ can be shown to decompose into subspaces whose elements transform according to some of the irreps $\Lambda^{(1)}, \Lambda^{(2)}, \ldots$ of $\mathcal{G}_\mathrm{p}$:[27] $V_\Gamma = m^{(p)}V(\Lambda^{(p)}) \oplus m^{(q)}V(\Lambda^{(q)}) \oplus \cdots$. Indeed, not all irreps existent for $\mathcal{G}_\mathrm{p}$ must occur in the decomposition; some irreps may also occur more than just once ($m^{(p)}, m^{(q)}, \ldots$ times). Eventually, it must hold that the

		character tr $D^{(j)}(\Lambda)$				
Symbol	dim Λ	E	C_n	I	σ_h	$C_2 \perp C_n$ or σ_v
A	1	+1	+1			
B	1	+1	−1			
E	2	+2				
T/F	3	+3				
X_g				+1		
X_u				−1		
X'					+1	
X''					−1	
Y_1						+1
Y_2						−1

TABLE 2.1: Symbols introduced by Mulliken [64, 65] for the irreps Λ of the crystallographic point groups. The character of a matrix representation $D(\Lambda)$ of the irrep equals its trace. The labels for the symmetry elements have the following meaning: $E \rightarrow$ identity; $C_n \rightarrow$ principal rotation; $I \rightarrow$ inversion; $\sigma_h \rightarrow$ horizontal mirror plane; $C_2 \rightarrow$ 2-fold rotation; $\sigma_v \rightarrow$ vertical mirror plane. A detailed explanation of these symbols as well as their geometrical meaning can be found in Dresselhaus et al. [63]. The symbol X can be any Mulliken symbol, while Y is limited to A, B. The table is reproduced with slight adjustments from Sander [11].

dimensions of all subspaces add up to the total number of modes per unit cell: $\sum_{V(\Lambda)\in V_\Gamma} \dim V(\Lambda) = 3N_{\text{nucl}}$. The dimensions of the subspaces are in accord with the level of degeneracy of the corresponding phonon mode: (i) $\dim V(\Lambda) = 1$ means the eigenvalue ω_m^2 is 1-fold degenerate, (ii) $\dim V(\Lambda) = 2$ means the eigenvalue is 2-fold degenerate, and (iii) $\dim V(\Lambda) = 3$ means the eigenvalue is 3-fold degenerate. What irreps appear in the decomposition as well as their number of occurrence depends on the space group and the crystal structure. If a phonon mode represented by an eigenvector $\mathbf{w}_m \in V(\Lambda^{(p)})$ transforms "according to the irrep $\Lambda^{(p)}$", this means that it transforms under the space group operations in a certain manner. For example, in case of the three dimensional irrep T_{1u} of the cubic point group O_h the transformation behaviour is that of a vector (x, y, z). In case of the inversion operation, this means that the eigenvectors change sign (subscript u: "ungerade") upon application of the respective space group operation (see eq. (2.30)). The irreps of $\mathcal{G}_\text{p}$ are labelled according to the symbols introduced by Mulliken [64, 65]. Their meaning is summarised in table 2.1. For a detailed explanation of the symbols used for the point symmetry elements as well as their geometrical meaning, the reader is referred to Dresselhaus et al. [63].

As seen above, the components of the Raman tensor obviously transform like the product of two polar vectors (rank-one tensors) $T_\mu T_{\mu'} \rightarrow \sum_{\nu\nu'}([D^{(j)}(S)]_{\mu\nu}T_\nu)([D^{(j)}(S)]_{\mu'\nu'}T_{\nu'})$; indeed, the product $T_\mu T_{\mu'} \equiv (\mathbf{T}\otimes\mathbf{T})_{\mu\mu'}$ defines a rank-two (polar) tensor (via the dyadic/outer/tensor product). Within the scope of the point group $\mathcal{G}_\text{p}$, a first-rank tensor transforms according to the (irreducible) representation of a polar vector Λ_vec. Inasmuch as $\{D^{(j)}(\Lambda_\text{vec})\}$ $(j = 1, \ldots, |\mathcal{G}_\text{p}|)$ is a (irreducible) matrix representation of Λ_vec, $\{D^{(j)}(\Lambda_\text{vec})\otimes D^{(j)}(\Lambda_\text{vec})\}$ is a, generally reducible,[63] matrix representation of the product representation $\Lambda_\text{vec}\otimes\Lambda_\text{vec}$ (via the Kronecker matrix product).[v] The (reducible) product representation can be decomposed into irreps of $\mathcal{G}_\text{p}$ by a suitable similarity transformation like $\Lambda_\text{vec}\otimes\Lambda_\text{vec} = c^{(s)}\Lambda^{(s)} \oplus c^{(t)}\Lambda^{(t)} \oplus \cdots$, with multiplicities $c^{(s)}, c^{(t)}, \ldots$.[61,63] It can be shown that if the irrep $\Lambda^{(p)}$ is contained in the product representation *at least once*, $\Lambda^{(p)} \subset \Lambda_\text{vec}\otimes\Lambda_\text{vec}$, the phonon modes transforming according to this irrep are Raman active,[61,63] i.e., their Raman tensors exhibit non-vanishing elements. An equivalent formulation is that the phonon mode transforms like a rank-two polar tensor, since evidently its irrep contributes to the product representation $\Lambda_\text{vec}\otimes\Lambda_\text{vec}$ that describes the transformation properties of a rank-two polar tensor under the elements of $\mathcal{G}_\text{p}$.

It is important to appreciate that the Raman tensor $\mathscr{R}^m$ generally is *not* invariant under the rotations of the point group $\mathcal{G}_\text{p}$. This is only valid for the totally symmetric irrep. This is best illustrated by an example: Consider the monoclinic point group $\mathcal{G}_\text{p} = C_{2h}$ $(2/m)$ with the four symmetry elements $E, C_{2y}, I, \sigma_y (\equiv IC_{2y})$. The irreps are A_g, B_g, A_u, B_u, but only A_g, B_g allow for Raman activity, and its character table is shown in table 2.2. The corresponding Raman tensors are

$$\mathscr{R}^{A_g} = \begin{pmatrix} a & 0 & d \\ 0 & b & 0 \\ d & 0 & c \end{pmatrix}, \tag{2.63a}$$

$$\mathscr{R}^{B_g} = \begin{pmatrix} 0 & e & 0 \\ e & 0 & f \\ 0 & f & 0 \end{pmatrix}, \tag{2.63b}$$

and the 3×3 unitary representation of the C_{2y} symmetry element is

$$D(C_{2y}) = \begin{pmatrix} -1 & 0 & 0 \\ 0 & 1 & 0 \\ 0 & 0 & -1 \end{pmatrix},$$

[v] A representation Λ' of a group is *reducible* if the corresponding matrix representations of all group operations can be brought to block-diagonal form by the *same* unitary matrix via a similarity transform. This amounts to finding another basis, thereby making the matrix representations as simple as possible.

	symmetry element			
irrep	E	C_{2y}	I	σ_y
A_g	1	1	1	1
B_g	1	−1	1	−1
A_u	1	1	−1	−1
B_u	1	−1	−1	1

TABLE 2.2: Character table of the C_{2h} point group (`http://www.cryst.ehu.es/cgi-bin/rep/programs/sam/point.py?sg=10&num=5`). The representation of a three dimensional vector is $\Lambda_{\text{vec}} = A_u \oplus 2B_u$.

yielding

$$\sum_{\nu\nu'}[D(C_{2y})]_{\mu\nu}[D(C_{2y})]_{\mu'\nu'}\mathscr{R}^{A_g}_{\nu\nu'} \rightarrow D(C_{2y})\mathscr{R}^{A_g}[D(C_{2y})]^T = \mathscr{R}^{A_g} \tag{2.64a}$$

$$\sum_{\nu\nu'}[D(C_{2y})]_{\mu\nu}[D(C_{2y})]_{\mu'\nu'}\mathscr{R}^{B_g}_{\nu\nu'} \rightarrow D(C_{2y})\mathscr{R}^{B_g}[D(C_{2y})]^T = -\mathscr{R}^{B_g}. \tag{2.64b}$$

Evidently, in accordance with table 2.1, the Raman tensor of the B_g irrep transforms unevenly upon application of the principal rotation $C_n \equiv C_{2y}$. Indeed, this can also be directly inferred from table 2.2. The totally symmetric irrep is A_g, since upon application of *all* corresponding symmetry elements the respective modes transform evenly.

A connection between the matrix irreps and the character table 2.2 can be established in the following way: Recall the $3N_{\text{nucl}} \times 3N_{\text{nucl}}$ dimensional matrix representations of the space group operations given by eq. (2.30). A reducible matrix representation of the point group $\mathcal{G}_{\text{p}}$ can be constructed by[27,28,61]

$$\mathscr{U}(S^{(j)};\mathbf{q}=\mathbf{0}) = \exp[i\mathbf{q}^T(\mathbf{v}^{(S^{(j)})}+\mathbf{R}_l)]\Gamma(\{S^{(j)}|\mathbf{v}(S^{(j)})+\mathbf{R}_l\};\mathbf{q}=\mathbf{0}). \tag{2.65}$$

It should be noted that the representation established by the set of matrices $\{\mathscr{U}(S^{(j)})\}$ is not a group representation in the ordinary sense, but a so-called "multiplier representation".[27,28,61] These matrices commute with the dynamical matrix, $\mathscr{U}(S^{(j)})C(\mathbf{q}=\mathbf{0})[\mathscr{U}(S^{(j)})]^{-1} = C(\mathbf{q}=\mathbf{0})$. Operating from the left with $\mathscr{U}(S^{(j)})$ on the eigenvalue equation eq. (2.23), it follows that ($\mathscr{D}^{s\,\mu}_{s'\mu'}(\mathbf{q}=\mathbf{0}) = C^{s\,\mu}_{s'\mu'}(\mathbf{q}=\mathbf{0})/(M_sM_{s'})^{1/2}$):

$$\mathscr{D}(\mathbf{q}=\mathbf{0})[\mathscr{U}(S^{(j)})\mathbf{w}_{m,\mathbf{q}=\mathbf{0}}] = \omega^2_{m,\mathbf{q}=\mathbf{0}}[\mathscr{U}(S^{(j)})\mathbf{w}_{m,\mathbf{q}=\mathbf{0}}], \tag{2.66}$$

implying that $[\mathscr{U}(S^{(j)})\mathbf{w}_{m,\mathbf{q}=\mathbf{0}}]$ also is an eigenvector with eigenvalue $\omega^2_{m,\mathbf{q}=\mathbf{0}}$ of the dynamical matrix at $\mathbf{q}=\mathbf{0}$, i.e., $[\mathscr{U}(S^{(j)})\mathbf{w}_{m,\mathbf{q}=\mathbf{0}}] \in V^{(\omega_m)}$. $V^{(\omega_m)}$ denotes the subspace of V_Γ corresponding to the eigenvalue(s) $\omega^2_{m,\mathbf{q}=\mathbf{0}}$ (possibly degenerate). The most that can be inferred from this information is that the rotated eigenvector is some linear combination of the $\mathbf{w}^{(\lambda)}_m \in V^{(\omega_m)}$:

$$\mathscr{U}(S^{(j)})\mathbf{w}^{(\lambda)}_m = \sum_{\lambda'=1}^{\dim V^{(\omega_m)}} \mathbf{w}^{(\lambda')}_m \tau^{(m)}_{\lambda'\lambda}(S^{(j)}), \tag{2.67}$$

with $\tau^{(m)}_{\lambda'\lambda}(S^{(j)}) = [\mathbf{w}^{(\lambda')}_m]^H\mathscr{U}(S^{(j)})\mathbf{w}^{(\lambda)}_m$, where $[\mathbf{w}^{(\lambda')}_m]^H$ is the conjugate-transpose of this vector. Evidently, the $\{\mathbf{w}^{(\lambda)}_m\}$ span a vector space that is invariant with respect to all symmetry operations of the point group $\mathcal{G}_{\text{p}}$. Indeed, since $\mathscr{D}(\mathbf{q}=\mathbf{0})$ is hermitian, all other eigenvectors with eigenvalues *different* from ω_m lie in the orthogonal complement $V^{(\omega_m)}_\perp = V_\Gamma \setminus V^{(\omega_m)}$ of $V^{(\omega_m)}$, from which immediately follows that $V^{(\omega_m)}$ has *no proper invariant subspaces*[vi] and hence is irreducible. In other words, the $\{\tau^{(m)}_{\lambda'\lambda}(S^{(j)})\}$ provide a unitary (multiplier) irrep of $\mathcal{G}_{\text{p}}$.[27,28,61]

Returning to table 2.2, it is evident that all irreps are one-dimensional; that is, phonon modes are non-degenerate. This means the irrep matrices $\tau^{(m)}_{\lambda'\lambda}(S^{(j)})$ are simple scalars and therefore equal their trace/character.

[vi] This means that there are *no subspaces of smaller dimension* which are invariant under the symmetry operations of the point group of the crystal. "Invariant" means that application of $\mathscr{U}(S^{(j)})$ to an eigenvector corresponding to eigenvalue ω^2_m maps that eigenvector to the same subspace. The subspace then may be called "closed" with respect to the operations of $\mathcal{G}_{\text{p}}$.

As a matter of fact, in this special case, the transformation properties of the eigenvectors $\mathbf{w}_m$ (and of the Raman tensors!) under the symmetry operations of $\mathcal{G}_\mathrm{p}$ are directly visible form the character table 2.2. However, if degeneracies larger than one occur, the character table may no longer be sufficient and an explicit form of the irrep matrices $\tau^{(m)}_{\lambda'\lambda}(S^{(j)})$ is required.

3 Results and Discussion

In the first part of this chapter (section 3.1) some theoretical methods developed/extended/adapted in the course work are outlined. The materials treated in this work are introduced in section 3.2. Based on the methods from section 3.1, in section 3.3, phonon dispersions and derived quantities such as phonon density of states and the thermodynamic functions are calculated. The investigated material systems are the three copper-oxide phases and, for demonstrative purposes, the wide-gap insulator CaF_2. In the last section (section 3.4), the focus shall be on the Raman scattering properties of monoclinic CuO and tetragonal Cu_4O_3. Special emphasis is put on the comparison of two phases of CuO existent a different temperatures that differ by their anti-ferromagnetic ordering. At last, the behaviour of the Raman active modes of Cu_4O_3 under exertion of hydrostatic pressure will be examined.

3.1 Theoretical contributions

In this section I will state my own contributions to theoretical methods employed in this work. This mainly contains extensions to already existent ideas and formulations to the theory of lattice dynamics. Further, the details of the implementation for calculating FCs/dynamical matrices and first-order Raman susceptibilities from first principle data are given.

3.1.1 Inclusion of dipole-dipole corrections into dynamical matrices from the direct method

In the preceeding section the direct method for obtaining FCs has been reviewed. The central cognisance of this chapter is that within this approach dynamical matrices at wavevectors commensurable with the chosen supercell can be calculated exactly.[31,42]

The goal of the present section is to outline how Gonze's method[19] for the treatment of dipole-dipole corrections in the dynamical matrices can be applied within the framework of the direct method. In fact, once the $C^{s\,\mu}_{s'\nu}(\mathbf{q}_c)$ are determined, the technical treatment proceeds along similar lines as in the case of dynamical matrices obtained from DFPT (see section 2.2.5.1: steps **(I)** to **(IV)**).

The procedure to be adopted can be summarised in the following way:

- **(i)** Based on a (primitive) crystal structure determine a supercell by specifiying the matrix M from section 2.2.4.
- **(ii)** Calculate the full (cummulative) FCs $C^{0\,s\,\mu}_{l's'\nu'}$ with eq. (2.42) using forces from DFT.
- **(iii)** Determine the grid of commensurable wavevectors ($\mathscr{G}_{\mathbf{q}_c}$) through the columns of M^{-T} (see again section 2.2.4). Calculate the exact dynamical matrices $C^{s\,\mu}_{s'\mu'}(\mathbf{q}_c)\ \forall \mathbf{q}_c \in \mathscr{G}_{\mathbf{q}_c}$ with the cummulative FCs using eq. (2.24).
- **(iv)** Now the starting position is the same as with dynamical matrices from DFPT: To interpolate dynamical matrices across the BZ (e.g., to compute the phonon frequency spectrum) follow section 2.2.5.1, steps **(I)** to **(IV)**. The commensurable wavevectors $\mathbf{q}_c$ here replace the $\mathbf{q}_{j_1 j_2 j_3}$ from section 2.2.5.1.

3.1.2 Using symmetries for finding a minimum set of displacements and forces

The FCs are calculated with the aid of eq. (2.42). In order to obtain all FCs for a supercell with $\det M \times N_{\text{nucl}}$ atoms $3 \times 2 \times \det M \times N_{\text{nucl}}$ self-consistent DFT calculations are necessary. For large supercells the corresponding computational effort is prohibitively large. Using the symmetry of the space group of the crystal not only tremendously reduces the computational load but also minimises numerical inaccuracies in the FCs.

Utilising symmetry for finding the independent set of displacements needed to calculate the FCs reduces to finding the independent displacements for a minimal set of atoms from which the rest of atoms in the supercell can be generated by applying all symmetry operations. Let $\{\{P|\mathbf{v}^{(P)} + \mathbf{R}_\mathrm{p}^{(l)}\}\}$ be the set of symmetry operations that map the atoms indexed by l, s onto itself. Successive application (of the rotational part P) of these symmetry operations to an initial test displacement $\mathbf{u}_{l,s}^{(\nu)}$ in general rotates it to a new displacement, possibly linearly independent of the old one. If from this initial displacement three linearly independent displacements can be created, it is taken as the independent set of displacement(s) needed for this atom. If one displacement does not suffice to generate three linearly independent displacements, another test displacement $\mathbf{u}_{l,s}^{(\nu')}$ is considered to which—in order to complete the set—again all symmetry operations are applied. This procedure is repeated until three displacements have been generated, and the underlying test displacements form the set of independent displacements.

However, eq. (2.42) demands usage of displacements in positive and negative directions. Therefore, the signs of the independent displacements generated previously are inverted and it is checked which displacements from the sign-inverted set can be generated from the initial set. The full set of displacements for atom l, s follows from the conjunction of the initial set and the displacements from the sign-inverted set not related to any displacement of the initial set. This procedure is to be executed for all symmetrically independent atoms in the supercell.

Once the forces for the required number of displacements have been calculated from a DFT self-consistency the above-mentioned approach is inverted in order to generate the remaining forces. If two atoms l', s' and l'_1, s'_1 are linked through symmetry operation $\{S|\mathbf{v}^{(S)} + \mathbf{R}_\mathrm{p}^{(\bar{l})}\}$, their displacements are related by $\mathbf{u}_{l'_1,s'_1}^{(\nu')} = S\mathbf{u}_{l,s}^{(\nu)}$, and the respective forces due to displacement $\mathbf{u}_{l'_1,s'_1}^{(\nu')}$ can be computed from the forces due to $\mathbf{u}_{l',s'}^{(\nu)}$ through[30,41]

$$\mathbf{F}_{l'',s''}(\mathbf{u}_{l'_1,s'_1}^{(\nu')}) = S\mathbf{F}_{l,s}(\mathbf{u}_{l',s'}^{(\nu)}) \text{ with } l, l'' = 1, \ldots, \det M,\ s, s'' = 1, \ldots, N_\mathrm{nucl}, \tag{3.1}$$

and $\mathbf{x}_{l'',s''} = \{S|\mathbf{v}^{(S)} + \mathbf{R}_\mathrm{p}^{(\bar{l})}\}\mathbf{x}_{l,s}$.

As a final point it should be mentioned that application of symmetries to a set of independent displacements not necessarily results in three orthogonal displacements (still linearly independent though) oriented along the Cartesian axes. Three such displacements $\{\overline{\mathbf{u}}_{l',s'}^{(\lambda)}\}$ can be generated from the linearly independent ones by performing a transformation[30,41]

$$\overline{\mathbf{u}}_{l',s'}^{(\lambda)} = \sum_{\nu=1}^{3} \mathbf{u}_{l',s'}^{(\nu)} A_{\nu\lambda}, \tag{3.2}$$

where A is the solution of the linear system of equations

$$[\hat{\mathbf{u}}_{l,'s'}^{(1)}, \hat{\mathbf{u}}_{l',s'}^{(2)}, \hat{\mathbf{u}}_{l',s'}^{(3)}]_\pm A = \begin{cases} +\mathbb{1}_{3\times3} & \text{for the set of positive displacements } (+), \\ -\mathbb{1}_{3\times3} & \text{for the set of negative displacements } (-), \end{cases} \tag{3.3}$$

and the same transformation is applied to the forces:

$$\mathbf{F}_{l,s}(\overline{\mathbf{u}}_{l',s'}^{(\lambda)}) = \sum_{\nu=1}^{3} \mathbf{F}_{l,s}(\overline{\mathbf{u}}_{l',s'}^{(\nu)}) A_{\nu\lambda}, \tag{3.4}$$

which are then to be used in eq. (2.42) to make the components of $C_{l's'\mu'}^{l\,s\,\mu}$ refer to the Cartesian axes.

3.1.3 Perturbation-like approach to first-order changes in phonon mode frequencies in the limit $\mathbf{q} \to \mathbf{0}$ for polar semiconductors

In this section a perturbation-like approach for the calculations of first-order changes of the phonon mode frequencies with $\mathbf{q}$ from in the limit of $\mathbf{q} \to \mathbf{0}$ along direction $\hat{\mathbf{q}}$ is outlined. Note that this method is not limited to dynamical matrices from the direct method but can also be used in conjunction with DFPT-calculated dynamical matrices. Further, the approach discussed in the following is not entirely new (see Born and Huang

[66] (chap. V), and Maradudin et al. [28] (chap. 6)) but has merely been generalised to the case of anisotropic Born effective charges by making use of the method of Gonze and Lee [19].

I shall consider the following change-of-phase for the dynamical matrix:[28]

$$\mathscr{C}^{s\,\mu}_{s'\mu'}(\mathbf{q}) = e^{+i\mathbf{q}^T\mathbf{x}_{s'}} C^{s\,\mu}_{s'\mu'}(\mathbf{q}) e^{-i\mathbf{q}^T\mathbf{x}_s}, \tag{3.5}$$

where $\mathbf{x}_s$ denotes an atomic position in the unit cell.

In order to develop the equations governing the $\mathbf{q} \to \mathbf{0}$ limit of the phonon mode frequencies I will work with the mass-reduced dynamical matrix $\mathscr{D}^{s\,\mu}_{s'\mu'}(\mathbf{q}) = \mathscr{C}^{s\,\mu}_{s'\mu'}(\mathbf{q}) \big/ (M_s M_{s'})^{1/2}$ whose eigenvalues and eigenvectors shall be denoted by $(\omega_{m\mathbf{q}})^2$ and $b^{s,\mu}_{m\mathbf{q}}$, respectively. Next, expand the single parts of the corresponding eigenvalue equation for fixed direction $\hat{\mathbf{q}}$ around $\mathbf{q} = \mathbf{0}$ ($\xi = |\mathbf{q}|$):

$$\mathscr{D}^{s\,\mu}_{s'\mu'} = \mathscr{D}_{0,s'\mu'}^{\;\;s\,\mu} + {}^{\mathrm{na}}\mathscr{D}^{s\,\mu}_{s'\mu'} + i\mathscr{D}_{1,s'\mu'}^{\;\;s\,\mu}\xi + \tfrac{1}{2}\mathscr{D}_{2,s'\mu'}^{\;\;s\,\mu}\xi^2 + \cdots \tag{3.6a}$$

$$b^{s,\mu}_{m,\mathbf{q}} = b_{0,m}^{\;\;s,\mu} + ib_{1,m}^{\;\;s,\mu}\xi + \tfrac{1}{2}b_{2,m}^{\;\;s,\mu}\xi^2 + \cdots \tag{3.6b}$$

$$\omega_{m\mathbf{q}} = \omega_{1,m,\hat{\mathbf{q}}}\xi + \tfrac{1}{2}\omega_{2,m,\hat{\mathbf{q}}}\xi^2 + \cdots, \tag{3.6c}$$

wherein ${}^{\mathrm{na}}\mathscr{D}^{s\,\mu}_{s'\mu'} \equiv {}^{\mathrm{na}}\mathscr{D}^{s\,\mu}_{s'\mu'}(\hat{\mathbf{q}}) = {}^{\mathrm{na}}\mathscr{C}^{s\,\mu}_{s'\mu'}(\hat{\mathbf{q}}) \big/ (M_s M_{s'})^{1/2}$, and the $\mathbf{q} = \mathbf{0}$ label has been suppressed in favor of a concise notation.

The parts of the set of equations (3.6) needed in the following are:

$$\mathscr{D}_{0,s'\mu'}^{\;\;s\,\mu} = {}^{\mathrm{sr}}\mathscr{D}_{0,s'\mu'}^{\;\;s\,\mu} + {}^{\mathrm{dd}}\mathscr{D}_{0,s'\mu'}^{\;\;s\,\mu} \tag{3.7a}$$

$$\mathscr{D}_{1,s'\mu'}^{\;\;s\,\mu} = \sum_{\gamma} \left({}^{\mathrm{sr}}\mathscr{D}_{1,s'\mu',\gamma}^{\;\;s\,\mu} + {}^{\mathrm{dd}}\mathscr{D}_{1,s'\mu',\gamma}^{\;\;s\,\mu} \right) \hat{q}_\gamma \tag{3.7b}$$

$$\mathscr{D}_{2,s'\mu'}^{\;\;s\,\mu} = \sum_{\gamma\lambda} \left({}^{\mathrm{sr}}\mathscr{D}_{2,s'\mu',\gamma\lambda}^{\;\;s\,\mu} + {}^{\mathrm{dd}}\mathscr{D}_{2,s'\mu',\gamma\lambda}^{\;\;s\,\mu} \right) \hat{q}_\gamma \hat{q}_\lambda, \tag{3.7c}$$

and

$$\omega_{1,m,\hat{\mathbf{q}}} = \sum_{\gamma} \left. \frac{\partial \omega_{m,\mathbf{q}}}{\partial q_\gamma} \right|_{\mathbf{q}=\mathbf{0}} \hat{q}_\gamma, \tag{3.8a}$$

$$b_{n,m}^{\;\;s,\mu} = \sum_{\gamma_1 \cdots \gamma_n} \left. \frac{\partial^n b^{s,\mu}_{m,\mathbf{q}}}{\partial q_{\gamma_1} \cdots \partial q_{\gamma_n}} \right|_{\mathbf{q}=\mathbf{0}} \hat{q}_{\gamma_1} \cdots \hat{q}_{\gamma_n}, \tag{3.8b}$$

while the derivatives with respect to the wavevector of the short-ranged part of the dynamical matrix at $\mathbf{q} = \mathbf{0}$ read

$${}^{\mathrm{sr}}\mathscr{D}_{1,s'\mu',\gamma}^{\;\;s\,\mu} = \sum_{l'} {}^{\mathrm{sr}}C^{0\,s\,\mu}_{l's'\mu'} \big/ (M_s M_{s'})^{1/2}\; d^{0\,s}_{l's'\gamma} \tag{3.9a}$$

$${}^{\mathrm{sr}}\mathscr{D}_{2,s'\mu',\gamma\lambda}^{\;\;s\,\mu} = -\sum_{l'} {}^{\mathrm{sr}}C^{0\,s\,\mu}_{l's'\mu'} \big/ (M_s M_{s'})^{1/2}\; d^{0\,s}_{l's'\gamma} d^{0\,s}_{l's'\lambda}. \tag{3.9b}$$

The derivatives of the dipole-dipole part require a careful treatment. Starting from a phase-changed version of eq. (2.51b), consider for the further treatment an expression of the form:

$$\begin{aligned}
{}^{\mathrm{dd}}\overline{\mathscr{C}}^{s\,\mu}_{s'\mu'}(\mathbf{q}) = {} & \frac{4\pi}{\Omega_0} \frac{q_\mu q_{\mu'}}{\epsilon^\infty(\mathbf{q})} \left(e^{-\epsilon^\infty(\mathbf{q})/4\eta^2} - 1 \right) \\
& + \frac{4\pi}{\Omega_0} \sum_{\substack{|\mathbf{G}|\neq 0 \\ \mathbf{K}=\mathbf{q}+\mathbf{G}}} K_\mu K_{\mu'} F_0(\mathbf{K}) e^{i\mathbf{G}^T(\mathbf{x}_s - \mathbf{x}_{s'})} \\
& - \sum_{\substack{l' \\ D^{0\,s}_{l's'} \neq 0}} \frac{\eta^3}{\sqrt{\det \epsilon^\infty}} e^{i\mathbf{q}^T \mathbf{d}^{0\,s}_{l's'}} H_{\mu\mu'}(\eta \boldsymbol{\Delta}^{0\,s}_{l's'}, \eta D^{0\,s}_{l's'}) \\
& - \frac{4}{3\sqrt{\pi}} \frac{\eta^3}{\sqrt{\det \epsilon^\infty}} \delta_{ss'} (\epsilon^\infty)^{-1}_{\mu\mu'},
\end{aligned} \tag{3.10}$$

which possesses a unique limiting value at vanishing wavevector. I use the abbreviations $\Delta^{0s}_{l's'\mu} = \sum_{\mu'} (\epsilon^\infty)^{-1}_{\mu\mu'} d^{0s}_{l's'\mu'}$, and $D^{0s}_{l's'} = \sqrt{\sum_\mu d^{0s}_{l's'\mu} \Delta^{0s}_{l's'\mu}}$, and further define for equation (3.10)

$$F_0(\mathbf{K}) = \frac{e^{-\epsilon^\infty(\mathbf{K})/4\eta^2}}{\epsilon^\infty(\mathbf{K})} \quad \text{with } \mathbf{K} = \mathbf{q} + \mathbf{G}, \tag{3.11}$$

with $\epsilon^\infty(\mathbf{K}) = \sum_{\mu\mu'} K_\mu \epsilon^\infty_{\mu\mu'} K_{\mu'}$.

The Born effective charges must be included in the first- and second-order changes in $\mathbf{q}$ of the dipole-dipole part:

$$^{\mathrm{dd}}\mathscr{D}^{\,s\,\mu}_{1,s'\mu',\gamma} = \sum_{\nu\nu'} \frac{Z^*_{s,\nu\mu} Z^*_{s',\nu'\mu'}}{(M_s M_{s'})^{1/2}} \lim_{\mathbf{q}\to\mathbf{0}} {}^{\mathrm{dd}}\overline{\mathscr{C}}^{\,s\,\nu}_{1,s'\nu',\gamma}(\mathbf{q}) \tag{3.12a}$$

$$^{\mathrm{dd}}\mathscr{D}^{\,s\,\mu}_{2,s'\mu',\gamma\lambda} = \sum_{\nu\nu'} \frac{Z^*_{s,\nu\mu} Z^*_{s',\nu'\mu'}}{(M_s M_{s'})^{1/2}} \lim_{\mathbf{q}\to\mathbf{0}} {}^{\mathrm{dd}}\overline{\mathscr{C}}^{\,s\,\nu}_{2,s'\nu',\gamma\lambda}(\mathbf{q}). \tag{3.12b}$$

The limits are related to the first and second derivatives of eq. (3.10):

$$\begin{aligned}
\lim_{\mathbf{q}\to\mathbf{0}} \frac{\partial}{\partial q_\gamma} {}^{\mathrm{dd}}\overline{\mathscr{C}}^{\,s\,\mu}_{s'\mu'}(\mathbf{q}) = {} & \frac{4\pi}{\Omega_0} \sum_{|\mathbf{G}|\neq 0} e^{i\mathbf{G}^T(\mathbf{x}_s - \mathbf{x}_{s'})} \\
& \times \left[\left(\delta_{\mu\gamma} G_{\mu'} + G_\mu \delta_{\mu'\gamma}\right) F_0(\mathbf{G}) + G_\mu G_{\mu'} \left(\epsilon^\infty \mathbf{G}\right)_\gamma F_1(\mathbf{G}) \right] \\
& - i \sum_{l, D^{0s}_{ls'}\neq 0} \frac{\eta^3}{\sqrt{\det \epsilon^\infty}} H_{\mu\mu'}(\eta \boldsymbol{\Delta}^{0s}_{ls'}, \eta D^{0s}_{ls'}) d^{0s}_{ls'\gamma},
\end{aligned} \tag{3.13a}$$

$$\begin{aligned}
\lim_{\mathbf{q}\to\mathbf{0}} \frac{\partial^2}{\partial q_\lambda \partial q_\gamma} {}^{\mathrm{dd}}\overline{\mathscr{C}}^{\,s\,\mu}_{s'\mu'}(\mathbf{q}) = {} & -\frac{4\pi}{\Omega_0} (4\eta^2)^{-1} (\delta_{\mu\gamma}\delta_{\mu'\lambda} + \delta_{\mu\lambda}\delta_{\mu'\gamma}) \\
& + \frac{4\pi}{\Omega_0} \sum_{|\mathbf{G}|\neq 0} e^{i\mathbf{G}^T(\mathbf{x}_s - \mathbf{x}_{s'})} \left[\left(\delta_{\mu\gamma}\delta_{\mu'\lambda} + \delta_{\mu\lambda}\delta_{\mu'\gamma}\right) F_0(\mathbf{G}) \right. \\
& + \left(\delta_{\mu\lambda} G_{\mu'} + G_\mu \delta_{\mu'\lambda}\right) \left(\epsilon^\infty \mathbf{G}\right)_\gamma F_1(\mathbf{G}) \\
& + \left(\delta_{\mu\gamma} G_{\mu'} + G_\mu \delta_{\mu'\gamma}\right) \left(\epsilon^\infty \mathbf{G}\right)_\lambda F_1(\mathbf{G}) \\
& \left. + G_\mu G_{\mu'} \epsilon^\infty_{\gamma\lambda} F_1(\mathbf{G}) + G_\mu G_{\mu'} \left(\epsilon^\infty \mathbf{G}\right)_\gamma \left(\epsilon^\infty \mathbf{G}\right)_\lambda F_2(\mathbf{G}) \right] \\
& + \sum_{l, D^{0s}_{ls'}\neq 0} \frac{\eta^3}{\sqrt{\det \epsilon^\infty}} H_{\mu\mu'}(\eta \boldsymbol{\Delta}^{0s}_{ls'}, \eta D^{0s}_{ls'}) d^{0s}_{ls'\gamma} d^{0s}_{ls'\lambda},
\end{aligned} \tag{3.13b}$$

wherein

$$F_1(\mathbf{K}) = -\frac{2F_0(\mathbf{K})}{4\eta^2} - \frac{2F_0(\mathbf{K})}{\epsilon^\infty(\mathbf{K})} \tag{3.14a}$$

$$F_2(\mathbf{K}) = -\frac{2F_1(\mathbf{K})}{4\eta^2} - \frac{2F_1(\mathbf{K})}{\epsilon^\infty(\mathbf{K})} + \frac{4F_0(\mathbf{K})}{(\epsilon^\infty(\mathbf{K}))^2}, \tag{3.14b}$$

such that

$$\lim_{\mathbf{q}\to\mathbf{0}} {}^{\mathrm{dd}}\overline{\mathscr{C}}^{\,s\,\mu}_{1,s'\mu',\gamma}(\mathbf{q}) = -i \lim_{\mathbf{q}\to\mathbf{0}} \frac{\partial}{\partial q_\gamma} {}^{\mathrm{dd}}\overline{\mathscr{C}}^{\,s\,\mu}_{s'\mu'}(\mathbf{q}) \tag{3.15a}$$

$$\lim_{\mathbf{q}\to\mathbf{0}} {}^{\mathrm{dd}}\overline{\mathscr{C}}^{\,s\,\mu}_{2,s'\mu',\gamma\lambda}(\mathbf{q}) = \lim_{\mathbf{q}\to\mathbf{0}} \frac{\partial^2}{\partial q_\lambda \partial q_\gamma} {}^{\mathrm{dd}}\overline{\mathscr{C}}^{\,s\,\mu}_{s'\mu'}(\mathbf{q}). \tag{3.15b}$$

Mind that the factor $-i$ in the first derivative has been included because a factor $+i$ was introduced in the term linear in ξ of eq. (3.6a).

I now return to the expansions in eqs. (3.6) and equate terms of like power in ξ up to order ξ^2 to arrive at the following set of equations:

$$\sum_{s'\mu'} \mathscr{D}_{0,s'\mu'}^{\ s\ \mu}\, b_{0,m}^{\ s',\mu'} = -\sum_{s'\mu'} {}^{\mathrm{na}}\mathscr{D}_{0,s'\mu'}^{\ s\ \mu}\, b_{0,m}^{\ s',\mu'} \tag{3.16a}$$

$$\begin{aligned} i\sum_{s'\mu'} \mathscr{D}_{0,s'\mu'}^{\ s\ \mu}\, b_{1,m}^{\ s',\mu'} &= -i\sum_{s'\mu'} {}^{\mathrm{na}}\mathscr{D}_{s'\mu'}^{s\ \mu}\, b_{1,m}^{\ s',\mu'} \\ &\quad - i\sum_{s'\mu'} \mathscr{D}_{1,s'\mu'}^{\ s\ \mu}\, b_{0,m}^{\ s',\mu'} \end{aligned} \tag{3.16b}$$

$$\begin{aligned} \tfrac{1}{2}\sum_{s'\mu'} \mathscr{D}_{0,s'\mu'}^{\ s\ \mu}\, b_{2,m}^{\ s',\mu'} &= \left(\omega_{1,m,\hat{\mathbf{q}}}\right)^2 b_{0,m}^{\ s,\mu} \\ &\quad - \tfrac{1}{2}\sum_{s'\mu'} {}^{\mathrm{na}}\mathscr{D}_{s'\mu'}^{s\ \mu}\, b_{2,m}^{\ s',\mu'} \\ &\quad + \sum_{s'\mu'} \mathscr{D}_{1,s'\mu'}^{\ s\ \mu}\, b_{1,m}^{\ s',\mu'} \\ &\quad - \tfrac{1}{2}\sum_{s'\mu'} \mathscr{D}_{2,s'\mu'}^{\ s\ \mu}\, b_{0,m}^{\ s',\mu'}. \end{aligned} \tag{3.16c}$$

Noting that the displacements of the acoustic modes are just a rigid displacement of all atoms, $b_{0,m}^{\ s,\mu} = \sqrt{M_s}u_{0,m}^{\ \mu}$, these equations may now be solved for the first-order changes in the phonon mode frequencies $\omega_{1,m,\hat{\mathbf{q}}}$. From eq. (3.16b) I get for the first-order eigenvector:

$$b_{1,m}^{\ s\mu} = -\sum_{\substack{s's''\\ \mu'\mu''}} \left[\left(\mathbb{1}^{\perp} + \mathscr{G}^{\perp\,\mathrm{na}}\mathscr{D}^{\perp}\right)^{-1}\mathscr{G}^{\perp}\right]_{s''\mu''}^{s\ \mu} \mathscr{D}_{1,s'\ \mu'}^{\ s''\mu''} \sqrt{M_{s'}}u_{0,m}^{\ \mu'}, \tag{3.17}$$

where I defined the Green's function of the subspace of optical modes $V^{\perp}$,

$$\mathscr{G}^{\perp s\ \mu}_{\ s'\mu'} = \sum_{m\in V^{\perp}} b_{0,m}^{\ s,\mu}[b_{0,m}^{\ s',\mu'}]^* \Big/ \left(\omega_{m,\mathbf{q}=\mathbf{0}}\right)^2, \tag{3.18}$$

and the subspace-projected non-analytical part:

$${}^{\mathrm{na}}\mathscr{D}^{\perp s\ \mu}_{\ s'\mu'} = \sum_{mm'\in V^{\perp}} b_{0,m}^{\ s,\mu} \sum_{\substack{s_1 s_{1'}\\ \mu_1\mu_{1'}}} [b_{0,m}^{\ s_1,\mu_1}]^*\, {}^{\mathrm{na}}\mathscr{D}_{s_1's_1\mu_{1'}\mu_1}\, b_{0,m'}^{\ s_{1'},\mu_{1'}}[b_{0,m'}^{\ s',\mu'}]^*, \tag{3.19}$$

and $\left(\omega_{m,\mathbf{q}=\mathbf{0}}\right)^2, b_{0,m}^{\ s,\mu}$ in this context denote the eigenvalues, eigenvectors of the dynamical matrix from (3.7a) (the analytical part).

The solvability condition of eq. (3.16c) is that the right-hand side is orthogonal to the subspace of acoustic modes:[28,66]

$$\begin{aligned} 0 = &\sum_{s\mu} \sqrt{M_s}u_{0,m}^{\ \mu} \sum_{s'\mu'} \left[\left(-\tfrac{1}{2}\mathscr{D}_{2,s'\mu'}^{\ s\ \mu} + \delta_{ss'}\delta_{\mu\mu'}\left(\omega_{1,m,\hat{\mathbf{q}}}\right)^2\right)\sqrt{M_{s'}}u_{0,m}^{\ \mu'}\right] \\ &+ \sum_{s\mu} \sqrt{M_s}u_{0,m}^{\ \mu} \sum_{s'\mu'} \left[\mathscr{D}_{1,s'\mu'}^{\ s\ \mu}\, b_{1,m}^{\ s'\mu'} - \tfrac{1}{2}{}^{\mathrm{na}}\mathscr{D}_{s'\mu'}^{s\ \mu}\, b_{2,m}^{\ s'\mu'}\right]. \end{aligned} \tag{3.20}$$

The last term featuring ${}^{\mathrm{na}}\mathscr{D}_{s'\mu'}^{s\ \mu}$ vanishes because of the charge neutrality condition $\sum_s Z^*_{s,\mu\mu'} = 0\ \forall\mu\mu'$ (cf. equation (2.57)). Since the displacements $u_{0,m}^{\ \mu}$ are arbitrary, it must hold $\forall\mu$:

$$\left[\sum_s M_s\right] u_{0,m}^{\ \mu}\left(\omega_{1,m,\hat{\mathbf{q}}}\right)^2 = \sum_{ss'\mu'} \left[\sqrt{M_s M_{s'}}\tfrac{1}{2}\mathscr{D}_{2,s'\mu'}^{\ s\ \mu}u_{0,m}^{\ \mu'} - \sqrt{M_s}\mathscr{D}_{1,s'\mu'}^{\ s\ \mu}\, b_{1,m}^{\ s'\mu'}\right], \tag{3.21}$$

which in combination with eq. (3.17) leads to the 3×3 eigenvalue problem

$$\sum_{\mu'} \left(\Xi_{\mu\mu'} - \delta_{\mu\mu'} \left(\omega_{1,m,\hat{\mathbf{q}}} \right)^2 \right) u_{0,m}^{\mu'} = 0, \tag{3.22}$$

with $\Xi_{\mu\mu'} = \sum_{ss'} \left(M_s M_{s'} \right)^{1/2} \Xi_{s'\mu'}^{s\,\mu} \,/\, \left[\sum_s M_s \right]$, and

$$\Xi_{s'\mu'}^{s\,\mu} = \tfrac{1}{2} \mathscr{D}_{2,s'\mu'}^{s\,\mu} + \sum_{\substack{s_1 s_1' \\ \mu_1 \mu_1'}} \mathscr{D}_{1,s_1\mu_1}^{s\,\mu} \left[\left(\mathbb{1}^{\perp} + \mathscr{G}^{\perp \mathrm{na}} \mathscr{D}^{\perp} \right)^{-1} \mathscr{G}^{\perp} \right]_{s_1'\mu_1'}^{s_1\,\mu_1} \mathscr{D}_{1,s'\,\mu'}^{s_1'\mu_1'}. \tag{3.23}$$

3.1.4 Calculation of Raman spectra from first principles data

In this section I will briefly outline the methods that were implemented in order to compute Raman spectroscopic properties of semiconducting solids from data extracted first principles calculations. First, the procedure for the computation of Raman spectra is described wherein the central quantity is the Raman susceptibility $\alpha_{\mu\mu'}^{m}$. This quantity requires the calculation of the dielectric susceptibility $\chi_{\mu\mu'}$ (or the dielectric tensor $\epsilon_{\mu\mu'}$) at distorted geometries, similarly as in the case of the dynamical matrices obtained within the framework of the direct method.

The equation for the Raman susceptibility is governed by the derivative of the dielectric susceptibility with respect to atomic displacements[67–69]

$$\alpha_{\mu\mu'}^{m}(\omega) = \sqrt{\Omega_0} \sum_{s\nu} \left[\frac{\partial}{\partial u_{s,\nu}} \chi_{\mu\mu'}(\omega) \right]_{\mathbf{u}_s = \mathbf{0}} \frac{w_{m,\mathbf{q}=\mathbf{0}}^{s,\nu}}{\sqrt{M_s}}, \tag{3.24}$$

where the eigenvectors $w_{m,\mathbf{q}=\mathbf{0}}^{s,\nu}$ are those from eq. (2.23). The susceptibility $\chi_{\mu\mu'}(\omega)$ generally is frequency-dependent, and for Raman spectroscopic applications particulary frequencies in the near infrared to ultra-violet part of the spectrum are of interest. As an alternative to the susceptibility the derivative in eq. (3.24) can be calculated using the dielectric tensor $\epsilon_{\mu\mu'}$. Both are related by $\epsilon_{\mu\mu'}(\omega) = \delta_{\mu\mu'} + 4\pi\chi_{\mu\mu'}(\omega)$, such that $\frac{\partial}{\partial u_{s,\nu}} \chi_{\mu\mu'}(\omega) = \frac{1}{4\pi} \frac{\partial}{\partial u_{s,\nu}} \epsilon_{\mu\mu'}(\omega)$. Several schemes and levels of approximation exist for calculating $\epsilon_{\mu\mu'}$ ranging from the independent particle approximation (IPA) to more involved methods based on many-body perturbation theory.[6,9,69–76] In this work, the calculation of the (frequency-dependent) dielectric tensor is limited to IPA based on the PAW method.[75] Following Gajdos et al. [75] the expression for the imaginary part reads

$$\begin{aligned} \epsilon_{\mu\mu'}^{(2)}(\omega) = \frac{4\pi^2}{\Omega_0} \lim_{\mathbf{q}\to\mathbf{0}} \frac{1}{q^2} \sum_{s=\uparrow,\downarrow} \sum_{c,v,\mathbf{k}} w_{\mathbf{k}} \delta(E_{c,\mathbf{k}}^{(s)} - E_{v,\mathbf{k}}^{(s)} - \omega) \\ \times \langle u_{c,\mathbf{k}+q\hat{\mathbf{e}}_\mu}^{(s)} |\, u_{v,\mathbf{k}}^{(s)} \rangle \, \langle u_{c,\mathbf{k}+q\hat{\mathbf{e}}_{\mu'}}^{(s)} |\, u_{v,\mathbf{k}}^{(s)} \rangle^{*}, \end{aligned} \tag{3.25}$$

wherein the summation extends over vertical transitions—the so-called optical limit ($\lim_{\mathbf{q}\to 0}$) for which $\mathbf{\Delta k} = \mathbf{0}$—between valence bands ($v$) and conduction bands ($c$). The band energies are $E_{v,\mathbf{k}}^{(s)}$ and $E_{c,\mathbf{k}}^{(s)}$, respectively, and the integral representation of the scalar products of the cell-periodic part of the Bloch functions is:[75]

$$\langle u_{c,\mathbf{k}+q\hat{\mathbf{e}}_\mu}^{(s)} |\, u_{v,\mathbf{k}}^{(s)} \rangle = \int_{\Omega_0} d^3\mathbf{r} \, [u_{c,\mathbf{k}+q\hat{\mathbf{e}}_\mu}^{(s)}(\mathbf{r})]^{*} \, u_{v,\mathbf{k}}^{(s)}(\mathbf{r}). \tag{3.26}$$

The unit vectors $\hat{\mathbf{e}}_\mu$, $\hat{\mathbf{e}}_{\mu'}$ are oriented along the Cartesian directions.

Since eq. (3.25) is evaluated in the limit $\mathbf{q} \to \mathbf{0}$, the Bloch functions $|u_{n,\mathbf{k}+\mathbf{q}}^{(s)}\rangle$ are expanded up to linear order in $\mathbf{q}$, $|u_{n,\mathbf{k}+\mathbf{q}}^{(s)}\rangle = |u_{n,\mathbf{k}}^{(s)}\rangle + \sum_\nu q_\nu \frac{\partial}{\partial k_\nu} |u_{n,\mathbf{k}}^{(s)}\rangle + O(\mathbf{q}^2)$, and the first-order change in $\mathbf{k}$ of the cell-periodic part of the Bloch functions comes from second-order perturbation theory:[75]

$$\frac{\partial}{\partial k_\nu} |u_{n,\mathbf{k}}^{(s)}\rangle = \sum_{n \neq n'} \frac{|u_{n',\mathbf{k}}^{(s)}\rangle \, \langle u_{n',\mathbf{k}}^{(s)}| \frac{\partial}{\partial k_\nu} (H_{\mathbf{k}} - E_{n,\mathbf{k}}^{(s)} S_{\mathbf{k}}) |u_{n,\mathbf{k}}^{(s)}\rangle}{E_{n,\mathbf{k}}^{(s)} - E_{n',\mathbf{k}}^{(s)}}, \tag{3.27}$$

wherein $H_{\mathbf{k}}$ is the Hamiltonian for the cell-periodic part of the Bloch function, and $S_{\mathbf{k}}$ is the corresponding overlap operator.

The real part of the dielectric function $\epsilon^{(1)}_{\mu\mu'}(\omega)$ is related to the imaginary part through Kramers-Kronig relations

$$\mathrm{Re}\,\epsilon_{\mu\mu'}(\omega+i\zeta)\big|_{\zeta\to 0^+} = \delta_{\mu\mu'} + \mathrm{Re}\left[\int_0^\infty \frac{d\omega'}{\pi}\left(\frac{\mathrm{Im}\,\epsilon_{\mu\mu'}(\omega')}{\omega'-\omega-i\zeta} + \frac{\mathrm{Im}\,\epsilon_{\mu\mu'}(\omega')}{\omega'+\omega+i\zeta}\right)\right]\Bigg|_{\zeta\to 0^+} \tag{3.28a}$$

$$\mathrm{Im}\,\epsilon_{\mu\mu'}(\omega+i\zeta)\big|_{\zeta\to 0^+} = \mathrm{Im}\left[\int_0^\infty \frac{d\omega'}{\pi}\left(\frac{\mathrm{Im}\,\epsilon_{\mu\mu'}(\omega')}{\omega'-\omega-i\zeta} + \frac{\mathrm{Im}\,\epsilon_{\mu\mu'}(\omega')}{\omega'+\omega+i\zeta}\right)\right]\Bigg|_{\zeta\to 0^+}, \tag{3.28b}$$

with ζ being positive infinitesimal.

The idea now is to approximate the derivative in eq. (3.24) through a finite difference scheme. For this to be accomplished the dielectric tensor must be evaluated at distorted atomic configurations. That is, a fully self-consistent calculation is carried out with one atom displaced (by a finite amount) from its equilibrium position. The resultant wavefunction in conjunction with its $\mathbf{k}$-derivative (cf. eq. (3.27)) is then used to determine the imaginary part of the dielectric tensor which in turn determines the real part through eq. (3.28). For the atomic displacements positive and negative (Cartesian) directions are used, allowing to write an approximation for the derivative $\frac{1}{4\pi}\frac{\partial}{\partial u_{s,\nu}}\epsilon_{\mu\mu'}(\omega)$ based on central differences

$$\frac{1}{4\pi}\frac{\partial}{\partial u_{s,\nu}}\epsilon_{\mu\mu'}(\omega) \approx \frac{1}{4\pi}\frac{\epsilon_{\mu\mu'}(\omega;+\mathbf{u}_s^{(\nu)}) - \epsilon_{\mu\mu'}(\omega;-\mathbf{u}_s^{(\nu)})}{2u_s^{(\nu)}}, \tag{3.29}$$

and $\epsilon_{\mu\mu'}(\omega;\pm\mathbf{u}_s^{(\nu)}) = [\mathrm{Re}\,\epsilon_{\mu\mu'} + i\,\mathrm{Im}\,\epsilon_{\mu\mu'}](\omega;\pm\mathbf{u}_s^{(\nu)})$ means that the dielectric tensor is evaluated at distorted geometries with an atom displaced by $\pm\mathbf{u}_s^{(\nu)}$.

Altogether, the total number of calculations to be performed is $3\times 2\times N_{\mathrm{nucl}}$. In order to reduce this number, symmetry operations of the space group can be used to lessen the workload. On the one hand, they determine the number of inequivalent atoms and on the other hand, they reduce the number of displacements to be accounted for per atomic site.

Let me address the latter point first. The number of displacements needed to determine $\frac{\partial}{\partial u_{s,\nu}}\epsilon_{\mu\mu'}(\omega)$ the sth atom in the unit cell is related to the set of symmetry operations that leave the atomic site invariant. The elements comprising this set will be called $\{P|\mathbf{v}^{(P)}\}$. The algorithm is to generate an initial displacement $\mathbf{u}_s^{(\nu)}$ and to apply the rotational part P of the aforementioned operations to this displacement vector thus generating another displacement, $\mathbf{u}_s^{(\nu')} = P\mathbf{u}_s^{(\nu)}$. New displacements are created until two sets of linearly independent vectors are created, one associated with positive and the other associated with negative directions. Positive and negative in this context means that all vectors forming the positive set have an associated vector with opposite sign in the negative set.

For each of the independent displacements the real and the imaginary part of the dielectric tensor are calculated. Now, let $\mathbf{u}_s^{(\nu)}$ be one of these displacements to which the associated dielectric tensor is $\epsilon_{\mu\mu'}(\omega;\mathbf{u}_s^{(\nu)})$, and further consider the primed displacement from above. Then, the tensor associated with the primed displacement is calculated from the one computed for the unprimed displacement by

$$\epsilon_{\mu\mu'}(\omega;\mathbf{u}_s^{(\nu')}) = \sum_{\gamma\gamma'} P_{\mu\gamma}P_{\mu'\gamma'}\epsilon_{\gamma\gamma'}(\omega;\mathbf{u}_s^{(\nu)}). \tag{3.30}$$

Note that the direction indexed by ν' may also be the negative of the one index by ν. The symmetry operations are applied until the previously mentioned sets are rebuilt.

It is, however, not generally the case that applications of all symmetry operations lead to two sets where one contains positive and the other negative Cartesian directions. A set of orthogonal displacements oriented along the Cartesian directions (positive and negative) can be constructed by performing corresponding linear combinations $\overline{\mathbf{u}}_s^{(\lambda)} = \sum_\nu \mathbf{u}_s^{(\nu)}A_{\nu\lambda}$ with $\lambda\in\{x,y,z\}$, and A is determined from eq. (3.3). The same linear transformation is applied to the dielectric tensor

$$\epsilon_{\mu\mu'}(\omega;\overline{\mathbf{u}}_s^{(\lambda)}) = \sum_\nu \epsilon_{\mu\mu'}(\omega;\mathbf{u}_s^{(\nu)})A_{\nu\lambda}, \tag{3.31}$$

with A to be determined for each of the two linearly independent sets of displacements (positive and negative).

The procedure just described gives $\frac{\partial}{\partial u_{s,\nu}}\epsilon_{\mu\mu'}(\omega)$ for atom s in the unit cell. This derivative defines a third-rank tensor associated with atom s and it must be invariant under application of all rotational parts of the symmetry operations that map the atom onto itself, $\frac{\partial}{\partial u_{s,\gamma}}\epsilon_{\eta\eta'}(\omega) \stackrel{!}{=} \sum_{\mu\mu'\nu} P_{\eta\mu}P_{\eta'\mu'}P_{\gamma\nu}[\frac{\partial}{\partial u_{s,\nu}}\epsilon_{\mu\mu'}(\omega)]\ \forall P$. If now the inversion operation is amongst these rotational parts, the formerly-stated transformation law reduces to $\frac{\partial}{\partial u_{s,\nu}}\epsilon_{\mu\mu'}(\omega) \stackrel{!}{=} (-1)^3\frac{\partial}{\partial u_{s,\nu}}\epsilon_{\mu\mu'}(\omega)$ from which it immediately follows that $\frac{\partial}{\partial u_{s,\nu}}\epsilon_{\mu\mu'}(\omega) = 0\ \forall\mu\mu'\nu$. As a result it is not necessary to consider the sth atom for the displacements.

3.2 Material systems

In this section the structural properties of the material systems treated in this work are referred to. Most of the work covers the copper-oxide phases. A detailed review on this material system can be found in Meyer et al. [23].

3.2.1 Copper-oxide phases

Copper-oxides are known to exist in three modifications: cubic Cu_2O (cuprite; cf Fig. 3.1a), monoclinic CuO (tenorite; cf. Fig. 3.1c), and tetragonal Cu_4O_3 (paramelaconite; cf. Fig. 3.1b). Amongst these, the natural p-type[77–79] conducting Cu_2O is currently of interest for solar cell applications and therefore appears to be well-studied, experimentally[23,80–88] as well as theoretically[88–101], over the last decades.

The monoclinic tenorite phase is a promising candidate for solar cell applications,[23] and high-T_C superconductors.[102] Density functional theory based investigations within the framework LDA+U[100,103], hybrid functionals,[100,104] and many-body perturbation theory[88,105] focused on the electronic structure which is governed by the interaction of the O $2p$ and Cu $3d$ states.[103,105] Experimental investigations considered the magnetic and related structural properties.[22,106–112] There exist two antiferromagnetic (AFM) orderings[22,108] with differing Néel temperatures $T_N^{(1)} = 231$ K (incommensurable phase), and $T_N^{(2)} = 213$ K (commensurable phase).[22,107–110] In the low-temperature ($T < T_N^{(2)}$) AFM phase with eight formula units per magnetic unit cell, apart from the Cu^{2+} ions (magnetic moment of $\sim 0.65\mu_B$), the oxygen ions also carry non-zero magnetic moments of $\sim 0.14\mu_B$.[22]

Tetragonal, antiferromagnetically ordered Cu_4O_3 is a phase considered to be intermediate to Cu_2O and CuO as it contains Cu atoms in two oxidation states, Cu^+ [Cu(I)] and Cu^{2+} [Cu(II)],[113] and the magnetic moments are located on the Cu^{2+} atoms. In recent years, efforts have been made to explore the electronic properties experimentally as well as computationally.[23,88,100,114–116]

		This work	Literature	
Phase	Parameter		Theory	Experiment
Cu_2O	a (Å)	4.303	4.2675[100]	4.2696[23]
	Cu–O (Å)	1.86	1.85[100]	1.85[23]
	Ω_0 (Å^3)	79.7	77.72[100]	77.83[23]
Cu_4O_3	a (Å)	5.873	5.8392[100],5.595[118]	5.837[119]
	c (Å)	9.990	9.8966[100],9.650[118]	9.932[119]
	z	0.1146	0.1142[100],0.115[118]	0.1173[119]
	Cu(I)–O(1) (Å)	1.86	1.85[100]	1.87[119]
	Cu(II)–O(2) (Å)	1.93	1.91[100]	1.92[119]
	Cu(II)–O(1) (Å)	2.00	1.98[100]	1.97[119]
	Ω_0 (Å^3)	344.6	337.44[100],302.08[118]	338.38[119]
CuO	a (Å)	4.6837[106]	4.5130[100],4.548[118]	4.6837[106]
	b (Å)	3.4226[106]	3.6121[100], 3.305[118]	3.4226[106]
	c (Å)	5.1288[106]	5.1408[100], 4.903[118]	5.1288[106]
	β (degree)	99.54[106]	97.06[100], 99.652[118]	99.54[106]
	Cu–O (Å)	1.93, 1.97	1.94[100]	1.96[106]
	Ω_0 (Å^3)	81.08[106]	83.49[100], 72.65[118]	81.08[106]

TABLE 3.1: Structural parameters for Cu_2O (GGA), and Cu_4O_3 (GGA+U[117]) compared to experimental and calculated values from the literature (Heinemann et al. [100]: HSE06, Debbichi et al. [118]: LDA+U). As mentioned in the text, the *experimental* lattice parameters from Åsbrink and Norrby [106] (fig. 3.2a) are used for CuO. The values listed for the lattice parameters, the β-angle, and the volume refer to their cell.[106] Based on these structural constants, the structure for the AFM groundstate[22] from fig. 3.2 is constructed. Only the atomic positions are relaxed resulting in two different interatomic distances (for a discussion of the symmetry breaking compared to the structure from Åsbrink and Norrby [106] see section 3.4.2.2). Ω_0 refers to the unit cell volume.

For all calculations for the copper-oxides phases I use the VASP[35–38] code. Calculations are based on the projector augmented-wave method[33,34] (PAW). The copper PAW potentials treat the Cu $3p^6 3d^{10} 4s^1$ electrons, and the O $2s^2 2p^4$ electrons as valence states. For Cu_2O and Cu_4O_3 I use the GGA parametrisation for the exchange correlation functional. Additionally, for Cu_4O_3 the rotationally invariant Hubbard U corrections as suggested by Liechtenstein et al. [120] are employed. For monoclinic CuO the LDA+U method is used. Any calculation involving Hubbard U corrections is conducted with the *ab initio* values of $U = 7.5$ eV and $J = 0.98$ eV that have been determined for a copper-oxide system.[117]

I only relax the structural parameters for cubic Cu_2O and tetragonal Cu_4O_3. Calculated values are listed in table 3.1 together with calculated and experimental data from the literature. For the structural relaxation a cut-off energy of 1200 eV and an energy tolerance of 10^{-8} eV for the self-consistency are used. In case of Cu_2O 12 **k**-points in each direction are selected for the BZ integration while for Cu_4O_3 8^3 **k**-points are chosen.

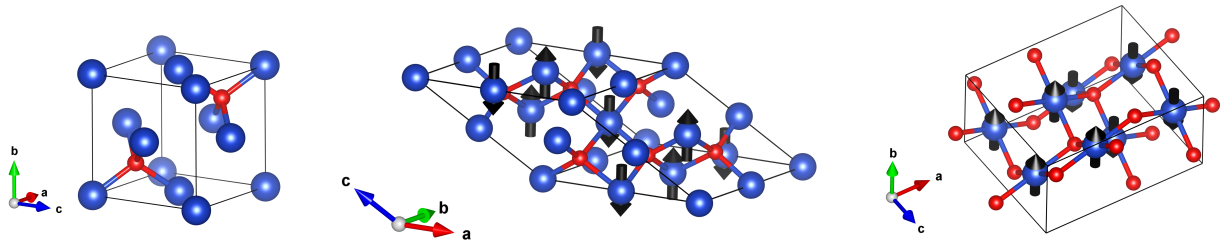

(a) Cu_2O (6 atoms) **(b)** Cu_4O_3 (14 atoms) **(c)** CuO (16 atoms)

FIGURE 3.1: Crystal structure of the three copper-oxide phases. Cu-atoms: blue; O-atoms: red. Black arrows indicate magnetic moments on the Cu^{2+} atoms. Cu_2O: Crystal lattice type: simple cubic. Choice of lattice vectors: $\mathbf{a} = (a, 0, 0)$, $\mathbf{b} = (0, a, 0)$, $\mathbf{c} = (0, 0, a)$, with a being the cubic lattice constant. Cu_4O_3: Crystal lattice type: body-centred tetragonal. Choice of lattice vectors: $\mathbf{a} = (-a, a, c)/2$, $\mathbf{b} = (a, -a, c)/2$, $\mathbf{c} = (a, a, -c)/2$,[121] with a, b being the lattice constants of a simple tetragonal lattice. CuO (AFM groundstate[22]): Crystal lattice type: simple monoclinic (unique axis b). The structure of CuO can be downloaded from `http://webbdcrista1.ehu.es/magndata/index.php?this_label=1.62` and follows Forsyth et al. [22]. The structure shown can be obtained by applying the linear combinations $(\mathbf{a} - \mathbf{c})/2$, $\mathbf{b}$, $(\mathbf{a} + \mathbf{c})/2$ to the lattice vectors $\mathbf{a}$, $\mathbf{b}$, $\mathbf{c}$ found on the webpage. The magnetic moments of the O-atoms are not shown.

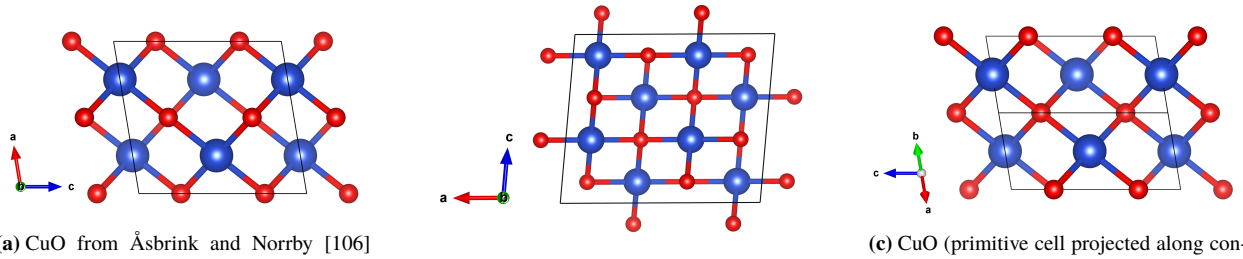

(a) CuO from Åsbrink and Norrby [106] (conventional cell choice; 8 atoms) **(b)** CuO (superstructure; 16 atoms) **(c)** CuO (primitive cell projected along conventional **b**-axis; 4 atoms)

FIGURE 3.2: Relation between the crystallographic cell of Åsbrink and Norrby [106] (conventional cell choice) and the superstructure necessary for the magnetic unit cell (cf. Fig. 3.1c). The lattice vectors of the conventional cell of Åsbrink and Norrby [106] (a, b, c: lattice constants) can be chosen as $\mathbf{a} = (a, 0, 0)$, $\mathbf{b} = (0, b, 0)$, $\mathbf{c} = (c\cos\beta, 0, c\sin\beta)$ such that the superstructure (magnetic unit cell) follows from the linear combinations $\mathbf{a} - \mathbf{c}$, $\mathbf{b}$, $\mathbf{a} + \mathbf{c}$. Note that a *primitive* crystallographic cell is obtained with the conventional lattice vectors as: $(\mathbf{a} + \mathbf{b})/2$, $(-\mathbf{a} + \mathbf{b})/2$, $\mathbf{c}$. Magnetic moments have been omitted in the figures.

The GGA(+U) approach for these phases reproduces experimental values for structural parameters[23,119] very well and also gives values in good agreement with recent theoretical investigations[100] based on hybrid-DFT (HSE06) methods.

Literature values for the lattice parameters of CuO based on LDA+U[100,118] calculations show deviations of about 2 % to 4 % from experiment. I therefore use the experimental lattice parameters $a = 4.6837$ Å, $b = 3.4226$ Å, $c = 5.1288$ Å and $\beta = 99.54°$ from Åsbrink and Norrby [106]. From these the magnetic unit cell for temperatures below $T_N^{(2)}$ with eight formula units (16 atoms) is constructed (cf. Fig. 3.2).

Apart from the AFM groundstate structure of CuO, the *primitive* crystal structure related to the (conventional) crystallographic cell from Åsbrink and Norrby [106] will be considered. It has half the volume of the conventional cell, contains 4 atoms, and has a monoclinic base-centred lattice type (contrary to the simple monoclinic lattice of the conventional unit cell with 8 atoms). In the context of this work this structure will be referred to as the room temperature (RT) structure of CuO. The relation of both choices of the unit cells is summarised in fig. 3.2.

The Brillouin zones (BZs) of all phases are shown in fig. 3.3.

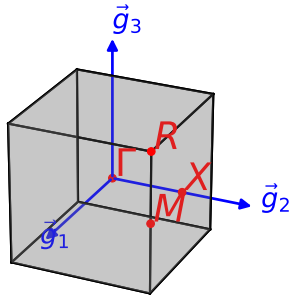

(a) Cu_2O (Fig. 3.1a)

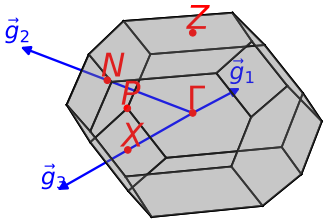

(b) Cu_4O_3 (Fig. 3.1b)

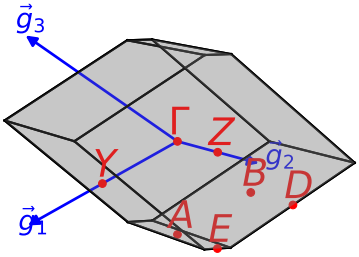

(c) CuO (Fig. 3.1c)

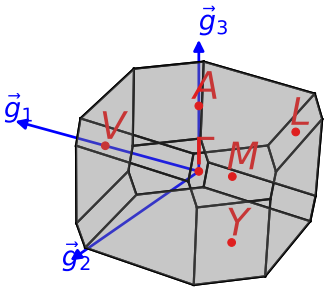

(d) CuO (Fig. 3.2c)

FIGURE 3.3: Brillouin zones of the copper-oxide phases. Cu_2O: $\Gamma = (0,0,0)$, $X = (0,1/2,0)$, $M = (1/2,1/2,0)$, $R = (1/2,1/2,1/2)$. Cu_4O_3:[121] $\Gamma = (0,0,0)$, $N = (0,1/2,0)$, $X = (0,0,1/2)$, $Z = (1/2,1/2,-1/2)$, $P = (1/4,1/4,1/4)$. CuO (Fig. 3.1c)[121]: $\Gamma = (0,0,0)$, $Y = (1/2,0,0)$, $E = (1/2,1/2,-1/2)$, $A = (1/2,0,-1/2)$, $B = (0,0,-1/2)$, $D = (0,1/2,-1/2)$, $Z = (0,1/2,0)$. CuO (Fig. 3.2c): $\Gamma = (0,0,0)$, $Y = (1/2,1/2,0)$, $(-1/2,1/2,0)$, $A = (0,0,1/2)$, $M = (1/2,1/2,1/2)$, $(-1/2,1/2,1/2)$, $V = (1/2,0,0)$, $L = (1/2,0,1/2)$, $(-1/2,0,1/2)$. These points can be found at `http://www.cryst.ehu.es/cgi-bin/cryst/programs/nph-kv-list` when choosing space group No. 15 (C_{2h}^6) with unique axis **b**.

3.2.2 Calcium fluoride (CaF_2)

CaF_2 (fluorite) is a cubic compound containing three atoms in its primitive face-centred cubic (fcc) unit cell. The atoms are located at $(0, 0, 0)$ (Ca), and $\pm(1/4, 1/4, 1/4)$ (F).

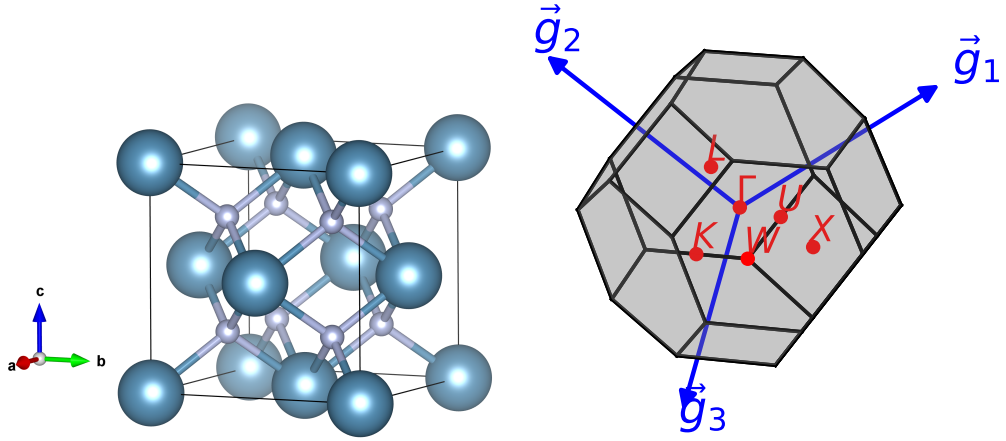

(a) **(b)**

FIGURE 3.4: (a) Conventional cubic unit cell of CaF_2 (Ca: blue; F: grey). The primitive lattice vectors can be chosen as $\mathbf{a}_1, \mathbf{a}_2, \mathbf{a}_3 = (0, a, a)/2, (a, 0, a)/2, (a, a, 0)/2$, where a is the cubic lattice constant. (b) Brillouin zone corresponding to the primitive real space fcc unit cell. Possible choices of the high-symmetry points in reciprocal space are: $\Gamma = (0, 0, 0)$, $X = (1/2, 0, 1/2)$, $L = (1/2, 1/2, 1/2)$, $W = (1/2, 1/4, 3/4)$, $U = (5/8, 1/4, 5/8)$, $K = (3/8, 3/8, 3/4)$. These points can be constructed by pre-multiplying the points given on the webpage `http://lampx.tugraz.at/~hadley/ss1/bzones/fcc.php` by the permutation matrix (to be read row-wise) $P = ((0, 0, 1), (1, 0, 0), (0, 1, 0))(= P^{-T})$. The reason is the following: The choice of lattice vectors on the webpage is $\mathbf{a}'_1, \mathbf{a}'_2, \mathbf{a}'_3 = (a, 0, a)/2, (a, a, 0)/2, (0, a, a)/2$. The primed and unprimed lattices can be related by a permutation $\mathbf{a}'_j = \sum_i \mathbf{a}_i P_{ij}$, while the relation for the reciprocal lattices is $\mathbf{g}'_j = \sum_i \mathbf{g}_i [P^{-T}]_{ij}$ (P^{-T}: inverse-transpose of P). Since $\mathbf{q} = \sum_i \mathbf{g}_i \widetilde{q}_i = \sum_i \mathbf{g}'_i \widetilde{q}'_i$ ($\widetilde{q}_i, \widetilde{q}'_i$: components of the wavevectors with respect to the (un)primed reciprocal lattice bases), the relation between the components is $\widetilde{q}_i = \sum_j [P^{-T}]_{ij} \widetilde{q}'_j$.

Experimentally, CaF_2 is found to be a wide-gap insulator with an direct band gap of 12.1 eV and the indirect gap ($X \rightarrow \Gamma$) is estimated to be 11.8 eV,[122] and the lattice constant is 5.4630 Å.[123] While first principles calculations based on the local density/generalised gradient approximation (LDA/GGA) fail to match the experimental gaps (e.g. 7.11 eV and 6.85 eV (direct and indirect gap) by Ma and Rohlfing [124]),[124,125] quasi-particle calculations based on the *GW*-scheme by Ma and Rohlfing [124] yield 11.8 eV (direct gap) and 11.5 eV (indirect gap).

Experimental analysis of the phonon spectrum was provided by Elcombe and Pryor [126] and Schmalzl et al. [127]. The stress-dependence of the phonon modes was investigated in the early 1980's,[128,129] and even earlier the Raman and infrared properties,[130,131] while (first-principles) calculations on vibrational properties have been carried out more recently.[51,125,127,132,133]

3.3 Phonon dispersions and derived quantities

This section is concerned with vibrational properties of polar semiconducting materials. Phonon dispersions and derived quantities (phonon density of states (PDOS), thermodynamic functions, ...) are computed with the direct method that has been introduced in section 2.2.4.

A lot of emphasis is put on the influence of the dipole-dipole corrections on the phonon dispersion. It is argued that these corrections are necessary in order to obtain a correct description of the phonon dispersion (also to allow for a decent comparison with experiment). It will also become apparent that changes in the dispersions due to these corrections are not solely limited to the direct vicinity of the BZ centre.

Most parts will deal with copper-oxide phases (section 3.3.2) for which calculated results will be compared to experimental data where available.

Before assessing the phonon properties of the copper-oxides in more detail, the focus will be on CaF_2 (section 3.3.1). Although this is not an oxide semiconductor, this compound is well-suited for carving out the differences of the two methods (Gonze and Lee [19] and Wang et al. [43]) for the inclusion of dipole-dipole corrections into dynamical matrices from the direct method.

3.3.1 Comparison of Gonze's and Wang's method for the treatment of dipole-dipole corrections in dynamical matrices obtained from the direct method

In this section I will compare the methods of Gonze and Lee [19] and Wang et al. [43] for treating the long-range dipole-dipole corrections in polar solids within the framework of the direct approach. Effects related to these methods will be illustrated for the insulator CaF_2 (cf. fig. 3.4a) which, due to its structural simplicity, lends itself nicely as prototype material.

For the current investigations rather large supercell sizes (large grids of commensurable wavevectors) are required. Since standard supercell calculations become more and more difficult as the number of atoms increases ($\gtrsim 1000$ atoms), a recently developed method for so-called non-diagonal supercells[20] is used. This approach greatly eases the endeavours undertaken to investigate the long-range nature of the FCs.

The method of non-diagonal supercells For this comparative study I use a recently proposed scheme by Lloyd-Williams and Monserrat [20] for so-called non-diagonal supercells. Non-diagonal in this context means that off-diagonal elements are allowed in the matrix M from section 2.2.4. What actually has been proven by Lloyd-Williams and Monserrat [20] is that a supercell describing a perturbation with wavevector $(m_1/\mathscr{N}_1, m_2/\mathscr{N}_2, m_3/\mathscr{N}_3)$ (reduced fractional coordinates) contains a number of primitive cells equal to the least common multiple of $\mathscr{N}_1, \mathscr{N}_2, \mathscr{N}_3$.

This procedure allows to choose a grid with division $\mathscr{N}_1 \times \mathscr{N}_2 \times \mathscr{N}_3$ of reciprocal space which can be symmetry-reduced (spatial operations of symmetry, as well as time-reversal symmetry; cf. section 2.2.2). Supercells (more precisely the matrices M) covering the commensurable wavevectors are conveniently constructed with the aid of the FORTRAN 90 programme offered in Supplemental Material of the article of Lloyd-Williams and Monserrat [20]. From forces calculated within each of these supercells exact dynamical matrices for all irreducible $\mathbf{q}_c$-points are constructed from eqs. (2.42) and (2.44). Crystal and time-reversal symmetry give access to dynamical matrices at the remaining commensurable wavevectors.[27]

Since generally the non-diagonal supercells are much smaller than the supercells that capture a full grid of $\mathbf{q}_c$-points at once, the computational load is tremendously reduced.[20] For example, in case of CaF_2 for a grid of wavevectors with $\mathscr{N}_i = 12\ \forall i$ the largest supercell to be considered contains 12 primitive cells (36 atoms). However, a diagonal supercell with $12^3 \times 3 = 5184$ atoms would scarcely be feasible using standard DFT methods.

Phonon dispersion of CaF_2 from Gonze's and Wang's method Calculations for CaF_2 presented in this section have been carried out with the experimental lattice parameter 5.4630 Å.[123] The pseudopotentials for the calculations presented here treat the Ca $3s^2 3p^6 4s^2$ and F $2s^2 2p^5$ electrons as valence states, and I use the GGA-PBE[134] exchange-correlation functional. Like in Wang et al. [51] Born effective charge tensors and the dielectric permittivity tensor are calculated with an energy cut-off of 500 eV and 15^3 **k**-points.

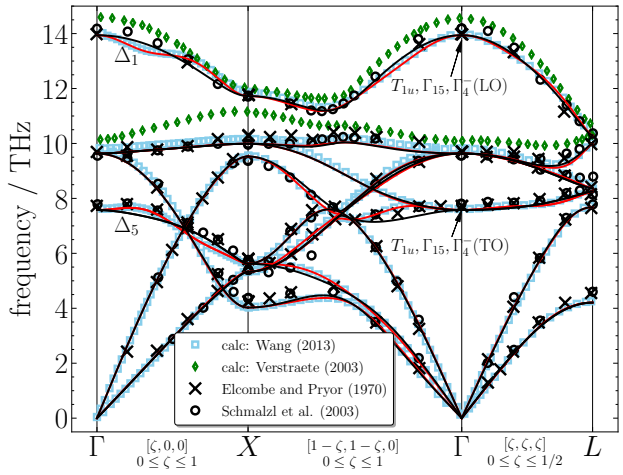

FIGURE 3.5: Phonon dispersion for CaF_2 from dynamical matrices evaluated on a 4^3 $\mathbf{q}_c$-grid. Dipole-dipole corrections have been accounted for through Gonze's (black solid line) and Wang's method (red solid line). Neutron scattering data from Elcombe and Pryor [126] and Schmalzl et al. [127] are shown. Calculated data from Wang et al. [51] and Verstraete and Gonze [125] are also included (extracted from Wang et al. [51, fig. 1]). From the dispersion of Verstraete and Gonze [125] only the high-frequency branches are shown for clarity (these branches are sufficient for the following discussion). Directions listed along the paths refer to the conventional choice of the unit cell for a fcc-type lattice. In the primitive basis (for the choice of the lattice vectors see fig. 3.4) the coordinates of the vectors become: $(1,0,0)_{\text{conv}} \rightarrow (0,1/2,1/2)$, $(1,1,0)_{\text{conv}} \rightarrow (1/2,1/2,1)$, and $(1/2,1/2,1/2)_{\text{conv}} \rightarrow (1/2,1/2,1/2)$. The labels of the phonon branches follow Elcombe and Pryor [126]. *Parameters for calculations*: Plane-wave cut-off of 400 eV, **k**-point density of 0.3 Å^{-1}, displacement length of 0.02 Å.

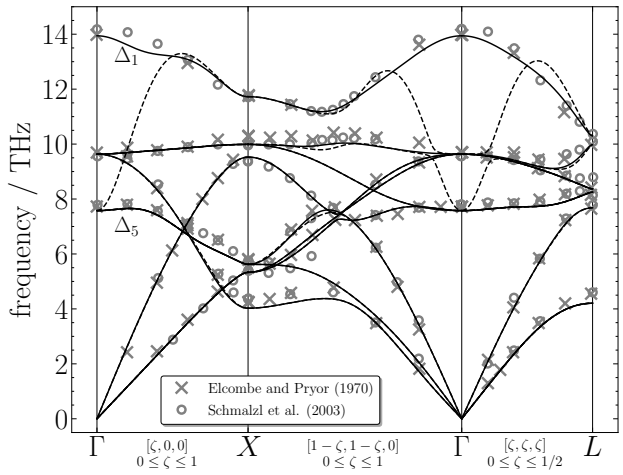

FIGURE 3.6: Same as fig. 3.5 but now: dipole-dipole corrections with Wang's method (black solid line) and without dipole-dipole corrections (black dashed line). *Parameters for calculations*: See fig. 3.5.

Fig. 3.5 displays the phonon dispersions for CaF_2 from dynamical matrices calculated on a 4^3 $\mathbf{q}_c$-grid together with neutron scattering data by Elcombe and Pryor [126] and Schmalzl et al. [127]. Therein I compare both approaches for the inclusion of dipole-dipole corrections. Although the dispersions coincide in most parts, essential differences are observed in the regions where the dipole-dipole corrections cause the splitting of the longitudinal optic (LO) and the transversal optic (TO) modes (these are the branches forming the $T_{1u}(\Gamma_{15}, \Gamma_4^-)$ modes at the Γ-point). This becomes particularly obvious along the $\Gamma \rightarrow X$ direction (splitting between ~7.5 THz to 14 THz). Contrary to Gonze's method, dispersions computed using Wang's method show a non-monotonic, somewhat artificial, evolution of the LO/TO branches along that direction. In fact, particularly for the Δ_1 and Δ_5 branches along the $\Gamma \rightarrow X$ direction, where experimental datapoints are very dense, measured phonon branches do not reflect that behaviour.

Wang et al. [51] claim their description of the phonon dispersion for CaF_2 (obtained using $4 \times 4 \times 4$ superstructure of the primitive unit cell with 192 atoms) based on Wang's method to be superior to DFPT calculations by Verstraete and Gonze [125] when comparing to experiment. Firstly, an overall worse description of the measured data (e.g., in the range of ~10 THz to 15 THz) by the linear response results[125] most likely traces back to the use of a different pseudopotential method (Troullier-Martins used by Verstraete and Gonze [125] vs. PAW used by Wang et al. [51]). Moreover, a different lattice parameter of 5.49 Å (Verstraete and Gonze [125]) is used, opposed a value of 5.4630 Å (Wang et al. [51]) from experiment[123]. Secondly, and even more importantly, the same comments hold for the description of the Δ_1 and Δ_5 branches already mentioned above: Experimental phonon frequencies of the Δ_1 branch are overestimated by the DFPT calculations by essentially the same amount as they are underestimated by the direct method in conjunction with Wang's method (see fig. 3.5).[51,125] However, the linear response calculations combined with Gonze's method capture the correct evolution of the Δ_1 branch (The calculations by Verstraete and Gonze [125] have been carried out with the ABINIT code[39] which has Gonze's method implemented according to Gonze and

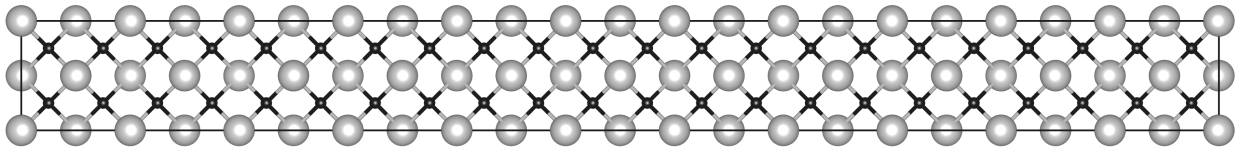

FIGURE 3.7: $1 \times 1 \times 11$ elongated conventional supercell (Ca: grey; F: black). This cell can be constructed from the primitive lattice vectors $\mathbf{a}_1, \mathbf{a}_2, \mathbf{a}_3 = (0, a, a)/2, (a, 0, a)/2, (a, a, 0)/2$ with the linear combinations $\mathbf{a}_{j,\mathrm{conv}} = \sum_i \mathbf{a}_i M_{ij}$, where (to be read row-wise) $M = ((-1, 1, 11), (1, -1, 11), (1, 1, -11))$. The result is $\mathbf{a}_{1,\mathrm{conv}}, \mathbf{a}_{2,\mathrm{conv}}, \mathbf{a}_{3,\mathrm{conv}} = (a, 0, 0), (0, a, 0), (0, 0, 11a)$.

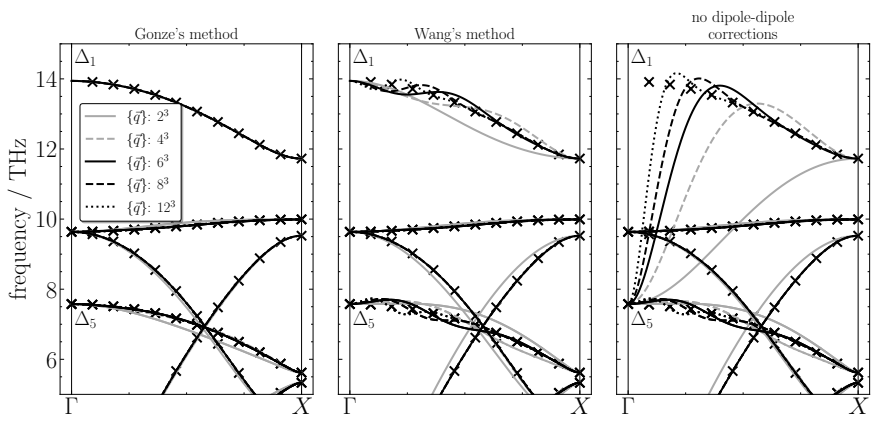

FIGURE 3.8: Phonon dispersion of CaF_2 along the $\Gamma \rightarrow X$ direction. Different $\mathbf{q}_c$-grids are shown. Dispersions have been calculated with Gonze's method (left panel), Wang's method (middle panel), and without dipole-dipole corrections (right panel). Exact frequencies from dynamical matrices obtained from a $1 \times 1 \times 11$ elongated conventional supercell are shown as crosses. *Parameters for calculations*: For the dynamical matrices computed on the different grids see fig. 3.5; $1 \times 1 \times 11$ elongated conventional supercell: Plane-wave cut-off of 400 eV, $4 \times 4 \times 1$-grid of $\mathbf{k}$-points (equivalent to a $\mathbf{k}$-point density of $0.3\,\text{Å}^{-1}$), displacement length of 0.03 Å.

Lee [19].).

Referring to fig. 3.6 it is clear that Wang's method nevertheless provides a tremendous improvement of the phonon bandstructure compared to the case of exclusion of dipole-dipole corrections. Ignoring the corrections results in an blemished description of the high-frequency branch that comprises the T_{1u}(LO) mode at the Γ-point. Note that the differences between the corrected and uncorrected dispersion is limited not only to the vicinity of the Γ-point. For example, the uppermost phonon branch of the $\Gamma \rightarrow L$ direction is not captured by the dashed line (representing the case without dipole-dipole corrections) along the full path. The frequencies only coincide at the BZ boundary (L-point) which is a $\mathbf{q}_c$-point commensurable with the 4^3-grid of wavevectors used for the Fourier interpolation.

I now shall discuss the differences between Gonze's and Wang's method more specifically. The dispersion of CaF_2 along the $\Gamma \rightarrow X$ direction will be considered in more detail. In fig. 3.8 the dispersions computed with Gonze's method (left panel), Wang's method (middle panel), and without any dipole-dipole corrections to the dynamical matrices (right panel) are displayed. These calculations have been carried out for different $\mathbf{q}_c$-grid sizes ranging from 2^3 to 12^3 points inside the first BZ (for details see table 3.2). Exact frequencies from an elongated $1 \times 1 \times 11$ conventional supercell (cf. fig. 3.7) are also included in order to assess the quality of the Fourier interpolation starting from different equidistant $\mathbf{q}_c$-grids. At wavevectors along $\Gamma \rightarrow X$ the $1 \times 1 \times 11$ supercell gives exact frequencies because through the imposed periodic boundary conditions interactions leading to the respective dynamical matrices are summed to infinity.

From fig. 3.8 the following is observed: Dispersions computed from Gonze's method quickly convergence to the exact frequencies for all grids of wavevectors containing more than 2^3 points. This is related to this method calculating the Fourier interpolation only for the short-ranged part of the FCs which is rapidly convergent with the number of interaction shells in real space (or likewise the size of the underlying $\mathbf{q}_c$-grid).

grid data		supercell data		
$\mathscr{N}_1\mathscr{N}_2\mathscr{N}_3$	$\mathscr{N}_{\mathrm{IBZ}}$	$\Omega_{\mathrm{sc}}^{\mathrm{max}}/\Omega_0$	$N_{\mathrm{calc}}^{\mathrm{sc}}$	$N_{\mathrm{atom}}^{\mathrm{diag-sc}}$
8	3	2	3	24
64	8	4	8	192
216	16	6	16	648
512	29	8	25	1536
1728	72	12	66	5184

TABLE 3.2: Information about the $\mathbf{q}_c$-grids used in the calculations for CaF_2 with the method from Lloyd-Williams and Monserrat [20] (fig. 3.8). $\mathscr{N}_i$ is the grid dimension along each generating vector of the reciprocal lattice (due to cubic symmetry: $\mathscr{N}_1 = \mathscr{N}_2 = \mathscr{N}_3 = \mathscr{N}$), $\mathscr{N}_{\mathrm{IBZ}}$ is the number of points in the irreducible BZ. $\Omega_{\mathrm{sc}}^{\mathrm{max}}/\Omega_0$ describes the ratio of the supercell with the maximal volume used in the calculations and the unit cell volume, and $N_{\mathrm{calc}}^{\mathrm{sc}}$ is the number of atoms contained in this supercell. $N_{\mathrm{atom}}^{\mathrm{diag-sc}}$ refers to the number of atoms contained in the corresponding *diagonal* supercell with volume $\mathscr{N}^3 \times \Omega_0$.

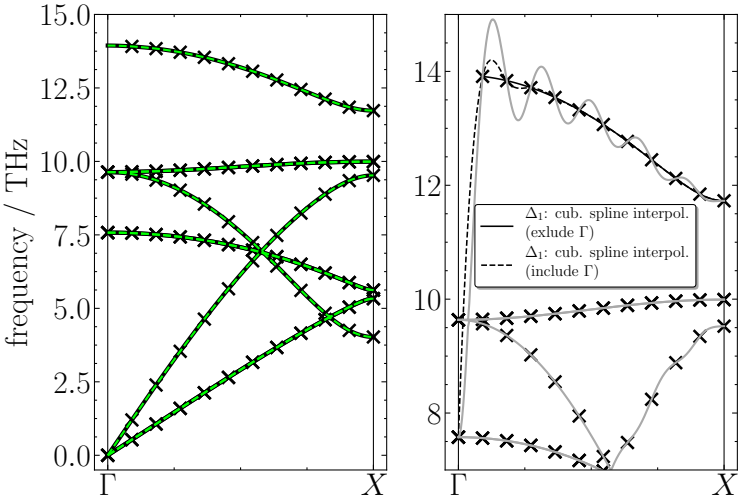

FIGURE 3.9: Phonon dispersion of CaF_2 along the $\Gamma \rightarrow X$ direction. (Left panel) Dispersions from Gonze's method (solid line) and Wang's method (dashed line) by Fourier interpolation based on the exact dynamical matrices from the elongated $1 \times 1 \times 11$ conventional supercell. (Right panel) Dispersion from dynamical matrices of the same supercell calculated *without* dipole-dipole corrections (grey line). Exact frequencies are shown as crosses. *Parameters for calculations*: See fig. 3.8

Wang's method, however, fails to smoothly interpolate the exact frequencies of the Δ_1 and the Δ_5 branch for grid sizes for which Gonze's method is already converged. Instead, Fourier interpolation based on this method keeps introducing artificial features even for very dense wavevector grids.

In fact, the convergence behaviour is very much similar to that observable for the dispersion obtained from Fourier interpolation based on the full FCs as extracted from the forces of the direct method (cf. eq. (2.42)). With increasing $\mathbf{q}_c$-grid sizes—i.e., increasing interaction ranges in real space—frequencies calculated from these FCs slowly converge towards the exact frequencies but nevertheless fail to reach the correct limiting value for $\mathbf{q} \rightarrow \mathbf{0}$. The latter is, of course, correctly reproduced by Wang's method because in the limit of vanishing wavevector this method contains the correct non-analytic term (eq. (2.57)) introduced by Cochran and Cowley [135].[43] Nevertheless, Fourier interpolation with Wang's methods produces oscillations in regions where branches from Fourier interpolation based on the full FCs bend down towards the TO frequencies (the limiting value of Δ_5 branch for $\mathbf{q} \rightarrow \mathbf{0}$; cf. fig. 3.5).

I may therefore conclude that Fourier interpolation in conjuction with Wang's method suffers from convergence issues due to the long-rangedness of the FCs in real space. In Gonze's method this is circumvented by considering the Fourier transform only for short-ranged FCs and separately treating the dipole-dipole part of the dynamical matrix. Indeed, Verstraete and Gonze[125] have investigated the decay of the FCs in real space for CaF_2 and found a decay proportional to the inverse of the third power of the interatomic distance, thereby confirming the long-range nature of the FCs.

Nevertheless, the question remains, if—apart from frequencies at commensurable $\mathbf{q}_c$-points—both methods can interpolate to the same results. Indeed, fig. 3.9 (left panel) demands the conclusion that, if the $\mathbf{q}$-grids are sufficiently dense, both methods must yield the same result. This is the case for the elongated $1 \times 1 \times 11$ supercell (fig. 3.7) which gives 12 $\mathbf{q}_c$-points along the $\Gamma \rightarrow X$ path. Actually, this finding is supported by the result from Wang et al. [50] where it is shown that including the dipole-dipole corrections as suggested by Wang's method correctly interpolates the phonon dispersions of MgO when considering an elongated conventional supercell.

As shown in fig. 3.9 (right panel) carrying out the Fourier interpolation with the dynamical matrices of the elongated supercell *without* dipole-dipole corrections results in oscillations between the commensurable $\mathbf{q}_c$-points along the $\Gamma \rightarrow X$ path (exact frequencies are, of course, reproduced correctly). This in particular holds for the high-frequency Δ_1 branch. Including a cubic spline interpolation of the frequencies of the Δ_1 branch that explicitly includes/excludes the Γ-point frequencies suggests that the oscillatory features result from the inclusion of the $\mathbf{q} = \mathbf{0}$ dynamical matrix for the Fourier interpolation. The Fourier interpolation appears to amplify the resulting oscillations compared to the cubic spline interpolation.

3.3.2 Phonon dispersion and related quantities for copper-oxide phases

As far as lattice dynamics are concerned, experimental studies of the past decades involving, for example, inelastic neutron scattering, Raman spectroscopy, and IR measurements, in particular focused on the cubic Cu_2O[10,136–159] and the monoclinic CuO[23,24,112,118,160–176] phase. For the latter, additional modes apart from those expected from a factor group analysis of the C_{2h}^6 space group have been observed in the low temperature regime ($T < T_N^{(2)}$).[24,112,161,164,166] This indicates the formation of a magnetic superlattice below the Néel temperature.[24] Some modes show a strong dependence on temperature below $T_N^{(2)}$ which was attributed to a strong coupling of the respective phonon modes to the magnetic ordering.[24] In very recent studies Raman spectra of the intermediate phase of Cu_4O_3 have been reported for samples grown by magnetron sputtering.[23,118]

Only a few calculations deal with vibrational properties of copper-oxide phases. Recent investigations use *ab initio* methods to describe the phonon structures within the harmonic approximation.[116,118,159,176–178] For cubic Cu_2O the direct method as well as DFPT have been employed.[159,177,178] For CuO and Cu_4O_3 recent calculations are solely based on the direct method.[116,118,176] However, apart from the case of Cu_2O (Bohnen et al. [159] and Rimmer et al. [178]), the polar nature of the chemical bonding has not been considered in the calculations of the phonon properties of copper-oxide phases. For monoclinic CuO, the correct groundstate magnetic order[22] has not been investigated yet.[118,176] I will therefore discuss the influence of the dipole-dipole corrections on the phonon dispersion of the copper-oxide phases and I will show calculations involving the magnetic groundstate structure[22] of CuO (see fig. 3.1c). Parts of this chapter have been published in Ref. [179].

Phonon bandstructure and density of states In fig. 3.10 I show the phonon bandstructure and the (atom-projected) PDOS of all three copper-oxide phases (for details on the calculation see the figure caption). In all cases the dipole-dipole corrections according to Gonze's method have been invoked. Their particular influence on the phonon dispersion will be discussed in more detail below.

The PDOS for cubic Cu_2O, tetragonal Cu_4O_3, and monoclinic CuO are quite different. The PDOS of Cu_2O is dominated by the large gap between the copper and the oxygen states. Sharp features are observable in PDOS of the low-lying (below $\sim 120\,\mathrm{cm}^{-1}$) Cu-related modes in Cu_2O and Cu_4O_3. Monoclinic CuO, however, shows a smoothly increasing PDOS below $100\,\mathrm{cm}^{-1}$ originating from a steep dispersion of the acoustic modes. A (moderately) peaked structure in the PDOS can be found at higher frequencies than in cases of Cu_2O and Cu_4O_3. As also discussed in Ref. [116], the difference in magnitude of the FCs for Cu(I) and Cu(II) atoms in the paramelaconite phase becomes very obvious from the different frequency regions the magnetic (Cu(II)) and non-magnetic (Cu(I)) copper atoms contribute to the PDOS.

In fig. 3.10a, for Cu_2O, I have included experimental phonon frequencies from the literature.[153,159,180] In particular for the low-lying Cu-driven modes agreement between calculated and measured values is excellent. Oxygen-related modes, on the contrary, are placed systematically too low ($\sim 10\,\mathrm{cm}^{-1}$ to $20\,\mathrm{cm}^{-1}$) compared to experiment. This has also been observed for GGA calculations.[159,178]

The influence of the dipole-dipole corrections on the phonon dispersion will now be assessed in more detail. Fig. 3.11 displays the phonon bandstructure of Cu_2O for different supercell/commensurable $\mathbf{q}_c$-grid sizes with and without the dipole-dipole corrections according to Gonze's method. Comparing particularly the upper panels of fig. 3.11 it is obvious that the size of the grid of commensurable wavevectors (or the interaction range in real space) influences the phonon dispersion quite strongly. This is especially true for the case without dipole-dipole corrections where the convergence of the high-frequency region with the size of the interaction range in real space is rather slow along $\Gamma \to X \to M \to \Gamma \to R$. If, however, dipole-dipole corrections are used, the dispersion for grid sizes larger than 3^3 are essentially indistinguishable. Note that the dipole-dipole corrections not only influence the dispersion in the direct vicinity of the Γ-point but also away from the BZ-centre (cf. e.g. the X-point).

The best way to estimate the quality of the Fourier interpolation is to compare interpolated frequencies to frequencies from dynamical matrices at commensurable wavevectors that are *not* in the grid of wavevectors used for the interpolation.

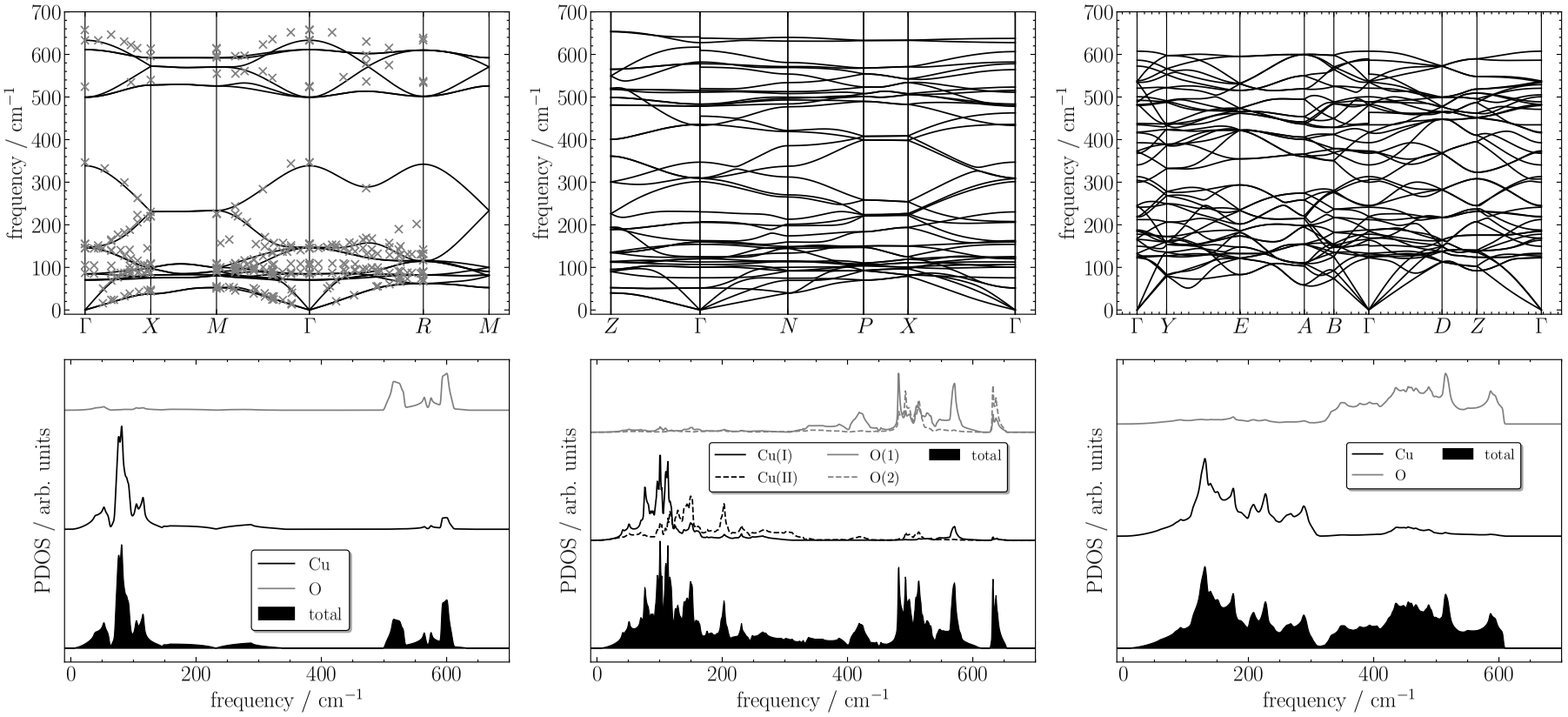

(a) Cu_2O **(b)** Cu_4O_3 **(c)** CuO

FIGURE 3.10: Phonon bandstructure and PDOS for all copper-oxide phases. Dipole-dipole corrections have been used in all cases. For Cu_2O experimental data (grey crosses) have been extracted from figures in Ref. [159] and covers Refs. [153, 159, 180]. Different references are not distinguished through use of different colours or symbols in the plot. For CuO the magnetic groundstate structure[22] is used (fig. 3.1c). *Parameters for calculations*: $\boxed{Cu_2O}$: Dynamical matrices on a 5^3-grid of wavevectors with the method of Lloyd-Williams and Monserrat [20], plane-wave cut-off of 800 eV, **k**-point density of 0.2 Å^{-1}, displacement length of 0.01 Å; Born effective charges and dielectric tensor: plane-wave cut-off of 800 eV and 16^3 **k**-points. $\boxed{Cu_4O_3}$: Dynamical matrices on a 4^3-grid of wavevectors from a $4\times4\times4$-supercell, plane-wave cut-off of 800 eV, one **k**-point, displacement length of 0.03 Å; Born effective charges and dielectric tensor: plane-wave cut-off of 800 eV and 10^3 **k**-points. $\boxed{CuO}$: Dynamical matrices on a $3\times6\times3$-grid of wavevectors from a $3\times6\times3$-supercell, plane-wave cut-off of 800 eV, one **k**-point, displacement length of 0.05 Å; Born effective charges and dielectric tensor: plane-wave cut-off of 800 eV and $8\times16\times8$ **k**-points.

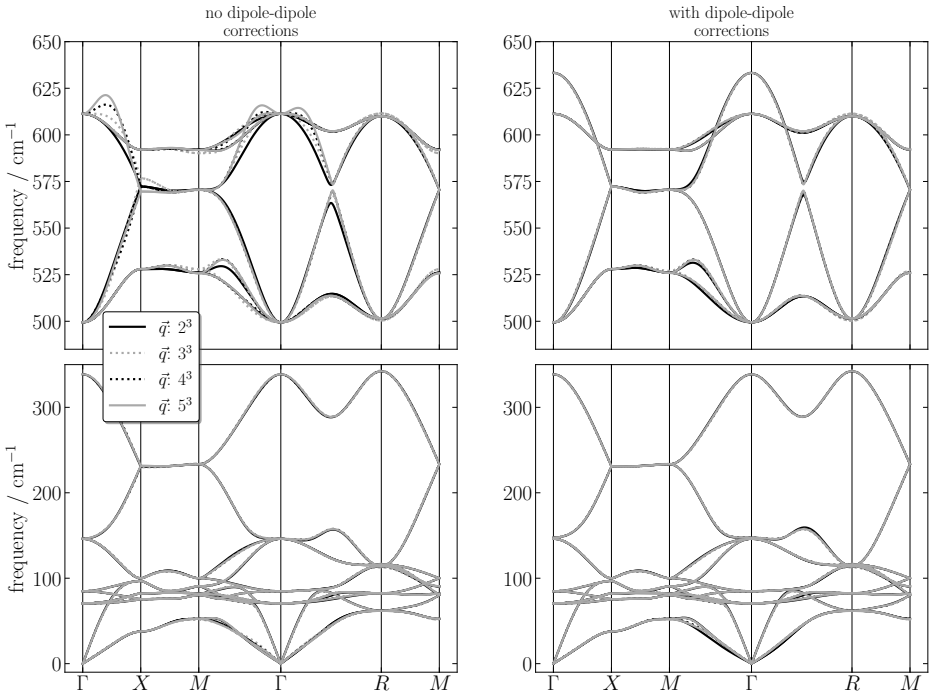

FIGURE 3.11: Phonon bandstructure of Cu_2O for different sizes of commensurable wavevector grids with/without dipole-dipole corrections following Gonze's method. *Parameters for calculations*: Plane-wave cut-off of 800 eV, **k**-point density of 0.2 Å^{-1}, displacement length of 0.01 Å; Born effective charges and dielectric tensor: See fig. 3.10 . Dynamical matrices on a 2^3-grid are obtained from a $2 \times 2 \times 2$ supercell. Dynamical matrices on grids of size 3^3, 4^3, and 5^3 have been calculated with the method of Lloyd-Williams and Monserrat [20].

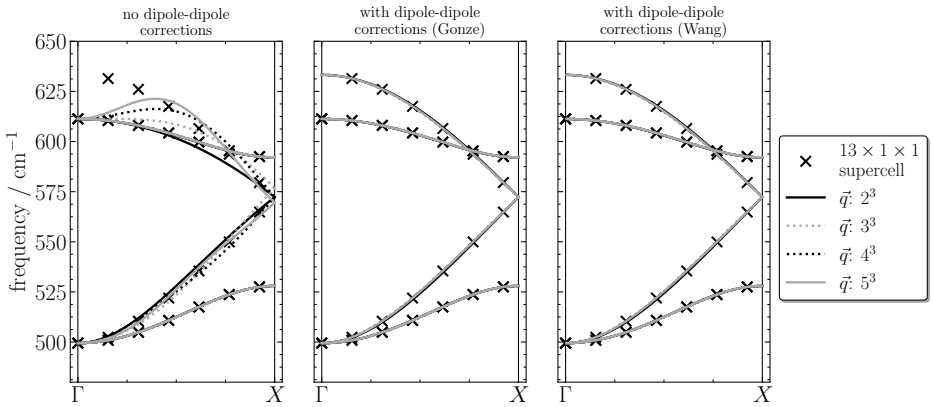

FIGURE 3.12: Phonon bandstructure of Cu_2O along $\Gamma \rightarrow X$ without/with dipole-dipole corrections based on Gonze's/Wang's method, compared to exact frequencies from an elongated $13 \times 1 \times 1$ supercell. For the details on the different $\mathbf{q}_c$-grids see fig. 3.11. Note that the topmost frequency from the $13 \times 1 \times 1$ supercell (~630 cm^{-1}) is *not* missing but coincides with the frequency directly below (between 600 cm^{-1} and 625 cm^{-1}). The reason is that the highest-frequency Γ phonon mode is accompanied by a macroscopic electric field which is incompliant with periodic boundary conditions imposed in DFT calculations. It should be emphasised that the (exact) frequencies from the $13 \times 1 \times 1$ are calculated *without* dipole-dipole corrections. *Parameters for calculations*: See fig. 3.11 with the exception that the displacement length for the $13 \times 1 \times 1$ supercell is 0.02 Å.

In fig. 3.12 I compare interpolated phonon frequencies for Cu_2O with and without dipole-dipole corrections from Gonze's/Wang's method with frequencies from an elongated $13 \times 1 \times 1$-supercell. While in the case without any dipole-dipole corrections the high-frequency phonon branches are poorly described, inclusion of the corrections results in a smooth interpolation of the exact frequencies at the commensurable $\mathbf{q}_c$-points. This holds for Gonze's (middle panel) as well as for Wang's method (right panel), while both methods result in virtually identical phonon bandstructures. It should be pointed out that even interpolated frequencies from the 2^3-grid adequately describe the phonon dispersion along that direction. Indeed, for this grid size the only commensurable wavevectors along $\Gamma \rightarrow X$ are the Γ- and the X-point.

Fig. 3.13 displays the the phonon dispersion of tetragonal Cu_4O_3 for different supercell/$\mathbf{q}_c$-grid sizes with (right panel) and without (left panel) dipole-dipole corrections following Gonze's method. Similar

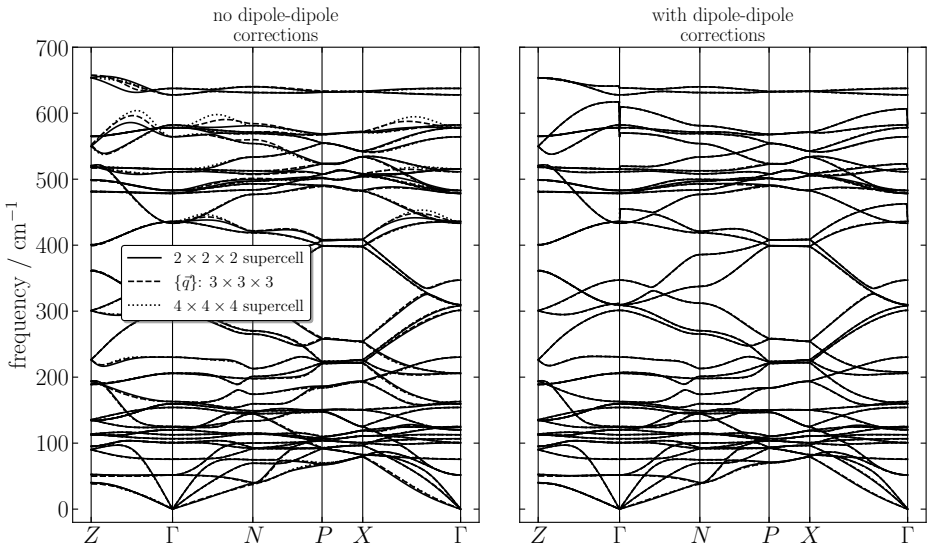

FIGURE 3.13: Phonon bandstructure of Cu_4O_3 without/with dipole-dipole corrections according to Gonze's method for different supercell/$\mathbf{q}_c$-grid sizes. *Parameters for calculations*: $2 \times 2 \times 2$ supercell: Plane-wave cut-off of 800 eV, 2^3 **k**-points, displacement length of 0.03 Å; 3^3-grid with the method of Lloyd-Williams and Monserrat [20]: Plane-wave cut-off of 800 eV, **k**-point density of 0.4 Å^{-1}, displacement length of 0.02 Å; $4 \times 4 \times 4$ supercell, Born effective charges and dielectric tensor: See fig. 3.10.

conclusions can be drawn as in the case of cubic Cu_2O. The dipole-dipole corrections tremendously improve the convergence of the phonon frequencies with respect to the interaction range in real space due to usage of the short-ranged part of the FCs for the Fourier interpolation. As a result, the comparatively small $2 \times 2 \times 2$ supercell ($2^3 \times 14 = 112$ atoms) already gives a phonon dispersion which is comparable to that of the 8-times larger $4 \times 4 \times 4$ supercell ($4^3 \times 14 = 896$ atoms).

When comparing Gonze's and Wang's method for Cu_4O_3, differences are comparable to the case of Cu_2O which are quite small, indeed. Therefore, this will not be subject to a further analysis.

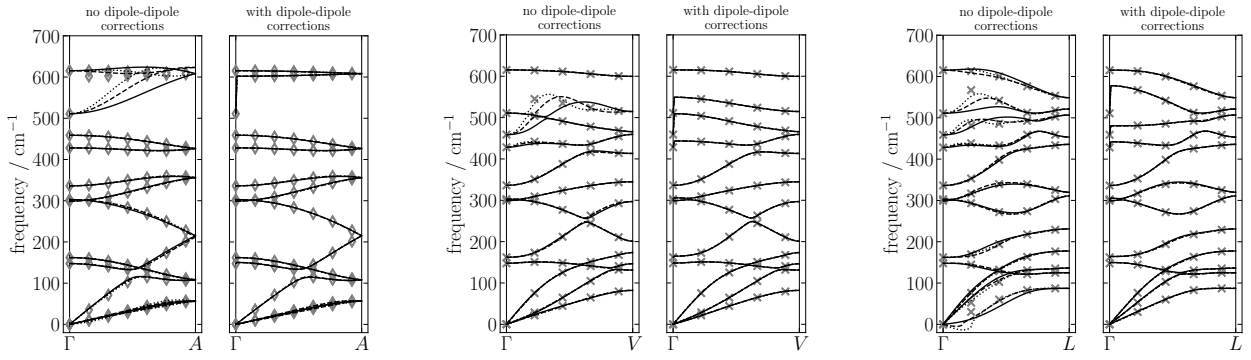

(a) $\Gamma \rightarrow A$ (0, 0, 1/2) **(b)** $\Gamma \rightarrow V$ (1/2, 0, 0) **(c)** $\Gamma \rightarrow L$ (1/2, 0, 1/2)

FIGURE 3.14: Phonon bandstructures of the primitive structure of CuO (cf. fig. 3.2c) along different directions in reciprocal space. Calculations without (left panel) and with (right panel) dipole-dipole corrections following Gonze's method are shown for $\mathbf{q}_c$-grids (Lloyd-Williams and Monserrat [20]) of sizes $4 \times 4 \times 2$ (solid black line), $6 \times 6 \times 3$ (dashed black line), and $8 \times 8 \times 4$ (dotted black line). Additionally, for the $\Gamma \rightarrow A$ direction exact frequencies from an elongated $1 \times 1 \times 13$ supercell (grey diamonds) are shown, and for the $\Gamma \rightarrow V, L$ directions exact frequencies from a $9 \times 1 \times 9$ $\mathbf{q}_c$-grid are included (grey crosses). The sudden drop of some mode frequencies at the Γ-point (infra-red active modes) for the case with dipole-dipole corrections comes about because, in order to avoid division by zero, in the Ewald summation from eq. (2.51) the $\mathbf{G} = \mathbf{0}$ term is skipped if $\mathbf{q} = \mathbf{0}$. The frequencies present at $\mathbf{q} = \mathbf{0}$ are those of the purely transversal modes (the eigenfrequencies of the *analytical* part of the dynamical matrix). *Parameters for calculations*: Plane-wave cut-off of 600 eV, **k**-point density of 0.45 Å^{-1}, displacement length of 0.02 Å; Born effective charges and dielectric tensor: Plane-wave cut-off of 600 eV and **k**-point density of 0.15 Å^{-1}.

Referring to fig. 3.14, similar considerations can be undertaken for CuO as just made for Cu_2O and Cu_4O_3. Therein I assess the influence of the dipole-dipole corrections on the phonon dispersion along different directions in reciprocal space for the room temperature (RT) primitive structure of CuO[106] (cf. fig. 3.2c). Commensurable $\mathbf{q}_c$-grids of the form $n_{\text{div}} \times n_{\text{div}} \times \frac{1}{2} n_{\text{div}}$ with $n_{\text{div}} = 4, 6, 8$ are considered. The reason for

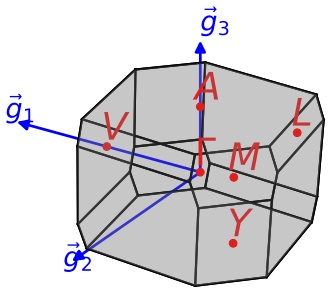

FIGURE 3.15: Brillouin zone of CuO (same as fig. 3.3d) shown for convenience in conjunction with fig. 3.14. Note that in the present figure the point $L = (-1/2, 0, 1/2)$ is used because its translational equivalent (as indicated below the bandstructure in fig. 3.14c) does not lie on one of the faces of the BZ. Since this point is equivalent by translation, it of course contains the same physical information.

using the primitive structure instead of the magnetic groundstate (fig. 3.1c) is that Reichardt et al. [163] have performed room-temperature measurements of the phonon bandstructure (inelastic neutron scattering) assuming the primitive four-atom unit cell. At room temperature the low-temperature magnetic phase is no longer valid, since additional phonon modes are only observed for $T < T_{\mathrm{N}}^{(2)}$.[24,112,161,164,166]

A detailed look at the phonon bandstructure along the $\Gamma \longrightarrow A$ direction (fig. 3.14a) shows that the course of the bands in the high-frequency region ($\sim$520 cm^{-1} to 620 cm^{-1}) is strongly dependent on the size of the $\mathbf{q}_{\mathrm{c}}$-grids used for the Fourier interpolation. This indicates that this part of the bandstructure is eminently governed by the long-ranged contributions to the FCs in real space. Indeed, spurious effects are introduced in the bandstructure when the full FCs (short-ranged+dipole-dipole) are used for the Fourier interpolation. This becomes clear from the left panel in fig. 3.14a when comparing the interpolated phonon dispersion to the exact frequencies from an elongated $1 \times 1 \times 13$ supercell (diamonds). The inclusion of the dipole-dipole corrections (right panel), however, results in phonon dispersions with scarcely any visible differences for all $\mathbf{q}_{\mathrm{c}}$-grid sizes, and the exact frequencies are nicely interpolated. While the influence of the dipole-dipole corrections in figs. 3.14a and 3.14b mainly manifests itself in changes of the dispersion of the optical (infra-red active) modes, an additional feature is discovered in fig. 3.14c. In the left panel the lowest acoustic mode as described through the full FCs exhibits negative frequencies.[i] This clearly is an unphysical behaviour as follows immediately from a comparison with the exact phonon frequencies from a $9 \times 1 \times 9$ $\mathbf{q}_{\mathrm{c}}$-grid which suggest a smooth (linear) increase of the frequencies of the acoustic modes. With the aid of the dipole-dipole corrections (right panel) this erroneous feature is obliterated, resulting in essentially indistinguishable dispersions for the acoustic branches for all wavevector grids considered for the Fourier interpolation. As a matter of fact, the exact frequencies are correctly interpolated. This suggests that, at least for certain directions, the long-ranged nature of the FCs in polar semiconducturs may also influence the small-wavevector acoustic modes and not only the optical modes.

Reichardt et al. [163] have measured the phonon dispersion along several directions in reciprocal space by inelastic neutron scattering. Their dispersions are shown in fig. 3.16 together with computed phonon dispersions along these directions. The calculated phonon branches provide a decent description of the measured frequency values. This is particularly true for the acoustic branches. It only appears that the calculated high frequency branches (at $\sim$600 cm^{-1}) are positioned systematically too low with respect to experiment.

Special attention should be paid to fig. 3.16c where the dispersion along the $\Gamma \longrightarrow A$ direction $[0, 0, \zeta]$, $[0, 0, \eta]$ (cf. fig. 3.3d) is shown. Recalling fig. 3.14a it is true that dipole-dipole corrections are needed in order to correctly assess the course of the high-frequency branches. Through the corrections these bands are described as being very close in frequency (< 20 cm^{-1}) and not far apart ($\sim$100 cm^{-1} without dipole-dipole corrections). This trend is clearly found in experiment. This underlines the importance of the inclusion of the dipole-dipole corrections for the calculation of phonon dispersions of polar semiconductors.

As a final point let me revisit the discussion from section 3.3.1. In fig. 3.17 the phonon dispersions with dipole-dipole corrections from Gonze's and Wang's method along the $\Gamma \longrightarrow A, L$ directions are shown.

[i] More precisely, there are negative eigenvalues of the dynamical matrices at these wavevectors. This means that the frequencies are purely imaginary. However, for the visualisation they are just given a negative sign.

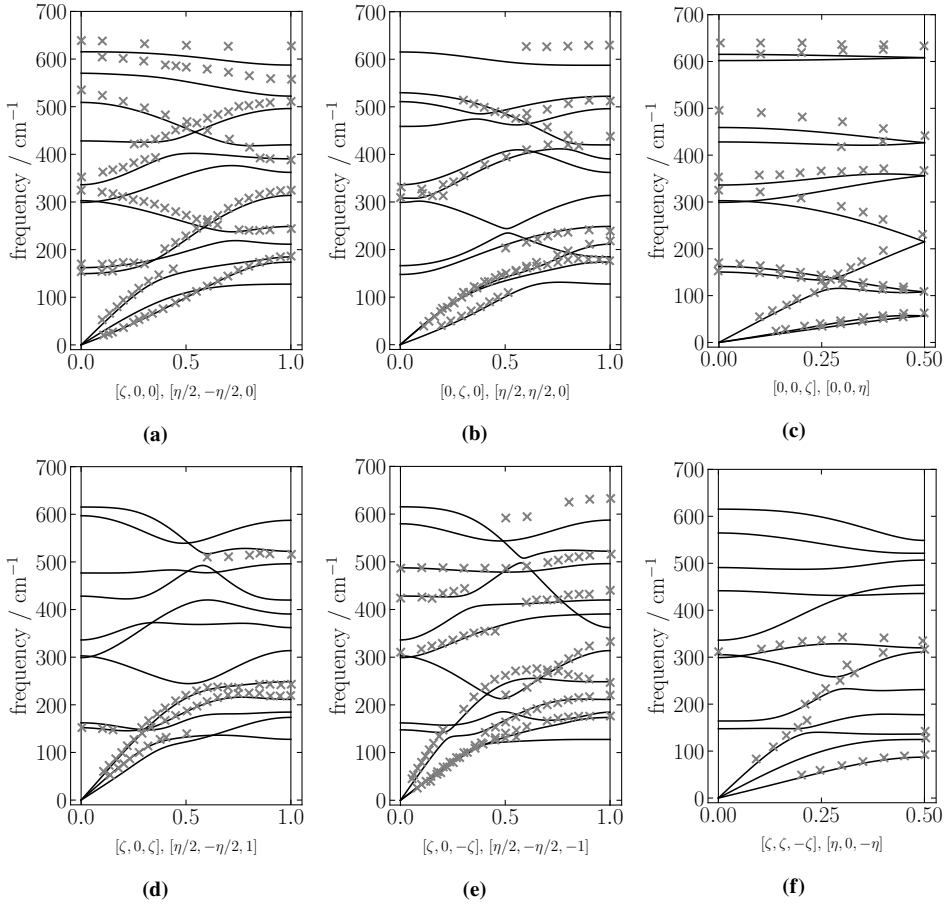

FIGURE 3.16: Phonon bandstructures of the primitive structure of CuO (cf. fig. 3.2c) along different directions in reciprocal space compared to experimental data from Reichardt et al. [163] (grey crosses). Dynamical matrices from the $8 \times 8 \times 4$ $\mathbf{q}_c$-grid have been used. The directions are given in the basis of the conventional monoclinic cell (label ζ; fig. 3.2a) and with respect to the primitive base-centred monoclinic cell (label η; fig. 3.2c). In order to avoid confusion when comparing to experiment, in contrast to fig. 3.14 the point $\mathbf{q} = \mathbf{0}$ is excluded. Instead, frequencies are computed up to a point very close to the Γ-point such that the correct limiting value for $\mathbf{q} \to \mathbf{0}$ of the infra-red active mode frequencies still is obtained. *Parameters for calculations*: See fig. 3.14.

While for the $\Gamma \to A$ direction both methods yield almost indistinguishable bandstructures, discrepancies for the $\Gamma \to L$ direction are more obvious. Wang's method retains artifacts found in the uncorrected phonon dispersion (meaning without dipole-dipole corrections) for some branches along the $\Gamma \to L$ path. As a result, the exact frequencies are not correctly interpolated for the lowest acoustic branches and some optical branches. Nonetheless, Wang's method correctly describes the phonon bandstructure along the $\Gamma \to A$ direction in relation to experiment (see fig. 3.16c).

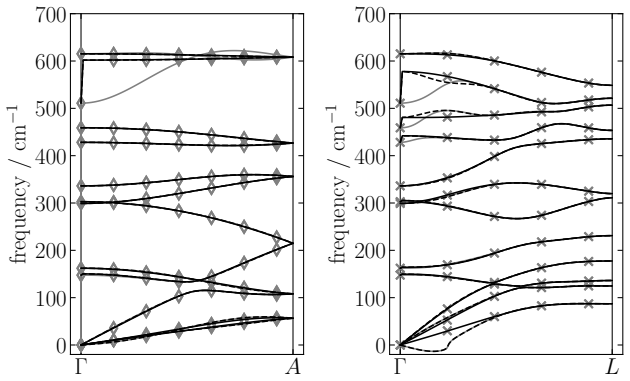

(a) $\Gamma \to A$ (0, 0, 1/2) **(b)** $\Gamma \to L$ (1/2, 0, 1/2)

FIGURE 3.17: Phonon bandstructures of the primitive structure of CuO (cf. fig. 3.2c) with dynamical matrices from the $8 \times 8 \times 4$ $\mathbf{q}_c$-grid. Dipole-dipole corrections with Gonze's/Wang's method: black solid/dashed line; without dipole-dipole corrections: grey solid line. Additionally, for the $\Gamma \to A$ direction exact frequencies from an elongated $1 \times 1 \times 13$ supercell (grey diamonds) are shown, and for the $\Gamma \to L$ direction exact frequencies from a $9 \times 1 \times 9$ $\mathbf{q}_c$-grid are included (grey crosses). *Parameters for calculations*: See fig. 3.14.

Acoustic phonon group velocities as derivatives of the phonon dispersion relation In this section the results for the group velocities of the acoustic phonon branches will be shown and compared to experiment. In order to directly compute $v^{\text{sound}}_{m,\hat{\mathbf{q}}} = \sum_\gamma \hat{q}_\gamma [\frac{\partial}{\partial q_\gamma} \omega_{m,\mathbf{q}}]_{\mathbf{q}=\mathbf{0}}$ the perturbation method introduced in section 3.1.3 will be used and compared to finite difference calculations of the derivatives of the dispersion relation.

In order to quantify the mode polarisation the center-of-mass displacement $\overline{u}^\mu_{m,\mathbf{q}} = \sum_s \overline{M_s} u^{s,\mu}_{m,\mathbf{q}}$ ($\overline{M}_s = M_s/[\sum_s M_s]$ and $u^{s,\mu}_{m,\mathbf{q}} = w^{s,\mu}_{m,\mathbf{q}}/\sqrt{M_s}$) of each phonon mode is used:

$$\text{mode polarisation} = \left| \hat{\mathbf{q}}^T \hat{\overline{\mathbf{u}}}_{m,\mathbf{q}} \right| \in [0,1] \quad \text{with } \hat{\overline{u}}^\mu_{m,\mathbf{q}} = \overline{u}^\mu_{m,\mathbf{q}}/|\overline{\mathbf{u}}_{m,\mathbf{q}}|. \tag{3.32}$$

Based on this projection the acoustic modes are classified as being (mainly) transversal (t) or (mainly) longitudinal (l).

The results from eq. (3.22) and finite difference calculations are compared table 3.3. The good agreement of both methods validates the technically quite involved procedure from section 3.1.3. Despite its complexity the perturbation method is to be preferred to the finite difference method since it naturally includes the $\mathbf{q} \to \mathbf{0}$ limit. It therefore can be readily used for any direction $\hat{\mathbf{q}}$ whereas a calculation of the derivative by finite differences requires the choice of a numerical step width which, at least in principle, has to be chosen anew for each direction.

Agreement with experiment is reasonably good for Cu_2O and CuO, only for the [001], [101], and the $[10\overline{1}]$-direction in case of CuO the computed longitudinal velocity of sound is vastly too small. However, the results by Reichardt et al. [163] have been determined at room temperature (296 K) whereas I have considered the AFM groundstate.[22]

While for many directions values for the velocities of sound obtained with/without dipole-dipole corrections are close, the dipole-dipole corrections can non-negligibly influence the phonon dispersion (see e.g. the smallest transversal velocities along the $[100], [11\overline{1}]$-directions for CuO, and along the $[11\overline{1}]$-direction for Cu_4O_3) for certain directions. Differences between the averaged velocities of sound ($\mathbb{S}^2$: unit sphere), $v^{\text{sound}}_{\text{av}} = \frac{1}{3}\sum_{m=1}^3 \int_{\mathbb{S}^2} \frac{d\hat{\mathbf{q}}}{4\pi}\, v^{\text{sound}}_{m\hat{\mathbf{q}}}$, calculated without/with dipole-dipole corrections are ~5 % for Cu_2O, ~2 % for Cu_4O_3, and ~3 % for CuO.

Dipole-dipole corrections can alter the slope of the acoustic branches for small values of $|\mathbf{q}|$ because such long-wavelength vibrations couple atoms at large distances, thereby depending on long-ranged FCs. Since the method of Gonze and Lee [19] is meant to correct the long-ranged interactions, differences in the acoustic branches (at least for certain directions $\hat{\mathbf{q}}$) appear plausible. Indeed, as discussed by Gaál-Nagy [181], an insufficient description of the long-ranged interactions can lead to artificial negative modes (also for non-polar semiconductors) if the grid of wavevectors on which full dynamical matrices initially are obtained is not dense enough around $\mathbf{q} = \mathbf{0}$. Indeed, this was noted already in the preceding discussion of Fig. 3.14c.

Lattice entropy and lattice heat capacity Based on the equations introduced in section 2.2.3 the vibrational contributions to the crystal entropy and heat capacity at constant volume can be calculated. Fig. 3.19 shows results for the constant-volume lattice heat capacity (eq. eq. (2.39)) and the vibrational contribution to the entropy (eq. (2.38)). To the best of my knowledge experimental data are only available for Cu_2O (Hu and Johnston [184]) and CuO (Junod et al. [162] and Hu and Johnston [187]).

For Cu_2O (fig. 3.19a) good agreement is found with experiment. The small overestimate of C_v^{ph} and S^{ph} for most temperatures might be due to the slightly overestimated lattice constant through the GGA exchange-correlation functional.

Experimentally, the heat capacity of monoclinic CuO has been studied extensively. Within these studies also the magnetic contributions to the heat capacity have been assessed.[162,187–191] The crystal structure of CuO in combination with the magnetic ordering is only valid in the low-temperature region. Therefore, comparison is limited to the temperatures below the antiferromagnetic commensurate to incommensurate transition at $T_{\text{N}}^{(2)} = 213\,\text{K}$.[22]

Fig. 3.19d is meant to verify Dulong-Petit's law according to which the heat capacity (per atom) assumes the constant value $3R$ (R: universal gas constant) for all solids. The data is normalised in such a manner (i.e., divided by the number of formula units per unit cell) that it approaches the number of atoms per formula unit: 3 for Cu_2O, 7 for Cu_4O_3, and 2 for CuO.

Phase	$\hat{\mathbf{q}}$	m	$v^{\text{sound}}_{m,\hat{\mathbf{q}}}$ (km s^{-1})		
			Dipole-dipole corrections		Experiment
			with	without	
Cu_2O	[100]	l	4.571 (4.571)	4.687 (4.687)	4.48[a], 4.49[b]
		t	1.150 (1.150), 1.150 (1.150)	1.150 (1.150), 1.150 (1.150)	1.41[a], 1.42[b]
	[110]	l	4.554 (4.554)	4.527 (4.527)	4.55[a], 4.55[b]
		t	1.150 (1.150), 1.216 (1.216)	1.150 (1.150), 1.671 (1.671)	1.14[a], 1.14[b], 1.41[b]
	[111]	l	4.549 (4.549)	4.473 (4.473)	-
		t	1.194 (1.194), 1.194 (1.194)	1.517 (1.517), 1.517 (1.517)	-
CuO	[100]	l	5.979 (5.979)	5.647 (5.647)	6.4[c]
		t	2.427 (2.428), 3.834 (3.834)	1.549 (1.551), 3.900 (3.900)	-
	[010]	l	3.941 (3.942)	4.518 (4.519)	4.1[c]
		t	1.760 (1.761), 3.863 (3.863)	1.759 (1.760), 3.859 (3.860)	-
	[001]	l	7.070 (7.071)	7.360 (7.360)	7.8[c]
		t	1.971 (1.972), 2.366 (2.367)	2.082 (2.083), 3.199 (3.199)	-
	[101]	l	4.830 (4.831)	4.830 (4.831)	5.4[c]
		t	2.748 (2.749), 3.685 (3.685)	2.873 (2.874), 3.685 (3.685)	-
	$[10\bar{1}]$	l	7.012 (7.012)	7.012 (7.012)	9.1[c]
		t	3.590 (3.591), 3.777 (3.778)	3.614 (3.615), 3.777 (3.778)	-
	$[11\bar{1}]$	l	6.205 (6.205)	6.182 (6.182)	6.8[c]
		t	1.605 (1.606), 3.466 (3.466)	2.338 (2.339), 3.481 (3.482)	-
Cu_4O_3	[010]	l	5.328 (5.328)	5.372 (5.372)	-
		t	1.225 (1.226), 2.794 (2.794)	1.254 (1.255), 2.891 (2.891)	-
	$[11\bar{1}]$	l	6.420 (6.420)	6.538 (6.538)	-
		t	1.575 (1.576), 1.575 (1.576)	1.988 (1.989), 1.988 (1.989)	-
	[001]	l	4.538 (4.538)	4.531 (4.531)	-
		t	1.540 (1.541), 3.435 (3.435)	1.377 (1.378), 3.503 (3.503)	-
	[111]	l	4.637 (4.638)	4.620 (4.620)	-
		t	2.125 (2.126), 3.229 (3.229)	2.159 (2.159), 3.323 (3.323)	-

[a] Berger [182]
[b] Manghnani et al. [183]
[c] Reichardt et al. [163]

TABLE 3.3: Velocities of sound $v^{\text{sound}}_{m,\hat{\mathbf{q}}}$ along direction $\hat{\mathbf{q}}$ of phonon modes with mainly longitudinal (l) or transversal (t) polarisation (m). Velocities are listed with (eq. (3.22)) and without dipole-dipole corrections. For reference, values for the derivative of the phonon dispersion from finite differences (step width $\Delta q = 10^{-4}$ Bohr^{-1}) are given in braces. Where available, experimental data is shown for comparison. For monoclinic CuO the direction labels follow Reichardt et al. [163]. For Cu_4O_3 the directions refer to a body-centred tetragonal lattice,[121] not to the conventional choice of the unit cell. The estimated accuracy for the velocities is $\sim 10^{-2}$ km s^{-1}. More digits, however, are given to capture the differences between values from numerical differentiation and values from the perturbation-like treatment. *Parameters for calculations*: See fig. 3.10.

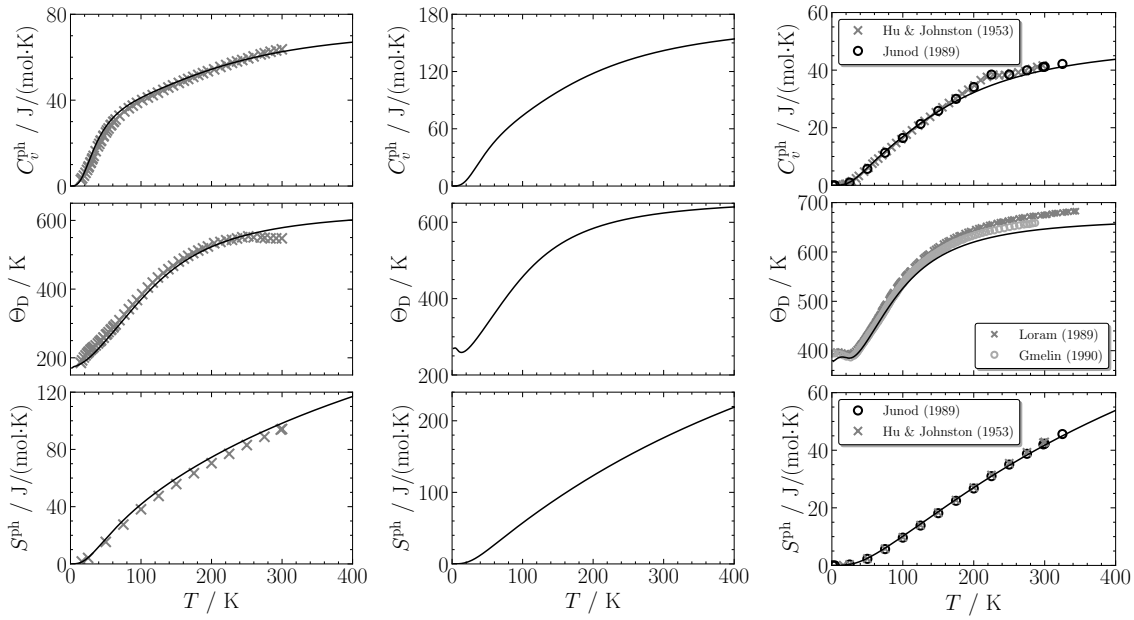

(a) Cu_2O **(b)** Cu_4O_3 **(c)** CuO

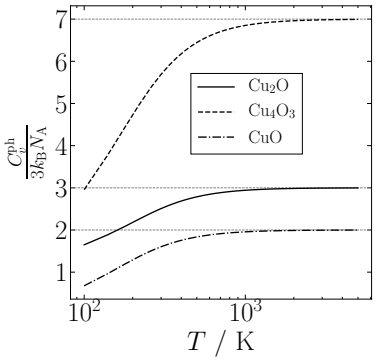

(d) Cu_2O, Cu_4O_3, and CuO: Verification of Dulong-Petit's law.

FIGURE 3.19: (a)-(c) Lattice heat capacity at constant volume (C_v^{ph}), Debye characteristic temperature (Θ_{D}), and lattice entropy (S^{ph}) for all copper-oxide phases. Θ_{D} is calculated with eq. (2.41). $\boxed{\mathrm{Cu_2O}}$: Experimental values for the constant-pressure heat capacity (C_p) and the entropy of Cu_2O have been taken from Hu and Johnston [184]. This data is also used to determine Θ_{D}. Constant-volume heat capacities (C_v) are obtained from the relation $C_p - C_v = V_{\mathrm{molar}} T \alpha^2 / \beta_T$ (V_{molar}: molar volume; α: coefficient of thermal expansion; β_T: isothermal compressibility) using the data of Manghnani et al. [183], Madelung et al. [185], and White [186]. In particular: $V_{\mathrm{molar}} = M_{\mathrm{molar}}/\rho$ with the molar mass $M_{\mathrm{molar}} = 2\times M_{\mathrm{molar}}^{(\mathrm{Cu})} + M_{\mathrm{molar}}^{(\mathrm{O})} = 143.0914\ \frac{\mathrm{g}}{\mathrm{mol}}$ ($M_{\mathrm{molar}}^{(\mathrm{Cu})} = 63.546\ \frac{\mathrm{g}}{\mathrm{mol}}$, $M_{\mathrm{molar}}^{(\mathrm{O})} = 15.9994\ \frac{\mathrm{g}}{\mathrm{mol}}$) and $\rho = 6.1\ \mathrm{g/cm^3}$;[183] $\beta_{T=298\,\mathrm{K}} = 8.93\times10^{-11}\ \mathrm{m^2\,N^{-1}}$;[185] and $\alpha(2\,\mathrm{K} \le T \le 30\,\mathrm{K})$ = interpolated data from White [186], $\alpha(30\,\mathrm{K} < T < 55\,\mathrm{K}) = -2\times10^{-6}\ \mathrm{K^{-1}}$,[185] $\alpha(55\,\mathrm{K} \le T \le 90\,\mathrm{K}) = -3\times10^{-6}\ \mathrm{K^{-1}}$,[185] and $\alpha(T > 90\,\mathrm{K}) = 23\times10^{-8}\ \mathrm{K^{-1}}$.[185] The resulting data points are shown as grey crosses. $\boxed{\mathrm{CuO}}$: In order to get C_v, experimental C_p-vs-T data for CuO from Junod et al. [162] and Hu and Johnston [187] is modified following the procedure of Loram et al. [188]. They use $C_p - C_v = \mathscr{A} C_v^2 T$ with $\mathscr{A} = 1.35\times10^{-6}\,(\mathrm{J/mol})^{-1}$. Values for Θ_{D} are taken from the figures in Loram et al. [188] and Gmelin et al. [189]. (d) Lattice heat capacity at constant volume C_v^{ph} divided by $3k_{\mathrm{B}}N_{\mathrm{A}} = 3R$ (k_{B}: Boltzmann constant, N_{A}: Avogadro constant, and $R \approx 24.94\,\mathrm{J/(mol\,K)}$: universal gas constant) for all phases in the (very) high-T region to verify Dulong-Petit's law. C_v^{ph} has been normalised such that it tends to the number of atoms per formula unit. Number of atoms and formula units per unit cell: $\boxed{\mathrm{Cu_2O}}$: 6 atoms, 2 formula units; $\boxed{\mathrm{Cu_4O_3}}$: 14 atoms, 2 formula units; $\boxed{\mathrm{CuO}}$: 16 atoms, 8 formula units. *Parameters for calculations*: See fig. 3.10.

Fig. 3.19c shows calculated results for the lattice heat capacity and entropy compared to experimental data from Junod et al. [162] and Hu and Johnston [187]. Agreement between calculated and measured values for the heat capacity is excellent up to the anomaly in the experimental curve that coincides with the first antiferromagnetic phase transition.[162,187–189,191] For the entropy the agreement prevails up to even higher temperatures.

3.4 Raman spectroscopic properties of CuO and Cu_4O_3

In this section the Raman scattering properties of the binary oxides CuO and Cu_4O_3 are considered. While the previous investigations from sections 3.3.1 and 3.3.2 featured phonons at wavevectors in the entire BZ, phonons involved in Raman scattering are solely from the Γ-point.

The case of cubic Cu_2O is not investigated in the present context. It has been shown that the Raman spectrum of Cu_2O is dominated by defects.[10,11] A detailed analysis of the Raman scattering properties would require to consider the different possible defect structures, indeed. Clearly, in order to account for sufficiently small defect concentrations, the calculations for the defect structures have to be carried out with supercells. Since DFT calculations are "plagued" with periodic boundary conditions, the chosen size of the supercells is a critical issue and too small supercell sizes can lead to unreasonable results for the calculated Raman scattering intensities. It might also happen that—depending on the size of the chosen supercell—the number of Raman active modes found in the Raman spectrum varies. This comes about because different non-zero **q**-points from the BZ of the primitive unit cell of Cu_2O "fold" to the Γ-point of the superstructure and become Raman active due to a change in symmetry induced through the defect. Indeed, the question concerning a physically decent as well as computationally efficient modelling of Raman scattering properties of defect structures is yet unsettled.

Firstly, a method used for the BZ integration needed in the calculation of the dielectric tensor is discussed (section 3.4.1). Based on this method, the Raman spectroscopic properties of monoclinic CuO and tetragonal Cu_4O_3 are investigated. In section 3.4.2 for CuO, the room-temperature structure and the AFM groundstate structure are compared concerning their electronic and Raman scattering features. In case of Cu_4O_3 (section 3.4.3), in addition to the phonon and Raman scattering properties of the equilibrium structure, the influence of hydrostatic pressure is considered.

3.4.1 Sampling the BZ

Referring to eq. (3.25), the essential parameters that influence the accuracy of the results are:

- The plane-wave cut-off that determines the accuracy of $|u^{(s)}_{n,\mathbf{k}}\rangle$ (and therefore $\frac{\partial}{\partial \mathbf{k}} |u^{(s)}_{n,\mathbf{k}}\rangle$).
- The total number of bands (valence+conduction) over which the summation is carried out.
- The size of the grid of **k**-points $|\mathscr{K}| = N_1 \times N_2 \times N_3$ ($N_j \in \mathbb{N}_{>0}$, $j = 1, 2, 3$).

Particularly the summation over the BZ is a very critical point for the accuracy of the components of $\epsilon(\omega)$.

Generally, the number of **k**-points to be summed over in eq. (3.25) must be chosen quite large in order to obtain a decent accuracy. For α^m the convergence with respect to $|\mathscr{K}|$ in principle is even harder to achieve (see also the discussion in Gillet [12, section 3.4.3]). The calculation of Raman susceptibilities α^m involves the calculation of $\epsilon(\omega)$ for distorted atomic geometries (cf. eq. (3.24)). As a result, the symmetry of the crystal will be lowered accordingly and the number of **k**-points in the calculation increases compared to the equilibrium structure. The larger $|\mathscr{K}|$ the higher the required memory and the higher the computational cost.

Therefore, it is desirable to have a method that allows to treat large **k**-point grids with a reduced memory requirement. In the following a scheme from Gillet [12] is adopted which is sketched in fig. 3.20. This method will be referred to as "multigrid method" because a fine grid of **k**-points $\mathscr{K} \equiv \mathscr{K}(N_1 \times N_2 \times N_3)$ is subdivided into n_s coarse grids $\mathscr{K}_p(M_1 \times M_2 \times M_3)$ with $1 \leq p \leq n_\mathrm{s}$ and $M_j \leq N_j \ \forall j$, each having a different shift vector $\mathbf{s}_p$ by which it is offset from the Γ-point:

$$
\begin{aligned}
\mathscr{K}_1 &= \left\{ \sum_{j=1}^{3} \frac{k_j - 1 + b_{\mathrm{s},j}}{M_j} \mathbf{g}_j + \mathbf{s}_1 \right\}, \quad 1 \leq k_j \leq M_j \\
\mathscr{K}_2 &= \mathscr{K}_1 + \mathbf{s}_2 \\
&\vdots \\
\mathscr{K}_{n_\mathrm{s}} &= \mathscr{K}_1 + \mathbf{s}_{n_\mathrm{s}},
\end{aligned}
\tag{3.33}
$$

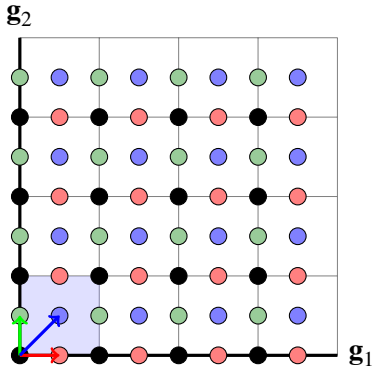

FIGURE 3.20: Schematic illustration of the multigrid method in 2D: The fine grid $\mathscr{K}(8\times8)$ (all points) is generated through the coarse grids $\mathscr{K}_p(4\times4)$ by $n_\mathrm{s}=4$ shifts $\mathbf{s}_1=(0,0)$ (black), $\mathbf{s}_2=(1/2,0)$ (red), $\mathbf{s}_3=(0,1/2)$ (green), $\mathbf{s}_4=(1/2,1/2)$ (blue). The coordinates of these points refer to the blue-shaded box at the origin. Note that no additional shift $\mathbf{b}_\mathrm{s}$ is applied to the fine grid (and accordingly to the coarse grids). The shift vectors $\mathbf{s}_p$ are indicated by the (coloured) arrows (apart from $\mathbf{s}_1$) and are given by all points located *completely inside* the shaded box at the origin. The box is bounded by grid lines of the unshifted coarse grid (shift vector $\mathbf{s}_1$).

where $\mathbf{g}_1,\mathbf{g}_2,\mathbf{g}_3$ are the reciprocal lattice vectors of the cystal structure, $\mathbf{s}_1=\mathbf{0}$, and

$$\mathscr{K}=\bigcup_{p=1}^{n_\mathrm{s}}\mathscr{K}_p. \tag{3.34}$$

The vector $\mathbf{b}_\mathrm{s}$ in this case denotes an *additional* shift vector by which the fine grid is offset from the Γ-point and which accordingly is applied to the coarse grids. The shift is such that the point $b_{\mathrm{s},1}/N_1\mathbf{g}_1+b_{\mathrm{s},2}/N_2\mathbf{g}_2+b_{\mathrm{s},3}/N_3\mathbf{g}_3$ is contained in the fine grid $\mathscr{K}$.

Writing the number of shifts as $n_\mathrm{s}=n_\mathrm{div}^3$, the fine grid is expressed by

$$\mathscr{K}(N_1\times N_2\times N_3)=\mathscr{K}((n_\mathrm{div}M_1)\times(n_\mathrm{div}M_2)\times(n_\mathrm{div}M_3)).$$

This means that the summation in eq. (3.25) is split up like (using a generic function $f_\mathbf{k}$ with summation weights $w_\mathbf{k}\in\mathbb{N}_{>0}$ with the condition $\sum_{\mathbf{k}\in\mathscr{K}}w_\mathbf{k}=|\mathscr{K}|$)

$$\sum_{\mathbf{k}\in\mathscr{K}}\frac{w_\mathbf{k}}{|\mathscr{K}|}f_\mathbf{k}=\frac{1}{n_\mathrm{div}^3}\sum_{\mathbf{k}\in\mathscr{K}}\frac{w_\mathbf{k}}{|\mathscr{K}_p|}f_\mathbf{k}=\frac{1}{n_\mathrm{div}^3}\sum_{p=1}^{n_\mathrm{div}^3}\sum_{\mathbf{k}\in\mathscr{K}_p}\frac{w_\mathbf{k}^{(p)}}{|\mathscr{K}_p|}f_\mathbf{k}^{(p)}, \tag{3.35}$$

with $\sum_{\mathbf{k}\in\mathscr{K}_p}w_\mathbf{k}^{(p)}=|\mathscr{K}_p|$ and $|\mathscr{K}|=\sum_{p=1}^{n_\mathrm{div}^3}|\mathscr{K}_p|=n_\mathrm{div}^3|\mathscr{K}_p|$ since $|\mathscr{K}_1|=\cdots=|\mathscr{K}_{n_\mathrm{s}}|=M_1\times M_2\times M_3$. The superscript "$(p)$" is added to the generic function $f_\mathbf{k}$ to indicate that the summation is carried out first over the $\mathbf{k}$ contained in $\mathscr{K}_p$ for *fixed* p and then the contributions from the coarse grids are summed. For each $\mathscr{K}_p$ the dielectric tensor $\epsilon(\mathbf{s}_p)$ is calculated by summing over $\mathbf{k}\in\mathscr{K}_p$ in eq. (3.25), and eventually all $\epsilon(\mathbf{s}_p)$'s are summed to the full ϵ for the fine grid,

$$\epsilon_{\mu\mu'}^\mathrm{av}(\omega)=\frac{1}{n_\mathrm{s}}\sum_{p=1}^{n_\mathrm{s}}\epsilon_{\mu\mu'}(\omega;\mathbf{s}_p). \tag{3.36}$$

Indeed, in practical calculations, the summation from eq. (3.36) only is a good approximation for the full expression eq. (3.25) (hence the superscript "av"). When $\epsilon(\mathbf{s}_p)$ is calculated by summing over $\mathscr{K}_p$ (eq. (3.25)), a frequency grid $\mathscr{G}_\omega^{(p)}$ is set up according to the energy eigenvalues $E_{n,\mathbf{k}}^{(s)}$ with $\mathbf{k}\in\mathscr{K}_p$ (furthermore, the Fermi energy will be different from grid to grid). Therefore, each $\epsilon(\mathbf{s}_p)$ is obtained on a slightly different grid of frequencies. These are in general different from the grid resulting from a calculation of ϵ on the fine grid $\mathscr{K}$. As a result, the technical implementation of the multigrid method requires to "interpolate" to a common frequency grid on which the $\epsilon(\mathbf{s}_p)$'s can be added. This is achieved by means of the Kramers-Kronig relations eq. (3.28).

The procedure of the multigrid method for calculating the dielectric tensor ϵ^av therefore is:

(i) Choose a fine grid $\mathscr{K}(N_1\times N_2\times N_3)$ and a set of coarse grids $\{\mathscr{K}_p(M_1\times M_2\times M_3)\}$ with associated shift vectors $\{\mathbf{s}_p\}$, and $p=1,\ldots,n_\mathrm{s}$.

(ii) Calculate the groundstate density (e.g., VASP's "CHGCAR") of the system at hand in a self-consistent (SCF) calculation.

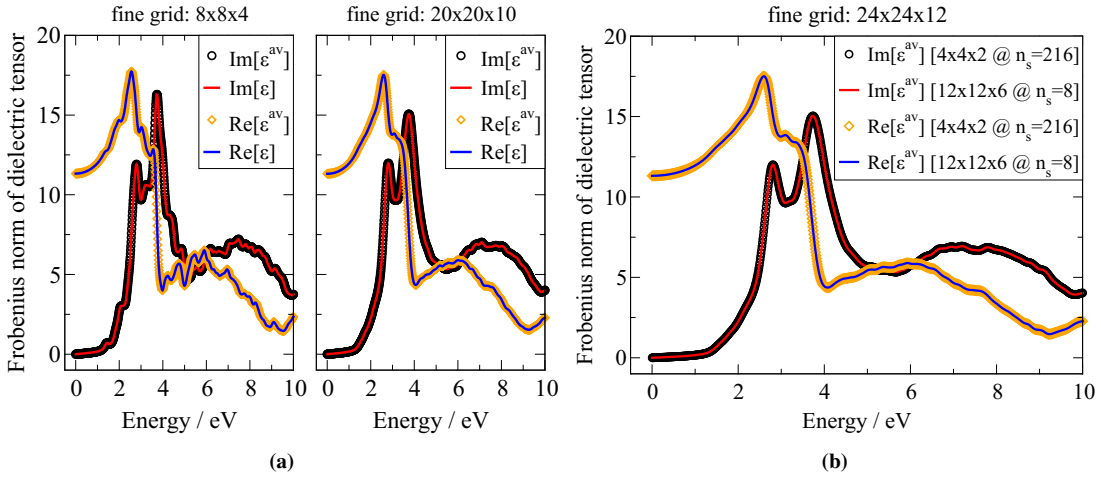

FIGURE 3.21: Dielectric tensor for the primitive structure of CuO (fig. 3.2c): (a) Frobenius norm of real, imaginary part of ϵ, ϵ^{av} vs energy calculated directly with VASP (ϵ) and using the multigrid method (ϵ^{av}). Two different fine grids are chosen: $\mathscr{K}(8\times8\times4)$ (left; coarse grid $\mathscr{K}_p(4\times4\times2)$ with $n_{\mathrm{s}} = 2^3 = 8$) and $\mathscr{K}(20\times20\times10)$ with an additional shift of $\mathbf{b}_{\mathrm{s}} = (1/2, 1/2, 1/2)$ (right; coarse grid $\mathscr{K}_p(4\times4\times2)$ with $n_{\mathrm{s}} = 5^3 = 125$). (b) Frobenius norm of real, imaginary part of ϵ^{av} vs energy calculated for different sizes $M_1\times M_2\times M_3$ of the coarse grid $\mathscr{K}_p$. A fine grid $\mathscr{K}(24\times24\times12)$ is obtained by choosing the number of shifts n_{s} as indicated in the figure. *Parameters for the relaxation of atomic positions*: Plane-wave cut-off: 800 eV, **k**-point density 0.25 Å^{-1}. *Parameters for the SCF calculation (density)*: plane-wave cut-off: 450 eV, **k**-point density 0.25 Å^{-1}. *Parameters for the calculation of the dielectric tensor (non-SCF)*: 200 bands (valence+conduction), 18 001 points in the energy grid, shift in eq. (3.28): $\eta = 0.1$ eV.

(iii) Compute $\mathrm{Im}\,\epsilon(\mathbf{s}_p)$ (eq. (3.25)) on the frequency grid $\mathscr{G}_\omega^{(p)}$ by summing over $\mathbf{k}\in\mathscr{K}_p$ for $p = 1,\ldots,n_{\mathrm{s}}$ at fixed density (non self-consistent calculation).

(iv) Set up a common frequency grid $\mathscr{G}_\omega$ to which *all* $\epsilon(\mathbf{s}_p)$ are interpolated.

(v) Use eq. (3.28) to implement the interpolation of the $\mathrm{Re}\,\epsilon(\mathbf{s}_p)$'s and $\mathrm{Im}\,\epsilon(\mathbf{s}_p)$'s and add up according to eq. (3.36) to obtain $\epsilon^{\mathrm{av}}(\omega)$, $\omega\in\mathscr{G}_\omega$.

(vi) *Eventually*: Compare to a calculation with eq. (3.25) for an "affordable" grid $\mathscr{K}$.

In fig. 3.21a the accuracy of the multigrid method is exemplified: ϵ^{av} from eq. (3.36) is compared to ϵ (more precisely their Frobenius norm) calculated by VASP using eq. (3.25). The chosen fine grids are $\mathscr{K}(8\times8\times4)$ and $\mathscr{K}(20\times20\times10)$ with an additional shift of $\mathbf{b}_{\mathrm{s}} = (1/2, 1/2, 1/2)$. For the multigrid method these grids are constructed with a coarse grid $\mathscr{K}_p(4\times4\times2)$ and $n_{\mathrm{s}} = 8$ and 125, respectively. Indeed, independently of the size of the fine grid $|\mathscr{K}|$, the multigrid method yields the same results as the calculation based on the summation over all $\mathbf{k}\in\mathscr{K}$ (eq. (3.25)).

In fig. 3.21b the dependence of the multigrid method on the divisions $M_1\times M_2\times M_3$ used for the coarse grid is investigated. ϵ^{av} is calculated on a fine grid $\mathscr{K}(24\times24\times12)$ while two different coarse grids $\mathscr{K}_p(4\times4\times2)$ ($n_{\mathrm{s}} = 6^3 = 216$) and $\mathscr{K}_p(12\times12\times6)$ ($n_{\mathrm{s}} = 2^3 = 8$) are employed. Obviously, the results from both choices of the division $M_1\times M_2\times M_3$ yield the same result for $\mathrm{Re}\,\epsilon^{\mathrm{av}}$, $\mathrm{Im}\,\epsilon^{\mathrm{av}}$.

Based on the multigrid method the convergence of the dielectric tensor with respect to the size of the grid of **k**-vectors will now be investigated. A typical convergence graph is shown in fig. 3.22. The size of the fine grid $|\mathscr{K}|$ is increased based on a coarse grid $\mathscr{K}_p(4\times4\times2)$ with $n_{\mathrm{s}} = 64$, 125, 216 and 343 ($n_{\mathrm{div}} = 4$, 5, 6 and 7). A rather characteristic feature of ϵ^{av} (as well as for ϵ) is to display oscillations in case the summation is carried out over too few **k**-points in the BZ. In order to amplify these oscillations, the energy derivative $(d/d\omega)$ is also shown in fig. 3.22. Increasing the size of $\mathscr{K}$ from left to right in fig. 3.22, it is obvious that the oscillations clearly visible in the region of 2 eV and for energies larger than 4 eV for $n_{\mathrm{s}} = 64$ ($\mathscr{K}(16\times16\times8)$) are continuously damped out. $\mathrm{Re}\,\epsilon^{\mathrm{av}}$, $\mathrm{Im}\,\epsilon^{\mathrm{av}}$ are essentially indistinguishable when going from $\mathscr{K}(24\times24\times12)$ to $\mathscr{K}(28\times28\times14)$, indicating convergence of ϵ^{av}.

It should be noted that the complex shift η from eq. (3.28) broadens the structure of ϵ^{av} thereby making it appear smooth. In general, the larger the chosen value of η the fewer oscillations of ϵ^{av} are expected to be visible for a chosen size of the fine grid of **k**-vectors $\mathscr{K}$. The significance and the role of the broadening parameter η will be discussed in the next section when comparing calculated results for the optical absorption spectra to experiment.

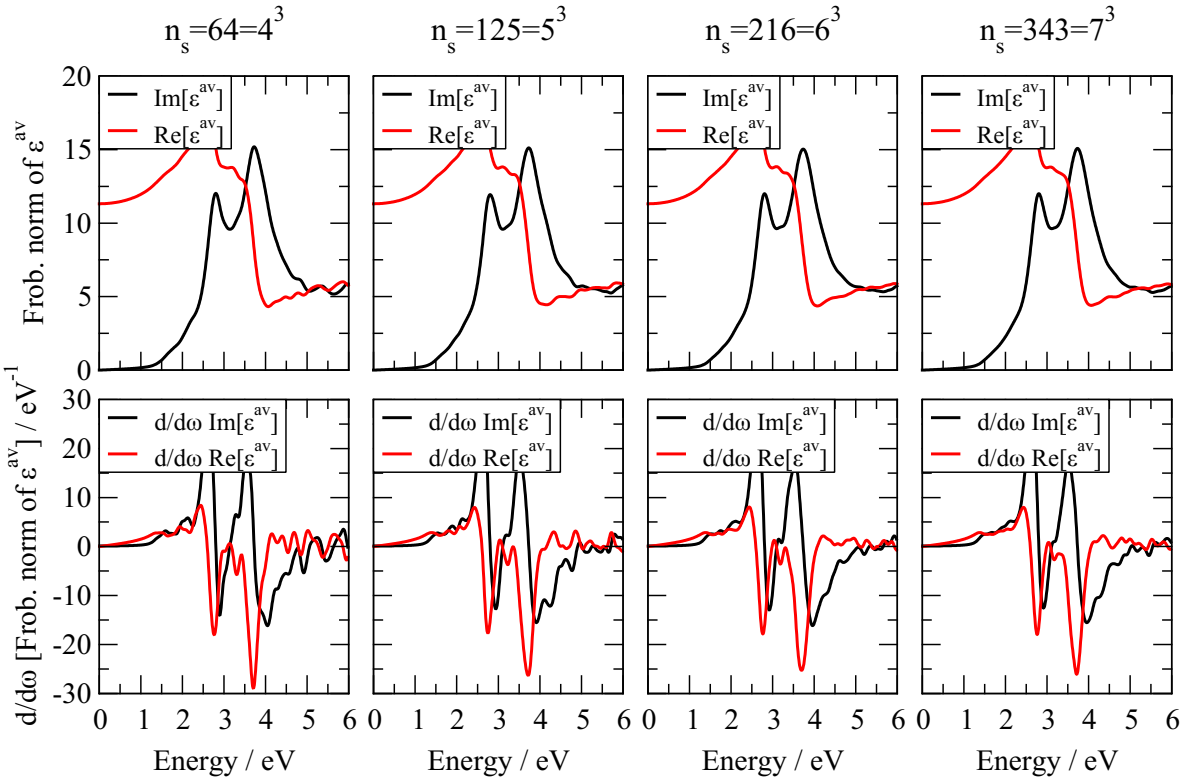

FIGURE 3.22: Dielectric tensor for the primitive structure of CuO (fig. 3.2c): Frobenius norm of real, imaginary part of ϵ^{av} (upper row) and their energy derivative ($d/d\omega$; lower row) for different sizes of the fine grid $\mathscr{K}$. The coarse grid is $\mathscr{K}_P(4\times4\times2)$ with n_{s} = 64, 125, 216 and 343 (n_{div} = 4, 5, 6 and 7) corresponding to $\mathscr{K}(16\times16\times8)$, $\mathscr{K}(20\times20\times10)$, $\mathscr{K}(24\times24\times12)$, and $\mathscr{K}(28\times28\times14)$. *Parameters for the calculations*: See fig. 3.21a.

3.4.2 Raman scattering in monoclinic CuO

In this section the focus is on the Raman scattering properties of CuO. Before the room temperature structure (fig. 3.2c) and the AFM groundstate structure (fig. 3.1c; valid below 213 K) are compared, some general features of the structures are unrolled. This includes optical absorption spectra and a (preliminary) analysis of the Raman active modes.

3.4.2.1 Room temperature structure

Determination of the optical absorption gap $E_{\mathrm{g,abs}}$ In many cases, the optical properties of solids are analysed in terms of the optical absorption coefficient $\alpha_{\mathrm{f}}^{\mathrm{abs}} \equiv \alpha_{\mathrm{f}}^{\mathrm{abs}}(\omega)$. It is related to one of the "optical coefficients" of a crystal, the extinction coefficient $\widetilde{k}_{\mathrm{f}}(\omega)$, by (the other coefficient being the refractive index $\widetilde{n}_{\mathrm{f}}(\omega)$):[23]

$$\alpha_{\mathrm{f}}^{\mathrm{abs}}(\omega) = \frac{2\omega}{c}\widetilde{k}_{\mathrm{f}}(\omega) = \frac{4\pi}{\lambda}\widetilde{k}_{\mathrm{f}}(\omega). \tag{3.37}$$

The connection between components of the dielectric function[ii] $\mathrm{Re}\,\epsilon_{\mathrm{f}} = \epsilon_{\mathrm{f}}^{(1)}$, $\mathrm{Im}\,\epsilon_{\mathrm{f}} = \epsilon_{\mathrm{f}}^{(2)}$ and the optical coefficients is

$$\epsilon_{\mathrm{f}}^{(1)} + i\epsilon_{\mathrm{f}}^{(2)} = (\widetilde{n}_{\mathrm{f}} + i\widetilde{k}_{\mathrm{f}})^2, \tag{3.38}$$

[ii] The subscript "f" is introduced to emphasise that the currently discussed quantities are not tensors of rank two (e.g., $\epsilon_{\mu\mu'}$) but simply scalar-valued *functions*. Particularly, $\epsilon_{\mathrm{f}} : \mathbb{R} \to \mathbb{C}$, whereas $\epsilon : \mathbb{R} \to \mathbb{C}^{3\times3}$.

leading to the set of equations

$$\epsilon_{\mathrm{f}}^{(1)} = \widetilde{n}_{\mathrm{f}}^2 - \widetilde{k}_{\mathrm{f}}^2 \tag{3.39a}$$

$$\epsilon_{\mathrm{f}}^{(2)} = 2\widetilde{n}_{\mathrm{f}}\widetilde{k}_{\mathrm{f}}, \tag{3.39b}$$

which eventually leads to

$$\widetilde{n}_{\mathrm{f}} = \sqrt{\tfrac{1}{2}\left(|\epsilon_{\mathrm{f}}| + \operatorname{Re}\epsilon_{\mathrm{f}}\right)} \tag{3.40a}$$

$$\widetilde{k}_{\mathrm{f}} = \sqrt{\tfrac{1}{2}\left(|\epsilon_{\mathrm{f}}| - \operatorname{Re}\epsilon_{\mathrm{f}}\right)}, \tag{3.40b}$$

where $|\epsilon_{\mathrm{f}}| = \sqrt{[\operatorname{Re}\epsilon_{\mathrm{f}}]^2 + [\operatorname{Im}\epsilon_{\mathrm{f}}]^2}$ is the absolute value of the complex-valued dielectric function.

The dielectric tensor $\epsilon_{\mu\mu'}$ can be related to a scalar-valued function depending on the direction $\hat{\mathbf{q}}$ through[192]

$$\epsilon_{\mathrm{f}}(\omega;\hat{\mathbf{q}}) = \hat{\mathbf{q}}^T\epsilon(\omega)\hat{\mathbf{q}} = \sum_{\mu\mu'}\hat{q}_\mu\epsilon_{\mu\mu'}(\omega)\hat{q}_{\mu'}. \tag{3.41}$$

Integrating out the directional dependence over the unit sphere $\mathbb{S}^2$ gives a direction-averaged ("avd") dielectric function

$$\epsilon_{\mathrm{f,avd}}(\omega) = \frac{1}{4\pi}\int_{\mathbb{S}^2} d\hat{\mathbf{q}}\ \epsilon_{\mathrm{f}}(\omega;\hat{\mathbf{q}}). \tag{3.42}$$

Numerically, this integral is evaluated on a grid that homogeneously samples the surface of the unit sphere. Here, grids from Lebedev and Laikov [193] are used which allow the approximation of the integral of a generic function f over the unit sphere[iii]

$$\int_{\mathbb{S}^2} d\hat{\mathbf{x}}\ f(\hat{\mathbf{x}}) \approx 4\pi\sum_{j=1}^{|\mathscr{L}|} w_j f(\hat{\mathbf{x}}_j), \tag{3.43}$$

where $\mathscr{L}$ is the grid from Lebedev and Laikov [193], and $\sum_{j=1}^{|\mathscr{L}|} w_j = 1$. In relation to eq. (3.42) this means

$$\epsilon_{\mathrm{f,avd}}(\omega) \approx \frac{1}{4\pi}\sum_{j=1}^{|\mathscr{L}|}(4\pi w_j)\epsilon_{\mathrm{f}}(\omega;\hat{\mathbf{q}}_j). \tag{3.44}$$

Since ϵ is a second-rank tensor, so is the absorption coefficient α^{abs}. In case of an *isotropic* dielectric tensor ($\epsilon_{\mu\mu'} = \epsilon_\mu\delta_{\mu\mu'}$ and hence $[\alpha^{\mathrm{abs}}]_{\mu\mu'} = [\alpha^{\mathrm{abs}}]_\mu\delta_{\mu\mu'}$), the above relation eq. (3.37) (which is derived for scalars) can can be directly applied since the tensor elements do not couple:

$$[\alpha^{\mathrm{abs}}]_{\mu\mu'}(\omega) = \frac{4\pi}{\lambda}\widetilde{k}_{\mu\mu'}(\omega) = \frac{4\pi}{\lambda}\sqrt{\tfrac{1}{2}\left(\left|\epsilon_\mu(\omega)\right| - \operatorname{Re}\epsilon_\mu(\omega)\right)}\delta_{\mu\mu'}. \tag{3.45}$$

If, however, the dielectric tensor is *non-isotropic* (i.e., it possess non-zero diagonal elements), eq. (3.37) must be calculated with the matrix square root. That is, $\epsilon(\omega)$ is brought to diagonal form by diagonalisation: $\mathscr{V}_\omega^{-1}\epsilon(\omega)\mathscr{V}_\omega$, where $\mathscr{V}_\omega$ contains the eigenvectors of $\epsilon(\omega)$ as columns. The absorption coefficient is then calculated in the eigenbasis:

$$[\alpha^{\mathrm{abs}}_{\mathrm{diag}}]_{\mu\mu'}(\omega) = \frac{4\pi}{\lambda}[\widetilde{k}_{\mathrm{diag}}]_{\mu\mu'}(\omega) = \frac{4\pi}{\lambda}\sqrt{\tfrac{1}{2}\left(\left|\epsilon_\mu^{\mathrm{diag}}(\omega)\right| - \operatorname{Re}\epsilon_\mu^{\mathrm{diag}}(\omega)\right)}\delta_{\mu\mu'}, \tag{3.46}$$

where $\epsilon_\mu^{\mathrm{diag}}(\omega)$ are the eigenvalues of $\epsilon(\omega)$, and eventually the tensor is transformed back to the original coordinate system by $\alpha^{\mathrm{abs}}(\omega) = \mathscr{V}_\omega\alpha^{\mathrm{abs}}_{\mathrm{diag}}(\omega)\mathscr{V}_\omega^{-1}$. Finally, as for eq. (3.44) in case of ϵ, the direction average for α^{abs} is calculated according to

$$\alpha^{\mathrm{abs}}_{\mathrm{f,avd}}(\omega) = \frac{1}{4\pi}\sum_{j=1}^{|\mathscr{L}|}(4\pi w_j)(\hat{\mathbf{q}}_j^T\alpha^{\mathrm{abs}}(\omega)\hat{\mathbf{q}}_j). \tag{3.47}$$

[iii] The Fortran routines for the generation of these grids can be downloaded from `http://www.ccl.net/cca/software/SOURCES/FORTRAN/Lebedev-Laikov-Grids/index.shtml`.

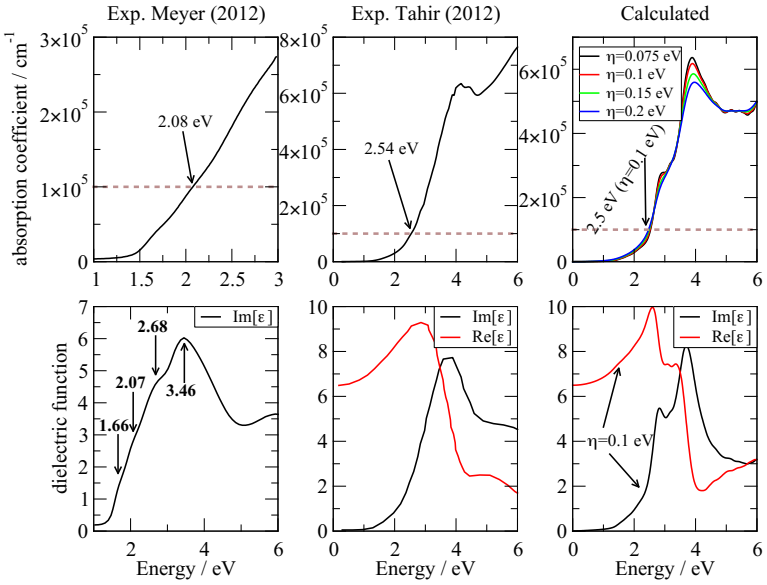

FIGURE 3.23: Absorption coefficient (upper row) and dielectric function (lower row). Experimental data from Meyer et al. [23] and Tahir and Tougaard [194] are shown. The annotations at the dielectric function in the lower left figure mark electronic transitions as listed in Meyer et al. [23, tab. 6]. The horizontal dashed line in the upper row marks an absorption value of 1×10^5 cm^{-1} and the respective energy value is indicated in the plot. The calculated absorption coefficient as well as the real and the imaginary part of the dielectric function (right side) are averaged over directions according to eqs. (3.44) and (3.47). The size $|\mathscr{L}|$ of the grid from Lebedev and Laikov [193] is 4802 points (grid-ID: 30). In case of the absorption coefficient, several values for the broadening parameter η used in eq. (3.28) are given, while for the dielectric function $\eta = 0.1$ eV is used. *Parameters for the relaxation of atomic positions*: See fig. 3.21a. *Parameters for the SCF calculation (density)*: Plane-wave cut-off: 550 eV, **k**-point density 0.25 Å^{-1}. *Parameters for the calculation of the dielectric tensor (non-SCF)*: 200 bands (valence+conduction), 18 001 points in the energy grid. The **k**-summation is based on a fine grid $\mathscr{K}(24 \times 24 \times 12)$ generated with a coarse grid $\mathscr{K}_P(8 \times 8 \times 4)$ and $n_s = 27 = 3^3$ shifts ($n_{\text{div}} = 3$).

In fig. 3.23 the calculated direction-averaged absorption coefficient (upper row) and the calculated direction-average dielectric function (lower row) are shown together with experimental data from Meyer et al. [23] and Tahir and Tougaard [194]. Obviously, experimental results are quite different: The absorption coefficient from Meyer et al. [23] increases almost linearly up to 3 eV whereas data from Tahir and Tougaard [194] displays clearly visible curvature in this energy range. In order to illustrate this difference, the energy where the absorption coefficient crosses 1×10^5 cm^{-1} is annotated. Indeed, the differences in the absorption curves from both experiments can be understood by looking at the experimental dielectric functions from the lower row. For Meyer et al. [23]'s data, several electronic transitions below 3 eV that either correspond to interband transitions or excitons[23] are observed (see annotated arrows in fig. 3.23). Clearly, no such transitions are present in the absorption curve from Tahir and Tougaard [194]. These transitions enhance absorption and most likely cause the differences in absorption behaviour observed in experiment.

The calculated curves for $\alpha^{\text{abs,av}}_{\text{f,avd}}$, $\text{Re}\,\epsilon^{\text{av}}_{\text{f,avd}}$, $\text{Im}\,\epsilon^{\text{av}}_{\text{f,avd}}$ [iv] are in quite good agreement with the measurements of Tahir and Tougaard [194] below 4 eV. The energy values at which calculated and measured absorption curves cross 1×10^5 cm^{-1} (2.5 eV and 2.54 eV, respectively) are very close. An additional shoulder at about 2.9 eV is present in case of the calculated absorption coefficient. The larger the value of the broadening parameter η used in eq. (3.28) the more this feature vanishes.

As a matter of fact, the good agreement with Tahir and Tougaard [194] motivates to use a finite value for η in eq. (3.28). From fig. 3.23, experimental curves do not show sharp absorption onsets but rather show a soft increase in the absorption coefficient (or likewise $\text{Im}\,\epsilon$, the absorptive part of the dielectric function). The optical absorption gap determined in experiment never equals the smallest direct (meaning "vertical" transitions in reciprocal space for which $\mathbf{\Delta k} = \mathbf{0}$) energy difference between valence and conduction bands. The main reasons for this presumably are:

- *Excitons*: Depending on the properties of the electron-hole coupling, excitons will introduce additional

[iv] The calculated absorption coefficient as well as the calculated dielectric functions are labelled as $\alpha^{\text{abs,av}}_{\text{f,avd}}$, $\epsilon^{\text{av}}_{\text{f,avd}}$ because (i) they are calculated with the multigrid method (superscript "av"), and (ii) they are averaged over directions according to eqs. (3.44) and (3.47) (subscript "avd").

"absorption channels" (not necessarily only in the sub-gap region). Thereby, the absorption spectrum is red-shifted (compared to, e.g., calculations based on the independent-particle approximation), and additional "spectral weight" is shuffled to lower energies. This is observed for oxide-semiconductors from Bethe-Salpeter (BSE) calculations by Rödl [195, p. 74 in fig. 5.1].

- *Finite temperature effects*: A finite lifetime of electronic states is introduced at finite temperature because electron-phonon interaction gets enhanced with increasing temperature. The effect on the absorption spectra (e.g, $\mathrm{Im}\,\epsilon$) of a solid will be a softening/broadening of the peaks corresponding to optical transitions. Furthermore, an enlarged "absorption tail" is introduced in the sub-gap region (see Gillet [12, p. 123 in fig. 46]).

Indeed, from a theoretical point of view, the inclusion of excitonic as well as temperature induced effects is desirable but also very challenging and computationally demanding. The influence of excitons and finite temperature effects on the optical and Raman spectroscopic properties of some solids is studied by Gillet [12].

In summary, choosing a finite value for η in eq. (3.28) appears appropriate. Reviewing eq. (3.28), the expression replacing the usual Cauchy principal value

$$\pi^{-1}\,\mathrm{pv}\int_{\mathbb{R}} d\omega'\ \ \mathrm{Im}\,\epsilon(\omega')/(\omega'-\omega) \tag{3.48}$$

involved in the Kramers-Kronig relations is an expression of the form

$$\pi^{-1}\int_{\mathbb{R}} d\omega'\ \ \mathrm{Im}\,\epsilon(\omega')/(\omega'-\omega-i\eta). \tag{3.49}$$

This corresponds to the convolution of $\mathrm{Im}\,\epsilon$ with a Lorentzian. Therefore, at most the effect of temperature broadening (finite lifetime effects) can be mimicked to some extent. However, since η is a simple parameter, its usage should by no means be exaggerated. In what follows, a value of $\eta = 0.1\,\mathrm{eV}$ is used which actually corresponds to the standard choice in VASP for linear response calculations (see the variable CSHIFT[v]).

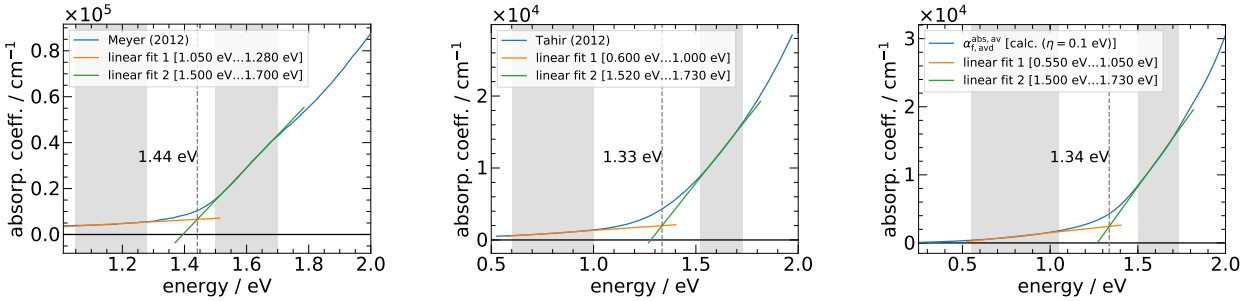

(a) Experiment: Meyer et al. [23].

(b) Experiment: Tahir and Tougaard [194].

(c) Calculated.

FIGURE 3.24: Determination of the optical absorption gap $E_{\mathrm{g,abs}}$. The gap is determined from (a) data of Meyer et al. [23], (b) data of Tahir and Tougaard [194], and (c) calculated data.. In (c) the calculated absorption coefficient is labelled as $\alpha^{\mathrm{abs,av}}_{\mathrm{f,avd}}$ because (i) it is calculated with the multigrid method (superscript "av"), and (ii) it is averaged over directions according to eq. (3.47) (subscript "avd"). $E_{\mathrm{g,abs}}$ is determined from the intersection of the linear fits as shown in the figures. The energy regions used for the linear approximation of the absorption coefficient are indicated by the grey-shaded regions and are given as numbers in the legend of the plot. *Parameters for the calculations*: See fig. 3.23

Optical absorption gaps $E_{\mathrm{g,abs}}$ for the calculated and the experimental absorption coefficients[23,194] are determined in fig. 3.24. The gaps are taken as the intersection of two linear fits: (1) A linear fit of the subgap absorption tail, and (2) a linear fit of the region of strong absorption beyond $E_{\mathrm{g,abs}}$. The thus determined values for the optical absorption gaps are 1.34 eV, 1.44 eV and 1.33 eV from the calculated and the experimental absorption coefficients from Meyer et al. [23] and Tahir and Tougaard [194], respectively. It should probably be noted that Tahir and Tougaard [194] determine an optical absorption gap of 1.0 eV by considering the inelastic cross section from REELS measurements. Nonetheless, these values are in reasonable agreement with reflectance and transmittance data from Marabelli et al. [196] where $E_{\mathrm{g,abs}}(300\,\mathrm{K}) = 1.34\,\mathrm{eV}$,[vi] and with a value of $E_{\mathrm{g,abs}}(300\,\mathrm{K}) = 1.44\,\mathrm{eV}$ from Wang et al. [88, tab. I].

[v] The manual can be found at `http://cms.mpi.univie.ac.at/wiki/index.php/The_VASP_Manual`

[vi] This value is not explicitly listed in the paper but can be found in Rödl et al. [105, tab. II].

From the electronic eigenvalues at the **k**-points used for the BZ integration the smallest direct transition energy from valence to conduction band is 1.41 eV (direct bandgap). This value (slightly) differs from the above determined value of 1.34 eV because the curve in fig. 3.24 is calculated with a broadening value of $\eta = 0.1\,\text{eV}$.

Calculation of the Raman susceptibilities α^m Recalling eq. (3.24), the Raman susceptibility $\alpha^m(\omega)$ is the directional derivative of the (linear) susceptibility tensor $\chi(\omega)$, where the direction is the displacement vector $u^{s,\nu}_{m,\mathbf{q}=\mathbf{0}} = w^{s,\nu}_{m,\mathbf{q}=\mathbf{0}}/\sqrt{M_s}$ of the mth phonon mode (see eq. (2.23)).

Numerically, one way to determine this derivative is to *first* calculate the gradient $\frac{\partial}{\partial u_{s,\nu}}\chi(\omega)$ (eq. (3.29)), and then to project the gradient on the displacement vector like in eq. (3.24). Another approach is to *directly* evaluate the directional derivative. This is accomplished by displacing the atoms in the unit cell by a finite amount along the displacement vector $\mathbf{u}_m$ and to calculate $\chi(\omega)$ (or rather $\operatorname{Im}\epsilon(\omega)$, and then $\operatorname{Re}\epsilon(\omega)$ by eq. (3.28)) for this distorted atomic geometry. If different displacement directions are considered, the directional derivative can be evaluated in a similar manner as in case of eq. (3.29).

Both methods for computing the directional derivative can be summarised as follows:

(I) Using equation eq. (3.29):
  (1) Solve eq. (2.23) for $\mathbf{q} = \mathbf{0}$ by diagonalising the dynamical matrix, yielding the displacement vectors $\mathbf{u}_m$.
  (2) For each atoms s at a time: Displace it from its equilibrium position $\mathbf{x}_s^{(0)} \to \mathbf{x}_s^{(0)} \pm \mathbf{u}_s^{(\nu)}$ with $\mathbf{u}_s^{(\nu)} = d_{\text{scale}}\hat{\mathbf{e}}_\nu$ and calculate the groundstate density in a self-consistent manner ($d_{\text{scale}} \equiv d^{(s)}_{\text{scale}}$: finite scaling length used for the displacement).
  (3) For all displacements $\pm\mathbf{u}_s^{(\nu)}$: Calculate $\operatorname{Im}\epsilon(\omega;\pm\mathbf{u}_s^{(\nu)})$ with eq. (3.25) from the SCF density (non-SCF calculation) and then $\operatorname{Re}\epsilon(\omega;\pm\mathbf{u}_s^{(\nu)})$ with eq. (3.28).
  (4) Gather the $\epsilon(\omega;\pm\mathbf{u}_s^{(\nu)})$'s and calculate $\frac{\partial}{\partial u_{s,\nu}}\chi(\omega)$ from eq. (3.29).
  (5) Calculate the directional derivative for eq. (3.24) to obtain α^m.

(II) Direct evaluation of the directional derivative for a Raman active mode m:
  (1) Normalise $\hat{\mathbf{u}}_m = \mathbf{u}_m/|\mathbf{u}_m|$ and add the scaled displacement vector to the atomic equilibrium position $\mathbf{x}_s^{(0)} \to \mathbf{x}_s^{(0)} \pm d_{\text{scale}}\hat{\mathbf{u}}_m^s$ and calculate the groundstate density for this distorted geometry.
  (2) Calculate $\operatorname{Im}\epsilon(\omega;\pm\mathbf{u}_m)$ with eq. (3.25) from the SCF density (non-SCF calculation) and then $\operatorname{Re}\epsilon(\omega;\pm\mathbf{u}_m)$ with eq. (3.28).
  (3) Calculate the directional derivative to obtain α^m:

$$\begin{aligned}\alpha^m(\omega) &\equiv \sqrt{\Omega_0}\frac{\partial\chi(\omega)}{\partial u_m} = \frac{\sqrt{\Omega_0}}{4\pi}\frac{d}{dt}\epsilon(\omega;\{\mathbf{x}_s^{(0)}\} + t\mathbf{u}_m)\Big|_{t=0} \\ &\approx \frac{\sqrt{\Omega_0}}{4\pi}\frac{\epsilon\left(\omega;+d_{\text{scale}}\hat{\mathbf{u}}_m\right) - \epsilon\left(\omega;-d_{\text{scale}}\hat{\mathbf{u}}_m\right)}{2d_{\text{scale}}}\,|\mathbf{u}_m|\,. \end{aligned} \tag{3.50}$$

  Note that, in order to obtain the same result as with eq. (3.29), it is indeed necessary to scale by the norm $|\mathbf{u}_m|$.

Beyond doubt, both methods must yield the same result for α^m within the accuracy of the numerical derivative. The approach based on eq. (3.29) appears to be more versatile, but a direct calculation of the directional derivative can be the method of choice if only a few Raman active modes of a crystal are of interest (e.g., in case the unit cell contains many atoms).

Based on the C^6_{2h} space group ($C2/c$, No. 15) symmetry of CuO at *room temperature*, a factor group analysis with the isomorphic point group C_{2h} reveals the irreducible representations (irreps) of the Raman active modes $A_g \oplus 2B_g$.[23,106] Choosing the 2-fold rotation axis of the C_{2h} point group along the **y**-axis of an orthogonal $(\mathbf{x},\mathbf{y},\mathbf{z})$ coordinate system, yields Raman tensors of the generic form[23]

$$\mathscr{R}^{A_g} = \begin{pmatrix} a & 0 & d \\ 0 & b & 0 \\ d & 0 & c \end{pmatrix}, \qquad \mathscr{R}^{B_g} = \begin{pmatrix} 0 & e & 0 \\ e & 0 & f \\ 0 & f & 0 \end{pmatrix}, \tag{3.51}$$

where it is understood that $\mathscr{R}^m{}_{\mu\mu'} : \mathbb{R}_{\geq 0} \to \mathbb{C}$.

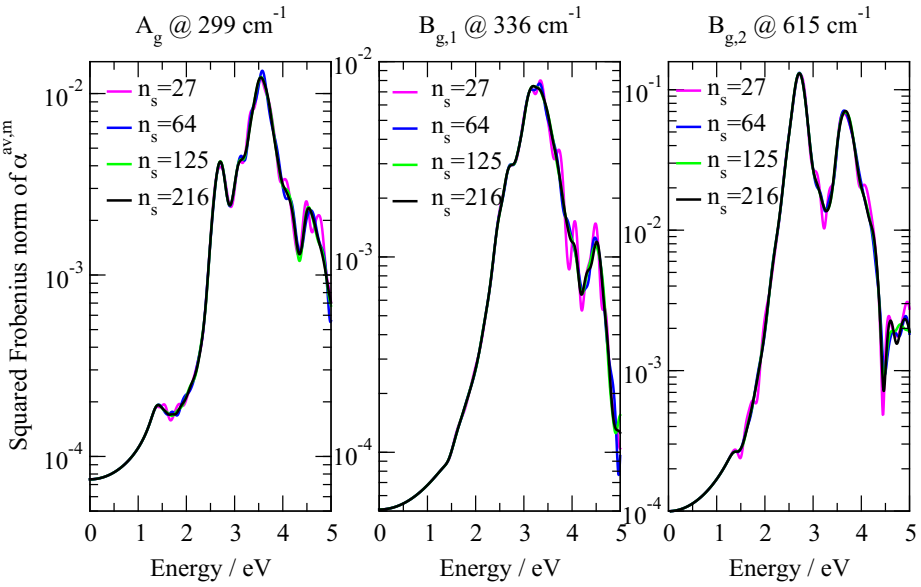

FIGURE 3.25: Convergence of $\alpha^{\mathrm{av},m}$ (in arbitrary units) with respect to the number of **k**-points. Raman active modes A_g, $B_{g,1}$, $B_{g,2}$ are shown from left to right. Based on a coarse grid $\mathscr{K}_p(6\times6\times3)$, different sizes of the fine **k**-point grid $\mathscr{K}$ are considered: The respective fine grids are $\mathscr{K}(18\times18\times9)$ ($n_\mathrm{s}=27=3^3$), $\mathscr{K}(24\times24\times12)$ ($n_\mathrm{s}=64=4^3$), $\mathscr{K}(30\times30\times15)$ ($n_\mathrm{s}=125=5^3$), and $\mathscr{K}(36\times36\times18)$ ($n_\mathrm{s}=216=6^3$). *Parameters for the relaxation of atomic positions/calculation of the dynamical matrix at* Γ: See fig. 3.21a and a displacement length of 0.01 Å. *Parameters for the SCF calculation (density)*: See fig. 3.23 with a displacement length of 0.01 Å. *Parameters for the calculation of the dielectric tensor (non-SCF)*: 150 bands (valence+conduction), 18 001 points in the energy grid, the broadening parameter for eq. (3.28) is $\eta=0.1$ eV.

The **k**-point convergence of $\alpha^{\mathrm{av},m}$ for modes $A_g, B_{g,1}, B_{g,2}$ is analysed in fig. 3.25. Fine grids are $\mathscr{K}(18\times18\times9)$ ($n_\mathrm{s}=27=3^3$), $\mathscr{K}(24\times24\times12)$ ($n_\mathrm{s}=64=4^3$), $\mathscr{K}(30\times30\times15)$ ($n_\mathrm{s}=125=5^3$), and $\mathscr{K}(36\times36\times18)$ ($n_\mathrm{s}=216=6^3$) based on a coarse grid $\mathscr{K}_p(6\times6\times3)$ are employed. All sizes $|\mathscr{K}|$ give (essentially) converged results for energies below 3 eV. Beyond 3 eV results from $\mathscr{K}(18\times18\times9)$ significantly deviate from the larger grids and convergence appears to be very hard to achieve above 4 eV. However, "typical" laser energies used in Raman scattering experiments are in the visible range of the electromagnetic spectrum.[vii] This part contains energies from ~1.59 eV to 3.26 eV[viii] which is a well-described region by all $\mathscr{K}$-grids larger than $\mathscr{K}(18\times18\times9)$.

The decomposition of the mode displacement vectors $\mathbf{u}_m$ of the Raman active modes in terms of atomic contributions is shown in fig. 3.26a. The modes $A_g, B_{g,1}, B_{g,2}$ are solely oxygen driven without any contribution from the copper sublattice. The A_g mode is "totally symmetric" which means that the mode displacement pattern does *not* alter the crystal symmetry. For this mode α^m from eqs. (3.29) and (3.50) is compared in fig. 3.26b. Obviously, both methods yield the same result for α^m, but the difficulty lies in the choice of the scaling length d_scale to be used for the mode displacement vector in eq. (3.50). The key issue is that multiple atoms are displaced *at once* in $\mathbf{u}_m$. Since the scaling length is used for the whole vector, atoms in general have different displacement lengths. The displacement lengths need to be large enough to cause a change

[vii] "Typical" laser energies used in Raman scattering experiments are:
- Ultra-violet (UV-A,B): 244 eV, 257 eV, 325 eV and 364 eV;
- **Visible**: 457 nm, 473 nm, 488 nm, 514 nm, 532 nm, 633 nm and 660 nm;
- Near infra-red (IR-A): 785 nm, 830 nm, 980 nm and 1064 nm.

See `http://www.horiba.com/scientific/products/raman-spectroscopy/raman-academy/raman-faqs/what-laser-wavelengths-are-used-for-raman-spectroscopy/`.

[viii] Following `http://halas.rice.edu/conversions`, the energies bounding the relevant part of the electromagnetic spectrum are:
- Mid UV (UV-B): 3.94 eV to 4.43 eV;
- Near UV (UA-A): 3.26 eV to 3.94 eV;
- **Visible**: 1.59 eV to 3.26 eV;
- Near infra-red (IR-A): 0.886 eV to 1.58 eV.

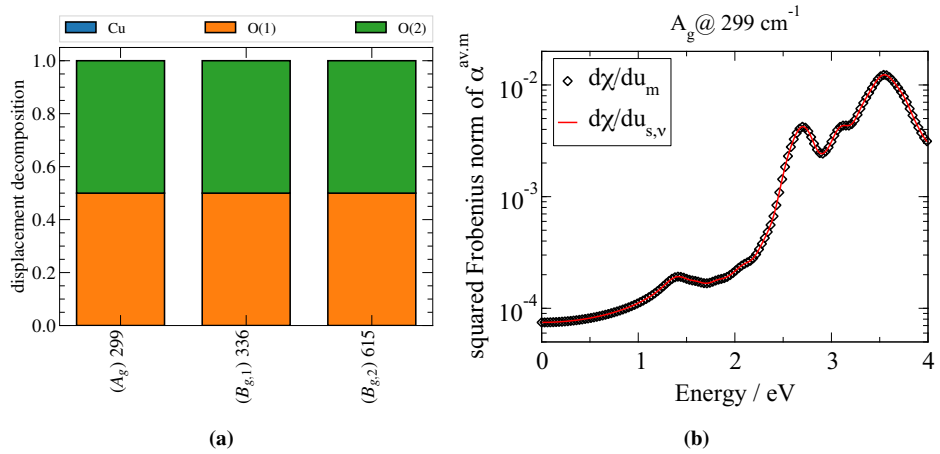

FIGURE 3.26: (a) Decomposition of the (squared) norm of the mode displacement vectors ($|\mathbf{u}_m|^2$) in terms of contributions from Cu and O atoms. Only Raman active modes A_g, $B_{g,1}$, $B_{g,2}$ are shown. The frequencies (in cm^{-1}) are listed with the symbols of the irreps. (b) Raman susceptibility $\alpha^{\mathrm{av},m}$ (in arbitrary units) of the A_g mode by (i) using eq. (3.29) ($\partial\chi/\partial u_{s,v}$), and (ii) by using eq. (3.50) ($\partial\chi/\partial u_m$). *Parameters for the relaxation of atomic positions/calculation of the dynamical matrix at* Γ: See fig. 3.25. *Parameters for the SCF calculation (density)*: See fig. 3.23 with a displacement length of 0.01 Å for eq. (3.29) and 0.0075 Å for eq. (3.50). *Parameters for the calculation of the dielectric tensor (non-SCF)*: See fig. 3.25, and a fine grid $\mathscr{K}(30\times30\times15)$ is used based on a coarse grid $\mathscr{K}_P(6\times6\times3)$ with $n_\mathrm{s} = 125 = 5^3$.

in $\epsilon(\omega)$ that is traceable with the chosen set of numerical parameters but small enough not to invalidate the linear approximation eq. (3.50).

3.4.2.2 Antiferromagnetic groundstate structure below $T_\mathrm{N}^{(2)} = 213\,\mathrm{K}$

Raman active phonon modes and experimental results Following Perez-Mato et al. [197] and Gallego et al. [198, 199],[ix] the AFM groundstate phase has the magnetic spacegroup BNS:P_a2_1/c (No. 14.80; Shubnikov type IV) which is based on the monoclinic Fedorov spacegroup $P2_1/c$ (C_{2h}^5, No. 14). The factor group of the C_{2h}^5 space group is isomorphic to the C_{2h} point group. Therefore, the Raman tensors of the AFM groundstate structure from fig. 3.1c have the generic form given by eq. (3.51) and the irreps of the Raman active modes are $6A_g \oplus 6B_g$.

When CuO undergoes the AFM phase transition at $T_\mathrm{N}^{(2)}$, the local symmetry of the atoms changes: While in the structure described by Åsbrink and Norrby [106] Cu and O atoms are at Wyckoff $4c$ (C_i symmetry) and Wyckoff $4e$ (C_2 symmetry) positions, the atoms in the structure from Forsyth et al. [22] (Cu as well as O) are located at symmetry-free positions with *crystallographic* C_1 symmetry (meaning irrespective of the magnetic symmetry group), i.e., they are in "general position".

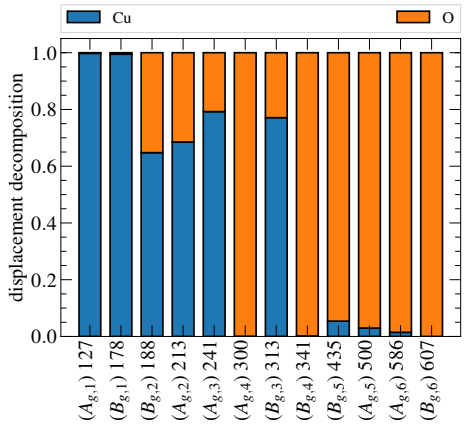

FIGURE 3.27: Decomposition of the (squared) norm of the mode displacement vectors ($|\mathbf{u}_m|^2$) in terms of contributions from Cu and O atoms. Only Raman active modes are shown. The frequencies (in cm^{-1}) are listed with the symbols of the irreps. *Parameters for the relaxation of atomic positions/calculation of the dynamical matrix at* Γ: Plane-wave cut-off: 800 eV, a $6\times12\times6$ **k**-point grid, a displacement length of 0.01 Å.

The decomposition of the mode displacement vectors $\mathbf{u}_m$ of the Raman active modes in terms of atomic contributions is shown in fig. 3.27. The situation is more complicated than in fig. 3.26a: Instead of only three

[ix] See also `http://webbdcrista1.ehu.es/magndata/index.php?this_label=1.62`

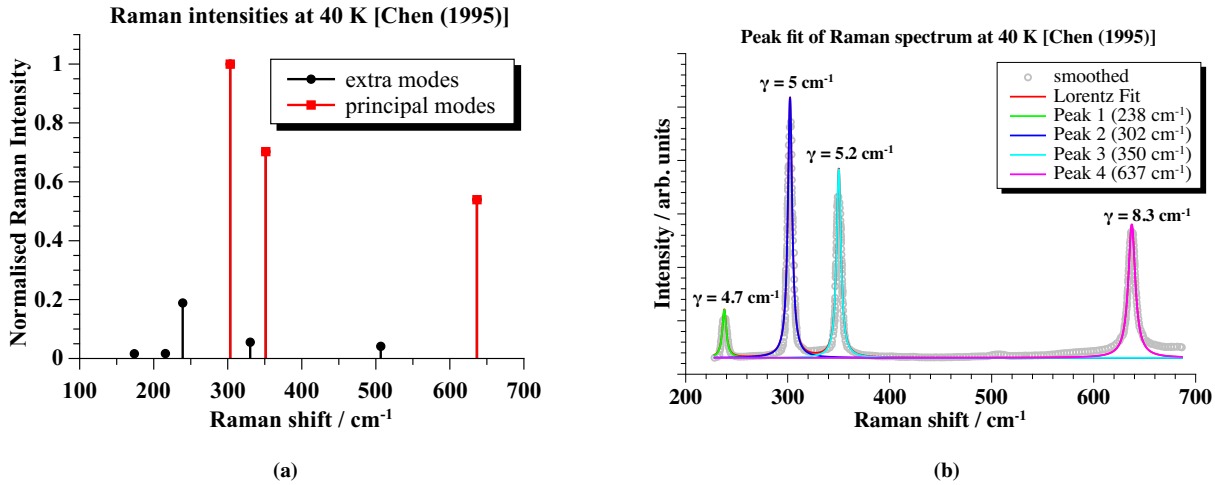

FIGURE 3.28: (a) Raman intensities extracted from of CuO from Chen et al. [24, fig. 1]. The peaks are normalised to the maximal peak height. Principal (red; peaks also present at room temperature) and extra Raman active modes (black; peaks that arise below $T_N^{(2)} = 213\,\mathrm{K}$) are distinguished. (b) Fit of the major peaks in the 40 K Raman spectrum of Chen et al. [24]. The fit is performed with a Lorentzian of the form $I_\gamma(\omega) = I_0 + 2A/\pi \times \gamma/(4(\omega-\omega_0)^2+\gamma^2)$ (`http://www.qtiplot.com`). The centring ω_0 and the broadening γ of the peaks are given in the plot. These values are additionally compiled in table 3.4 and compared to the peak positions from Chen et al. [24].

Raman active modes, there now are twelve. In particular, for the low-frequency modes also copper atoms contribute to the mode displacement vectors. Nevertheless, the modes from fig. 3.26a are easily identified as those only consisting of oxygen vibrations. The modes are slightly shifted in frequency compared to the RT structure: $300\,\mathrm{cm}^{-1}$, $341\,\mathrm{cm}^{-1}$ and $607\,\mathrm{cm}^{-1}$ opposed to $299\,\mathrm{cm}^{-1}$, $336\,\mathrm{cm}^{-1}$ and $615\,\mathrm{cm}^{-1}$.

Obviously, as a consequence of the AFM phase transition at $T_N^{(2)}$, additional modes will be visible in the Raman spectrum. Indeed, this is what is observed in experiment when cooling below $T_N^{(2)}$: Chen et al. [24] find five new modes at $175\,\mathrm{cm}^{-1}$, $218\,\mathrm{cm}^{-1}$, $240\,\mathrm{cm}^{-1}$, $331\,\mathrm{cm}^{-1}$ and $508\,\mathrm{cm}^{-1}$ in the Raman spectrum when cooling to 40 K (see fig. 3.28a). The mode at $240\,\mathrm{cm}^{-1}$ is identified to be a A_g mode which is mainly driven by vibrations of the copper sublattice.[24] This is verified by Chen et al. [24] where ^{63}Cu is changed to ^{65}Cu which shifts the peak to smaller frequencies. Indeed, the irrep for the mode with calculated frequency $241\,\mathrm{cm}^{-1}$ is A_g (see fig. 3.27). Furthermore, a strong dependence on temperature is documented for this mode.[24,166]

In fig. 3.28b the major peaks of the Raman spectrum from Chen et al. [24] are fitted in order to obtain their broadening. The thus obtained values for the peak broadening and the peak positions are summarised in table 3.4.

	peak position ω_0 / cm^{-1}		peak broadening / cm^{-1}	
Peak	fitted	Ref. [24]	γ	$\zeta = \gamma/2$
1	238	240	4.7	2.35
2	302	303	5.0	2.5
3	350	350	5.2	2.6
4	637	636	8.3	4.15

TABLE 3.4: Values from the fit of the 40 K Raman spectrum of Chen et al. [24] in fig. 3.28b. Each peak is fitted with a Lorentzian of the form $I_{\gamma(\zeta)}(\omega) = I_0 + 2A/\pi \times \gamma/(4(\omega-\omega_0)^2+\gamma^2) = I_0 + 2A/\pi \times (2\zeta)/(4(\omega-\omega_0)^2+(2\zeta)^2)$. The relation between the broadening parameters is $\gamma = 2\zeta$. The mean value of ζ is $\overline{\zeta} = 2.9\,\mathrm{cm}^{-1}$.

Concerning the emergence of new phonon modes compared to the RT structure, Chen et al. [24] argue that appearance of these modes is related to a folding of the X-point from the BZ of the (conventional) RT structure to the BZ centre of the AFM groundstate structure. Referring to Güntherodt et al. [200] and Bauhofer et al. [201], they assume that a modulation of the magnetic exchange constant(s) by the vibrational pattern of some phonon modes related to the zone-folding makes these modes appear in the Raman spectrum below $T_N^{(2)}$. It is neglected, however, that Bauhofer et al. [201] explicitly mention a symmetry lowering due to the formation of a magnetic superstructure ($D_{3d} \rightarrow C_{2h}$ for vanadium dihalides), making additional modes Raman active.[x] A further constraint placed on additional modes to contribute to Raman scattering is

[x] "The magnetic ordering reduces the original D_{3d} point group symmetry of the crystallographic unit cell to a rhombohedral prism formed by the eight metal sites represented schematically in Fig. 11(c). [...] forming a C_{2h} subgroup of the original D_{3d}

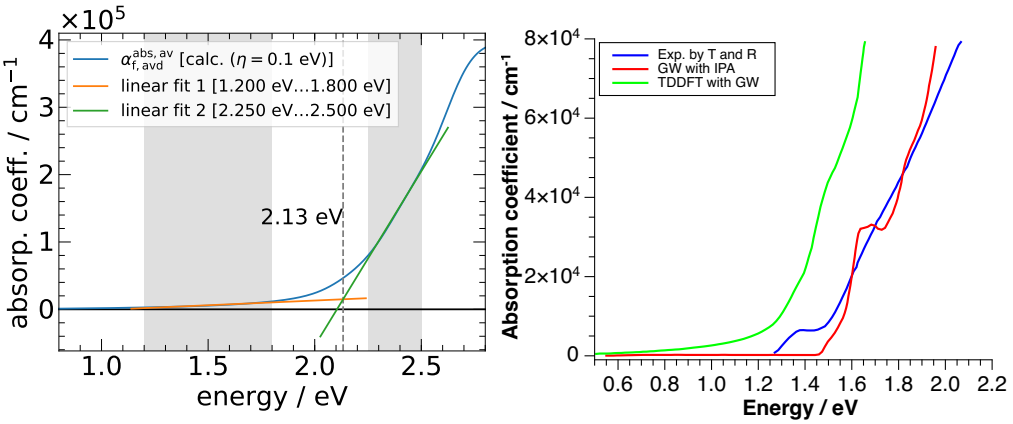

(a) **(b)**

FIGURE 3.29: (a) Determination of the optical absorption gap $E_{\mathrm{g,abs}}$ from the calculated direction-averaged absorption coefficient $\alpha^{\mathrm{abs,av}}_{\mathrm{f,avd}}$ (cf. eq. (3.47)). $E_{\mathrm{g,abs}}$ is obtained from the intersection of two linear fits of (i) the sub-gap absorption tail, and (ii) the region just beyond the absorption gap. The resulting value of 2.13 eV annotates the vertical dashed line. (b) Experimental and calculated absorption coefficients extracted from Wang et al. [88, fig. 2b]. Calculations presented in Ref. [88] are based on the PBE+U method with a value of $U = 5$ eV. The AFM groundstate structure[22] with 16 atoms is assumed. The calculated absorption gap from the GW calculations is 1.46 eV and the experimental value is 1.44 eV (determined at room temperature). *Parameters for the relaxation of atomic positions*: See fig. 3.27. *Parameters for the SCF calculation (density)*: Plane-wave cut-off: 550 eV, a $6 \times 12 \times 6$ **k**-point grid. *Parameters for the calculation of the dielectric tensor (non-SCF)*: 350 bands (valence+conduction), 18 001 points in the energy grid, the broadening parameter for eq. (3.28) is $\eta = 0.1$ eV. The **k**-summation is based on a fine grid $\mathscr{K}(12 \times 24 \times 12)$ (shifted by $\mathbf{b}_{\mathrm{s}} = (0, 1/2, 0)$) generated with a coarse grid $\mathscr{K}_P(4 \times 8 \times 4)$ and $n_{\mathrm{s}} = 27 = 3^3$ shifts ($n_{\mathrm{div}} = 3$).

that they modulate the magnetic exchange.[200,201] That implies that even if a phonon mode of the magnetic superstructure transforms according to some irrep that allows for Raman activity (that would be the "gerade" (g) modes in case of monoclinic CuO), it must *additionally* modulate the magnetic exchange in order to be visible in the Raman spectrum. And indeed, when the transformation properties of the phonon modes under the symmetry operations are investigated, more than just the modes shown in fig. 3.27 are found to transform like A_g, B_g. A detailed analysis if the modes that actually are Raman active modulate the magnetic exchange is not provided at this point.

Determination of the optical absorption gap $E_{\mathrm{g,abs}}$ The optical absorption gap $E_{\mathrm{g,abs}}$ for the AFM groundstate structure of CuO is determined from the direction-averaged optical absorption coefficient in fig. 3.29a. The procedure is the same as in fig. 3.24 with a result of $E_{\mathrm{g,abs}} = 2.13$ eV.

In fig. 3.29b literature results from Wang et al. [88] are shown. They employ GW and time-dependent DFT (TDDFT) calculations as well as experimental techniques to determine $E_{\mathrm{g,abs}}$ from the optical absorption coefficient. It should be remarked that the experimental value of 1.44 eV is the result of a room temperature measurement, while the calculations assume the 16-atom AFM groundstate structure which is valid only below $T_{\mathrm{N}}^{(2)}$.[22,88] The GW value $E_{\mathrm{g,abs}} = 1.46$ eV is in very good agreement with their experimental value. However, based on the thoughts from section 3.4.2.1, the question indeed is, if the GW calculation is very predictive in terms of the optical absorption spectrum. A more realistic approach in this context appears to be the TDDFT calculation which naturally incorporates excitonic effects. The typical red-shift of the absorption spectrum due to the inclusion of excitons is very obvious. However, the absorption spectrum compares worse to the experimental one than in the GW case. This indicates that CuO indeed is a complicated system which remains a crucial test case for electronic structure theory.[88]

From the electronic eigenvalues at the **k**-points used for the BZ integration the smallest direct transition energy from valence to conduction band is 2.06 eV (direct bandgap). This value (slightly) differs from the above determined value of 2.13 eV because the curve in fig. 3.29a is calculated with a broadening value of $\eta = 0.1$ eV.

The calculated value of $E_{\mathrm{g,abs}} = 2.13$ eV must ultimately be compared to the absorption gaps of Masumi

symmetry group. The projection of the inversion centre onto the xy plane is indicated by a (*) in Fig. 12. The A_u modes now have even symmetry with respect to this inversion centre and are, therefore, Raman active." (from Bauhofer et al. [201, p. 5881, 2nd paragraph])

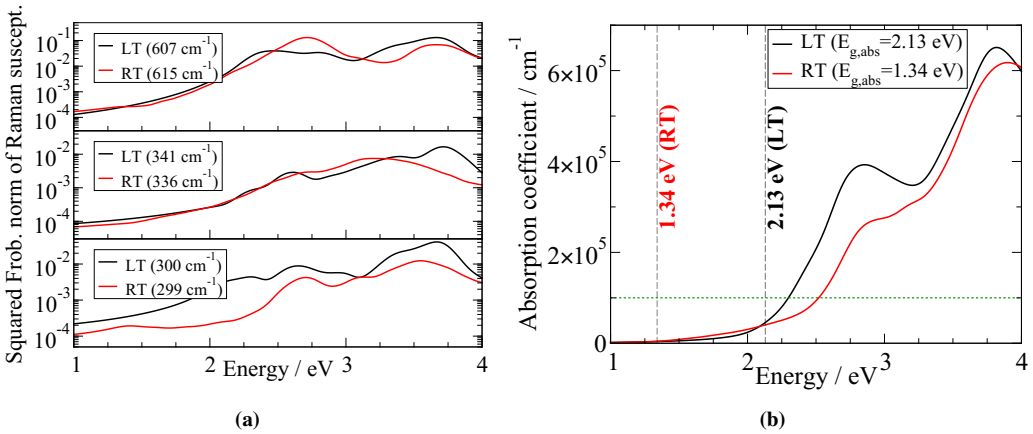

FIGURE 3.30: (a) Raman susceptibilities vs energy (in arb. units) for the Raman active modes from figs. 3.26a and 3.27 that are common to the RT and LT structure of CuO. (b) Direction-averaged absorption coefficients of the RT and the LT structure of CuO. Vertical dashed lines show the optical absorption gaps from figs. 3.24 and 3.29a. The horizontal dashed line indicates an absorption value of $1 \times 10^5\,\mathrm{cm}^{-1}$. *Parameters for the calculation of Raman susceptibilities in (a) for the RT structure*: See fig. 3.26b; *Parameters for the calculation of the absorption coefficient in (b) for the RT structure*: See fig. 3.24. *Parameters for the calculation of Raman susceptibilities in (a) for the LT structure*: Relaxation of atomic positions/calculation of the dynamical matrix at Γ: See fig. 3.27; Parameters for the SCF calculation (density): A plane-wave cut-off of 550 eV, a $6 \times 12 \times 6$ **k**-point grid, a displacement length of 0.01 Å; Parameters for the calculation of the dielectric tensor (non-SCF): 350 bands (valence+conduction), 18 001 points in the energy grid, the broadening parameter for eq. (3.28) is $\eta = 0.1$ eV. The **k**-summation is based on a fine grid $\mathscr{K}\,(12 \times 24 \times 12)$ (shifted by $\mathbf{b}_s = (0, 1/2, 0)$) generated with a coarse grid $\mathscr{K}_P\,(4 \times 8 \times 4)$ and $n_s = 27 = 3^3$ shifts ($n_{\mathrm{div}} = 3$). *Parameters for the calculation of the absorption coefficient in (b) for the LT structure*: See fig. 3.29a.

et al. [202] (1.6 eV from optical absorption at 7 K), and Marabelli et al. [196] (1.67 eV from reflectance and transmittance, extrapolated to 0 K). The deviations of 0.53 eV and 0.46 eV are quite large and must be used as correction values for the calculated optical absorption gap when Raman spectra at different laser excitation energies are considered.

When Raman scattering intensities are computed for different laser excitation energies ω_{L}, the difference $\Delta E_{\mathrm{g,abs}}$ is used to "map" the calculated energy scale to the experimental one. Defining an "effective" laser excitation energy $\omega_{\mathrm{L}}^{\mathrm{eff}} = \omega_{\mathrm{L}} + \Delta E_{\mathrm{g,abs}}$, the Raman susceptibilities are evaluated at corrected energies $(\alpha^m(\omega_{\mathrm{L}}^{\mathrm{eff}}))$ in order to closer resemble the real absorption properties of the material.

3.4.2.3 Comparison of the room temperature and the low temperature structure

In the preceding sections some properties of the room temperature (RT) and the low temperature (LT) structure (AFM groundstate structure[22]) of monoclinic CuO have been discussed. In the following, the differences observed in the Raman scattering properties of both phases are studied.

As remarked earlier, the Raman active modes of the RT structure from fig. 3.26a can be identified as the oxygen-only modes in fig. 3.27 at frequencies $300\,\mathrm{cm}^{-1}$, $341\,\mathrm{cm}^{-1}$ and $607\,\mathrm{cm}^{-1}$ (compared to $299\,\mathrm{cm}^{-1}$, $336\,\mathrm{cm}^{-1}$ and $615\,\mathrm{cm}^{-1}$ for the RT structure).

Indeed, when comparing the determined absorption gaps of both structures (1.34 eV for the RT structure vs 2.13 eV for the LT structure) to the relevant experiments, obviously the RT structures compares nicely while the LT structures yields rather poor results. Apart from $E_{\mathrm{g,abs}}$, the absorption coefficient of the RT structures is in reasonable agreement with the measurements from Tahir and Tougaard [194]. Nevertheless, since results from LDA+U generally show a large dependence on the choice of the U parameter,[100,105] the quality of the agreement should not be overrated but rather considered a convenient incident.

The differences in the electronic structure are obvious from fig. 3.30b, where the absorption coefficients of the RT and the LT structures are shown. As the differences in frequencies are only between $1\,\mathrm{cm}^{-1}$ to $8\,\mathrm{cm}^{-1}$, deviations present in the Raman susceptibilities of both structures (see fig. 3.30a) are most likely due to differing light absorption properties as expressed through, e.g., the absorption coefficient. Obviously, distinct dependencies of α^m on energy of both structures do not necessarily scale with the difference in frequency: Albeit $\omega_{A_g} = 299\,\mathrm{cm}^{-1}$ (RT structure) and $\omega_{A_{g,4}} = 300\,\mathrm{cm}^{-1}$ (LT structure), their Raman susceptibilities are very diverse, not only in terms of absolute value but particularly in terms of dependence on energy. In contrast, differences observable for $B_{g,1}$, $B_{g,4}$ and $B_{g,2}$, $B_{g,6}$ are smaller although their differences in frequency are

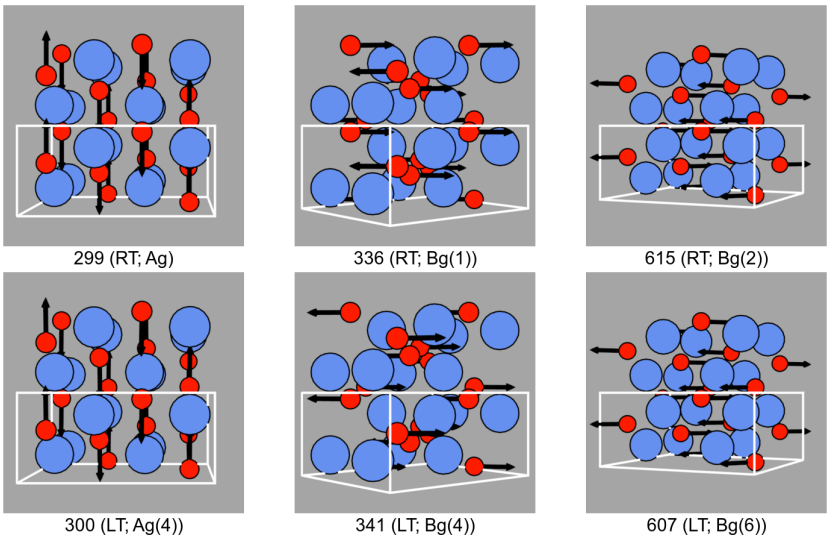

FIGURE 3.31: Visualisation of the phonon modes common to the RT and the LT structure. The displacement pattern of the RT structure (fig. 3.2c) is transformed to the unit cell describing the LT structure (fig. 3.1c). Since here only Γ-modes are considered, this merely implies a translation of the atomic displacement vectors. Based on the lattice vectors for the primitive unit cell ($\mathbf{a}_\mathrm{p}$, $\mathbf{b}_\mathrm{p}$, $\mathbf{c}_\mathrm{p}$) from fig. 3.2c, the lattice vectors of the LT structure are obtained from the linear combinations $\mathbf{a}_\mathrm{p} - \mathbf{b}_\mathrm{p} - \mathbf{c}_\mathrm{p}$, $\mathbf{a}_\mathrm{p} + \mathbf{b}_\mathrm{p}$, $\mathbf{a}_\mathrm{p} - \mathbf{b}_\mathrm{p} + \mathbf{c}_\mathrm{p}$, yielding a unit cell with 4 times the volume of the primitive cell. The frequencies of the modes are printed below the images. The displacement patterns in the middle only differ by a sign which comes from the diagonalisation routine.[203]

larger. A visualisation of the Raman active modes common to both structures ("principal modes") can be found in fig. 3.31.

It was seen in fig. 3.27 that, apart from the modes common to the RT structure, additional modes arise in the LT phase. This is in accordance with experimental measurements below $T_\mathrm{N}^{(2)}$;[24] however, the number of additional modes in the calculation is larger than the number of new modes detected in experiment: 9 calculated vs 5 measured.

In order to capture all Raman active modes *at once*, Raman powder spectra are used in the further discussion. Powder spectra are based on invariants of the Raman tensor (Raman susceptibilities) and are calculated according to (considering only Stokes processes, i.e., *creation* of a phonon):[204]

$$\begin{aligned}\mathscr{I}^m_\mathrm{powder}(\omega_\mathrm{L}) = &\frac{(\omega_\mathrm{L}-\omega_m)^4}{c^4}\frac{n_m(T)+1}{30\omega_m}\\ &\times\left\{[10g_0^m(\omega_\mathrm{L})+4g_2^m(\omega_\mathrm{L})]+[5g_1^m(\omega_\mathrm{L})+3g_2^m(\omega_\mathrm{L})]\right\},\end{aligned} \tag{3.52}$$

with the "tensor invariants"[204]

$$g_0^m = \tfrac{1}{3}|\alpha_{xx}^m+\alpha_{yy}^m+\alpha_{zz}^m|^2 \tag{3.53a}$$

$$g_1^m = \tfrac{1}{2}[|\alpha_{xy}^m-\alpha_{yx}^m|^2+|\alpha_{xz}^m-\alpha_{zx}^m|^2+|\alpha_{zy}^m-\alpha_{yz}^m|^2] \tag{3.53b}$$

$$\begin{aligned}g_2^m = &\tfrac{1}{2}[|\alpha_{xy}^m+\alpha_{yx}^m|^2+|\alpha_{xz}^m+\alpha_{zx}^m|^2+|\alpha_{zy}^m+\alpha_{yz}^m|^2]\\ &+\tfrac{1}{3}[|\alpha_{xx}^m-\alpha_{yy}^m|^2+|\alpha_{xx}^m-\alpha_{zz}^m|^2+|\alpha_{yy}^m-\alpha_{zz}^m|^2],\end{aligned} \tag{3.53c}$$

and the Bose-Einstein distribution function $n_m(T) = [\exp(\omega_m/k_\mathrm{B}T)-1]^{-1}$. A "Raman spectrum" is obtained by introducing a broadening function $\delta_\zeta(\omega-\omega_0) = \mathrm{Im}\{\pi[(\omega-\omega_0)+i\zeta]\}^{-1} = \pi^{-1}\zeta/[(\omega-\omega_0)^2+\zeta^2]$ that is normalised like $\int_\mathbb{R} dx\ \delta_\zeta(x) = 1$:

$$\mathscr{I}_\mathrm{powder}(\omega;\omega_\mathrm{L}) = \sum_m \mathscr{I}^m_\mathrm{powder}(\omega_\mathrm{L})\delta_\zeta(\omega-\omega_m). \tag{3.54}$$

In fig. 3.32 (normalised) powder spectra $\mathscr{I}_\mathrm{powder}$ are shown for the RT (left) and the LT (right) structure. Calculated and experimental[24] peak positions are indicated for comparison. Obviously, all additional experimental frequencies that emerge in the Raman spectrum at low temperatures[24] have a calculated counterpart from the LT structure: 175 cm^{-1} and 178 cm^{-1}, 218 cm^{-1} and 213 cm^{-1}, 240 cm^{-1} and 241 cm^{-1}, 331 cm^{-1} and 313 cm^{-1}, 508 cm^{-1} and 500 cm^{-1}. Even though the calculated $B_{g,3}$ mode at 313 cm^{-1} is 18 cm^{-1} away from the measured frequency at 331 cm^{-1}, it is located (see the small shoulder for $\lambda_\mathrm{L} = 568$ nm in the right plot) directly between the $A_{g,4}$, $B_{g,4}$ modes (which are also common to the RT structure). Indeed,

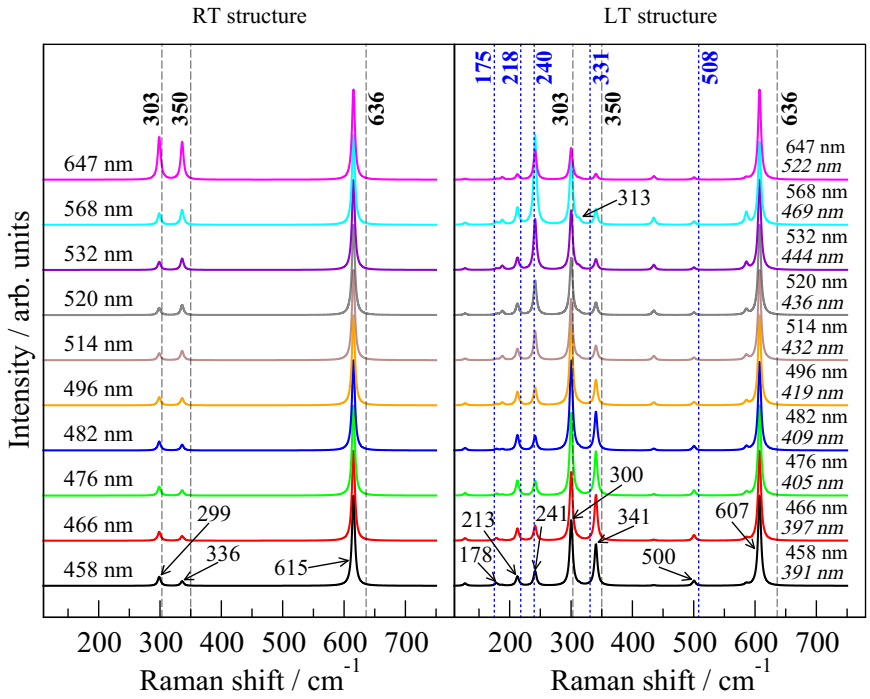

FIGURE 3.32: Raman powder spectra for the RT (left) and the LT (right) structure. Each spectrum is normalised to the maximum intensity such that the change in relative intensities with the laser wavelengths is the only relevant quantity. Different laser wavelengths λ_L are used as indicated in the plots. For the LT structure an absorption gap correction of 0.46 eV[196] is used and the corresponding values of λ_L^{eff} are listed below those of λ_L in the right plot (slanted font). Calculated mode frequencies (in cm^{-1}) of the main peaks are shown by arrows in the plots. Experimental frequencies (in cm^{-1}) are indicated by annotated vertical lines (bold face numbers).[24] The frequencies of modes that appear at low temperatures (below $T_N^{(2)}$) are printed in blue, while those already present at RT are printed in black. *Parameters for the calculations*: See fig. 3.30. *Parameters for the calculation of the Raman intensities*: Temperature $T = 298$ K, broadening for the spectra $\zeta = 2.9\,\text{cm}^{-1}$ (mean value from table 3.4).

from fig. 3.28a, this obviously is also the case in the measured spectrum, thereby justifying the assignment of the calculated and the measured mode.

The main peaks in the experimental spectrum from fig. 3.28a are related to the modes at $240\,\text{cm}^{-1}$, $303\,\text{cm}^{-1}$, $350\,\text{cm}^{-1}$ and $636\,\text{cm}^{-1}$. The corresponding calculated modes also have the largest intensities in the calculated powder spectra. However, since the experimental measurements are for a single crystal, the relative intensities cannot be directly compared. The additional peaks from the calculations produce quite small peaks in the powder spectra, irrespective of the applied laser wavelengths. It therefore appears that this might be the reason why they are not detected in experiment. It is true, nonetheless, that the intensities found for modes at $175\,\text{cm}^{-1}$ and $500\,\text{cm}^{-1}$ (which have an experimental counterpart) are of the same order as for the peaks not visible in experiment. Taking into account the number of approximations involved in the calculations [e.g., neglect of excitons, neglect of resonant terms in the equation of the Raman susceptibilities (see, e.g. Gillet [12, Appendix A])], these "irregularities" can be considered to be within the error of the methods at use.

The Raman powder spectra of the RT structure are dominated by the $B_{g,2}$ mode at $615\,\text{cm}^{-1}$ for all laser wavelengths. The modes at frequencies $299\,\text{cm}^{-1}$ and $336\,\text{cm}^{-1}$ only have $\lesssim 10\,\%$ of the maximal peak height, and their intensities are interchanged when the laser wavelength is decreased (from bottom to top).

Although the powder spectra of the LT structure as well are dominated by the $B_{g,6}$ mode at $607\,\text{cm}^{-1}$, more variation of the relative peak heights is observable below $350\,\text{cm}^{-1}$: The relative peak heights of the modes at $300\,\text{cm}^{-1}$ and $341\,\text{cm}^{-1}$ (the modes also found for the RT structure) systematically change in favour of the $300\,\text{cm}^{-1}$ mode when λ_L is increased. The $A_{g,3}$ mode at $241\,\text{cm}^{-1}$ shows the opposite behaviour upon decreasing λ_L, and considerably gains intensity compared to the other Raman active modes.

As a final point of this section, the nature of the extra modes found in the Raman spectrum is elucidated in more detail. Obviously, the unit cell describing the LT structure (fig. 3.2b) has four times the volume of the RT structure (fig. 3.2c). Based on the AFM ordering used for the RT structure (one atom "spin up", the

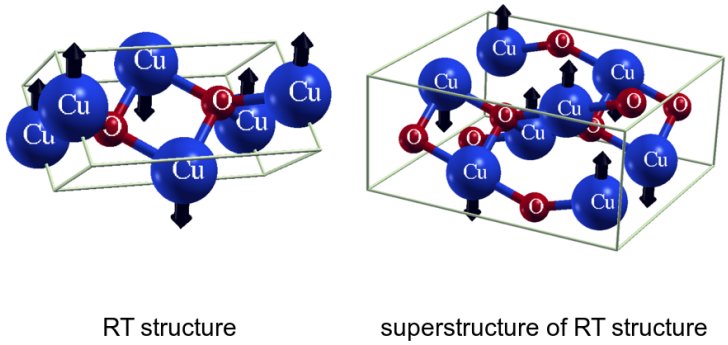

FIGURE 3.33: Relation between the (primitive) RT structure from fig. 3.2c and a supercell with the same volume as the LT structure from fig. 3.2b. Magnetic moments are shown as black arrows and are taken along the monoclinic **b**-axis ($\parallel$ **y**). Note that the AFM ordering necessarily is the same as in case of the RT structure and as such is different from the AFM groundstate ordering. The connection between the generating lattice vectors (in real space) of the structures is given in fig. 3.31.

other "spin down"), a unit cell with the *same* volume as the unit cell of the LT structure but with a magnetic ordering *different* from that of the AFM groundstate can be constructed. This scenario is shown in fig. 3.33

Since the superstructure is a periodic repetition of the RT structure, several (3 in this case) non-zero wavevectors will "fold" to the Γ-point of the superstructure in reciprocal space. The two generating lattices in real space of the RT structure and its superstructure are related by the linear combination matrix $((1,-1,-1),(1,1,0),(1,-1,1))$ (to be read row-wise; see caption of fig. 3.31). It follows that the four wavevectors commensurable with the superstructure are $\mathbf{q}_1 = (0,0,0), \mathbf{q}_2 = (1/2,1/2,0), \mathbf{q}_3 = (1/4,3/4,1/2), \mathbf{q}_4 = (3/4,1/4,1/2)$, where the components of the wavevectors refer to the reciprocal lattice vectors of the RT structure (primitive unit cell). The wavevectors $\mathbf{q}_3, \mathbf{q}_4$ are related by a 2-fold rotation about the **y**-axis and therefore deliver the same phonon frequencies. In some cases it is rather common to express the wavevectors in terms of the reciprocal lattice vectors of a *conventional* unit cell in real space. For monoclinic CuO this cell is given by Åsbrink and Norrby [106] and is depicted in fig. 3.2a. With respect to this reciprocal basis, the wavevectors $\mathbf{q}_2, \mathbf{q}_3$ read $(0,1,0), (-1/2,1,1/2)$. Since the translational equivalents of the wavevectors $\mathbf{q}_2, \mathbf{q}_3$ can equally well be chosen as commensurable wavevectors (particularly, in the primitive basis: $\mathbf{q}_2 = (1/2,1/2,0) \equiv (\pm 1/2, \pm 1/2, 0)$), the components with respect to the conventional basis can also be written $X = (1,0,0), A = (\pm 1/2, 0, \pm 1/2)$, where the labelling from Kuz'menko et al. [174, tab. III] is adopted.[xi] These are the candidate wavevectors which may give rise to the additional Raman active modes.

In table 3.5 the Raman and infra-red active modes of the LT structure of CuO are correlated with phonon modes form the Γ, X points of the RT structure. Indeed, all additional ("extra") Raman and infra-red active modes found for the LT structure originate from the X-point. The twelve vibrational modes introduced at the Γ-point of the LT structure split into nine extra Raman modes and three extra infra-red active modes, leading to the irreps $[A_g \oplus 2B_g]_{\text{principal}} \oplus [5A_g \oplus 4B_g]_{\text{extra}}$ (Raman), and $[3A_u \oplus 3B_u]_{\text{principal}} \oplus [2A_u \oplus B_u]_{\text{extra}}$ (infra-red). Chen et al. [24] and Kuz'menko et al. [174] suggested that the extra Raman active modes closely resemble frequencies from the X-point measured with inelastic neutron scattering by Reichardt et al. [163]. Kuz'menko et al. [174] have measured extra infra-red active modes. Most of these were correlated with phonon frequencies from the A-point of the RT structure. However, calculated mode frequencies of the LT structure related to the A-point are neither Raman active nor infra-red active. The measurements of Kuz'menko et al. [174] have further revealed that some extra infra-red active modes are also present at 300 K and all the way down to low temperatures (7 K). This is clearly *not* the case for the Raman active modes. Therefore, measurements of Raman and infra-red activities cannot be fully reconciled.

Generally, agreement between calculated and measured mode frequencies is reasonably good. This particularly holds in case of the Raman active modes, for the principal as well as for the extra modes. Differences are larger for the high-frequency infra-red active modes. However, experimental frequencies for the $A_{u,3}, B_{u,2}, B_{u,3}$ (irrep labels refer to the RT structure) have spreads of at least 60 cm^{-1}, and the calculated frequencies are either within the measured frequency range or ~10 cm^{-1} to 15 cm^{-1} away from the lower bound.

[xi] The components $(1/2,-1/2,0)$ in the primitive basis lead to the components $(1,0,0)$ in the conventional basis.

LT structure			RT (super)structure (fig. 3.33)			Literature (ω_m)	
irrep	activity	ω_m	irrep	ω_m	wavevector	calculated	measured
$A_{g,4}$ (p)	Raman	300	A_g	299	Γ	319[a]	296;[a] 303[b,e]
$B_{g,4}$ (p)		341	$B_{g,1}$	336	Γ	382[a]	346;[a] 350[b,e]
$B_{g,6}$ (p)		607	$B_{g,2}$	615	Γ	639[a]	631;[a] 636[b,e]
$A_{g,1}$ (e)		127		128	X (Y)	–	–
$A_{g,2}$ (e)		213		211	X (Y)	–	218;[b] 220[f]
$A_{g,3}$ (e)		241		249	X (Y)	–	240;[b] 243[f]
$A_{g,5}$ (e)		500		496	X (Y)	–	508;[b] 513[f]
$A_{g,6}$ (e)		586		587	X (Y)	–	–
$B_{g,1}$ (e)		178		174	X (Y)	–	175;[b] 177[f]
$B_{g,2}$ (e)		188		185	X (Y)	–	–
$B_{g,3}$ (e)		313		314	X (Y)	–	331;[b] 330[f]
$B_{g,5}$ (e)		435		420	X (Y)	–	–
$A_{u,1}$ (p)	infra-red	166	$A_{u,1}$	162	Γ	164[a]	160–168;[c] 163[d]
$A_{u,2}$ (p)		304	$A_{u,2}$	303	Γ	327[a]	321–326;[c] 324[d]
$A_{u,4}$ (p)		438	$A_{u,3}$	428	Γ	457[a]	409–478;[c] 379[d]
$B_{u,1}$ (p)		150	$B_{u,1}$	148	Γ	141[a]	142–150;[c] 147[d]
$B_{u,3}$ (p)		471	$B_{u,2}$	459	Γ	503[a]	470–530;[c] 481[d]
$B_{u,4}$ (p)		505	$B_{u,3}$	511	Γ	568[a]	520–590;[c] 536[d]
$A_{u,3}$ (e)		367		362	X (Y)	–	–
$A_{u,5}$ (e)		521		522	X (Y)	–	–
$B_{u,2}$ (e)		393		391	X (Y)	–	–

[a] Debbichi et al. [118]
[b] Chen et al. [24]
[c] Reichardt et al. [163], Kliche and Popovic [168], Guha et al. [170, 171], Narang et al. [172], Homes et al. [173], and Kuz'menko et al. [174] (77 K[172] and 300 K)
[d] Kuz'menko et al. [174] at 7 K
[e] Chrzanowski and Irwin [161]
[f] Reichardt et al. [163] (neutron scattering at X; see Kuz'menko et al. [174, tab. III])

TABLE 3.5: Correlation of the Raman and infra-red active modes (TO only) of the LT structure with the AFM groundstate ordering (fig. 3.1c) with modes from the supercell of the RT structure (fig. 3.33). Frequencies (in cm^{-1}) are ordered according to their activity (Raman or infra-red) and their irreps. The label in braces behind the irreps of the LT structure indicates whether the respective mode also is a Γ mode of the RT structure ("principal mode"), or if it occurs at a non-zero wavevector ("extra mode"). In case of the RT structure, only irreps for the principal modes are given. Since the $X(Y)$-point also has C_{2h} symmetry, the irreps of the extra modes originating from this wavevector necessarily are the same as that of the corresponding Γ modes of the LT structure. The Y-point refers to $(\pm 1/2, \pm 1/2, 0)$ in the basis of the reciprocal lattice of the primitive RT structure. The coordinates of the X-point are $(1, 0, 0)$ in the basis of the reciprocal lattice of the conventional unit cell.[106] *Parameters for the calculation of the phonon frequencies of the RT superstructure*: See fig. 3.26a.

As an example, the calculated extra Raman active modes of the LT structure and related modes from the X-point of the RT structure are shown in fig. 3.34.

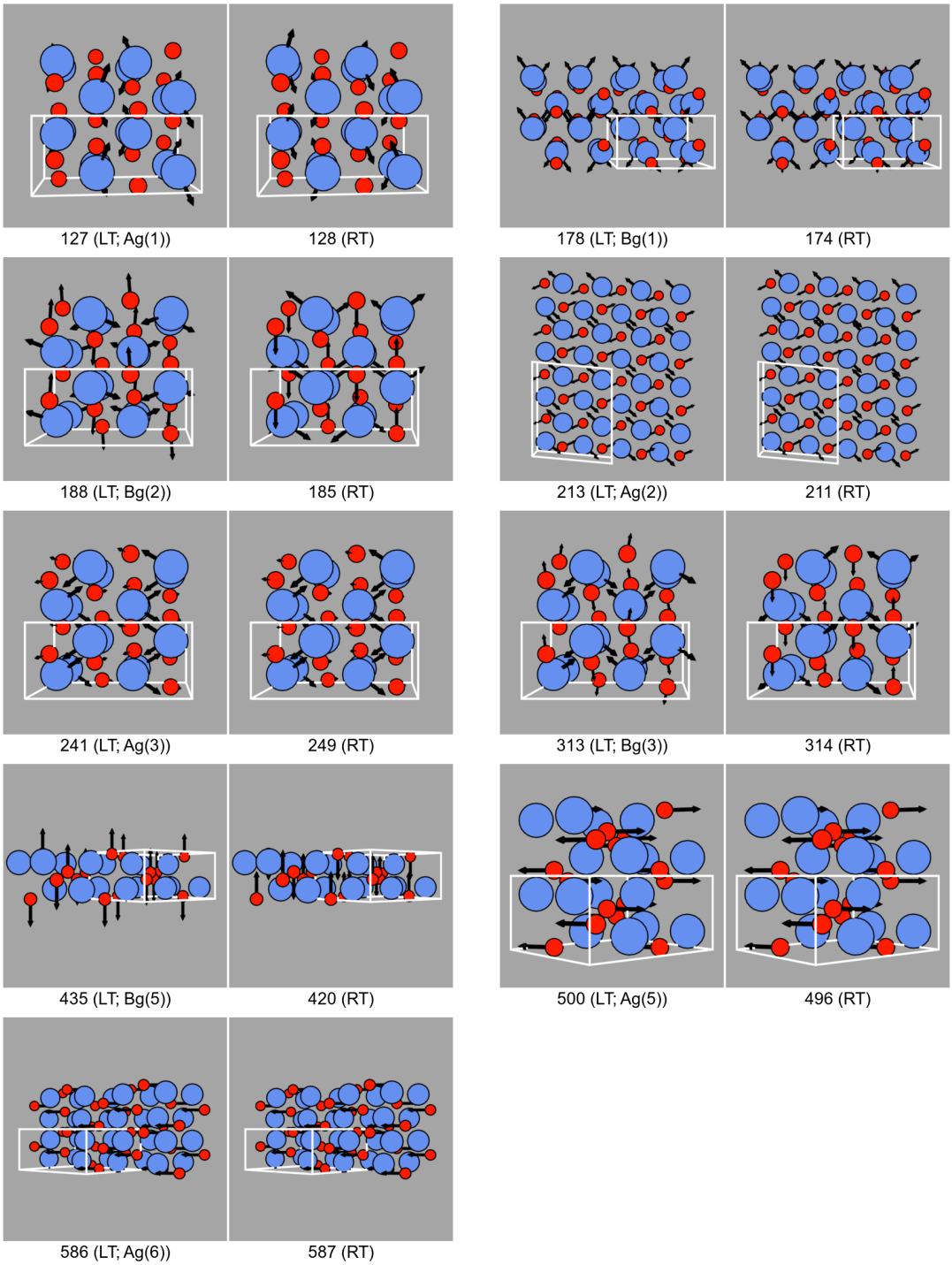

FIGURE 3.34: Visualisation of the (calculated) extra Raman active modes of the LT structure and related modes from the RT superstructure (see fig. 3.33) at the X-point. For a complete listing of the modes of the LT structure and their relation to modes of the RT structure see table 3.5.

3.4.3 Raman scattering in Cu_4O_3

While the monoclinic CuO phase of copper oxides is rather well studied in terms of its Raman spectroscopic properties,[xii] only few articles deal with Raman scattering in tetragonal Cu_4O_3.[23,118] This section is dedicated to the analysis of the Raman active modes and their light scattering properties.

Experimentally grown Cu_4O_3 samples Cu_4O_3 (paramelaconite) was discovered in 1870 as a mineral in the Copper Queen mine located at Bisbee (Arizona, US).[23] A first crystallographic determination of its structure was done by Frondel [205], and another by O'Keeffe and Bovin [119]. In recent years the method of choice for producing thin films of Cu_4O_3 has been sputter deposition (see Meyer et al. [23], Pierson et al. [114, 115], and Debbichi et al. [118]). The preferential orientations of these films are (i) (110) (Meyer et al.

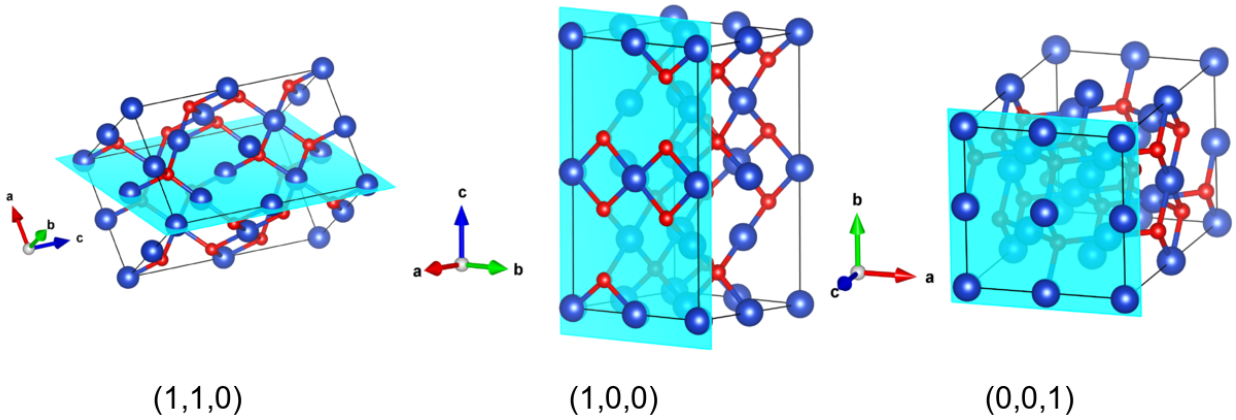

FIGURE 3.35: Lattice planes of the *conventional* cell of Cu_4O_3 corresponding to the preferential orientations found in Refs. [23, 114].

[23]), (ii) (100) and (001) (Pierson et al. [114]). The corresponding lattice planes are depicted in fig. 3.35.

Determination of the optical absorption gap $E_{g,abs}$ In fig. 3.36a the calculated optical absorption gap of Cu_4O_3 is determined to be $E_{g,abs} = 1.74\,eV$. Compared to 1.5 eV and 1.37 eV form Meyer et al. [23] and Wang et al. [88], this implies differences of $\Delta E_{g,abs} = 0.24\,eV$ and 0.37 eV, respectively (see figs. 3.36b and 3.36c). Therefore, agreement is slightly better than in case of the AFM groundstate structure of CuO (fig. 3.29a). The unbroadened, direction-averaged absorption coefficient is depicted in fig. 3.37: Two energies, 1.45 eV and 1.85 eV, are indicated by vertical lines. The first energy corresponds to the *smallest direct transition energy between valence and conduction band* as determined from the **k**-points used for the BZ integration. Absorption indeed is very small directly above this energy while it is much larger (10^3 to 10^4 times) beyond 1.85 eV. Therefore, the energy value of 1.85 eV is interpreted as a "true" absorption threshold. The value of 1.74 eV determined for $E_{g,abs}$ in fig. 3.36a closely resembles the second absorption threshold; the values differ because the curve in fig. 3.36a is broadened. The first absorption onset at 1.45 eV is smeared out through the broadening of $\eta = 0.1\,eV$.

Effective laser excitation energies corresponding to some "typical" laser energies are summarised in table 3.6.

From the scales in figs. 3.36b and 3.36c it is inferred that the measured optical absorption of Wang et al. [88] is much larger in the sub-gap region than the optical absorption of Meyer et al. [23]. Phonon-assisted absorption via a small indirect band gap (particularly at finite temperatures) as well as excitons are considered as likely reasons for such large absorption at low energies.[88] Compared to experiment,[88] the *GW* method performs worse than the TDDFT calculation which naturally includes excitonic effects. This causes a red-shift of about 150 meV[88] (compared to *GW*) and brings the thus determined absorption coefficient quite close to the measured values. Indeed, this might suggest the necessity of accounting for excitonic effects in calculations of optical spectra for Cu_4O_3.

[xii] 23, 24, 112, 118, 161, 164, 166, 169–171, 176.

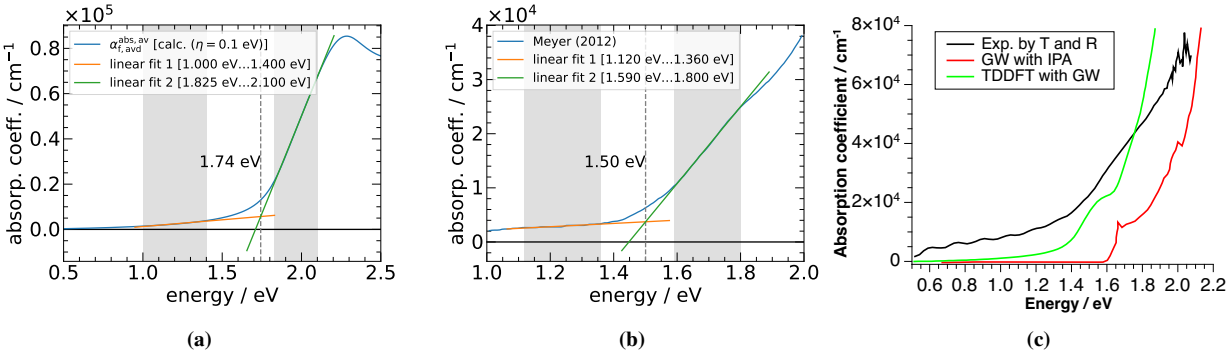

FIGURE 3.36: (a) Determination of the optical absorption gap $E_{g,abs}$ from the calculated direction-averaged absorption coefficient $\alpha^{abs,av}_{f,avd}$ (cf. eq. (3.47)). $E_{g,abs}$ is obtained from the intersection of two linear fits of (i) the sub-gap absorption tail, and (ii) the region just beyond the absorption gap. The resulting value of 1.74 eV annotates the vertical dashed line. (b) Determination of the optical absorption gap $E_{g,abs}$ from the absorption coefficient of Meyer et al. [23]. The procedure is the same as in (a). The resulting value of 1.50 eV annotates the vertical dashed line.
(c) Experimental and calculated absorption coefficients from Wang et al. [88, fig. 2a]. Calculations presented in Ref. [88] are based on the PBE+U method with a value of $U = 5$ eV. The experimental absorption gap of 1.37 eV is derived from the intersection of the linear fits of the two absorption regimes. $E_{g,abs} = 1.61$ eV from the *GW* calculation. *Parameters for the relaxation of atomic positions*: See fig. 3.38. *Parameters for the SCF calculation (density)*: Plane-wave cut-off: 550 eV, a $8 \times 8 \times 8$ **k**-point grid. *Parameters for the calculation of the dielectric tensor (non-SCF)*: 350 bands (valence+conduction), 18 001 points in the energy grid, the broadening parameter for eq. (3.28) is $\eta = 0.1$ eV. The **k**-summation is based on a fine grid $\mathscr{K}(16 \times 16 \times 16)$ generated with a coarse grid $\mathscr{K}_P(4 \times 4 \times 4)$ and $n_s = 64 = 4^3$ shifts ($n_{div} = 4$).

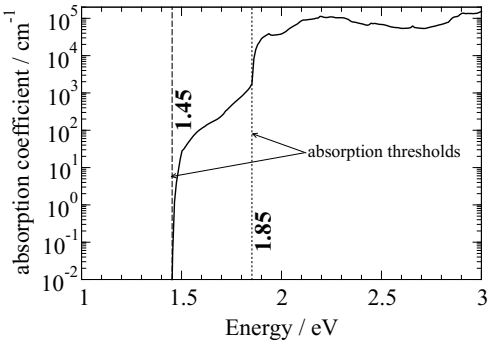

FIGURE 3.37: Unbroadened absorption coefficient calculated with the tetrahedron method. Two different absorption onsets (thresholds) are marked by the vertical lines. Only the second value of 1.85 eV is retained when the dielectric function is broadened like in fig. 3.36a. *Parameters for the calculations*: See fig. 3.36a.

		λ_L^{eff} (ω_L^{eff})	
Spectral range	λ_L (ω_L)	$\Delta E_{g,abs}$(exp) = 0.24 eV[23]	$\Delta E_{g,abs}$(exp) = 0.37 eV[88]
UV	244 (5.08)	233 (5.32)	227 (5.45)
	257 (4.82)	245 (5.06)	239 (5.19)
	325 (3.81)	306 (4.05)	296 (4.18)
	364 (3.41)	340 (3.65)	328 (3.78)
Visible	457 (2.71)	420 (2.95)	402 (3.08)
	473 (2.62)	433 (2.86)	414 (2.99)
	488 (2.54)	446 (2.78)	426 (2.91)
	514 (2.41)	467 (2.65)	446 (2.78)
	532 (2.33)	482 (2.57)	459 (2.70)
	633 (1.96)	564 (2.20)	532 (2.33)
	660 (1.88)	585 (2.12)	551 (2.25)
Near IR	785 (1.58)	681 (1.82)	636 (1.95)
	830 (1.49)	715 (1.73)	665 (1.86)
	980 (1.27)	824 (1.51)	758 (1.64)
	1064 (1.17)	882 (1.41)	808 (1.54)

TABLE 3.6: Typical Raman laser wavelengths (λ_L) in the UV/visible/near infra-red (IR) range of the electromagnetic spectrum (`http://www.horiba.com/scientific/products/raman-spectroscopy/raman-academy/raman-faqs/what-laser-wavelengths-are-used-for-raman-spectroscopy/`). The "effective laser energy" $\omega_L^{eff} = \omega_L + \Delta E_{g,abs}$ is calculated with $\Delta E_{g,abs} = E_{g,abs}(\eta = 0.1\,\text{eV}) - E_{g,abs}(\text{exp})$ and $E_{g,abs}(\eta = 0.1\,\text{eV}) = 1.74$ eV (see fig. 3.36b). The experimental values for $E_{g,abs}$ are 1.5 eV and 1.37 eV for Meyer et al. [23] and Wang et al. [88], respectively. Units for λ_L (λ_L^{eff}): nm; units for ω_L (ω_L^{eff}): eV.

Raman active modes The decomposition of Raman active modes in tetragonal Cu_4O_3 in terms of the contribution of certain "types" of atoms is shown in fig. 3.38. Cu_4O_3 has space group symmetry D_{4h}^{19} and four different types of atoms in the unit cell: Cu(I) at Wyckhoff 8*c* (C_{2h} symmetry), Cu(II) at Wyckhoff 8*d* (C_{2h} symmetry), O(1) at Wyckhoff 8*e* (C_{2v} symmetry), and O(2) at Wyckhoff 4*b* (D_{2d} symmetry).[206] The

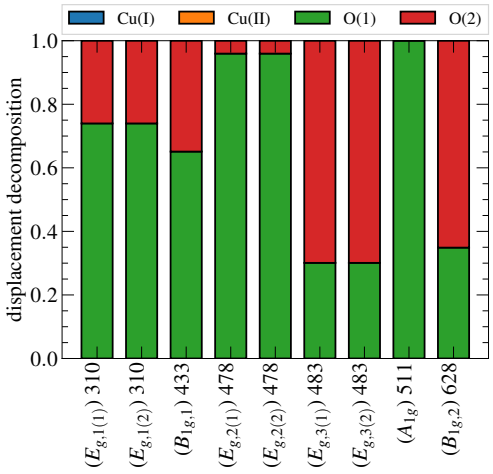

FIGURE 3.38: Decomposition of the (squared) norm of the mode displacement vectors ($|\mathbf{u}_m|^2$) in terms of contributions from Cu and O atoms. Only Raman active modes are shown. The frequencies (in cm^{-1}) are listed with the symbols of the irreps. For Cu_4O_3 with space group D_{4h}^{19} ($I4_1/amd$, No. 141), four "types" of atoms can be distinguished by their local symmetry: Cu(I) at Wyckhoff 8*c* (C_{2h} symmetry), Cu(II) at Wyckhoff 8*d* (C_{2h} symmetry), O(1) at Wyckhoff 8*e* (C_{2v} symmetry), and O(2) at Wyckhoff 4*b* (D_{2d} symmetry).[206] *Parameters for the relaxation of atomic positions/calculation of the dynamical matrix at* Γ: Plane-wave cut-off: 800 eV, a $8\times8\times8$ **k**-point grid, a displacement length of 0.01 Å.

contribution due to each atom type is given in fig. 3.38. Obviously, only oxygen atoms are involved in the atomic vibration patterns that allow for Raman activity. Which kind of oxygen atom dominates (O(1) or O(2)), depends on the respective mode. Only in case of the totally symmetric A_{1g} mode solely the O(1) atoms constitute the vibrational pattern.

The D_{4h} point group is isomorphic to the factor group of the D_{4h}^{19} space group. A factor group analysis yields the Raman active modes $A_{1g} \oplus 2B_{1g} \oplus 3E_g$.[23] Choosing the 4-fold rotation axis of the D_{4h} point group along the **z**-axis of an orthogonal (**x**, **y**, **z**) coordinate system, yields Raman tensors of the generic form[23]

$$\mathscr{R}^{A_{1g}} = \begin{pmatrix} a & 0 & 0 \\ 0 & a & 0 \\ 0 & 0 & b \end{pmatrix}, \quad \mathscr{R}^{B_{1g}} = \begin{pmatrix} c & 0 & 0 \\ 0 & -c & 0 \\ 0 & 0 & 0 \end{pmatrix}, \quad \mathscr{R}^{E_{g(1)}} = \begin{pmatrix} 0 & 0 & e \\ 0 & 0 & 0 \\ e & 0 & 0 \end{pmatrix}, \quad \mathscr{R}^{E_{g(2)}} = \begin{pmatrix} 0 & 0 & 0 \\ 0 & 0 & e \\ 0 & e & 0 \end{pmatrix}. \tag{3.55}$$

Since the E_g modes are 2-fold degenerate, the eigenvectors $\mathbf{w}_{E_{g(1)}}, \mathbf{w}_{E_{g(2)}}$ can be chosen arbitrarily in the degenerate subspace belonging to the respective eigenvalue. In a numerical calculation, the eigenvalue routine[203] will generally not return the eigenvectors in a form suitable for the above (eq. (3.55)) generic Raman tensors. Then, suitable linear combinations $\gamma_1\mathbf{w}_{E_{g(1)}} + \gamma_2\mathbf{w}_{E_{g(2)}}$ ($\gamma_{1,2} \in \mathbb{C}$) must be found in order to get the tabulated form of the $\mathscr{R}^{E_g}$'s.

Energy dependence of the Raman scattering intensity Before addressing Raman scattering properties of particular crystal surfaces (crystal orientations) of Cu_4O_3, the general energy dependence of the Raman intensities will be discussed.

In order not to limit the discussion to a specific mode of $A_{1g} \oplus 2B_{1g} \oplus 3E_g$, Raman powder intensities $\mathscr{I}^m_{\text{powder}}$, that include averages over all possible orientations of the crystal, are adducted for the discussion. Irrespective of the relative intensities, all modes allowing for Raman activity in principle are visible in the Raman spectrum.

The dependence of the Raman powder spectrum on λ_L is portrayed in fig. 3.39a. The laser wavelengths are λ_L = 660 nm, 633 nm, 532 nm, 514 nm and 488 nm with an absorption gap correction of 0.37 eV.[88] In the figure, each spectrum is normalised to its maximum intensity, so that the only relevant quantities in this case are the relative mode intensities. For the two smallest laser wavelengths the totally symmetric A_g mode at 511 cm^{-1} clearly dominates the Raman spectrum. The only mode visible apart from the A_g mode is the 2-fold degenerate $E_{g,3}$ mode at 483 cm^{-1}. At larger values of λ_L the $E_{g,1}, E_{g,3}$ modes have intensities comparable to that of the A_{1g} mode. This observation can be understood from fig. 3.39b. Therein, the Raman powder intensity $\mathscr{I}^m_{\text{powder}}$ for the Raman active modes from fig. 3.38 is shown as a function of energy. The (effective) laser wavelengths used in fig. 3.39a are indicated by vertical lines. For smaller energies (below 2.2 eV), the powder intensities of the A_{1g} mode and the E_g modes are well separated. While $\mathscr{I}^m_{\text{powder}}$ increases rather monotonically for $E_{g,1}, E_{g,3}$ between 2 eV to 3 eV, the A_g intensity assumes a local minimum in this energy range. At λ_L = 532 nm, 514 nm and 488 nm the intensities of $E_{g,1}, E_{g,3}$ are very close and only slightly below that of the A_{1g} mode. However, since $\mathscr{I}^m_{\text{powder}}$ is the *same* for $E_{g(1)}$ and $E_{g(2)}$ (see eq. (3.55)), and since the intensity of the 2-fold degenerate E_g counts *twice* in the Raman spectrum at 310 cm^{-1}, 478 cm^{-1} and

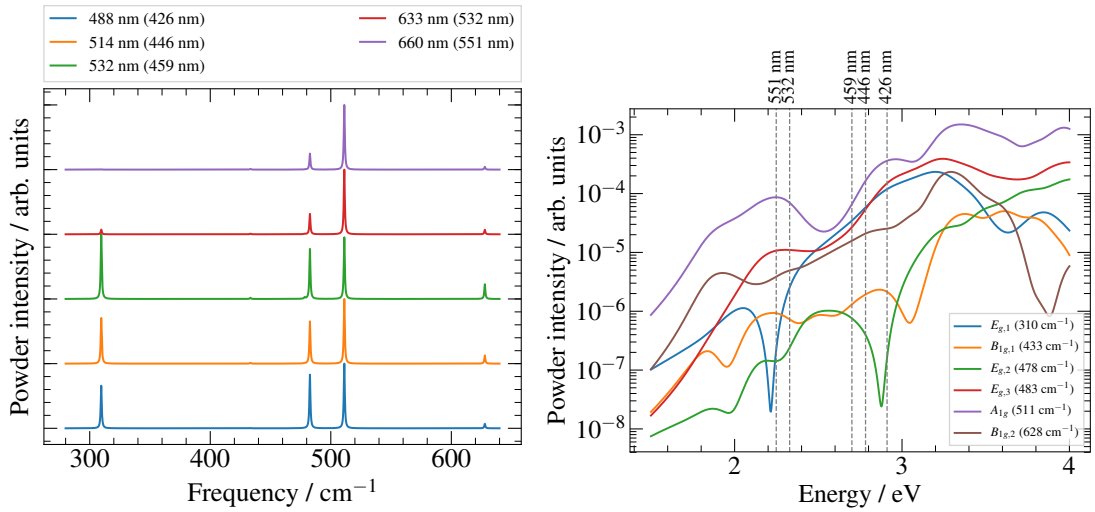

(a) **(b)**

FIGURE 3.39: (a) Raman powder spectra for laser wavelengths $\lambda_L = 660\,\text{nm}$, 633 nm, 532 nm, 514 nm and 488 nm. An absorption gap correction of $\Delta E_{g,abs} = 0.37\,\text{eV}$[88] is used and the corresponding values of λ_L^{eff} are given in braces. Each spectrum is normalised to the maximum intensity. Therefore, the relative intensity is the only relevant quantity in this case. (b) Raman powder intensities $\mathscr{I}^{m}_{\text{powder}}$ for the Raman active mode from fig. 3.38 as a function of energy. The effective laser wavelengths from (a) are indicated by the vertical dashed lines and the values are annotated at the top of the figure. Since for each 2-fold degenerate E_g mode the intensity for $E_{g(1)}$ and $E_{g(2)}$ is the *same* for all energies, only one graph is shown for each of the three E_g modes. *Parameters for the relaxation of atomic positions/calculation of the dynamical matrix at* Γ: See fig. 3.38. *Parameters for the SCF calculation (density)*: A plane-wave cut-off of 550 eV, a $8 \times 8 \times 8$ **k**-point grid, a displacement length of 0.01 Å. *Parameters for the calculation of the dielectric tensor (non-SCF)*: 350 bands (valence+conduction), 18 001 points in the energy grid, the broadening parameter for eq. (3.28) is $\eta = 0.1\,\text{eV}$. The **k**-summation is based on a fine grid $\mathscr{K}(16 \times 16 \times 16)$ generated with a coarse grid $\mathscr{K}_P(4 \times 4 \times 4)$ and $n_s = 64 = 4^3$ shifts ($n_{\text{div}} = 4$). *Parameters for the calculation of the Raman intensities*: Temperature $T = 298\,\text{K}$, broadening for the spectra in (a) $\zeta = 0.5\,\text{cm}^{-1}$.

$483\,\text{cm}^{-1}$, the intensities of some E_g modes indeed can exceed that of the A_g mode (or at least can be of comparable magnitude). This is the case for $\lambda_L = 532\,\text{nm}$ in fig. 3.39a, although admittedly the difference is very small.

Angular dependence of the Raman scattering intensity Owing to the tensor nature of the $\mathscr{R}^m$'s, the Raman scattering intensity of each mode in general depends on the orientation of the crystal (characterised by Miller's indices (hkl)) with respect to the incoming laser beam.

Each crystal surface (or likewise lattice plane) is characterised by a surface normal vector $\hat{\mathbf{n}}_{\text{surf}}$ which is orthogonal to any vector lying in the surface. Therefore, this normal vector can be constructed from the indices (hkl) according to

$$\hat{\mathbf{n}}_{\text{surf}} \equiv \hat{\mathbf{n}}^{(hkl)}_{\text{surf}} = (h\mathbf{g}_1 + k\mathbf{g}_2 + l\mathbf{g}_3)/|h\mathbf{g}_1 + k\mathbf{g}_2 + l\mathbf{g}_3|\,, \tag{3.56}$$

where $\{\mathbf{g}_i\}_{i=1,2,3}$ are reciprocal lattice vectors of the crystal structure. Based on the surface normal vector, each crystal surface can be assigned a local, orthonormal coordinate system $\mathbf{x}_{\text{loc}}, \mathbf{y}_{\text{loc}}, \mathbf{z}_{\text{loc}}$ with $\mathbf{x}_{\text{loc}} \parallel \hat{\mathbf{n}}_{\text{surf}}$:

$$\mathbf{x}_{\text{loc}} = (\sin\theta\cos\varphi, \sin\theta\sin\varphi, \cos\theta) \tag{3.57a}$$
$$\mathbf{y}_{\text{loc}} = (\cos\theta\cos\varphi, \cos\theta\sin\varphi, -\sin\theta) \tag{3.57b}$$
$$\mathbf{z}_{\text{loc}} = (-\sin\varphi, \cos\varphi, 0), \tag{3.57c}$$

with $\theta = \arccos(x^{(3)}_{\text{loc}})$, $\varphi = \text{atan2}(x^{(2)}_{\text{loc}}, x^{(1)}_{\text{loc}})$.

The polarisation vectors $\mathbf{e}_{\text{in}}, \mathbf{e}_{\text{out}}$ ("in": ingoing, "out": outgoing) are constructed with their components referring to $\mathbf{x}_{\text{loc}}, \mathbf{y}_{\text{loc}}, \mathbf{z}_{\text{loc}}$ (cf. fig. 3.40):

$$\mathbf{e}_{\text{in}} = \cos\phi_{\text{in}}\mathbf{y}_{\text{loc}} + \sin\phi_{\text{in}}\mathbf{z}_{\text{loc}}, \tag{3.58a}$$
$$\mathbf{e}_{\text{out}} = \cos\phi_{\text{out}}\mathbf{y}_{\text{loc}} + \sin\phi_{\text{out}}\mathbf{z}_{\text{loc}}. \tag{3.58b}$$

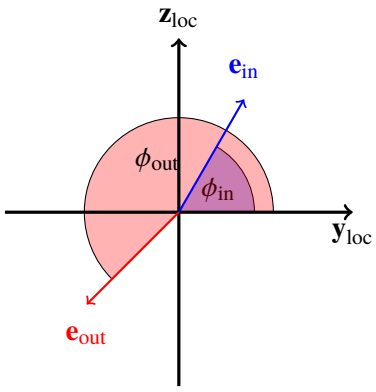

FIGURE 3.40: Schematic drawing of the polarisation vectors $\mathbf{e}_{\text{in,out}}$ and their relation to the local coordinate system spanned by $\mathbf{x}_{\text{loc}}, \mathbf{y}_{\text{loc}}, \mathbf{z}_{\text{loc}}$ with $\hat{\mathbf{n}}_{\text{surf}} \parallel \mathbf{x}_{\text{loc}}$. The angles $\phi_{\text{in,out}}$ are measured from the $\mathbf{y}_{\text{loc}}$-axis.

With this choice of the polarisation vectors, their projection on $\mathscr{R}^m$ becomes

$$\begin{aligned}\mathscr{I}^m \equiv \mathscr{I}^m_{hkl}(\omega_{\text{L}}, \phi_{\text{in}}, \phi_{\text{out}}) &= \left| \left[\mathscr{A}_{\text{loc}} \mathbf{e}^{\text{surf}}_{\text{out}}\right]^T \mathscr{R}^m(\omega_{\text{L}}) \left[\mathscr{A}_{\text{loc}} \mathbf{e}^{\text{surf}}_{\text{in}}\right] \right|^2 \\ &= \left| \left[\mathbf{e}^{\text{surf}}_{\text{out}}\right]^T \left[\mathscr{A}^T_{\text{loc}} \mathscr{R}^m(\omega_{\text{L}}) \mathscr{A}_{\text{loc}}\right] \mathbf{e}^{\text{surf}}_{\text{in}} \right|^2, \end{aligned} \tag{3.59}$$

i.e., the tensor $\mathscr{R}^m(\omega_{\text{L}}) = (\omega_{\text{L}} - \omega_m)^4 c^{-4} (n_m + 1)(2\omega_m)^{-1} \alpha^m(\omega_{\text{L}})$ can be transformed from the global to the local coordinate system by $\mathscr{A}^T_{\text{loc}} \mathscr{R}^m \mathscr{A}_{\text{loc}}$, with $\mathscr{A}_{\text{loc}} = (\mathbf{x}_{\text{loc}}, \mathbf{y}_{\text{loc}}, \mathbf{z}_{\text{loc}})$.[xiii] The polarisation vectors are chosen in the local coordinate system and, since $\hat{\mathbf{n}}_{\text{surf}} \parallel \mathbf{x}_{\text{loc}}$, these vectors are of the form $\mathbf{e}^{\text{surf}}_{\text{in,out}} = (0, \cos\phi_{\text{in,out}}, \sin\phi_{\text{in,out}})$, where the angle $\phi_{\text{in,out}}$ is measured from the $\mathbf{y}_{\text{loc}}$-axis.

In summary, the procedure for calculating $\mathscr{I}^m_{hkl}$ is:

(i) Determine the Miller indices (hkl) of the crystal orientation of interest.
(ii) Determine the surface normal $\hat{\mathbf{n}}_{\text{surf}}$ from eq. (3.56).
(iii) Based on $\hat{\mathbf{n}}_{\text{surf}}$, obtain the local coordinate system $\mathbf{x}_{\text{loc}}, \mathbf{y}_{\text{loc}}, \mathbf{z}_{\text{loc}}$ through eq. (3.57).
(iv) Choose the polarisation angles $\phi_{\text{in}}, \phi_{\text{out}}$ and deduce the polarisation vectors $\mathbf{e}_{\text{in}}, \mathbf{e}_{\text{out}}$ using eq. (3.58).
(v) Use the polarisation vectors to project out the desired elements from the $\mathscr{R}^m$'s.

A common practise is to choose the polarisation vectors either collinear ($\mathbf{e}_{\text{in}} \parallel \mathbf{e}_{\text{out}}$) or orthogonal ($\mathbf{e}_{\text{in}} \perp \mathbf{e}_{\text{out}}$). Letting $\phi = \phi_{\text{in}} = \phi_{\text{out}}$, the ϕ-dependence of $\mathscr{I}^m_{hkl} = |[\mathbf{e}_{\text{out}}]^T \mathscr{R}^m \mathbf{e}_{\text{in}}|^2$ can be parametrised for some surface orientation (hkl). In the parallel scattering configuration the polarisation vectors are $\mathbf{e}_{\text{in}} = \mathbf{e}_{\text{out}} = \cos\phi \mathbf{y}_{\text{loc}} + \sin\phi \mathbf{z}_{\text{loc}}$, while in the perpendicular scattering configuration $\mathbf{e}_{\text{out}} = -\sin\phi \mathbf{y}_{\text{loc}} + \cos\phi \mathbf{z}_{\text{loc}} \perp \mathbf{e}_{\text{in}}$, such that $[\mathbf{e}_{\text{out}}]^T \mathbf{e}_{\text{in}} = 0 \; \forall \phi$. The dependence on the "polarisation angle" ϕ of $\mathscr{I}^m_{hkl}$ for the surface orientations from fig. 3.35 is collected in table 3.7. It is emphasised that the Miller indices (hkl) refer to the reciprocal lattice of the *conventional* tetragonal unit cell.

The expressions for the angular dependence of $\mathscr{I}^m_{hkl}$ in table 3.7 is obtained from (using Dirac's notation for the moment)[207]

$$\begin{aligned}\mathscr{I}^m_{hkl}(\phi_{\text{in}}, \phi_{\text{out}}) &= \langle \mathbf{e}_{\text{out}} | \mathscr{R}^m | \mathbf{e}_{\text{in}} \rangle \langle \mathbf{e}_{\text{out}} | \mathscr{R}^m | \mathbf{e}_{\text{in}} \rangle^* \\ &= \langle \mathbf{e}_{\text{out}} | \mathscr{R}^m | \mathbf{e}_{\text{in}} \rangle \langle \mathbf{e}_{\text{in}} | [\mathscr{R}^m]^H | \mathbf{e}_{\text{out}} \rangle = \langle \mathbf{e}_{\text{out}} | \mathscr{R}^m | \mathbf{e}_{\text{in}} \rangle \langle \mathbf{e}_{\text{in}} | [\mathscr{R}^m]^* | \mathbf{e}_{\text{out}} \rangle \\ &= \left[[\mathbf{e}_{\text{out}}]^T \mathscr{R}^m \mathbf{e}_{\text{in}} \right] \left[[\mathbf{e}_{\text{in}}]^T [\mathscr{R}^m]^* \mathbf{e}_{\text{out}} \right], \end{aligned}$$

which follows from the conjugate symmetry of the inner product $\langle f | g \rangle = \langle f | g \rangle^*$, $[\mathscr{R}^m]^H = [\mathscr{R}^m]^*$ because $[\mathscr{R}^m]^T = \mathscr{R}^m$,[xiv] and the fact the the polarisation vectors are real-valued.

The equations for the A_{1g} mode are particularly interesting because they depend on the *relative phase* $\chi_{ab} = \chi_a - \chi_b$ (see caption of table 3.7) of the tensor elements a, b from eq. (3.55). Since generally $\chi_{ab} \equiv \chi_{ab}(\lambda_{\text{L}})$, it appears instructive to investigate the laser excitation energy dependence. This is done in fig. 3.41 where $\mathscr{I}^m_{hkl}$ is displayed for $(hkl) = (100)$ ($\mathbf{e}_{\text{in}} \parallel \mathbf{e}_{\text{out}}$) and $(hkl) = (110)$ ($\mathbf{e}_{\text{in}} \perp \mathbf{e}_{\text{out}}$). From table 3.7, for $(hkl) = (110)$ and $\mathbf{e}_{\text{in}} \perp \mathbf{e}_{\text{out}}$ (right part of fig. 3.41), the influence of changes in χ_{ab} due to λ_{L} is simply a

[xiii] The vectors $\mathbf{x}_{\text{loc}}, \mathbf{y}_{\text{loc}}, \mathbf{z}_{\text{loc}}$ form the *columns* of the matrix $(\mathbf{x}_{\text{loc}}, \mathbf{y}_{\text{loc}}, \mathbf{z}_{\text{loc}})$.
[xiv] $[\mathscr{R}^m]^H$ is the hermitian conjugate of $\mathscr{R}^m$, i.e., its conjugate-transpose.

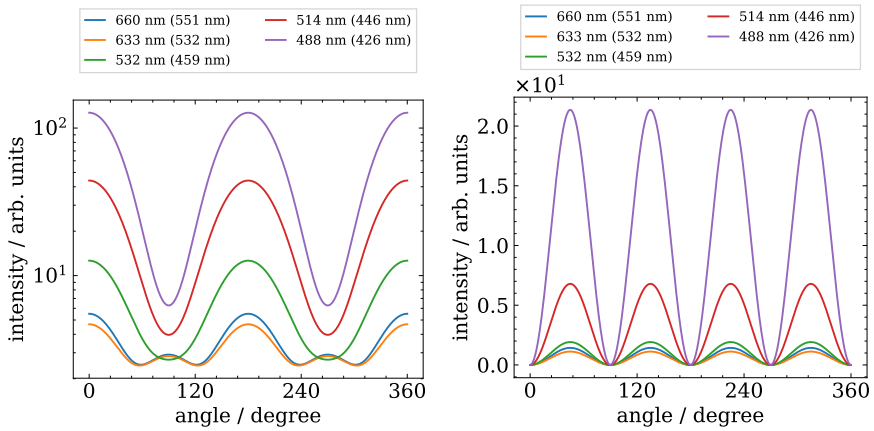

(a) $(hkl) = (100)$ and $\mathbf{e}_{\text{in}} \parallel \mathbf{e}_{\text{out}}$. **(b)** $(hkl) = (110)$ and $\mathbf{e}_{\text{in}} \perp \mathbf{e}_{\text{out}}$.

FIGURE 3.41: $\mathscr{I}^m_{hkl}$ of the A_{1g} mode for several laser wavelengths λ_{L}. An absorption gap correction $\Delta E_{\text{g,abs}} = 0.37\,\text{eV}$[88] is used and the effective laser wavelengths $\lambda_{\text{L}}^{\text{eff}}$ are given in braces behind λ_{L} (see table 3.7). *Parameters for the calculations*: See fig. 3.39.

scaling of the total intensity, since the $2\,|a|\,|b|\cos\chi_{ab}$ factor only occurs in the braces and has no separate ϕ-dependence. The ϕ-dependence in case of $(hkl) = (100)$ and $\mathbf{e}_{\text{in}} \parallel \mathbf{e}_{\text{out}}$, however, is more intricate. The term containing $\cos\chi_{ab}$ itself depends on ϕ and is additive to $|a|^2\sin^4\phi + |b|^2\cos^4\phi$. Therefore, its influence is not just an overall scaling, but a modification of the intensity for certain angles, which is readily observed in the left part of fig. 3.41. Indeed, considerable influence of λ_{L} on the overall shape of $\mathscr{I}^m_{hkl}$ as a function of ϕ is observable.

In fig. 3.42 the angle dependence of $\mathscr{I}^m_{hkl}$ is shown for all Raman active modes form fig. 3.38. The same scattering configurations as in fig. 3.41 are used. A laser wavelength of 633 nm is assumed and an absorption gap correction of $\Delta E_{\text{g,abs}} = 0.37\,\text{eV}$[88] is applied ($\lambda_{\text{L}}^{\text{eff}} = 532\,\text{nm}$). $\mathscr{I}^m_{hkl}$ is calculated for a finite number of angles and, in order to verify the correctness of the expressions listed in table 3.7, the resulting data points are fitted with the suitable equations.

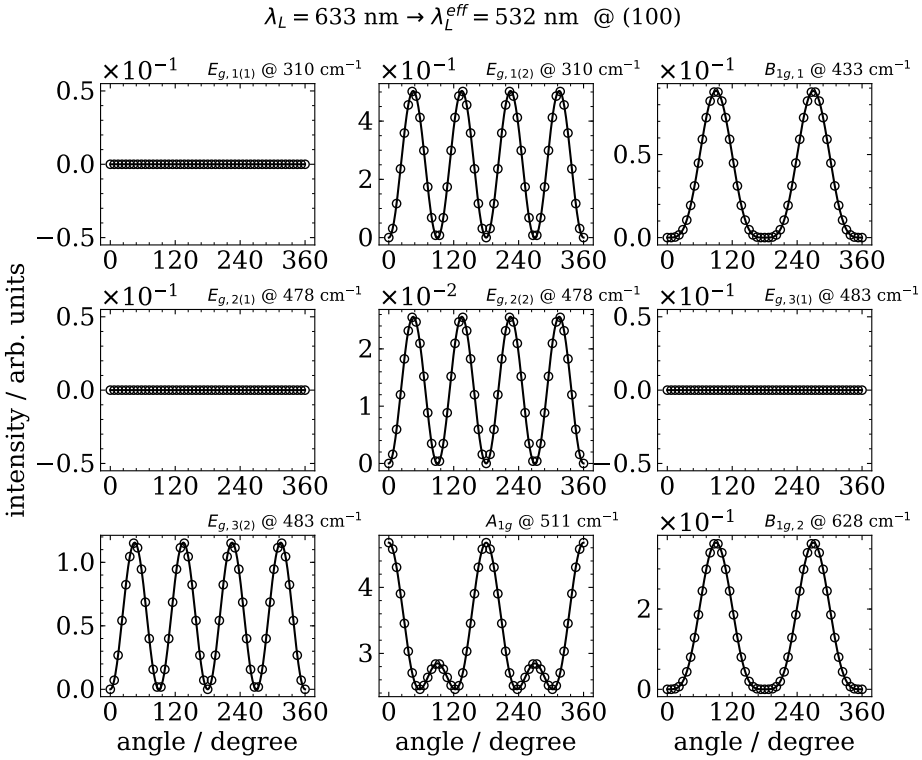

(a) (hkl) = (100) and $\mathbf{e}_{\text{in}} \parallel \mathbf{e}_{\text{out}}$.

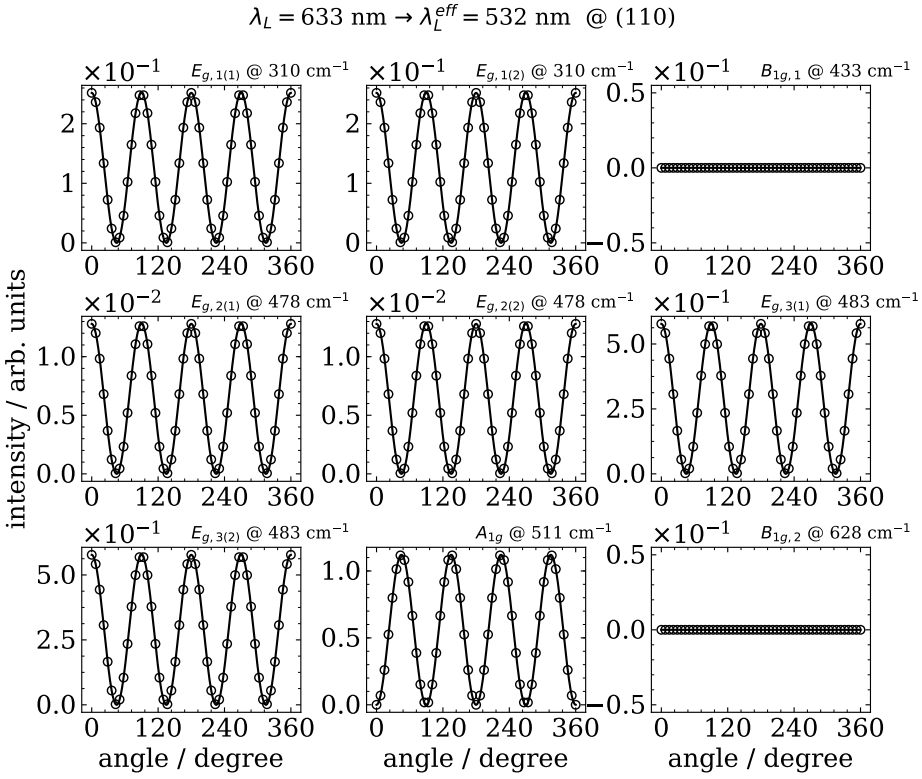

(b) (hkl) = (110) and $\mathbf{e}_{\text{in}} \perp \mathbf{e}_{\text{out}}$.

FIGURE 3.42: $\mathscr{I}^m_{hkl}$ for (a) (hkl) = (100) and a parallel ($\mathbf{e}_{\text{in}} \parallel \mathbf{e}_{\text{out}}$) scattering configuration, (b) (hkl) = (110) and a perpendicular ($\mathbf{e}_{\text{in}} \perp \mathbf{e}_{\text{out}}$) scattering configuration. An absorption gap correction $\Delta E_{\text{g,abs}} = 0.37\,\text{eV}$[88] is used yielding $\lambda_{\text{L}}^{\text{eff}} = 532\,\text{nm}$ for $\lambda_{\text{L}} = 633\,\text{nm}$ (table 3.6). The black circles are calculated data points that are fitted (solid black lines) with the adequate expressions from table 3.7. *Parameters for the calculations*: See fig. 3.39.

(hkl)	$\mathbf{e}_{\text{in}}$ vs $\mathbf{e}_{\text{out}}$ vs $\equiv \parallel, \perp$	$\mathbf{x}_{\text{loc}}, \mathbf{y}_{\text{loc}}, \mathbf{z}_{\text{loc}}$	irrep	$\left\lvert[\mathbf{e}_{\text{out}}(\phi)]^T \mathscr{R}^m \mathbf{e}_{\text{in}}(\phi)\right\rvert^2$
(100)	$\parallel$	$\mathbf{x}, -\mathbf{z}, \mathbf{y}$	A_{1g}	$\lvert a\rvert^2 \sin^4\phi + 2\lvert a\rvert\lvert b\rvert \sin^2\phi\cos^2\phi\cos\chi_{ab} + \lvert b\rvert^2\cos^4\phi$
			B_{1g}	$\lvert c\rvert^2 \sin^4\phi$
			$E_{g(1)}$	0
			$E_{g(2)}$	$\lvert e\rvert^2 \sin^2 2\phi$
	$\perp$		A_{1g}	$\sin^2\phi\cos^2\phi[\lvert a\rvert^2 + \lvert b\rvert^2 - 2\lvert a\rvert\lvert b\rvert\cos\chi_{ab}]$
			B_{1g}	$\lvert c\rvert^2\cos^2\phi\sin^2\phi$
			$E_{g(1)}$	0
			$E_{g(2)}$	$\lvert e\rvert^2\cos^2 2\phi$
(001)	$\parallel$	$\mathbf{z}, \mathbf{x}, \mathbf{y}$	A_{1g}	$\lvert a\rvert^2$
			B_{1g}	$\lvert c\rvert^2\cos^2 2\phi$
			$E_{g(1)}$	0
			$E_{g(2)}$	0
	$\perp$		A_{1g}	0
			B_{1g}	$\lvert c\rvert^2\sin^2 2\phi$
			$E_{g(1)}$	0
			$E_{g(2)}$	0
(110)	$\parallel$	$\frac{1}{\sqrt{2}}(\mathbf{x}+\mathbf{y}), -\mathbf{z}, \frac{1}{\sqrt{2}}(-\mathbf{x}+\mathbf{y})$	A_{1g}	$\lvert a\rvert^2 \sin^4\phi + 2\lvert a\rvert\lvert b\rvert \sin^2\phi\cos^2\phi\cos\chi_{ab} + \lvert b\rvert^2\cos^4\phi$
			B_{1g}	0
			$E_{g(1)}$	$2\lvert e\rvert^2\sin^2\phi\cos^2\phi$
			$E_{g(2)}$	$2\lvert e\rvert^2\sin^2\phi\cos^2\phi$
	$\perp$		A_{1g}	$\sin^2\phi\cos^2\phi[\lvert a\rvert^2 + \lvert b\rvert^2 - 2\lvert a\rvert\lvert b\rvert\cos\chi_{ab}]$
			B_{1g}	0
			$E_{g(1)}$	$\frac{1}{2}\lvert e\rvert^2\cos^2 2\phi$
			$E_{g(2)}$	$\frac{1}{2}\lvert e\rvert^2\cos^2 2\phi$

TABLE 3.7: Angular dependence of the Raman intensity $|[\mathbf{e}_{\text{out}}(\phi)]^T \mathscr{R}^m \mathbf{e}_{\text{in}}(\phi)|^2$ for different surface orientations (hkl) (the indices refer to the reciprocal lattice of the conventional unit cell in real space). The complex-valued tensor components from eq. (3.55) are written in the form $a = |a|\exp(i\chi_a)$, $b = |b|\exp(i\chi_b)$, $c = |c|\exp(i\chi_c)$, $e = |e|\exp(i\chi_e)$, and $\chi_{ab} = \chi_a - \chi_b$. The polarisation vectors (ingoing, outgoing) with respect to the global coordinate system $\mathbf{x}, \mathbf{y}, \mathbf{z}$ are [$\mathbf{e}_{\text{in}} \parallel \mathbf{e}_{\text{out}}$]: $\mathbf{e}_{\text{in}} = \mathbf{e}_{\text{out}} = \cos\phi\mathbf{y}_{\text{loc}} + \sin\phi\mathbf{z}_{\text{loc}}$, and [$\mathbf{e}_{\text{in}} \perp \mathbf{e}_{\text{out}}$]: $\mathbf{e}_{\text{out}} = -\sin\phi\mathbf{y}_{\text{loc}} + \cos\phi\mathbf{z}_{\text{loc}}$ ($\mathbf{x}_{\text{loc}}, \mathbf{y}_{\text{loc}}, \mathbf{z}_{\text{loc}}$: local coordinate system with surface normal $\mathbf{x}_{\text{loc}}$). Global coordinate system: $\mathbf{x} = (1, 0, 0)$, $\mathbf{y} = (0, 1, 0)$, $\mathbf{z} = (0, 0, 1)$. Based in the primitive lattice vectors listed in the caption of fig. 3.1b, the conventional unit cell is constructed from $\mathbf{a}^{(j)}_{\text{conv}} = \sum_i \mathbf{a}^{(i)}_{\text{prim}} M_{ij}$ with $M = ((0, 1, 1), (1, 0, 1), (1, 1, 0))$ (to be read row-wise), resulting in $\mathbf{a}^{(1)}_{\text{conv}}, \mathbf{a}^{(2)}_{\text{conv}}, \mathbf{a}^{(3)}_{\text{conv}} = ((a, 0, 0), (0, a, 0), (0, 0, c))$.

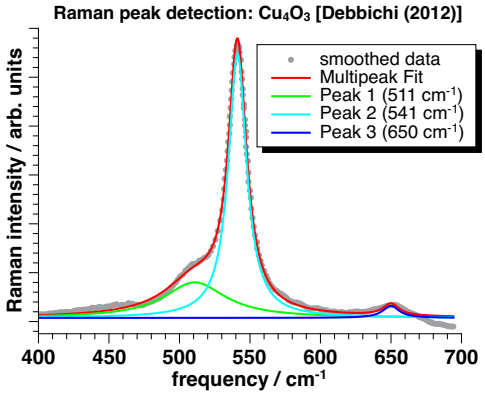

FIGURE 3.43: Fit of (some) peaks in the Raman spectrum from Debbichi et al. [118] (the laser wavelength is $\lambda_L = 514\,\text{nm}$). Results for centring and broadening values of the peaks are compiled in table 3.8. In order to get similar values for the centring position of the peaks like Debbichi et al. [118], it is necessary to start the fit at $400\,\text{cm}^{-1}$ and to neglect the small shoulder at $\sim 460\,\text{cm}^{-1}$.

Comparison to experiment—semi-polarised Raman spectra Experimental measurements for the Raman scattering intensities have been carried out by Debbichi et al. [118]. A fit of (some) peaks of the experimental Raman spectrum is given in fig. 3.43 and the values of the peak positions and their broadening are gathered in table 3.8. In particular the broadening of the peaks is of interest when comparing calculated and measured Raman spectra. For the calculation of the spectra the broadening value of the A_{1g} mode ($\zeta = 7.8\,\text{eV}$) will be used.

		peak position ω_0 / cm^{-1}		peak broadening / cm^{-1}	
peak	irrep	fitted	Ref. [118]	γ	$\zeta = \gamma/2$
–	$E_{g,1}$	–	318	–	–
1	$E_{g,3}$	510.8	510	53.1	26.6
2	A_{1g}	541.1	541	15.6	7.8
3	$B_{1g,2}$	650.0	651	14.2	7.1

TABLE 3.8: Determination of (some) experimental Raman peak positions and broadening parameters from Debbichi et al. [118] (see fig. 3.43). Each peak is fitted with a Lorentzian of the from $I_{\gamma(\zeta)}(\omega) = I_0 + 2A/\pi \times \gamma/(4(\omega-\omega_0)^2+\gamma^2) = I_0 + 2A/\pi \times (2\zeta)/(4(\omega-\omega_0)^2 + (2\zeta)^2)$. The relation between the broadening parameters is $\gamma = 2\zeta$.

In Ref. [118] Cu_4O_3 samples are grown by magnetron sputtering and for details about the growth the reader is referred to Pierson et al. [114]. However, no detailed information is given about the orientation of the sputtered samples. Since sputter deposition in case of Cu_4O_3 is known to deliver well-orientated samples,[23,114,115] a well-defined orientation can be assumed in case of Debbichi et al. [118]. It will therefore be supposed that the orientations are the same as in Pierson et al. [114] ($(hkl) = (100), (001)$).

Since apart from that, no specific choices for the polarisation vectors $\mathbf{e}_{\text{in}}, \mathbf{e}_{\text{out}}$ are given,[118] it shall be assumed that only the *ingoing* laser beam is polarised and the outgoing beam is completely *unpolarised*.[208] In order to calculate this, the Raman scattering intensity must be averaged over the polarisation angle ϕ_{out} for a fixed choice of ϕ_{in}. An equation describing this would be

$$\mathscr{I}^{m,\text{av}}_{hkl}(\omega_L, \phi_{\text{in}}) = \int_0^{2\pi} \frac{d\phi_{\text{out}}}{2\pi}\, \mathscr{I}^{m}_{hkl}(\omega_L, \phi_{\text{in}}, \phi_{\text{out}}), \tag{3.60}$$

where the factor $(2\pi)^{-1}$ is for normalisation. As the thus obtained intensity $\mathscr{I}^{m,\text{av}}_{hkl}(\phi_{\text{in}})$ is solely dependent on the polarisation of the ingoing photon (and not on that of the outgoing photon), the resulting spectra will be referred to as "semi-polarised". A schematic drawing of the averaging can be found in fig. 3.44. Similarly, as in table 3.7, the Raman scattering intensity averaged according to eq. (3.60) can be parametrised in terms of the polarisation angle ϕ_{in}. For the surfaces with Miller indices $(hkl) = (100), (001), (110)$[23,114] the corresponding expressions for the irreps $A_{1g}, B_{1g}, E_{g(1)}, E_{g(2)}$ are listed in table 3.9.

Obviously, the (001) surface can be ruled out, because the E_g modes are not detectable for any choice of the polarisation vectors $\mathbf{e}_{\text{in}}, \mathbf{e}_{\text{out}}$ (cf. eq. (3.55) and table 3.7). However, these modes clearly occur in the experimental spectrum as follows from, e.g., fig. 3.43 and tables 3.8 to 3.10.[118] Furthermore, the (110) surface found by Meyer et al. [23] is also out of question, since the B_{1g} modes are not visible for this surface orientation. From tables 3.8 and 3.10, the B_{1g} modes are measured by Debbichi et al. [118], indeed.

In table 3.9 the ϕ_{in} dependence of eq. (3.60) is compiled for surface orientations $(hkl) = (100), (001), (110)$. In what follows, Raman spectra for different choices of the ϕ_{in} polarisation angle will be computed for the (100) surface. The goal is to investigate if the spectrum presented in Ref. [118] can be obtained based on the assumptions made about the experimental conditions in this paragraph.

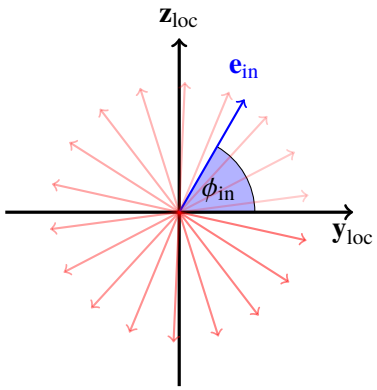

FIGURE 3.44: Schematic drawing of the averaging over the outgoing polarisation (red-coloured arrows) vectors for fixed ingoing polarisation (eq. (3.60)).

	$\mathscr{I}^{m,\mathrm{av}}_{hkl}(\phi_{\mathrm{in}})$		
irrep	(100)	(001)	(110)
A_{1g}	$\frac{1}{2}[\lvert a\rvert^2 \sin^2\phi_{\mathrm{in}} + \lvert b\rvert^2 \cos^2\phi_{\mathrm{in}}]$	$\frac{1}{2}\lvert a\rvert^2$	$\frac{1}{2}[\lvert a\rvert^2 \sin^2\phi_{\mathrm{in}} + \lvert b\rvert^2 \cos^2\phi_{\mathrm{in}}]$
B_{1g}	$\frac{1}{2}\lvert c\rvert^2 \sin^2\phi_{\mathrm{in}}$	$\frac{1}{2}\lvert c\rvert^2$	0
$E_{g(1)}$	0	0	$\frac{1}{4}\lvert e\rvert^2$
$E_{g(2)}$	$\frac{1}{2}\lvert e\rvert^2$	0	$\frac{1}{4}\lvert e\rvert^2$

TABLE 3.9: ϕ_{in} dependence of eq. (3.60) for some surface orientations (hkl). For the choice of the local coordinate system $\mathbf{x}_{\mathrm{loc}}, \mathbf{y}_{\mathrm{loc}}, \mathbf{z}_{\mathrm{loc}}$ the reader is referred to table 3.7. The ingoing and outgoing polarisation vectors are written as $\mathbf{e}_{\mathrm{in,out}} = \cos\phi_{\mathrm{in,out}}\mathbf{y}_{\mathrm{loc}} + \sin\phi_{\mathrm{in,out}}\mathbf{z}_{\mathrm{loc}}$.

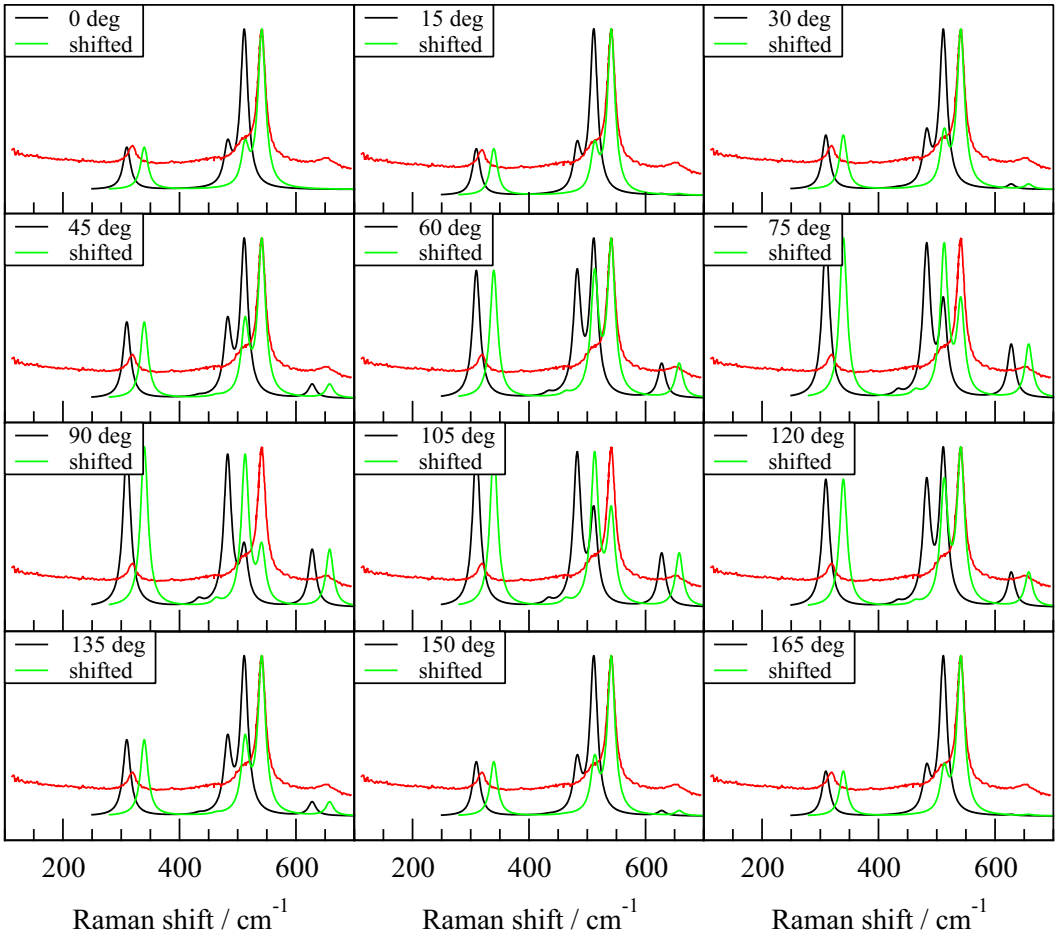

FIGURE 3.45: Semi-polarised Raman spectra (black solid line) for the surface orientation $(hkl) = (100)$. All spectra are renormalized with respect to the highest peak. Different polarisation angles of the ingoing photon (ϕ_{in}) are considered. The angle is measured from the $\mathbf{y}_{\mathrm{loc}}$-axis (see table 3.7). The experimental spectrum from Debbichi et al. [118] is also included (red solid line). Additionally, the calculated spectrum is shifted by 30 cm^{-1} (green solid line). The Raman intensity is expressed in arbitrary units. *Parameters for the calculations*: See fig. 3.39.

In fig. 3.45 semi-polarised Raman spectra for a (100) surface are compared to the experimental spectrum from Debbichi et al. [118]. Different polarisation angles of the ingoing photon (ϕ_{in}) are considered, where the angle is measured from the $\mathbf{y}_{\text{loc}}$-axis (see table 3.7). Only angles in the range $[0, \pi)$ are considered, since the functions describing the ϕ_{in} dependence in table 3.9 for $(hkl) = (100)$ are π-periodic. Indeed, for some angles ϕ_{in} agreement with respect to the relative intensities is reasonable (e.g., below 60° and above 120°). This particularly obvious when considering the spectra shifted by $30\,\text{cm}^{-1}$ (this is the difference between the calculated and the measured frequency[118] of the A_{1g} mode; see table 3.10).

From table 3.9 it follows that the intensities of the A_{1g}, B_{1g} modes depend on the angle ϕ_{in}, while that of the E_g modes is *constant*. Therefore, the relative intensities may change significantly when varying the polarisation angle of the ingoing photon. This particularly can "spoil" the dominance of the A_{1g} mode found in experiment. Obviously, it would be of great value to have measured data available for the orientation/polarisation dependence of the Raman scattering intensity of Cu_4O_3.

3.4.4 Raman scattering in Cu_4O_3 under hydrostatic pressure

While so far Raman scattering properties of Cu_4O_3 have been investigated for the equilibrium lattice constants (table 3.1), in this section their behaviour under hydrostatic pressure will be discussed.

Pressure dependence of the phonon modes At first, the evolution of the Raman and infra-red active modes with increasing values of the hydrostatic pressure P exerted on the unit cell will be studied. In fig. 3.46a the pressure dependence of the Raman active modes will be assessed. For the functional relationship between ω_m and P its is assumed that $\omega_m(P) \approx \omega_m(P=0) + [\partial_P \omega_m|_{P=0}]P + \frac{1}{2}[\partial_P^2 \omega_m|_{P=0}]P^2$, which is found to provide a decent description. Values obtained for the linear coefficients are compiled in table 3.10.

Introducing the (dimensionless) reduced volume $\Omega'_P = \Omega_P/\Omega_{P=0}$, where the subscript "$P$" merely indicates that a volume compression results in non-zero pressure ($\Omega'_{P=0}$: equilibrium volume), a similar parametrisation is: $\omega_m(\Omega'_P) \approx \omega_m(\Omega'_P = 1) + [\partial_{\Omega'_P} \omega_m|_{\Omega'_P=1}]\Omega'_P + \frac{1}{2}[\partial^2_{\Omega'_P} \omega_m|_{\Omega'_P=1}]\Omega'^2_P$. This form will be useful when discussing the differences of calculated and measured frequencies.

The highest pressure considered for Cu_4O_3 is 7.6 GPa. For higher values of P the structure is found to be unstable.

	$\omega_m(\Omega)$			ω_m (Ref. [118])	
irrep	$\Omega_{P=0}$	Ω_{exp}	$\frac{\partial\omega_m}{\partial P}$	calculated	measured
Raman active modes					
A_{1g}	511	527	7.1	521	541
$B_{1g,1}$	433	450	7.6	448	–
$B_{1g,2}$	628	644	6.9	627	651
$E_{g,1}$	310	320	5.4	321	318
$E_{g,2}$	478	491	3.7	484	–
$E_{g,3}$	483	494	5.5	506	510
infra-red active modes					
$A_{2u,2}$	126	125	<0.5	127	–
$A_{2u,3}$	230	234	1.4	224	–
$A_{2u,4}$	308	318	4.5	309	322
$A_{2u,5}$	564	583	8.4	576	–
$A_{2u,6}$	638	657	7.6	649	–
$E_{u,2}$	52	51	<0.5	50	–
$E_{u,3}$	101	100	<0.5	99	–
$E_{u,4}$	120	120	<0.5	121	–
$E_{u,5}$	160	159	<0.5	168	164
$E_{u,6}$	206	208	1.0	214	212
$E_{u,7}$	436	449	6.9	454	463
$E_{u,8}$	515	530	6.8	538	548
$E_{u,9}$	578	594	5.5	603	607

TABLE 3.10: Phonon mode frequencies ω_m at $P = 0$ GPa (in cm^{-1}) and their first-order change with pressure (slope) $\partial\omega_m/\partial P$ (in cm^{-1}/GPa; see fig. 3.46a). Additionally, the frequencies for the experimental volume[119] (Ω_{exp}) are given. From the accuracy of the calculation ($\lesssim 1\,\text{cm}^{-1}$ for ω_m), only slopes with *absolute values* well above $0.5\,\text{cm}^{-1}$/GPa are reliable. These values are indicated by "< 0.5", irrespective of the sign of the slope. Frequencies from Debbichi et al. [118] (calculated with the LDA+U method with U, J=7.5 eV and 0.98 eV, and measured) are listed for comparison.

In table 3.10 frequencies and slopes $\partial\omega_m/\partial P$ (form fig. 3.46a) are summarised. For comparison, calculated and measured frequencies from Debbichi et al. [118] are also listed. The frequencies of all Raman active modes shift upwards with increasing pressure p with slopes $\partial\omega_m/\partial P$ of at least $3.7\,\text{cm}^{-1}$/GPa ($E_{g,2}$). In case of the infra-red active A_{2u} modes all but one increase in frequency with rising pressure values. While the

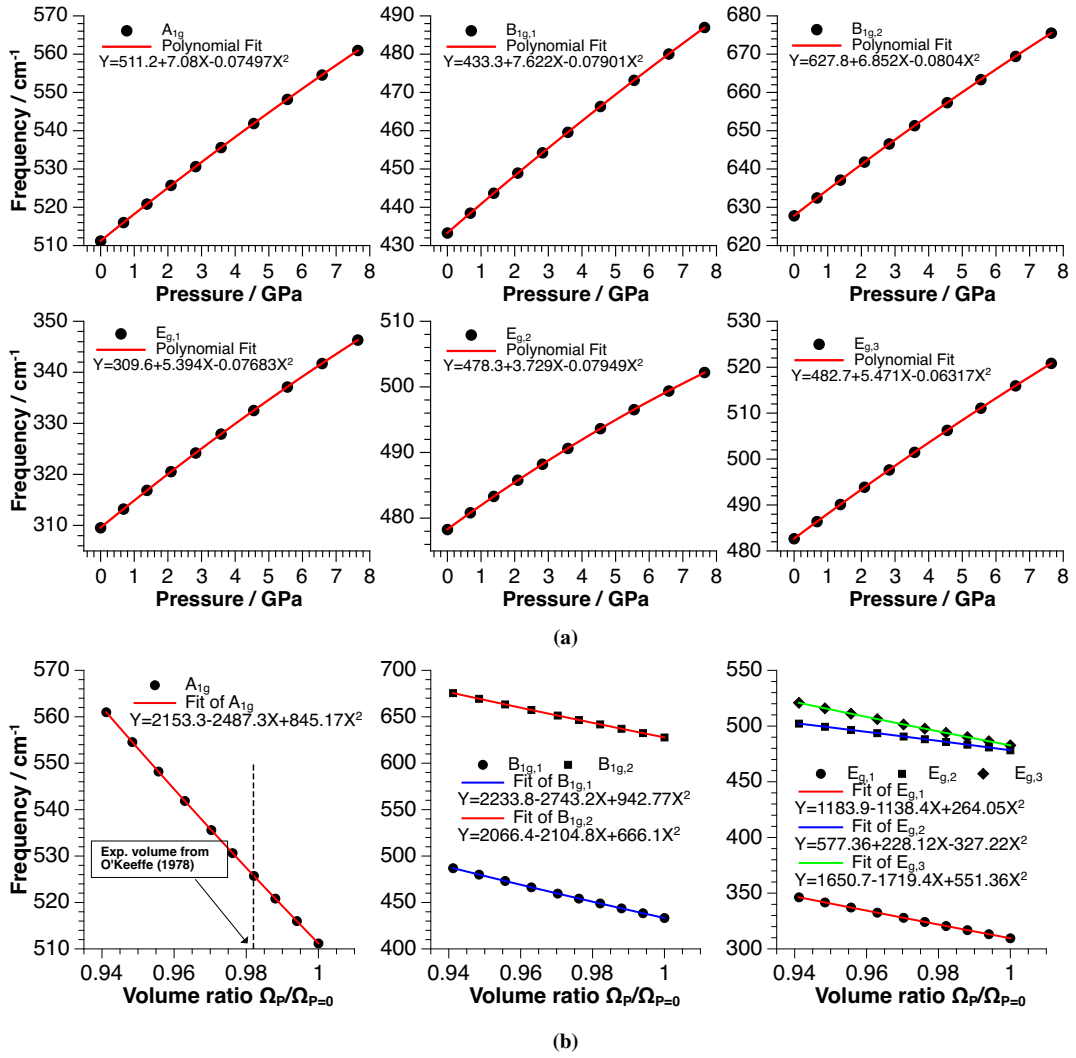

FIGURE 3.46: (a) Raman active modes A_{1g}, B_{1g}, E_g as a function of pressure. (b) Raman active modes A_{1g}, B_{1g}, E_g as a function of the volume ratio $\Omega'_P = \Omega_P/\Omega_{P=0}$ (reduced volume). For each frequency a fit with a second-order polynomial is performed. The unit of the linear coefficient $\partial\omega_m/\partial P$ is $\mathrm{cm}^{-1}/\mathrm{GPa}$, and that of the quadratic coefficient $\frac{1}{2}\partial^2\omega_m/\partial P^2$ is $\mathrm{cm}^{-1}/\mathrm{GPa}^2$. The unit of the coefficients $\partial\omega_m/\partial\Omega'_P$ and $\frac{1}{2}\partial^2\omega_m/\partial\Omega'^2_P$ is cm^{-1}. *Parameters for the calculations*: See fig. 3.38.

$A_{2u,1}$ mode displays negligible change with pressure, higher frequency modes have slopes $\geq 1.4\,\mathrm{cm}^{-1}/\mathrm{GPa}$. E_u modes with frequencies smaller than $160\,\mathrm{cm}^{-1}$ ($E_{u,5}$) have slopes below $0.5\,\mathrm{cm}^{-1}/\mathrm{GPa}$. Only modes with frequencies larger than that of the $E_{u,6}$ mode ($206\,\mathrm{cm}^{-1}$) have slopes well above $5\,\mathrm{cm}^{-1}/\mathrm{GPa}$.

Indeed, calculated frequencies from Ref. [118] (see table 3.10) in many cases compare better to their measured frequency values than the frequencies obtained in this work with the GGA+U method (U, J=7.5 eV and 0.98 eV). However, their lattice parameters underestimate experimental values[xv] by 4.1 % and 2.6 % for a, c, which on the one hand is large, but on the other hand is a typical result (concerning the trend) for the LDA which tends to overbind. On the contrary, the GGA+U method results in differences of < 1 % (see table 3.1). These observations do not qualify any method over the other. It seems that a decent description of the vibrational properties of a solid does not necessarily presuppose a pre-eminent description of its structural parameters, and vice versa. Altogether, this underlines the complexity of Cu_4O_3 in terms of a decent theoretical description.

Remembering fig. 3.45, the experimental peak positions in the Raman spectrum can (partly) be reproduced by shifting the calculated spectrum by $30\,\mathrm{cm}^{-1}$ (this amounts to the difference of the calculated A_{1g} mode frequency at $511\,\mathrm{cm}^{-1}$ and the measured frequency at $541\,\mathrm{cm}^{-1}$). Obviously, from fig. 3.46a, the Raman

[xv] Experimental values for the lattice parameters are:[119,205]: a = 5.837 Å and 5.83 Å, c = 9.932 Å and 9.88 Å.

active modes are very sensitive to the external pressure, or likewise to a change in volume due to compression of the unit cell in accordance with an isotropic stress tensor. The ratio between the experimental volume and the calculated equilibrium volume is 0.982.[xvi] Based on the fitting result from fig. 3.46b, this means that for this volume the frequency of the A_{1g} mode is 526 cm^{-1}, which halves the difference between calculated measured frequency. Indeed, this number can only be a rough estimate because most likely the experimental structure from O'Keeffe and Bovin [119], when used as input for a DFT calculation (with GGA+U and $U, J = 7.5\,\mathrm{eV}$ and 0.98 eV), will *not* result in an isotropic stress tensor (meaning that the pressure acting on the unit cell is not hydrostatic). In any case, this suggests that the strong *underestimate* of the measured frequencies[118] (at least for the Raman active modes) results from an *overestimate* of the lattice parameters (the unit cell volume by roughly 2 %) compared to experiment.[119]

Equilibrium volume vs experimental[119] volume Before investigating the influence of hydrostatic pressure on the Raman scattering intensities, the difference between the equilibrium structure ($P = 0\,\mathrm{GPa}$) and a structure based on the experimental lattice constants[119] are discussed.

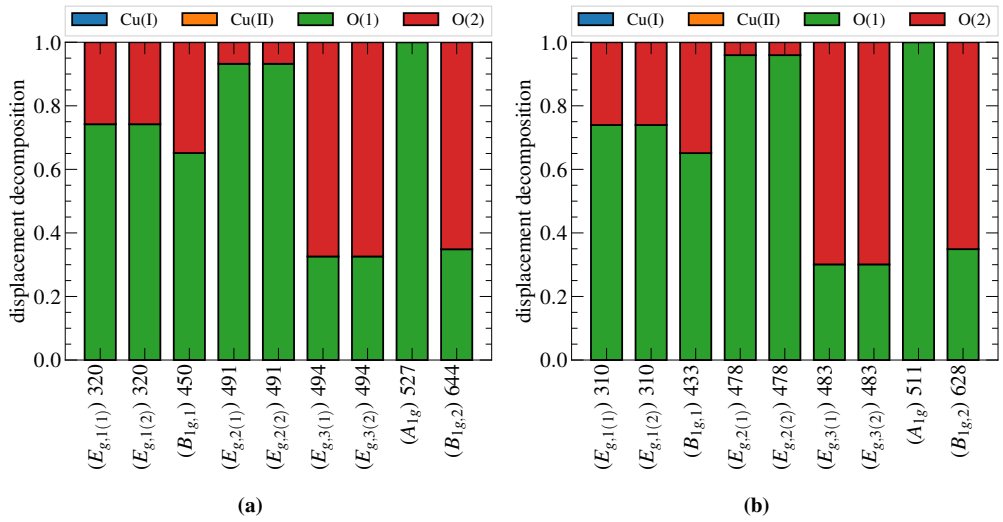

FIGURE 3.47: (a) Same as fig. 3.38, but the *experimental* lattice parameters from O'Keeffe and Bovin [119] are used for the calculation. (b) Same as (a), but for the equilibrium structure with $P = 0\,\mathrm{GPa}$ (reproduced from fig. 3.38). *Parameters for the calculations*: See fig. 3.38.

In fig. 3.47 the displacements of the Raman active modes are decomposed into contributions from the different "types" of atoms (see fig. 3.38). This is done for (a) the experimental lattice parameters,[119] and (b) the $P = 0\,\mathrm{GPa}$ structure (reproduction of fig. 3.38). Indeed, contributions of the different atom types to the mode displacement vectors are virtually the same for both calculations. Solely in case of the $E_{g,2}$ modes a larger contribution through the O(2) atoms may be stated for the calculation featuring the experimental lattice parameters from O'Keeffe and Bovin [119]. On the contrary, frequencies obtained for both volumes differ by at least $10\,\mathrm{cm}^{-1}$ (for the $E_{g,1}$ modes) and at most by $17\,\mathrm{cm}^{-1}$ (for the $B_{1g,1}$ mode).

Frequencies computed with the experimental lattice parameters on average differ by $\sim 10\,\mathrm{cm}^{-1}$ from the measured frequencies of the Raman active modes in table 3.10. This can be taken as an error bar for the frequencies and may serve as an estimate of the "physical accuracy" of the method in terms of a description of the vibrational properties of Cu_4O_3.[xvii] The frequencies of the Raman active as well as of the infra-red active modes of both volumes are listed in table 3.10.

In style of fig. 3.45, for $\phi_{\mathrm{in}} = 30°$, the Raman spectra for both the $P = 0\,\mathrm{GPa}$ structure and the structure with the experimental lattice parameters[119] are compared to the measured one from Debbichi et al. [116] in fig. 3.48a. Using the experimental lattice parameters instead of the equilibrium structure, indeed results

[xvi] For the *conventional* unit cell the volume is $\Omega = a^2 c$. With the values from table 3.1 it follows that $\Omega_{\mathrm{exp}}/\Omega_{P=0} = \frac{(5.837\,\text{Å})^2 \times 9.932\,\text{Å}}{(5.873\,\text{Å})^2 \times 9.990\,\text{Å}} = 0.982$.

[xvii] This interpretation was brought to me in discussions with Prof. Simone Sanna and Prof. Christian Heiliger.

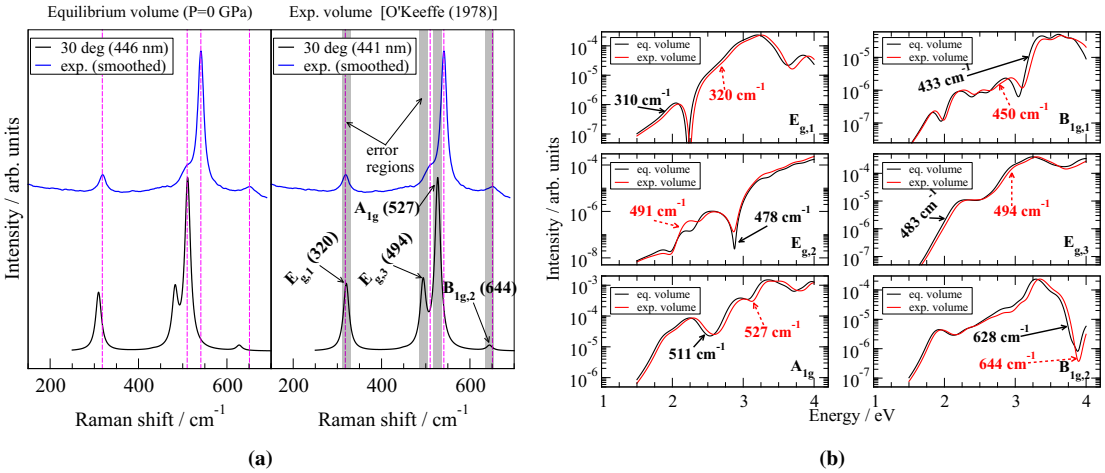

FIGURE 3.48: (a) Semi-polarised Raman spectrum in style of fig. 3.45 for (left) the $P = 0$ GPa structure and (right) the structure with experimental lattice parameters.[119] All spectra are renormalized with respect to the highest peak. The polarisation angle of the ingoing photon is $\phi_{\text{in}} = 30°$. The laser wavelength is $\lambda_{\text{L}} = 514$ nm with absorption gap corrections of 0.37 eV (left; $\lambda_{\text{L}}^{\text{eff}} = 446$ nm), and 0.4 eV (right; $E_{\text{g,abs}} = 1.77$ eV; $\lambda_{\text{L}}^{\text{eff}} = 441$ nm).[88] The experimental spectrum from Debbichi et al. [118] is also included. Vertical dashed lines indicate the measured Raman frequencies from table 3.10. The grey-shaded regions in the right panel are "error regions" of width $\pm 10\,\text{cm}^{-1}$ and illustrate the "physical accuracy" of the method. (b) Raman powder intensities $\mathscr{I}^m_{\text{powder}}$ vs energy for the $P = 0$ GPa structure and the structure with experimental lattice parameters. The frequencies of the modes from both structures are annotated in the figures. Since for each 2-fold degenerate E_g mode the intensity for $E_{g(1)}$ and $E_{g(2)}$ is the *same* for all energies, only one graph is shown for each of the three E_g modes. *Parameters for the calculations*: See fig. 3.39.

in a considerable improvement of the peak positions in relation to experiment. For the $E_{g,1}, B_{1g,2}$ modes the experimental frequencies fall into the error regions (grey-shaded areas in fig. 3.48a) bounded by the just-mentioned $\pm 10\,\text{cm}^{-1}$.

The differences in energy dependence of $\mathscr{I}^m_{\text{powder}}$ of both structures are shown in fig. 3.48b. Generally speaking, the curves resulting from the calculation with the experimental lattice parameters are essentially offset along the energy axes compared to those from the equilibrium structure.

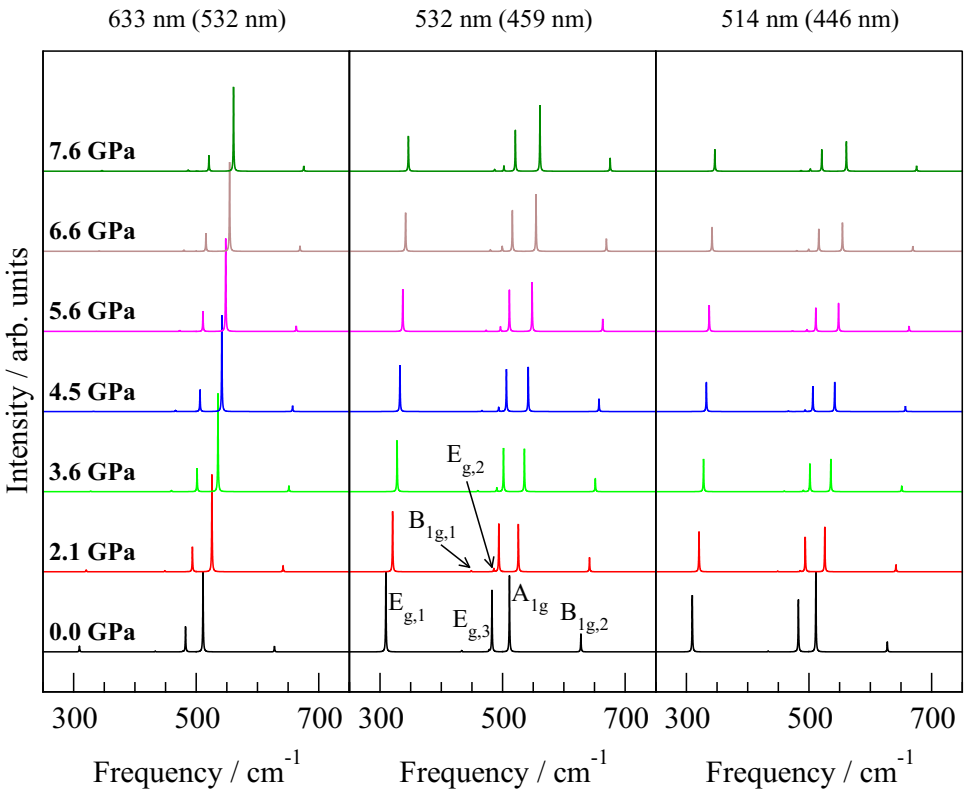

FIGURE 3.49: Pressure dependence of Raman powder spectra for laser wavelengths $\lambda_L = 633\,\text{nm}$, 532 nm and 514 nm. An absorption gap correction of $\Delta E_{g,abs} = 0.37\,\text{eV}$[88] is used and the corresponding values of λ_L^{eff} are given in braces. Each spectrum is normalised to the maximum intensity of the spectrum at $p = 0\,\text{GPa}$. *Parameters for the calculations*: See fig. 3.39.

Raman scattering intensities under hydrostatic pressure For pressures in the range 0 GPa to 7.6 GPa Raman powder spectra are shown in fig. 3.49. The laser wavelengths $\lambda_L = 633\,\text{nm}$, 532 nm and 514 nm with an absorption gap correction of 0.37 eV[88] are considered. The underlying assumption is that the optical absorption gap for higher pressures is overestimated by the same amount (see figs. 3.36a and 3.36c), as it is the case for the equilibrium ($P = 0\,\text{GPa}$) structure. In order to follow the changes in the relative intensities, each powder spectrum is normalised to the highest peak in the spectrum at $P = 0\,\text{GPa}$.

Quite different features of the Raman spectra are observed at different laser wavelengths: For $\lambda_L = 633\,\text{nm}$, the A_{1g} mode has the highest peak and its Raman intensity increases with rising P-values, while the $E_{g,1}$, $E_{g,3}$ modes lose intensity. Indeed, the $E_{g,1}$ mode is barely visible for $P = 0\,\text{GPa}$ and is completely absent at higher pressures. In case of $\lambda_L = 532\,\text{nm}$, the modes $E_{g,1}$, A_{1g} start with almost equal intensity. When increasing the pressure, the $E_{g,1}$, A_{1g} mode intensities are gradually lowered, thereby essentially maintaining relative intensities up to $P = 4.5\,\text{GPa}$. For larger pressures, the A_{1g} mode gains intensity while the $E_{g,1}$ mode intensity keeps shrinking. As a result, for pressures $\geq 5.6\,\text{GPa}$, the A_{1g} mode dominates the Raman powder spectrum. Finally, for $\lambda_L = 514\,\text{nm}$, the order of peaks with the major intensities at vanishing pressure is $\mathscr{I}^{E_{g,1}}_{\text{powder}} \approx \mathscr{I}^{E_{g,3}}_{\text{powder}} < \mathscr{I}^{A_{1g}}_{\text{powder}}$. The relative intensities are essentially unchanged when increasing the pressure, but intensities compared to the $P = 0\,\text{GPa}$ case are lowered.

A more detailed view on the Raman powder intensities $\mathscr{I}^m_{\text{powder}}$ vs energy is provided in fig. 3.50. The effective laser wavelengths used in fig. 3.49 are indicated by vertical dashed lines. For many modes, the change of $\mathscr{I}^m_{\text{powder}}$ with pressure is anything but trivial (e.g., many crossings of the curves) and strongly depends on energy. In some selected cases definite trends can be observed: From 2.25 eV to 3.25 eV the intensity of the $E_{g,1}$ mode clearly *de*creases with *in*creasing pressure. The same holds below 2.25 eV for the $E_{g,3}$ mode. The order of intensities can be the same as that of the pressure values (meaning that if pressure increases, the intensity increases as well); indeed, for the A_{1g} this is the case for the energy range bounded by the wavelengths 532 nm and 459 nm, while intensities are ordered contrariwise to the pressure values just below 532 nm.

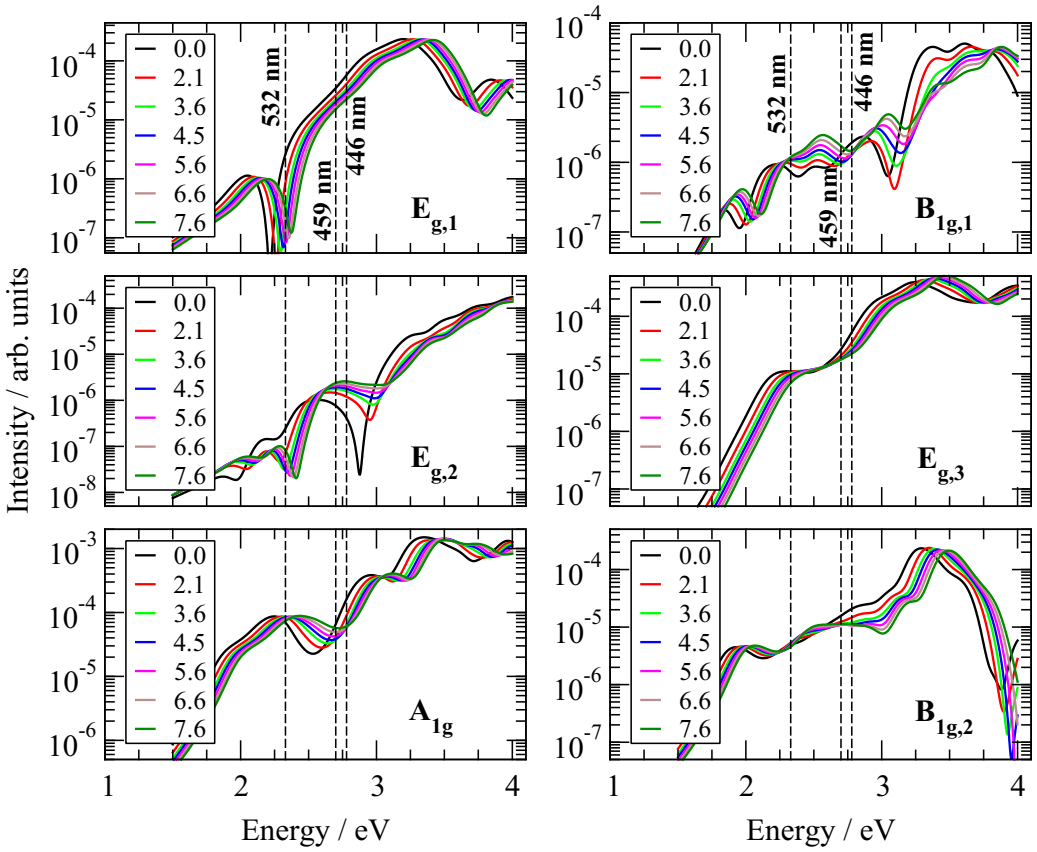

FIGURE 3.50: Raman powder intensities $\mathscr{I}^{m}_{\text{powder}}$ vs energy for different values of the hydrostatic pressure (see legends of the plots; units: GPa). The effective laser wavelengths $\lambda_{\text{L}}^{\text{eff}}$ used in fig. 3.49 are indicated by vertical dashed lines and are annotated in the topmost plots. Since for each 2-fold degenerate E_g mode the intensity for $E_{g(1)}$ and $E_{g(2)}$ is the *same* for all energies, only one graph is shown for each of the three E_g modes. *Parameters for the calculations*: See fig. 3.39.

4 Conclusion

In the present work the vibrational properties of all copper oxide phases (Cu_2O, Cu_4O_3, and CuO) are investigated by *ab initio* methods. Furthermore, the Raman scattering properties of Cu_4O_3 and CuO are subject to a detailed analysis.

Throughout the analysis of the phonon dispersions in sections 3.3.1 and 3.3.2 (which indeed comprises a rather technical part of this work) special attention is paid to the treatment of the dipole-dipole contributions to the FCs/dynamical matrices present for polar semiconductors/insulators. In the long wavelength limit, dipoles created by atomic displacements induce macroscopic electric fields that alter the phonon frequencies of some modes (infra-red active modes) near the BZ centre. The inclusion of dipole-dipole effects is called "dipole-dipole corrections" in this work. In order to treat this effect, two methods have emerged in the literature.[19,43] While Gonze's method[19] is traditionally used in conjunction with dynamical matrices from DFPT,[39,40,44] Wang's method[43] is the usual technique used within the framework of the direct method in the literature.[43,45–53] It is therefore shown that the method due to Gonze and Lee [19] can also be used together with dynamical matrices from the direct method. This actually is not too surprising: The direct method gives exact dynamical matrices (within the numerical accuracy of the method) at wavevectors that are reciprocal lattice vectors of the chosen supercell.[30,31] In the basis of the unit cell, these wavevectors comprise a grid that (homogeneously) samples the BZ. From a technical point of view, this puts me in the same positions as in the case of DFPT calculations for dynamical matrices. With DFPT, dynamical matrices are directly determined for a predefined set of **q**-vectors.[17–19] Therefore, from this point on, the technicalities are the same for both methods.

Gonze's method[19] and Wang's method[43] are compared in terms of their description of the phonon dispersion of the prototype material CaF_2 (section 3.3.1). In this study, extensive use is made of the method

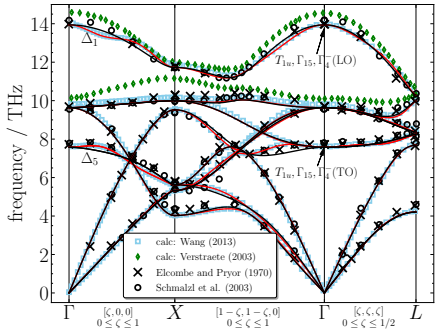

FIGURE 4.1: Phonon dispersion of CaF_2 from dynamical matrices evaluated on a 4^3 $\mathbf{q}_c$-grid. Comparison of Gonze's[19] and Wang's[43] method for the inclusion of dipole-dipole corrections and experimental data from Elcombe and Pryor [126] and Schmalzl et al. [127]. Reproduced from fig. 3.5.

of Lloyd-Williams and Monserrat [20]. Their approach allows to calculate dynamical matrices on a grid of wavevectors from rather small supercells using the direct method.

Indeed, Gonze's method is superior in terms of the convergence of the optical phonon bands with respect to the number **q**-points used in the Fourier interpolation (cf. fig. 4.1). The key to this observation is that Gonze's method circumvents the issue of slow convergence of the Fourier transform of the FCs by only calculating it for some "sufficiently short-ranged" FCs and treating the long-ranged part in a different way (Ewald summations).[19] Wang's method can introduce artificial features in the phonon bandstructure along some directions in reciprocal space. This is exceptionally obvious when interpolated phonon frequencies are compared to exact frequencies at wavevectors not in the **q**-grid used for the Fourier interpolation.

Similar considerations are also made for the copper oxides (section 3.3.2). Reasonable agreement between calculated and measured (Reichardt et al. [163]) phonon bandstructures is achieved for the room temperature structure of monoclinic CuO. In some cases, it is overwhelmingly obvious that dipole-dipole interactions indeed must be included in the calculation of the phonon dispersion in order to achieve agreement with

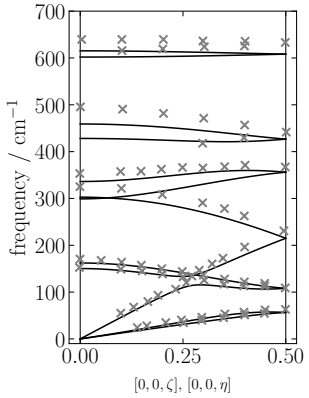

FIGURE 4.2: Phonon bandstructures of the primitive structure of CuO (cf. fig. 3.2c) compared to experimental data from Reichardt et al. [163]. Reproduced from fig. 3.16c

experiment (cf. fig. 4.2). Otherwise, some bands will be deficiently described. While generally only some optical branches are influenced by the dipole-dipole corrections, it may happen (although these cases are rare) that also acoustic phonon branches are affected by the corrections. For the anisotropic material CuO, neglecting the dipole-dipole corrections *or* using Wang's method, can lead to negative eigenvalues of the dynamical matrix for some acoustic branches near the Γ point. By contrast, Gonze's method yields correct frequencies of these phonon modes because it correctly accounts for the long-rangedness of the interactions included in the FCs for polar materials.

The full phonon dispersion of the copper oxides is calculated on the basis of the direct method. In case of monoclinic CuO, the antiferromagnetic groundstate structure[22] is also considered for the phonon calculations which so far has not been the case in literature. Particularly good agreement is found for the lattice contribution to the heat capacity and entropy for Cu_2O and CuO in comparison to experiment.

The second objective of this work is to investigate the Raman scattering properties of CuO and Cu_4O_3 (sections 3.4.2 and 3.4.3). In its room temperature phase CuO is quite extensively studied. In the low temperature regime ($T < 213\,\mathrm{K}$),[22] additional peaks arise in the Raman spectrum compared to room temperature.[24] Only one of the extra Raman active modes (at $\sim 240\,\mathrm{cm}^{-1}$) is well documented in the literature, presumably because it exhibits the largest intensity of all extra modes.[24] In order to contribute to the understanding of the observed phenomena for CuO, the Raman spectra and corresponding phonon modes of the room temperature phase and the low temperature structure (that constitutes the AFM groundstate[22]) are analysed (section 3.4.2). According to the calculations, more additional modes than observed in experiment arise in the Raman spectrum of the low temperature structure. The extra modes from the measurements,[24] however, can be assigned to calculated phonon modes, indeed. It is further shown that the additional Raman active modes (and some additional infra-red active modes) trace back to the X-point of the room temperature structure.[i] The modes become Raman active due to a change in symmetry resulting from a change in magnetic ordering when temperature passes below 213 K.

Experimental Raman spectroscopic investigations of Cu_4O_3 have only recently been carried out.[23,118] So far no calculations involving Raman spectroscopy appear to be present in the literature. In this context, angle dependent Raman intensities are considered for surface orientations found for samples grown by sputter deposition.[23,114] By considering specific scattering geometries, calculations can essentially reproduce the relative peak intensities observed in the measured Raman spectrum (see section 3.4.3).[118]

As a further point (section 3.4.4), the dependence on hydrostatic pressure P of the Raman active modes is investigated. All Raman active modes display changes in frequency of at least $\partial\omega_m/\partial P = 3.7\,\mathrm{cm}^{-1}/\mathrm{GPa}$. Therefore, differences of calculated and measured lattice parameters < 1 % can lead to rather large differences between calculated and measured phonon frequencies. Indeed, agreement between calculated and experimental frequencies is best, if the experimental lattice parameters[119] are used in the calculations (fig. 4.3). While *ab initio* calculations can give a decent account of the vibrational properties of materials (in particular, if experimental lattice parameters are used in the calculations), the much more difficult part is the description of

[i] The label of the **q**-point is adopted from by Kuz'menko et al. [174] and refers to the *conventional* cell choice for the monoclinic unit cell of the room temperature structure.[106]

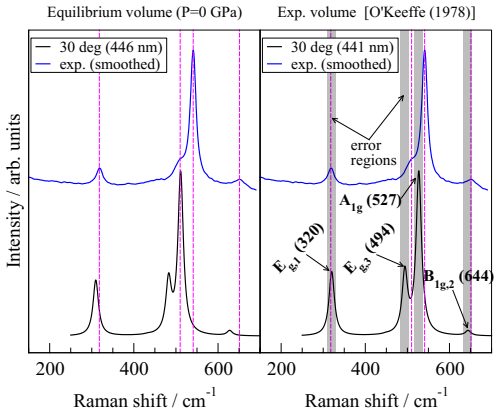

FIGURE 4.3: Semi-polarised Raman spectra of Cu_4O_3 for (left) the $P = 0\,\mathrm{GPa}$ structure and (right) the structure with experimental lattice parameters.[119] Reproduced form fig. 3.48a.

the optical absorption spectra. This directly transfers to the calculation of the Raman scattering intensities. The independent particle approximation used in this work really neglects many contributions to the dielectric function: Neither does it include local field effects (loosely speaking, these are changes in the density on a microscopic scale due to an applied external electric field) nor does it account for excitons. Both effects might be important for a physically adequate description of optical absorption. However, not many theoretical studies involving Raman spectroscopy include the laser frequency dependence of the Raman intensities,[12,209–212] and even fewer consider excitonic effects.[12] Since the dependence of Raman intensities on the laser energy can be substantial, the IPA offers a convenient method which comes with a maintainable computational effort. Indeed, if the number of atoms to be considered for the physical system at hand is rather large ($\gtrsim$100?) it presumably is the only feasible method. Generally, the independent particle framework gives a good "first-order impression" of the frequency dependence of the Raman intensities, but inclusion of excitonic effects might lead to improved comparability to experiment.[12] The calculation of Raman spectra is rather demanding because dielectric functions must be evaluated for several distorted atomic geometries. Inclusion of local field effects, for instance, would require to resort to the *GW* method, making the computational effort "explode".

Finally, it must be appreciated that a good theoretical description of Raman scattering is based on (a) a good description of the phonon structure, and (b) a good description of optical absorption. To my mind, the first point is slightly more essential: The phonon frequencies determine the position of the peaks in the Raman spectrum, while the peak intensities are driven by optical absorption and the phonon eigendisplacements. In particular, if the crystal structure is complicated (e.g., many atoms and low symmetry) many peaks will be visible in the Raman spectrum. If the phonon frequencies compare to within let's say $\sim 5\,\mathrm{cm}^{-1}$ to $10\,\mathrm{cm}^{-1}$ to experiment (and the number of Raman active modes is correct) a valuable contribution to the understanding of measured Raman spectra is achieved. In case the relative intensities of the modes are also well described, this can serve as a beautiful example of a combined theoretical and experimental study. Science, like it should be ...

References

[1] P. Hohenberg, and W. Kohn, Phys. Rev. **136**, B864 (1964) (cit. on pp. iii, 2).

[2] W. Kohn, and L. J. Sham, Phys. Rev. **140**, A1133 (1965) (cit. on pp. iii, 3).

[3] M. Levy, Proc. Natl. Acad. Sci. **76**, 6062 (1979) (cit. on pp. iii, 2).

[4] W. Kohn, Rev. Mod. Phys. **71**, 1253 (1999) (cit. on pp. iii, 3).

[5] E. Runge, and E. K. U. Gross, Phys. Rev. Lett. **52**, 997 (1984) (cit. on p. iii).

[6] S. Botti, A. Schindlmayr, R. D. Sole, and L. Reining, Rep. Prog. Phys. **70**, 357 (2007) (cit. on pp. iii, 24).

[7] L. Hedin, Phys. Rev. **139**, A796 (1965) (cit. on p. iii).

[8] M. van Schilfgaarde, T. Kotani, and S. Faleev, Phys. Rev. Lett. **96**, 226402 (2006) (cit. on p. iii).

[9] G. Onida, L. Reining, and A. Rubio, Rev. Mod. Phys. **74**, 601 (2002) (cit. on pp. iii, 24).

[10] T. Sander, C. T. Reindl, M. Giar, B. Eifert, M. Heinemann, C. Heiliger, and P. J. Klar, Phys. Rev. B **90**, 045203 (2014) (cit. on pp. iii, v, 35, 45).

[11] T. Sander, "Monitoring defect-induced perturbations of the ideal crystal structure of ZnO and Cu_2O by Raman spectroscopy", PhD thesis (Justus-Liebig-Universität Giessen, 2015) (cit. on pp. iii, v, 16, 45).

[12] Y. Gillet, "Ab initio study of Raman and optical spectra of crystalline materials and their temperature dependence", PhD thesis (Université catholique de Louvain, 2017) (cit. on pp. iii–v, 14, 15, 45, 51, 59, 81).

[13] J. Heyd, G. E. Scuseria, and M. Ernzerhof, The Journal of Chemical Physics **118**, 8207 (2003) (cit. on p. iv).

[14] J. Heyd, and G. E. Scuseria, The Journal of Chemical Physics **121**, 1187 (2004) (cit. on p. iv).

[15] J. Heyd, G. E. Scuseria, and M. Ernzerhof, The Journal of Chemical Physics **124**, 219906 (2006) (cit. on p. iv).

[16] A. V. Krukau, O. A. Vydrov, A. F. Izmaylov, and G. E. Scuseria, The Journal of Chemical Physics **125**, 224106 (2006) (cit. on p. iv).

[17] P. Giannozzi, S. de Gironcoli, P. Pavone, and S. Baroni, Phys. Rev. B **43**, 7231 (1991) (cit. on pp. iv, 8, 79).

[18] S. Baroni, S. de Gironcoli, A. Dal Corso, and P. Giannozzi, Rev. Mod. Phys. **73**, 515 (2001) (cit. on pp. iv, 8, 79).

[19] X. Gonze, and C. Lee, Phys. Rev. B **55**, 10355 (1997) (cit. on pp. iv, 8–11, 19, 21, 31, 32, 41, 79).

[20] J. H. Lloyd-Williams, and B. Monserrat, Phys. Rev. B **92**, 184301 (2015) (cit. on pp. iv, 31, 33, 36–38, 79).

[21] A. Compaan, and H. J. Trodahl, Phys. Rev. B **29**, 793 (1984) (cit. on p. v).

[22] J. B. Forsyth, P. J. Brown, and B. M. Wanklyn, J. Phys. C: Solid State Phys. **21**, 2917 (1988) (cit. on pp. v, 27, 28, 35, 36, 41, 54, 56, 57, 80).

[23] B. K. Meyer, A. Polity, D. Reppin, M. Becker, P. Hering, P. J. Klar, T. Sander, C. Reindl, J. Benz, M. Eickhoff, C. Heiliger, M. Heinemann, J. Bläsing, A. Krost, S. Shokovets, C. Müller, and C. Ronning, Phys. Status Solidi B **249**, 1487 (2012) (cit. on pp. v, 27, 28, 35, 48, 50–52, 63–65, 71, 80).

[24] X. K. Chen, J. C. Irwin, and J. P. Franck, Phys. Rev. B **52**, R13130 (1995) (cit. on pp. v, 35, 39, 55, 58–61, 63, 80).

[25] M. Born, and R. Oppenheimer, Ann. Phys. **389**, 457 (1927) (cit. on p. 1).

[26] C.-O. Almbladh, and U. von Barth, Phys. Rev. B **31**, 3231 (1985) (cit. on p. 3).

[27] A. A. Maradudin, and S. H. Vosko, Rev. Mod. Phys. **40**, 1 (1968) (cit. on pp. 6, 7, 15, 17, 31).

[28] A. A. Maradudin, E. W. Montroll, G. H. Weiss, and I. P. Ipatova, *The theory of lattice dynamics in the harmonic approximation*, edited by H. Ehrenreich, F. Seitz, and D. Turnbull, 2nd ed., Solid State Physics, Suppl. 3 (Academic Press, 1971) (cit. on pp. 7, 14, 17, 21, 23).

[29] X. Gonze, Phys. Rev. B **55**, 10337 (1997) (cit. on p. 8).

[30] G. Kresse, J. Furthmüller, and J. Hafner, Europhys. Lett. **32**, 729 (1995) (cit. on pp. 8, 20, 79).

[31] K. Parlinski, Z.-Q. Li, and Y. Kawazoe, Phys. Rev. Lett. **78**, 4063 (1997) (cit. on pp. 8, 9, 19, 79).

[32] A. van de Walle, and G. Ceder, Rev. Mod. Phys. **74**, 11 (2002) (cit. on p. 8).

[33] G. Kresse, and D. Joubert, Phys. Rev. B **59**, 1758 (1999) (cit. on pp. 8, 27).

[34] P. E. Blöchl, Phys. Rev. B **50**, 17953 (1994) (cit. on pp. 8, 27).

[35] G. Kresse, and J. Hafner, Phys. Rev. B **47**, 558 (1993) (cit. on pp. 8, 27).

[36] G. Kresse, and J. Hafner, Phys. Rev. B **49**, 14251 (1994) (cit. on pp. 8, 27).

[37] G. Kresse, and J. Furthmüller, Phys. Rev. B **54**, 11169 (1996) (cit. on pp. 8, 27).

[38] G. Kresse, and J. Furthmüller, Comput. Mat. Sci. **6**, 15 (1996) (cit. on pp. 8, 27).

[39] X. Gonze, B. Amadon, P.-M. Anglade, J.-M. Beuken, F. Bottin, P. Boulanger, F. Bruneval, D. Caliste, R. Caracas, M. Côté, T. Deutsch, L. Genovese, P. Ghosez, M. Giantomassi, S. Goedecker, D. Hamann, P. Hermet, F. Jollet, G. Jomard, S. Leroux, M. Mancini, S. Mazevet, M. Oliveira, G. Onida, Y. Pouillon, T. Rangel, G.-M. Rignanese, D. Sangalli, R. Shaltaf, M. Torrent, M. Verstraete, G. Zérah, and J. Zwanziger, Comput. Phys. Commun. **180**, 2582 (2009) (cit. on pp. 8, 10, 11, 32, 79).

[40] P. Giannozzi, S. Baroni, N. Bonini, M. Calandra, R. Car, C. Cavazzoni, D. Ceresoli, G. L. Chiarotti, M. Cococcioni, I. Dabo, A. D. Corso, S. de Gironcoli, S. Fabris, G. Fratesi, R. Gebauer, U. Gerstmann, C. Gougoussis, A. Kokalj, M. Lazzeri, L. Martin-Samos, N. Marzari, F. Mauri, R. Mazzarello, S. Paolini, A. Pasquarello, L. Paulatto, C. Sbraccia, S. Scandolo, G. Sclauzero, A. P. Seitsonen, A. Smogunov, P. Umari, and R. M. Wentzcovitch, J. Phys.: Condens. Matter **21**, 395502 (2009) (cit. on pp. 8, 10, 11, 79).

[41] D. Alfé, Compt. Phys. Commun. **180**, 2622 (2009) (cit. on pp. 8, 9, 20).

[42] G. Kern, G. Kresse, and J. Hafner, Phys. Rev. B **59**, 8551 (1999) (cit. on pp. 9, 19).

[43] Y. Wang, J. J. Wang, W. Y. Wang, Z. G. Mei, S. L. Shang, L. Q. Chen, and Z. K. Liu, J. Phys.: Condens. Matter **22**, 202201 (2010) (cit. on pp. 10, 13, 31, 34, 79).

[44] S. J. Clark, M. D. Segall, C. J. Pickard, P. J. Hasnip, M. I. J. Probert, K. Refson, and M. C. Payne, Z. Kristallogr. **220**, 567 (2005) (cit. on pp. 10, 11, 79).

[45] Y. Wang, J. E. Saal, Z. Mei, P. Wu, J. Wang, S. Shang, Z.-K. Liu, and L.-Q. Chen, Appl. Phys. Lett. **97**, 162907 (2010) (cit. on pp. 10, 79).

[46] Y. Wang, J. E. Saal, J.-J. Wang, A. Saengdeejing, S.-L. Shang, L.-Q. Chen, and Z.-K. Liu, Phys. Rev. B **82**, 081104 (2010) (cit. on pp. 10, 79).

[47] Y. Wang, J. J. Wang, J. E. Saal, S. L. Shang, L.-Q. Chen, and Z.-K. Liu, Phys. Rev. B **82**, 172503 (2010) (cit. on pp. 10, 79).

[48] Y. Wang, J. E. Saal, P. Wu, J. Wang, S. Shang, Z.-K. Liu, and L.-Q. Chen, Acta Mater. **59**, 4229 (2011) (cit. on pp. 10, 79).

[49] Y. Wang, H. Fang, C. L. Zacherl, Z. Mei, S. Shang, L.-Q. Chen, P. D. Jablonski, and Z.-K. Liu, Surf. Sci. **606**, 1422 (2012) (cit. on pp. 10, 79).

[50] Y. Wang, S. Shang, Z.-K. Liu, and L.-Q. Chen, Phys. Rev. B **85**, 224303 (2012) (cit. on pp. 10, 13, 34, 79).

[51] Y. Wang, L. A. Zhang, S. Shang, Z.-K. Liu, and L.-Q. Chen, Phys. Rev. B **88**, 024304 (2013) (cit. on pp. 10, 30–32, 79).

[52] Y. Wang, L.-Q. Chen, and Z.-K. Liu, Comput. Phys. Commun. **185**, 2950 (2014) (cit. on pp. 10, 79).

[53] A. Togo, L. Chaput, and I. Tanaka, Phys. Rev. B **91**, 094306 (2015) (cit. on pp. 10, 79).

[54] A. Togo, F. Oba, and I. Tanaka, Phys. Rev. B **78**, 134106 (2008) (cit. on p. 10).

[55] R. Dovesi, R. Orlando, A. Erba, C. M. Zicovich-Wilson, B. Civalleri, S. Casassa, L. Maschio, M. Ferrabone, M. De La Pierre, P. D'Arco, Y. Noël, M. Causá, M. Rérat, and B. Kirtman, Int. J. Quantum Chem. **114**, 1287 (2014) (cit. on p. 10).

[56] W. Li, J. Carrete, N. A. Katcho, and N. Mingo, Comput. Phys. Commun. **185**, 1747 (2014) (cit. on p. 10).

[57] A. Chernatynskiy, and S. R. Phillpot, Comput. Phys. Commun. **192**, 196 (2015) (cit. on p. 10).

[58] C. V. Raman, Ind. J. Phys. **2**, 387 (1928) (cit. on p. 13).

[59] C. V. Raman, Nature **121**, 619 (1928) (cit. on p. 13).

[60] P. Y. Yu, and M. Cardona, *Fundamentals of semiconductors*, edited by C.-D. Bachem, 3rd ed. (Springer Berlin Heidelberg New York, 2005) (cit. on pp. 13–15).

[61] A. Authier, ed., *International tables for crystallography, volume d: physical properties of crystals*, 1st (Kluwer Academic Publishers, 2003) (cit. on pp. 14, 16, 17).

[62] M. Veithen, X. Gonze, and P. Ghosez, Phys. Rev. B **71**, 125107 (2005) (cit. on p. 14).

[63] M. S. Dresselhaus, G. Dresselhaus, and A. Jorio, *Group theory: application to the physics of condensed matter*, 1st ed. (Springer-Verlag Berlin Heidelberg, 2008) (cit. on pp. 15, 16).

[64] R. S. Mulliken, The Journal of Chemical Physics **23**, 1997 (1955) (cit. on p. 16).

[65] R. S. Mulliken, The Journal of Chemical Physics **24**, 1118 (1956) (cit. on p. 16).

[66] M. Born, and K. Huang, *Dynamical theory of crystal lattices*, edited by E. F. Mott, E. C. Bullard, and D. H. Wilkinson, (Oxford Press, 1954) (cit. on pp. 20, 23).

[67] P. Umari, A. Pasquarello, and A. Dal Corso, Phys. Rev. B **63**, 094305 (2001) (cit. on p. 24).

[68] M. Veithen, X. Gonze, and P. Ghosez, Phys. Rev. B **71**, 125107 (2005) (cit. on p. 24).

[69] Y. Gillet, M. Giantomassi, and X. Gonze, Phys. Rev. B **88**, 094305 (2013) (cit. on p. 24).

[70] S. L. Adler, Phys. Rev. **126**, 413 (1962) (cit. on p. 24).

[71] N. Wiser, Phys. Rev. **129**, 62 (1963) (cit. on p. 24).

[72] S. Albrecht, L. Reining, R. Del Sole, and G. Onida, Phys. Rev. Lett. **80**, 4510 (1998) (cit. on p. 24).

[73] L. X. Benedict, E. L. Shirley, and R. B. Bohn, Phys. Rev. Lett. **80**, 4514 (1998) (cit. on p. 24).

[74] M. Rohlfing, and S. G. Louie, Phys. Rev. Lett. **81**, 2312 (1998) (cit. on p. 24).

[75] M. Gajdos, K. Hummer, G. Kresse, J. Furthmüller, and F. Bechstedt, Phys. Rev. B **73**, 045112 (2006) (cit. on p. 24).

[76] D. Kammerlander, S. Botti, M. A. L. Marques, A. Marini, and C. Attaccalite, Phys. Rev. B **86**, 125203 (2012) (cit. on p. 24).

[77] L. O. Grondahl, Rev. Mod. Phys. **5**, 141 (1933) (cit. on p. 27).

[78] W. H. Brattain, Rev. Mod. Phys. **23**, 203 (1951) (cit. on p. 27).

[79] Y. Wang, P. Miska, D. Pilloud, D. Horwat, F. Mücklich, and J. F. Pierson, J. Appl. Phys. **115**, 073505 (2014) (cit. on p. 27).

[80] P. W. Baumeister, Phys. Rev. **121**, 359 (1961) (cit. on p. 27).

[81] S. P. Tandon, and J. P. Gupta, Phys. Status Solidi B **37**, 43 (1970) (cit. on p. 27).

[82] B. Rai, Sol. Cells **25**, 265 (1988) (cit. on p. 27).

[83] J. Ghijsen, L. H. Tjeng, J. van Elp, H. Eskes, J. Westerink, G. A. Sawatzky, and M. T. Czyzyk, Phys. Rev. B **38**, 11322 (1988) (cit. on p. 27).

[84] A. Önsten, M. Månsson, T. Claesson, T. Muro, T. Matsushita, T. Nakamura, T. Kinoshita, U. O. Karlsson, and O. Tjernberg, Phys. Rev. B **76**, 115127 (2007) (cit. on p. 27).

[85] J. P. Hu, D. J. Payne, R. G. Egdell, P.-A. Glans, T. Learmonth, K. E. Smith, J. Guo, and N. M. Harrison, Phys. Rev. B **77**, 155115 (2008) (cit. on p. 27).

[86] T. Minami, Y. Nishi, and T. Miyata, Appl. Phys. Lett. **105**, 212104 (2014) (cit. on p. 27).

[87] Y. Ievskaya, R. Hoye, A. Sadhanala, K. Musselman, and J. MacManus-Driscoll, Sol. Energy Mater. Sol. Cells **135**, 43 (2015) (cit. on p. 27).

[88] Y. Wang, S. Lany, J. Ghanbaja, Y. Fagot-Revurat, Y. P. Chen, F. Soldera, D. Horwat, F. Mücklich, and J. F. Pierson, Phys. Rev. B **94**, 245418 (2016) (cit. on pp. 27, 51, 56, 63–66, 68, 69, 76, 77).

[89] J. Dahl, and A. Switendick, J. Phys. Chem. Solids **27**, 931 (1966) (cit. on p. 27).

[90] P. Marksteiner, P. Blaha, and K. Schwarz, Z. Phys. B: Condens. Matter **64**, 119 (1986) (cit. on p. 27).

[91] W. Y. Ching, Y.-N. Xu, and K. W. Wong, Phys. Rev. B **40**, 7684 (1989) (cit. on p. 27).

[92] E. Ruiz, S. Alvarez, P. Alemany, and R. A. Evarestov, Phys. Rev. B **56**, 7189 (1997) (cit. on p. 27).

[93] R. Laskowski, P. Blaha, and K. Schwarz, Phys. Rev. B **67**, 075102 (2003) (cit. on p. 27).

[94] M. Nolan, and S. D. Elliott, Phys. Chem. Chem. Phys. **8**, 5350 (2006) (cit. on p. 27).

[95] F. Bruneval, N. Vast, L. Reining, M. Izquierdo, F. Sirotti, and N. Barrett, Phys. Rev. Lett. **97**, 267601 (2006) (cit. on p. 27).

[96] T. Kotani, M. van Schilfgaarde, and S. V. Faleev, Phys. Rev. B **76**, 165106 (2007) (cit. on p. 27).

[97] D. O. Scanlon, B. J. Morgan, and G. W. Watson, J. Chem. Phys. **131**, 124703, 124703 (2009) (cit. on p. 27).

[98] D. O. Scanlon, B. J. Morgan, G. W. Watson, and A. Walsh, Phys. Rev. Lett. **103**, 096405 (2009) (cit. on p. 27).

[99] F. Tran, and P. Blaha, Phys. Rev. B **83**, 235118 (2011) (cit. on p. 27).

[100] M. Heinemann, B. Eifert, and C. Heiliger, Phys. Rev. B **87**, 115111 (2013) (cit. on pp. 27, 28, 57).

[101] X.-G. Yan, L. Xu, W.-Q. Huang, G.-F. Huang, Z.-M. Yang, S.-Q. Zhan, and J.-P. Long, Mater. Sci. Semicond. Process. **23**, 34 (2014) (cit. on p. 27).

[102] X. G. Zheng, C. N. Xu, Y. Tomokiyo, E. Tanaka, H. Yamada, and Y. Soejima, Phys. Rev. Lett. **85**, 5170 (2000) (cit. on p. 27).

[103] C. Ekuma, V. Anisimov, J. Moreno, and M. Jarrell, Eur. Phys. J. B **87**, 23 (2014) (cit. on p. 27).

[104] X. Rocquefelte, M.-H. Whangbo, A. Villesuzanne, S. Jobic, F. Tran, K. Schwarz, and P. Blaha, J. Phys.: Condens. Matter **22**, 045502 (2010) (cit. on p. 27).

[105] C. Rödl, F. Sottile, and L. Reining, Phys. Rev. B **91**, 045102 (2015) (cit. on pp. 27, 51, 57).

[106] S. Åsbrink, and L.-J. Norrby, Acta Crystallogr. Sect. B **26**, 8 (1970) (cit. on pp. 27, 28, 38, 52, 54, 60, 61, 80).

[107] B. X. Yang, J. M. Tranquada, and G. Shirane, Phys. Rev. B **38**, 174 (1988) (cit. on p. 27).

[108] B. X. Yang, T. R. Thurston, J. M. Tranquada, and G. Shirane, Phys. Rev. B **39**, 4343 (1989) (cit. on p. 27).

[109] M. Aïn, W. Reichardt, B. Hennion, G. Pepy, and B. M. Wanklyn, Physica C: Supercond. **162**, 1279 (1989) (cit. on p. 27).

[110] P. J. Brown, T. Chattopadhyay, J. B. Forsyth, and V. Nunez, J. Phys.: Condens. Matter **3**, 4281 (1991) (cit. on p. 27).

[111] H. Yamada, X.-G. Zheng, Y. Soejima, and M. Kawaminami, Phys. Rev. B **69**, 104104 (2004) (cit. on p. 27).

[112] K.-Y. Choi, W.-J. Lee, A. Glamazda, P. Lemmens, D. Wulferding, Y. Sekio, and T. Kimura, Phys. Rev. B **87**, 184407 (2013) (cit. on pp. 27, 35, 39, 63).

[113] M.-H. Whangbo, and H.-J. Koo, Inorg. Chem. **41**, 3570 (2002) (cit. on p. 27).

[114] J. Pierson, A. Thobor-Keck, and A. Billard, Appl. Surf. Sci. **210**, 359 (2003) (cit. on pp. 27, 63, 71, 80).

[115] J. Pierson, E. Duverger, and O. Banakh, J. Solid State Chem. **180**, 968 (2007) (cit. on pp. 27, 63, 71).

[116] L. Debbichi, M. C. M. de Lucas, and P. Krüger, Mater. Chem. Phys. **148**, 293 (2014) (cit. on pp. 27, 35, 75).

[117] V. I. Anisimov, J. Zaanen, and O. K. Andersen, Phys. Rev. B **44**, 943 (1991) (cit. on p. 27).

[118] L. Debbichi, M. C. M. de Lucas, J. F. Pierson, and P. Krüger, J. Phys. Chem. C **116**, 10232 (2012) (cit. on pp. 27, 28, 35, 61, 63, 71–76, 80).

[119] M. O'Keeffe, and J.-O. Bovin, Am. Mineral. **63**, 180 (1978) (cit. on pp. 27, 28, 63, 73–76, 80, 81).

[120] A. I. Liechtenstein, V. I. Anisimov, and J. Zaanen, Phys. Rev. B **52**, R5467 (1995) (cit. on p. 27).

[121] C. J. Bradley, and A. P. Cracknell, *The mathematical theory of symmetry in solids* (Oxford University Press, 1972) (cit. on pp. 28, 29, 42).

[122] G. W. Rubloff, Phys. Rev. B **5**, 662 (1972) (cit. on p. 30).

[123] R. W. G. Wyckoff, *Crystal structures*, 9th ed., Vol. 1 (Interscience/John Wiley, New York, 1963) (cit. on pp. 30–32).

[124] Y. Ma, and M. Rohlfing, Phys. Rev. B **75**, 205114 (2007) (cit. on p. 30).

[125] M. Verstraete, and X. Gonze, Phys. Rev. B **68**, 195123 (2003) (cit. on pp. 30, 32, 34).

[126] M. M. Elcombe, and A. W. Pryor, J. Phys C: Solid State Phys. **3**, 492 (1970) (cit. on pp. 30, 32, 79).

[127] K. Schmalzl, D. Strauch, and H. Schober, Phys. Rev. B **68**, 144301 (2003) (cit. on pp. 30, 32, 79).

[128] A. K. McCurdy, Phys. Rev. B **26**, 6971 (1982) (cit. on p. 30).

[129] A. Feldman, and R. M. Waxler, Phys. Rev. Lett. **45**, 126 (1980) (cit. on p. 30).

[130] W. Kaiser, W. G. Spitzer, R. H. Kaiser, and L. E. Howarth, Phys. Rev. **127**, 1950 (1962) (cit. on p. 30).

[131] J. P. Russell, Proc. Phys. Soc. London 85, 194 (1965). **85**, 194 (1965) (cit. on p. 30).

[132] C. Yan, H. Cui-E, Z. Zhao-Yi, G. Min, and G. Qing-Quan, Commun. Theor. Phys. (Beijing, China) **51**, 904 (2009) (cit. on p. 30).

[133] H. R. Soni, S. K. Gupta, M. Talati, and P. K. Jha, J. Phys. Chem. Solids **72**, 934 (2011) (cit. on p. 30).

[134] J. P. Perdew, K. Burke, and M. Ernzerhof, Phys. Rev. Lett. **77**, 3865 (1996) (cit. on p. 31).

[135] W. Cochran, and R. Cowley, J. Phys. Chem. Solids **23**, 447 (1962) (cit. on p. 34).

[136] M. O'Keeffe, J. Chem. Phys. **39**, 1789 (1963) (cit. on p. 35).

[137] K. Huang, Z. Phys. **171**, 213 (1963) (cit. on p. 35).

[138] E. C. Heltemes, Phys. Rev. **141**, 803 (1966) (cit. on p. 35).

[139] M. Balkanski, M. A. Nusimovici, and J. Reydellet, Solid State Commun. **7**, 815 (1969) (cit. on p. 35).

[140] C. Carabatos, Phys. Status Solidi B **37**, 773 (1970) (cit. on p. 35).

[141] C. Carabatos, and B. Prevot, Phys. Status Solidi B **44**, 701 (1971) (cit. on p. 35).

[142] J. Reydellet, M. Balkanski, and D. Trivich, Phys. Status Solidi B **52**, 175 (1972) (cit. on p. 35).

[143] P. F. Williams, and S. P. S. Porto, Phys. Rev. B **8**, 1782 (1973) (cit. on p. 35).

[144] P. Dawson, M. M. Hargreave, and G. Wilkinson, J. Phys. Chem. Solids **34**, 2201 (1973) (cit. on p. 35).

[145] A. Compaan, and H. Z. Cummins, Phys. Rev. Lett. **31**, 41 (1973) (cit. on p. 35).

[146] P. Y. Yu, Y. R. Shen, Y. Petroff, and L. M. Falicov, Phys. Rev. Lett. **30**, 283 (1973) (cit. on p. 35).

[147] P. Yu, Y. Shen, and Y. Petroff, Solid State Commun. **12**, 973 (1973) (cit. on p. 35).

[148] C.-H. Wu, and J. L. Birman, Solid State Commun. **14**, 465 (1974) (cit. on p. 35).

[149] P. Y. Yu, and Y. R. Shen, Phys. Rev. Lett. **32**, 373 (1974) (cit. on p. 35).

[150] A. Compaan, Solid State Commun. **16**, 293 (1975) (cit. on p. 35).

[151] Y. Petroff, P. Y. Yu, and Y. R. Shen, Phys. Rev. B **12**, 2488 (1975) (cit. on p. 35).

[152] D. Powell, A. Compaan, J. R. Macdonald, and R. A. Forman, Phys. Rev. B **12**, 20 (1975) (cit. on p. 35).

[153] M. M. Beg, and S. M. Shapiro, Phys. Rev. B **13**, 1728 (1976) (cit. on pp. 35, 36).

[154] P. Y. Yu, and Y. R. Shen, Phys. Rev. B **17**, 4017 (1978) (cit. on p. 35).

[155] M. A. Washington, A. Z. Genack, H. Z. Cummins, R. H. Bruce, A. Compaan, and R. A. Forman, Phys. Rev. B **15**, 2145 (1977) (cit. on p. 35).

[156] K. Reimann, and K. Syassen, Phys. Rev. B **39**, 11113 (1989) (cit. on p. 35).

[157] M. Ivanda, D. Waasmaier, A. Endriss, J. Ihringer, A. Kirfel, and W. Kiefer, J. Raman Spectrosc. **28**, 487 (1997) (cit. on p. 35).

[158] R. Mittal, S. L. Chaplot, S. K. Mishra, and P. P. Bose, Phys. Rev. B **75**, 174303 (2007) (cit. on p. 35).

[159] K.-P. Bohnen, R. Heid, L. Pintschovius, A. Soon, and C. Stampfl, Phys. Rev. B **80**, 134304 (2009) (cit. on pp. 35, 36).

[160] Z. Popovic, C. Thomsen, M. Cardona, R. Liu, G. Stanisic, R. Kremer, and W. König, Solid State Commun. **66**, 965 (1988) (cit. on p. 35).

[161] J. Chrzanowski, and J. C. Irwin, Solid State Commun. **70**, 11 (1989) (cit. on pp. 35, 39, 61, 63).

[162] A. Junod, D. Eckert, G. Triscone, J. Müller, and W. Reichardt, J. Phys.: Condens. Matter **1**, 8021 (1989) (cit. on pp. 35, 41, 43, 44).

[163] W. Reichardt, F. Gompf, M. Aïn, and B. M. Wanklyn, Z. Phys. B Condens. Matter **81**, 19 (1990) (cit. on pp. 35, 39–42, 60, 61, 79, 80).

[164] H. Hagemann, H. Bill, W. Sadowski, E. Walker, and M. François, Solid State Commun. **73**, 447 (1990) (cit. on pp. 35, 39, 63).

[165] H. F. Goldstein, D. S. Kim, P. Y. Yu, L. C. Bourne, J.-P. Chaminade, and L. Nganga, Phys. Rev. B **41**, 7192 (1990) (cit. on p. 35).

[166] J. Irwin, J. Chrzanowski, T. Wei, D. Lockwood, and A. Wold, Physica C: Supercond. **166**, 456 (1990) (cit. on pp. 35, 39, 55, 63).

[167] K. Reimann, and K. Syassen, Solid State Commun. **76**, 137 (1990) (cit. on p. 35).

[168] G. Kliche, and Z. V. Popovic, Phys. Rev. B **42**, 10060 (1990) (cit. on pp. 35, 61).

[169] J. C. Irwin, T. Weit, and J. Franck, J. Phys.: Condens. Matter **3**, 299 (1991) (cit. on pp. 35, 63).

[170] S. Guha, D. Peebles, and T. J. Wieting, English, Bull. Mater. Sci. **14**, 539 (1991) (cit. on pp. 35, 61, 63).

[171] S. Guha, D. Peebles, and T. J. Wieting, Phys. Rev. B **43**, 13092 (1991) (cit. on pp. 35, 61, 63).

[172] S. N. Narang, V. Kartha, and N. Patel, Physica C: Supercond. **204**, 8 (1992) (cit. on pp. 35, 61).

[173] C. C. Homes, M. Ziaei, B. P. Clayman, J. C. Irwin, and J. P. Franck, Phys. Rev. B **51**, 3140 (1995) (cit. on pp. 35, 61).

[174] A. B. Kuz'menko, D. van der Marel, P. J. M. van Bentum, E. A. Tishchenko, C. Presura, and A. A. Bush, Phys. Rev. B **63**, 094303 (2001) (cit. on pp. 35, 60, 61, 80).

[175] Z. Wang, V. Pischedda, S. K. Saxena, and P. Lazor, Solid State Commun. **121**, 275 (2002) (cit. on p. 35).

[176] A. P. Litvinchuk, A. Möller, L. D. P. Krüger, M. N. Iliev, and M. M. Gospodinov, J. Phys.: Condens. Matter **25**, 105402 (2013) (cit. on pp. 35, 63).

[177] M. K. Gupta, R. Mittal, S. L. Chaplot, and S. Rols, J. Appl Phys. **115**, 093507 (2014) (cit. on p. 35).

[178] L. H. N. Rimmer, M. T. Dove, B. Winkler, D. J. Wilson, K. Refson, and A. L. Goodwin, Phys. Rev. B **89**, 214115 (2014) (cit. on p. 35).

[179] M. Giar, M. Heinemann, and C. Heiliger, Phys. Rev. B **96**, 075202 (2017) (cit. on p. 35).

[180] G. E. Kugel, C. Carabatos, and W. Kress, "*Ab Initio* calculation of phonon spectra", in, edited by J. T. Devreese, V. E. V. Doren, and P. E. V. Camp, (Plenum, New York, 1983), p. 101 (cit. on pp. 35, 36).

[181] K. Gaál-Nagy, Phys. Rev. B **77**, 024309 (2008) (cit. on p. 41).

[182] J. Berger, Solid State Commun. **26**, 403 (1978) (cit. on p. 42).

[183] M. H. Manghnani, W. S. Brower, and H. S. Parker, Phys. Status Solidi A **25**, 69 (1974) (cit. on pp. 42, 43).

[184] J.-H. Hu, and H. L. Johnston, J. Am. Chem. Soc. **73**, 4550 (1951) (cit. on pp. 41, 43).

[185] O. Madelung, U. Rössler, and M. Schulz, eds., *Landolt-börnstein: numerical data and functional relationships in science and technology*, Vol. III/41, C: Non-Tetrahedrally Bonded Elements and Binary Compounds I (Springer-Verlag Berlin Heidelberg, 1998) (cit. on p. 43).

[186] G. K. White, J. Phys. C: Solid State Phys. **11**, 2171 (1978) (cit. on p. 43).

[187] J.-H. Hu, and H. L. Johnston, J. Am. Chem. Soc. **75**, 2471 (1953) (cit. on pp. 41, 43, 44).

[188] J. W. Loram, K. A. Mirza, C. P. Joyce, and A. J. Osborne, Europhys. Lett. **8**, 263 (1989) (cit. on pp. 41, 43, 44).

[189] E. Gmelin, W. Brill, and T. Chattopadhyay, Thermochim. Acta **160**, 43 (1990) (cit. on pp. 41, 43, 44).

[190] R. W. Millar, J. Am. Chem. Soc. **51**, 215 (1929) (cit. on p. 41).

[191] E. Gmelin, U. Köbler, W. Brill, T. Chattopadhyay, and S. Sastry, Bull. Mater. Sci. **14**, 117 (1991) (cit. on pp. 41, 44).

[192] J. Harl, "The linear response function in density functional theory: optical spectra and improved description of the electron correlation", PhD thesis (Unversität Wien, 2008) (cit. on p. 49).

[193] V. Lebedev, and D. Laikov, Doklady Mathematics **59**, 477 (1999) (cit. on pp. 49, 50).

[194] D. Tahir, and S. Tougaard, J. Phys.: Condens. Matter **24**, 175002 (2012) (cit. on pp. 50, 51, 57).

[195] C. Rödl, "Elektronische und exzitonische Anregungen in magnetischen Isolatoren", PhD thesis (Friedrich-Schiller-Universität Jena, 2009) (cit. on p. 51).

[196] F. Marabelli, G. B. Parravicini, and F. Salghetti-Drioli, Phys. Rev. B **52**, 1433 (1995) (cit. on pp. 51, 57, 59).

[197] J. Perez-Mato, S. Gallego, E. Tasci, L. Elcoro, G. de la Flor, and M. Aroyo, Annu. Rev. Mater. Res. **45**, 217 (2015) (cit. on p. 54).

[198] S. V. Gallego, J. M. Perez-Mato, L. Elcoro, E. S. Tasci, R. M. Hanson, K. Momma, M. I. Aroyo, and G. Madariaga, J. Appl. Crystallogr. **49**, 1750 (2016) (cit. on p. 54).

[199] S. V. Gallego, J. M. Perez-Mato, L. Elcoro, E. S. Tasci, R. M. Hanson, M. I. Aroyo, and G. Madariaga, J. Appl. Crystallogr. **49**, 1941 (2016) (cit. on p. 54).

[200] G. Güntherodt, W. Bauhofer, and G. Benedek, Phys. Rev. Lett. **43**, 1427 (1979) (cit. on pp. 55, 56).

[201] W. Bauhofer, G. Güntherodt, E. Anastassakis, A. Frey, and G. Benedek, Phys. Rev. B **22**, 5873 (1980) (cit. on pp. 55, 56).

[202] T. Masumi, H. Yamaguchi, T. Ito, and H. Shimoyama, J. Phys. Soc. Jpn. **67**, 67 (1998) (cit. on p. 56).

[203] E. Anderson, Z. Bai, C. Bischof, S. Blackford, J. Demmel, J. Dongarra, J. Du Croz, A. Greenbaum, S. Hammarling, A. McKenney, and D. Sorensen, *LAPACK users' guide*, Third (Society for Industrial and Applied Mathematics, Philadelphia, PA, 1999) (cit. on pp. 58, 65).

[204] S. A. Prosandeev, U. Waghmare, I. Levin, and J. Maslar, Phys. Rev. B **71**, 214307 (2005) (cit. on p. 58).

[205] C. Frondel, Am. Mineral. **26**, 657 (1941) (cit. on pp. 63, 74).

[206] H. T. Stokes, and D. M. Hatch, J. Appl. Crystallogr. **38**, 237 (2005) (cit. on pp. 64, 65).

[207] W. R. Inc., *Mathematica, Version 10.2.0.0*, Champaign, IL, 2017 (cit. on p. 67).

[208] M. Weinhold, and P. P. J. Klar, private communications, 2017 (cit. on p. 71).

[209] P. Puschnig, C. Ambrosch-Draxl, R. W. Henn, and A. Simon, Phys. Rev. B **64**, 024519 (2001) (cit. on p. 81).

[210] C. Ambrosch-Draxl, H. Auer, R. Kouba, E. Y. Sherman, P. Knoll, and M. Mayer, Phys. Rev. B **65**, 064501 (2002) (cit. on p. 81).

[211] P. Ravindran, A. Kjekshus, H. Fjellvåg, P. Puschnig, C. Ambrosch-Draxl, L. Nordström, and B. Johansson, Phys. Rev. B **67**, 104507 (2003) (cit. on p. 81).

[212] S. Sanna, S. Neufeld, M. Rüsing, G. Berth, A. Zrenner, and W. G. Schmidt, Phys. Rev. B **91**, 224302 (2015) (cit. on p. 81).

Acknowledgements

Firstly, I want to sincerely thank my advisor Prof. Dr. Christian Heiliger for letting me work on this challenging topic. His great physical intuition and his keen insight helped me understand and solve the problems that arose during the course of this work. His immense patience, his constant encouragement to try out new things, and his willingness to discuss seemingly trivial issues always gave me the feeling that he believed more in my work than I do. I particularly find our very instructional conference trips memorable.

I also want to express my gratitude to Prof. Dr. Simone Sanna who, although he has only recently joined us at the theory department, has immediately proved to be an invaluable partner for discussions. I particularly had much benefit from his knowledge in the field of solid state spectroscopy. I also thank him for rendering the second opinion on this thesis.

My thanks also go to Carsten Mahr and my (former) colleagues Dr. Robert Henrich, Markus Heinemann, Dr. Michael Bachmann, and Dr. Christian Franz. Carsten tremendously refined my mathematical understanding of theoretical solid state physics, while Markus and Michael indeed were good scientific "role models". I am also grateful for the joyful long evenings we had over the past years.

Dr. Michael Czerner always had an open ear for programming related questions. I am particularly indepted to him for introducing me to HPC cluster administration.

Together with Dr. Michael Feldmann I had the chance to visit many interesting "HiPerCH" workshops. With him, I very much enjoyed discussing Linux and programming related topics and issues.

I had the pleasure to have many long discussions with Prof. Dr. Peter Klar, Dr. Limei Chen, and Dr. Thomas Sander that helped me understand details of the Raman effect and to get to know an experimentalist's perspective.

I want to thank the technical and administrative staff of the Institut für Theoretische Physik and the I. Physikalisches Institut for keeping all the "little things" (travel applications and so forth) running so well.

I acknowledge funding from the Justus-Liebig-Universität Gießen via the postgraduate scholarship (Graduiertenstipendium).

Last but above all, I am deeply grateful to my parents for supporting me so much over the last ten years and helping me keep my head up. I doubt having finished this work without their encouragement. And of course Petra: thank you for your love, your passionate endorsement and your everlasting patience; I cannot imagine anything better than you having happened to me.

Eidesstattliche Erklärung

Ich erkläre: Ich habe die vorgelegte Dissertation selbständig und ohne unerlaubte fremde Hilfe und nur mit den Hilfen angefertigt, die ich in der Dissertation angegeben habe. Alle Textstellen, die wörtlich oder sinngemäß aus veröffentlichten Schriften entnommen sind, und alle Angaben, die auf mündlichen Auskünften beruhen, sind als solche kenntlich gemacht. Bei den von mir durchgeführten und in der Dissertation erwähnten Untersuchungen habe ich die Grundsätze guter wissenschaftlicher Praxis, wie sie in der „Satzung der Justus-Liebig-Universität Gießen zur Sicherung guter wissenschaftlicher Praxis“ niedergelegt sind, eingehalten.

Marcel Giar

Gießen, den 9. Oktober 2017